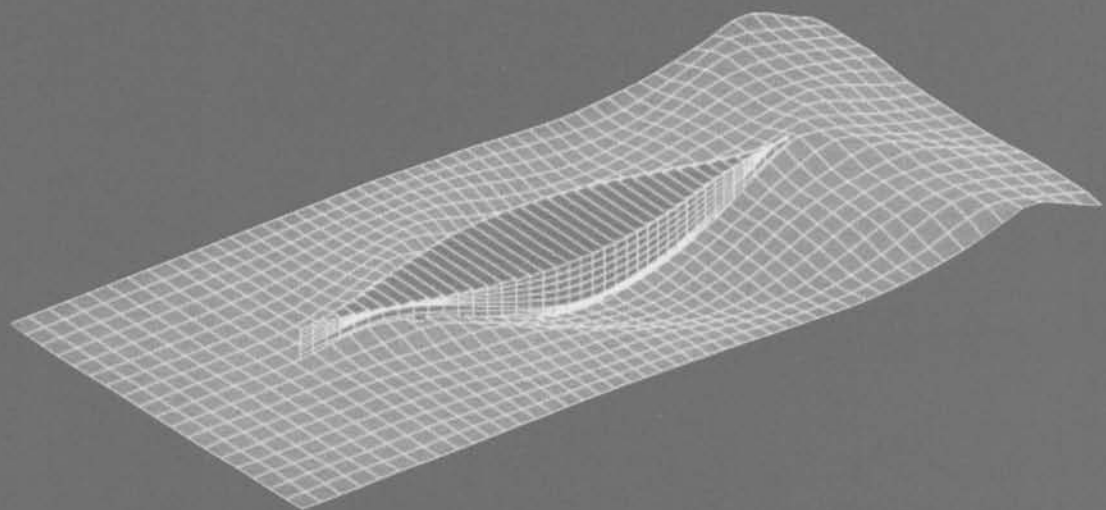


Proceedings  
13th International Workshop  
on  
Water Waves and Floating Bodies



29 March - 1 April 1998

Alphen aan den Rijn,

The Netherlands

Editor: A.J. Hermans

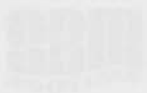


122251

The Workshop is sponsored by



bluewater engineering Busseler Engineering



AM, Department



**P r o c e e d i n g s**

**13th International Workshop**

**on**

**Water Waves and Floating Bodies**

**29 March - 1 April 1998**

**Alphen aan den Rijn,**

**The Netherlands**

**Bibliotheek TU Delft**



**C 0003814055**

*Edited by A.J. Hermans*

**Department of Applied Mathematics**

**Delft University of Technology**

**2414  
404  
0**

ISBN 90-407-1673-0

Copyright © 1998 by: A.J. Hermans

All rights reserved. No part of the material protected by this copyright notice may be reproduced or utilized in any form or by any means, electronic or mechanical, including photocopying, recording or by any information storage and retrieval system, without permission from the publisher.

Printed in the Netherlands

The Workshop is sponsored by

 **TU Delft**

Delft University of Technology

Delft University of Technology

 **Allseas**  
Engineering bv

Allseas Engineering

 **MARIN**

Maritime Research Institute Netherlands

bluewater engineering b.v. Bluewater Engineering

 **SBN**  
OFFSHORE SYSTEMS

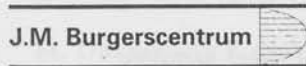
Single Buoy Moorings Inc.

 **IHC GUSTO**  
ENGINEERING

IHC Gusto Engineering B.V.

 **H**  
MARINE  
CONTRACTORS

Heerema Offshore Construction Group b.v.

 **J.M. Burgerscentrum**

Onderzoekschool voor Stromingsleer



Ministerie van Verkeer en Waterstaat/  
Directoraat-Generaal Goederenvervoer



Office of Naval Research Europe

This work relates to Department of the Navy Grant N00014-98-1-1021 issued by the Office of Naval Research European Office. The United States has a royalty-free license throughout the world in all copyrightable material contained herein.

## CONTENTS

<b>T.S. Angell, G.C. Hsiao, R.E. Kleinman and T. Miloh, <i>On minimizing wave resistance or drag</i></b> .....	1
<b>Harry B. Bingham, <i>Computing the Green function for linear wave-body interaction</i></b> .....	5
<b>Bjarne Buchmann, Pierre Ferrant and Jesper Skourup, <i>Runup on a Body in Waves and Current. Fully Non-Linear and Finite Order Calculations</i></b> .....	9
<b>Tim H.J. Bunnik and Aad J. Hermans, <i>Stability analysis for the 3D unsteady free-surface condition with raised panels</i></b> .....	13
<b>Xiao-Bo Chen and Francis Noblesse, <i>Super Green functions for generic dispersive waves</i></b> .....	17
<b>Alain Clément, <i>Computation of impulse response function using differential properties of the time-domain Green function</i></b> .....	21
<b>Heike Cramer, Volker Bertram and Gerhart Thiart, <i>A fully 3-d Rankine method for ship seakeeping</i></b> .....	25
<b>Donald Danmeier, <i>Multiple-body simulations using a higher-order panel code</i></b> .....	28
<b>Odd M. Faltinsen and Rong Zhao, <i>Water entry of a wedge into a channel</i></b> .....	32
<b>Emmanuel Fontaine and M.P. Tulin, <i>On the generation of wave free oscillatory bodies and of trapped modes</i></b> .....	36
<b>Stéphan T. Grilli and Zhimin Hu, <i>Modeling of instabilities of oil containment systems by a vortex sheet method</i></b> .....	40
<b>Morton Huseby and John Grue, <i>An experimental investigation of higher harmonic forces on a vertical cylinder in long waves</i></b> .....	43
<b>D. Indejtchev and Yu. Mochalova, <i>Trapped modes in wave channel with an elastic plate on the bottom</i></b> .....	47
<b>Hidetsugu Iwashita, <i>Influence of the steady flow in seakeeping of a blunt ship through the free-surface condition</i></b> .....	51
<b>Hiroshi Kagimoto, <i>Wave decay characteristics along a long array of cylindrical legs</i></b> .....	55
<b>Seppo Kalske, <i>Unsteady bow wave field and added resistance of ships in short waves</i></b> .....	59
<b>Masashi Kashiwagi, <i>A new direct method for calculating hydroelastic deflection of a very large floating structure in waves</i></b> .....	63
<b>Tatyana Khabakhpasheva and Alexander Korobkin, <i>One-side inequalities in the problem of wave impact</i></b> .....	67

<b>Yonghwan Kim and P.D. Schlavounos</b> , <i>A finite-depth unified theory of ship motion</i> .....	71
<b>M. Landrini, O. Oshri, T. Waseda and M.P. Tulin</b> , <i>Long time evolution of gravity wave systems</i> .....	75
<b>C. Levi, S. Welch, E. Fontaine and M.P. Tulin</b> , <i>Experiments on the ringing response of an elastic cylinder in breaking wave groups</i> .....	79
<b>C.M. Linton</b> , <i>Rapidly convergent representations for free-surface Green's functions</i> .....	83
<b>Q.W. Ma, G.X. Wu and R. Eatock Taylor</b> , <i>Numerical simulation of sloshing waves in a 3D tank</i> .....	87
<b>V.L.F. Matos, A.N. Simos and J.A.P. Aranha</b> , <i>Geometric synthesis of 2D submerged bodies</i> .....	91
<b>Maureen McIver</b> , <i>Uniqueness, trapped modes and the cut-off frequency</i> .....	95
<b>P. McIver</b> , <i>On the completeness of eigenfunction expansions in water-wave problems</i> .....	99
<b>Bernard Molin and Y. Stassen</b> , <i>A procedure to remove secularity in third-order numerical wave tanks</i> .....	103
<b>O. Motygin and N. Kuznetsov</b> , <i>Non-uniqueness in the water-wave problem: an example violating the inside John condition</i> .....	107
<b>Joost Moulijn</b> , <i>Added resistance of surface effect ships</i> .....	111
<b>J.N. Newman</b> , <i>Hydrodynamic analysis of the McIver toriod</i> .....	115
<b>M. Ohkusu and Y. Nanba</b> , <i>Some problems of hydroelastic behaviour of a floating thin plate in shallow water waves</i> .....	119
<b>Enok Palm and John Grue</b> , <i>On the wave field due to a moving two-dimensional, submerged body oscillating near the critical frequency</i> .....	123
<b>R. Porter and D.V. Evans</b> , <i>Prediction of resonances due to waves interacting with finite linear arrays of cylinders</i> .....	127
<b>Hoyte C. Raven and Henk J. Prins</b> , <i>Wave pattern analysis applied to nonlinear ship wave calculations</i> .....	131
<b>Yves-Marie Scolan and Š. Malenica</b> , <i>Experimental and numerical second order diffracted waves around an array of 4 cylinders</i> .....	135
<b>Anil K. Subramani, Robert F. Beck and William W. Schultz</b> , <i>Suppression of wave-breaking in nonlinear water wave computations</i> .....	139

---

<b>Ken Takagi</b> , <i>Water waves beneath a floating elastic plate</i> .....	143
<b>Peter S. Tromans and I. Ketut Suastika</b> , <i>Spectral response surfaces, designer waves and the ringing of offshore structures</i> .....	147
<b>Peder A. Tyvand</b> , <i>Free-surface evolution at the edge of an impulsively upwelling fluid layer</i> .....	151
<b>Fritz Ursell</b> , <i>On the validity of multipole expansions</i> .....	155
<b>T. Utsunomiya and R. Eatock Taylor</b> , <i>Analogies for resonances in wave diffraction problems</i> .....	159
<b>Riaan van 't Veer</b> , <i>Experimental validation of a Rankine panel method</i> .....	163
<b>William C. Webster and Xinyu Zhang</b> , <i>A waterfall springing from unsteady flow over an uneven bottom</i> .....	167
<b>Jaap-Harm Westhuis and Andonowati</b> , <i>Applying the finite element method in numerically solving the two dimensional free-surface water wave equations</i> .....	171
<b>D.J. Wood and D.H. Peregrine</b> , <i>Pressure-impulse theory for water wave impact on a structure with trapped air</i> .....	175
<b>Sheguang Zhang, Woei-Min Lin, Kenneth Weems and Dick K.P. Yue</b> , <i>A hybrid boundary-element method for non-wall-sided bodies with or without forward speed</i> .....	179

### On Minimizing Wave Resistance or Drag

T.S. Angell, G.C. Hsiao and R. E. Kleinman

Center for Mathematics of Waves  
Dept. of Mathematical sciences  
University of Delaware  
Newark, Delaware 19716

T. Miloh

Dept. of Fluid Mechanics  
and Heat Transfer  
Tel Aviv University  
Ramat Aviv 69978 Israel

This paper treats the problem of determining the hull form for a ship of constant volume and fixed draft moving with constant Froude number which minimizes either wave resistance or total drag (ignoring spraying and wave breaking). We choose one of these quantities as a constraint and minimize the other over a set of admissible hull forms. We treat this constrained problem by simultaneously determining the hull form and the velocity potential for that particular hull form. Unlike the traditional approach of minimizing the Michell integral for the wave resistance (e.g. Chapter 6 of [3]), the present paper goes a step further in applying modern shape optimization techniques to the Kelvin-Neumann integral equation by finding an optimal solution for the total (wave plus viscous) drag. The procedure is similar to that employed in shape optimization for zero forward speed [1],[2].

Consider a ship with wetted surface  $S$  enclosing (together with the water plane) a constant volume  $V_0$  moving with a constant forward speed  $U_0$  in the  $x$ -direction and employ the standard linearized free surface boundary condition. We choose to represent the velocity potential of the wave problem as a center plane source distribution [4],

$$\phi(\mathbf{r}) = \int_{S_0} M(\mathbf{r}') G(\mathbf{r}, \mathbf{r}') ds' + U_0 x \quad (1)$$

where  $S_0$  is the center plane, a planar region contained in the projection of  $S$  on the  $(x, z)$  plane,  $G(\mathbf{r}, \mathbf{r}')$  is the Green's function for the Kelvin-Neumann problem in the absence of the ship and  $M$  is the unknown source distribution.  $M$  is a solution of the first kind integral equation

$$\frac{\partial}{\partial n} \int_{S_0} M(\mathbf{r}') G(\mathbf{r}, \mathbf{r}') ds' = -U_0 \hat{\mathbf{n}} \cdot \hat{\mathbf{x}}, \quad \mathbf{r} \text{ on } S \quad (2)$$

and  $\hat{\mathbf{n}}$  is taken to be the outward normal (into the fluid) on  $S$ .

In terms of the Havelock function  $H(\mathbf{r}, \mathbf{r}')$

$$G(\mathbf{r}, \mathbf{r}') = -\frac{1}{|\mathbf{r} - \mathbf{r}'|} - \frac{1}{|\mathbf{r} + \mathbf{r}'|} + H(\mathbf{r}, \mathbf{r}') \quad (3)$$

where  $\mathbf{r}'_1 = (x', y', -z')$ , the wave resistance can be expressed as

$$D_w = \int_{S_0} \int_{S_0} M(\mathbf{r}) M(\mathbf{r}') \frac{\partial}{\partial x} H(\mathbf{r}, \mathbf{r}') ds ds' \quad (4)$$

and the viscous drag, for simplicity, is assumed to be proportional to the surface area, i.e.,

$$D_v = \int_S ds. \quad (5)$$

We confine attention to a set of admissible surfaces,  $\mathcal{A}_{v_0, \lambda_0}$ , with constant volume, symmetric about the center plane with a rectangular shape of fixed draft/waterplane length as follows:

$$S \in \mathcal{A}_{v_0, \lambda_0} \text{ if } S = S^+ \cup S^-$$

where

$$S^+ = \{ \mathbf{r} | y = f(x, z) \geq 0, |x| \leq x_0, \int_{-x_0}^{x_0} \int_0^{z_0} f(x, z) dz dx = \frac{V_0}{2}, \\ 0 \leq z \leq z_0, f \in C^2(\text{supp} f), \text{supp} f \subset [-x_0, x_0] \times [0, z_0], \frac{z_0}{x_0} = \lambda_0 \}$$

and

$$S^- = \{ \mathbf{r} = (x, -y, z) | (x, y, z) \in S^+ \}$$

On  $S^\pm$ , we have  $\hat{n} = \frac{(-f_x, \pm 1, -f_z)}{\sqrt{1+f_x^2+f_z^2}}$ .

Then we may define the defect in satisfying the integral equation as

$$\left\| \frac{\partial}{\partial n} \int_{S_0} M(\mathbf{r}') G(\mathbf{r}, \mathbf{r}') ds' + U_0 \hat{n} \cdot \hat{\mathbf{x}} \right\|_{L^2(S_0)}^2. \quad (6)$$

However  $S$  is not known. This quantity may be expressed in terms of integrals over planar regions in the  $(x, z)$  plane as

$$J = \int_{-\alpha x_0}^{\alpha x_0} \int_0^{\alpha z_0} |U_0 f_x + \left( f_x \frac{\partial}{\partial x} - \frac{\partial}{\partial y} + f_x \frac{\partial}{\partial z} \right) \int_{S_0} M(\mathbf{r}') G(\mathbf{r}, \mathbf{r}') ds' \Big|_{y=f(x, z)}|^2 \\ \cdot \sqrt{1+f_x^2+f_z^2} dz dx \quad (7)$$

when  $0 < \alpha < 1$  is a constant and  $x_0$  and  $z_0$  are respectively the half-length and draft. This functional involves both the unknown source distribution as well as the unknown surface.

Similarly the wave resistance has the form

$$D_w = \int_{-\alpha x_0}^{\alpha x_0} \int_0^{\alpha z_0} \int_{-\alpha x_0}^{\alpha x_0} \int_0^{\alpha z_0} M(x, z) M(x', z') \frac{\partial H}{\partial x}(x, z, x', z') dx dz dx' dz'. \quad (8)$$

while the viscous drag can be expressed approximately in terms of the unknown surface as

$$D_v = \int_{-x_0}^{x_0} \int_0^{z_0} \sqrt{1 + f_x^2 + f_z^2} dz dx \quad (9)$$

Introducing new variables  $L\tilde{x} = x$ ,  $L\tilde{z} = z$ , and defining  $\tilde{f}(\tilde{x}, \tilde{z}) := \frac{1}{L}f(x, z)$ , the functionals  $J$  and  $D_w$  may be rewritten so as to entail integration over the fixed domain  $[-\alpha, \alpha] \times [0, \lambda_0\alpha]$ :

$$J = \int_{-\alpha}^{\alpha} \int_0^{\alpha\lambda_0} |U_0 \tilde{f}_{\tilde{x}} + \left( \tilde{f}_{\tilde{x}} \frac{\partial}{\partial \tilde{x}} - \frac{\partial}{\partial \tilde{y}} + \tilde{f}_{\tilde{z}} \frac{\partial}{\partial \tilde{z}} \right) \int_{-\alpha}^{\alpha} \int_0^{\alpha\lambda_0} M(\tilde{x}, \tilde{y}) G(L\mathbf{r}, L\mathbf{r}') \Big|_{\tilde{y}=\tilde{f}(\tilde{x}, \tilde{z})}^2 \cdot \sqrt{1 + \tilde{f}_{\tilde{x}}^2 + \tilde{f}_{\tilde{z}}^2} (L^2) d\tilde{z} d\tilde{x}, \quad (10)$$

and

$$D_w = L^2 \int_{-\alpha}^{\alpha} \int_{-\alpha}^{\alpha\lambda_0} \int_0^{\alpha\lambda_0} \tilde{M}(\tilde{x}, \tilde{z}) \tilde{M}(\tilde{x}', \tilde{z}') \frac{\partial}{\partial \tilde{x}} H(\tilde{x}, \tilde{z}, \tilde{x}', \tilde{z}') d\tilde{x} d\tilde{z} d\tilde{x}' d\tilde{z}' \quad (11)$$

while  $D_v$  has the form

$$D_v = L^2 \int_{-1}^1 \int_0^{\lambda_0} \sqrt{1 + \tilde{f}_{\tilde{x}}^2 + \tilde{f}_{\tilde{z}}^2} d\tilde{z} d\tilde{x}. \quad (12)$$

We choose to study, here, optimization problems which can be formulated in terms of these expressions for fixed  $\lambda_0$ ,

$$(PI) \quad \text{minimize } D_v + V_0 J$$

over the class  $U_{\lambda_0}$  subject to the constraint

$$D_w \leq K$$

where  $K$  is some preassigned constant, and

$$(PII) \quad \text{minimize } D_w + V_0 J$$

over the class  $U_{\lambda_0}$  subject to the constraint

$$D_v \leq K.$$

The new concept of shape optimization may be found useful in ship design.

#### References

1. Angell, T.S., Hsiao, G.C., and Kleinman, R.E., An optimal design problem for submerged bodies. *Math. Meth. Appl. Sci.* **8** (1986), 50-76.
2. Angell, T.S., and Kleinman, R.E., A constructive method for shape optimization: a problem in hydromechanics. *IMA J. Appl. Math.* **47** (1991), 265-281.
3. Kostyukov, A.A., *Theory of Ship Waves and Wave Resistance* (M. Oppenheimer, tr.), Effective Communications Inc., Iowa City, Iowa, 1968.
4. Miloh, T., and Landweber, L., Ship centerplane source distribution. *J. Ship Res.* **24** (1980), 8-23.

## Computing The Green Function for linear wave-body interaction

H. B. Bingham \*

The interaction between surface gravity waves and a structure in (or near) the free-surface is often analysed using potential theory, with linearised conditions applied on the body and the free-surface boundaries. Having assumed linearity, the response of the structure is described by a set of canonical radiation and diffraction response functions, which can be superposed with particular wave data to obtain particular solutions. These response functions are solutions to special distributions of normal velocity over the body which correspond to certain physical problems (*i.e.* forced motion of the body, or diffraction of a long-crested incident wave.) Another way of representing the interaction of waves with a structure is to compute The Green Function for the body. By "The Green Function" we refer to the particular Green function that satisfies the homogeneous form of the initial-boundary-value problem (including the body boundary condition) except at one singular point on the body surface (see [1]). Any desired quantity related to wave-body interaction may be expressed in terms of The Green Function. In general, the standard approach will be computationally more efficient than computing The Green Function, but there exist some situations where it may be advantageous to use a discrete form of The Green Function instead. Assume that a body is to be analysed which has  $J$  degrees of freedom, (6 rigid-body modes plus some number of flexible modes) and is subject to incident wave forcing from  $N_\beta$  heading angles. As explained below, computing the discrete form of The Green Function requires solving  $N$  hydrodynamic problems where  $N$  is the number of panels required to obtain converged results for the quantities of interest and a given body. Thus if the analysis is very complex, such that  $J + N_\beta > N$ , then computing The Green Function will be more efficient. Another situation where computing The Green Function might be attractive is when it is impractical (or impossible) to split the incident wave field into a finite sum of long-crested (uniform along one horizontal dimension) waves. For example, a body subject to incident waves which are diffracted and/or refracted by nearby corners or variable bottom topography.

The linear wave-body interaction problem can be expressed succinctly via the equations of motion in convolution form,

$$\sum_{k=1}^J (M_{jk} + a_{jk}) \ddot{x}_k + b_{jk} \dot{x}_k + (C_{jk} + c_{jk}) x_k + \int_{-\infty}^t d\tau K_{jk}(t-\tau) \dot{x}_k(\tau) = F_{jD}(t),$$

$$j = 1, 2, \dots, J. \quad (1)$$

In this expression, an over-dot indicates differentiation with respect to time. The body's inertia matrix is  $M_{jk}$ , and the hydrostatic restoring-force coefficients are given by  $C_{jk}$ . The force due to the radiation of waves by the body motion is expressed as a convolution of the radiation impulse-response functions  $K_{jk}$ ,  $a_{jk}$ ,  $b_{jk}$ , and  $c_{jk}$ ; with the body velocity components in  $J$  degrees of freedom. The wave exciting force  $F_{jD}(t)$  is typically taken to be a superposition of long-crested waves and is thereby expressed in the following convolution form

$$F_{jD}(t) = \int_0^{2\pi} d\beta F_{jD}(t, \beta) = \int_0^{2\pi} d\beta \int_{-\infty}^{\infty} d\tau K_{jD}(t-\tau, \beta) \zeta(\tau, \beta), \quad (2)$$

where  $\zeta(t, \beta)$  is a time history of the elevation of the long-crested incident wave with heading angle  $\beta$  (the angle between the positive  $x$ -axis and the wave propagation direction) and  $K_{jD}(t, \beta)$  is the impulse-response function for the diffraction force due to an impulsive long-crested wave from heading angle  $\beta$ . (In following seas with  $U \neq 0$ , there are three convolutions of this form which must be summed.) The diffraction force can also be expressed in terms of solutions to radiation problems via the Haskind-Newman relations

$$F_{jD}(t) = -\rho \int_{-\infty}^t d\tau \iint_{S_b} d\vec{\xi} \left[ \dot{\phi}^j(\vec{\xi}, \tau) \phi_{jn}^-(\vec{\xi}, t-\tau) - \phi_j^-(\vec{\xi}, t-\tau) \dot{\phi}_n^j(\vec{\xi}, \tau) \right], \quad (3)$$

\*International Research Centre for Computational Hydrodynamics (ICCH), Agern Allé 5, DK-2970 Hørsholm, Denmark, icch@dhi.dk

where  $\phi_j^-$  is the solution to the "reverse-flow" radiation problem (i.e. the radiation problem with the direction of the steady translation reversed.) Note that the Haskind-Newman relations provide the force, but no other information about the diffraction flow, and that a number of assumptions are involved in their derivation for  $U \neq 0$ , making them of limited appeal in that case.

If the incident wave is restricted to be time harmonic with frequency of encounter  $\omega$ , amplitude  $A$ , and heading angle  $\beta$ , then  $\zeta(t) = A \Re\{e^{i\omega t}\}$ , and as  $t \rightarrow \infty$  the response becomes  $x_k(t) = \Re\{\xi_k(\omega, \beta) e^{i\omega t}\}$ , and the equation of motion tend to

$$\sum_{k=1}^J \{-\omega^2 [M_{jk} + A_{jk}(\omega)] + i\omega B_{jk}(\omega) + C_{jk} + c_{jk}\} \frac{\xi_k(\omega, \beta)}{A} = X_{jD}(\omega, \beta); \quad j = 1, 2, \dots, J. \quad (4)$$

The quantity  $\xi_k/A$  is usually called the response-amplitude operator (RAO). The frequency-response functions on the left-hand side of (4) (the added-mass and damping coefficients) are related to the radiation impulse-response functions through the Fourier transforms

$$A_{jk}(\omega) = a_{jk} - \frac{1}{\omega} \int_0^\infty dt K_{jk}(t) \sin \omega t; \quad B_{jk}(\omega) = b_{jk} + \int_0^\infty dt K_{jk}(t) \cos \omega t. \quad (5)$$

The frequency-response function on the right-hand side of (4) (the exciting force coefficient) is related to the diffraction impulse-response function through the Fourier transform

$$X_{jD}(\omega, \beta) = \int_{-\infty}^\infty dt K_{jD}(t, \beta) e^{-i\omega t}. \quad (6)$$

As in the time-domain, the diffraction force can be expressed in terms of radiation potentials via the Haskind-Newman relations

$$X_{jD}(\omega, \beta) = -i\omega\rho \iint_{S_b} d\vec{\xi} \left[ \phi^I(\vec{\xi}, \omega, \beta) \phi_{jn}^-(\vec{\xi}, \omega) - \phi_j^-(\vec{\xi}, \omega) \phi_n^I(\vec{\xi}, \omega, \beta) \right]. \quad (7)$$

The physically motivated canonical radiation and diffraction problems defined above provide a complete picture of the linear interaction between waves and a structure. Another, perhaps less physically intuitive means of capturing this information is to compute The Green Function  $\phi(\vec{x}; \vec{\xi}, t)$  for the body. This function satisfies the Laplace equation at every point in the fluid domain, the linear free-surface boundary condition on the free-surface boundary, and homogeneous Neumann conditions on the body boundary except at one singular point, thus

$$\vec{n} \cdot \nabla_{\vec{x}} \phi(\vec{x}; \vec{\xi}, t) = \delta(\vec{x} - \vec{\xi}, t); \quad \vec{\xi} \in S_b. \quad (8)$$

Any imaginable flow quantity can be expressed in terms of this function. For example, the corresponding first-order dynamic pressure impulse-response function (with  $U = 0$  for illustration purposes) is

$$p(\vec{x}; \vec{\xi}, t) = -\rho \dot{\phi}(\vec{x}; \vec{\xi}, t), \quad (9)$$

and the force impulse-response function is

$$F_j(\vec{\xi}, t) = \iint_{S_b} d\vec{x} p(\vec{x}; \vec{\xi}, t) n_j(\vec{x}). \quad (10)$$

With these definitions, we can express the force on the body due to an arbitrary distribution of fluid velocity,  $\vec{V}(\vec{x}, t)$ , as

$$F_j(t) = \iint_{S_b} d\vec{\xi} \int_{-\infty}^\infty d\tau \vec{n}(\vec{\xi}) \cdot \vec{V}(\vec{\xi}, \tau) F_j(\vec{\xi}, t - \tau). \quad (11)$$

This expression is quite general and equally applicable to any distribution of normal velocity  $\vec{n} \cdot \vec{V}$ . For example, by setting  $\vec{n} \cdot \vec{V} = n_1 \delta(t)$  we can recover the six surge radiation impulse-response functions. Diffraction of an incident wave by the fixed body can be similarly represented. Consider an incident wave,  $\zeta_I$ , with corresponding fluid velocity  $\vec{V}_I(\vec{x}, t)$  and (first-order) dynamic pressure  $p_I(\vec{x}, t)$ . The diffraction force on the body can be split into two parts,  $F_{jD}(t) = F_{jI}(t) + F_{jS}(t)$ , where the first term

$$F_{jI}(t) = -\rho \iint_{S_b} d\vec{x} p^I(\vec{x}, t) n_j \quad (12)$$

is often referred to as the Froude-Krilov force, and  $F_{jS}$  is the scattering force. Letting  $\vec{V} = \vec{V}_I$  in Equation (11) gives the scattering force due to an arbitrary incident wave

$$F_{jS}(t) = \iint_{S_b} d\vec{\xi} \int_{-\infty}^{\infty} d\tau V_{In}(\vec{\xi}, \tau) F_j(\vec{\xi}, t - \tau). \quad (13)$$

The same exercise may be carried out with a time-harmonic incident wave. In this case, let  $\phi(\vec{x}; \vec{\xi}, t) = \Re\{\tilde{\phi}(\vec{x}; \vec{\xi}, \omega)e^{i\omega t}\}$  with

$$\vec{n} \cdot \nabla_{\vec{x}} \tilde{\phi}(\vec{x}; \vec{\xi}, \omega) = \delta(\vec{x} - \vec{\xi}), \quad \vec{\xi} \in S_b. \quad (14)$$

Again, any flow quantity can be defined in terms of The Green Function. For example, the dynamic pressure frequency-response function is (again with  $U = 0$  for illustration)

$$\tilde{p}(\vec{x}; \vec{\xi}, \omega) = -i\omega\rho \tilde{\phi}(\vec{x}; \vec{\xi}, \omega), \quad (15)$$

and the force frequency-response function is

$$\tilde{F}_j(\vec{\xi}, \omega) = \iint_{S_b} d\vec{x} \tilde{p}(\vec{x}; \vec{\xi}, \omega) n_j(\vec{x}), \quad (16)$$

which gives the corresponding general expression for the force on the body due to the fluid velocity  $\vec{V}(\vec{x}, \omega)$

$$\tilde{F}_j(\omega) = \iint_{S_b} d\vec{\xi} \vec{n}(\vec{\xi}) \cdot \vec{V}(\vec{\xi}, \omega) \tilde{F}_j(\vec{\xi}, \omega). \quad (17)$$

Similarly, the added-mass, damping, and long-crested wave exciting force coefficients can be recovered by considering the appropriate distributions of  $\vec{n} \cdot \vec{V}$ .

To demonstrate the practical application of The Green Function, we compute it for a bottom mounted circular cylinder, and then use it to recover the diffraction force due to long-crested incident waves. The accuracy is then compared to a direct solution of the canonical diffraction problem. The calculations are made using the low-order panel method program WAMIT. In the context of a low-order (constant strength) panel method, the discrete analogue to the boundary conditions on  $\phi$  and  $\tilde{\phi}$  are

$$\vec{n} \cdot \nabla \phi_{jk}(t) = \begin{cases} \delta(t); & j = k \\ 0; & j \neq k \end{cases} \quad j = 1, 2, \dots, N; \quad k = 1, 2, \dots, N; \quad (18)$$

and

$$\vec{n} \cdot \nabla \tilde{\phi}_{jk}(t) = \begin{cases} 1; & j = k \\ 0; & j \neq k \end{cases} \quad j = 1, 2, \dots, N; \quad k = 1, 2, \dots, N; \quad (19)$$

which can be thought of as  $N$  special generalised radiation problems.

Figure 1 shows the magnitude of the horizontal wave exciting force on the cylinder as a function of frequency, while Figure 2 shows the absolute error in the two calculations. Both calculations were made using  $N = 252$  panels at 120 evenly spaced frequencies. Using The Green Function produces results of comparable, although typically slightly lower accuracy. This is not surprising since using The Green Function requires another set of integrations over the body surface which can be expected to introduce additional errors into the calculations.

## Acknowledgments

This work is supported by the Danish National Research Council.

## References

- [1] P.M. Morse and H. Feshbach. *Methods of Theoretical Physics*. McGraw-Hill, New York, 1953.

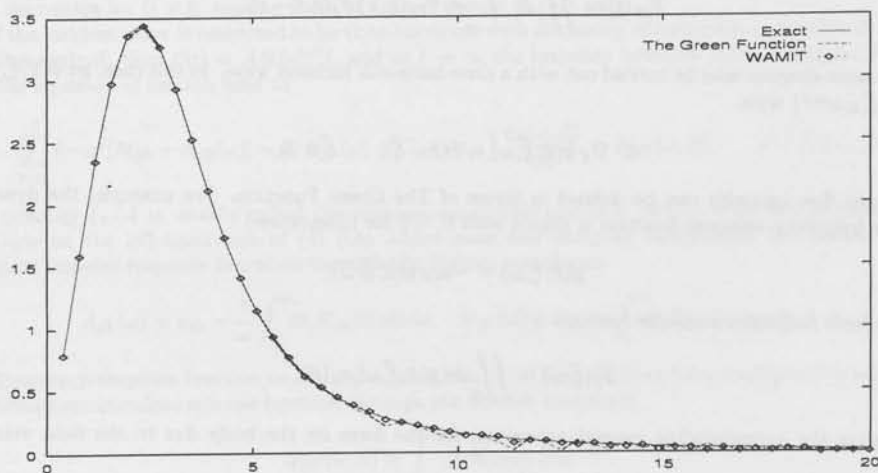


Figure 1: Magnitude of the non-dimensional surge exciting force  $\frac{X_1}{\rho g R^2 A}$  for a bottom mounted circular cylinder of radius  $R$ , in water of depth  $H = 1$ , plotted against  $(\frac{g}{R})^{\frac{1}{2}} \omega$ .

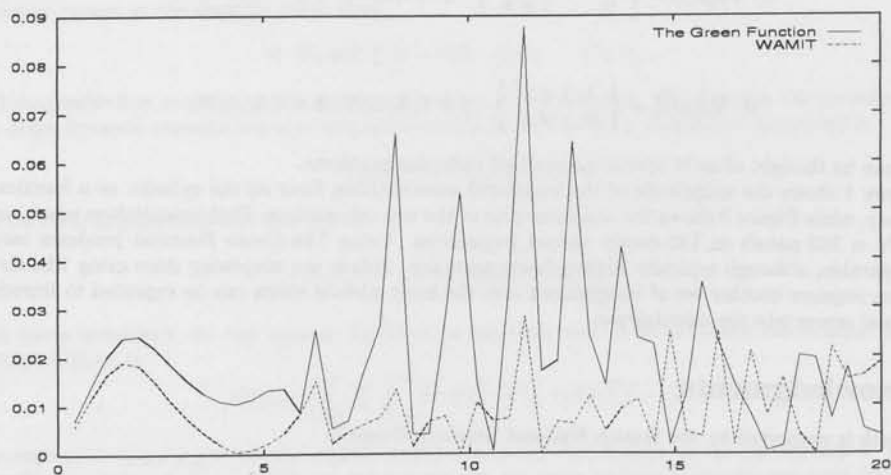


Figure 2: Absolute error of the two methods in the magnitude of the surge exciting force.

## RUNUP ON A BODY IN WAVES AND CURRENT. FULLY NON-LINEAR AND FINITE ORDER CALCULATIONS.

Bjarne Büchmann<sup>1</sup>, Pierre Ferrant<sup>2</sup> and Jesper Skourup<sup>3</sup>.

### INTRODUCTION

At the previous workshop last year in Marseille, a comparison was proposed between a fully non-linear Boundary Element Model (BEM) by Ferrant (1997) and a second order BEM by Skourup *et al.* (1997). This paper is dedicated to such a comparison.

Water waves are basically a non-linear phenomenon, and in recent years the interaction between waves, currents and structures in the sea has been given much attention. The fully non-linear BEMs tend to be very demanding with respect to computational time, and to reduce the computational time needed to solve such problems, finite order BEMs based on perturbation theory have been developed both in the frequency domain and in the time domain. Linear frequency domain models for strong and weak current have been developed by Nakos (1990) and by Nossen *et al.* (1991), or Malenica *et al.* (1995), while lower order time domain models with current have been developed by *e.g.* Kring (1994), Cheung *et al.* (1996) and Sierewogel and Hermans (1996).

By the very nature of the perturbation procedure about the still water level, the lower order models are restricted to the wave steepness not being too large. In order to find the range of validity of lower order models with respect to incoming wave steepness and Froude number, comparison with results from a fully nonlinear model is especially useful.

This abstract concerns the comparison of two particular BEMs, namely the fully non-linear BEM ANSWAVE by Ferrant (1997) and the lower order BEM WAVETANK by Skourup *et al.* (1997). This comparison will serve both as validation of both models in the low Froude number and low wave steepness regime, and as a method for defining the domain of validity of the finite order model.

### MATHEMATICAL FORMULATIONS

The problems considered fall in the frame of potential theory. The governing equation for the velocity potential,  $\phi$ , is the Laplace equation. Using Gauss' theorem this equation can be transformed into an integral equation on the boundary of the domain.

A collocation procedure is used employing linear and continuous basis functions over triangular or quadrilateral elements and collocation points (nodes) at the element vertices. In points where the boundary has discontinuous derivative, multiple nodes are placed at the same geometrical position satisfying one boundary condition per normal direction. Thus the Boundary Integral Equation is reduced to a dense linear system of equations to be solved for the normal velocity at the free surface and the potential on the remaining boundaries. The resulting linear system of equations depends only on the boundary geometry.

The potential and surface elevation,  $\eta$ , are divided into an incident field, which is unaffected by the structure, and a scattered field, which radiates from the body of interest, and the numerical problem is solved for the scattered field alone. The fully non-linear model uses stream function theory to describe the incident wave field, whereas the lower order model uses a formulation for second order Stokes waves riding on a uniform current.

To time integrate the potential and the free surface elevation the fully non-linear model follows a semi-Lagrangian formulation of the kinematic and dynamic free surface boundary conditions, nodes being allowed to move in the vertical direction only. Neumann conditions are implemented to model both the impermeable boundary at the body and truncation boundaries. At each time step the boundary conditions are used to update  $\phi$  and  $\eta$  on the free surface and  $\partial\phi/\partial n$  on the rest of the boundaries. Time integration is made using a 4th order Runge-Kutta method with frozen coefficients. The boundary integral equations are solved to obtain the rest of the unknowns. For further details see Ferrant (1996). The lower order model apply Taylor series of the free surface conditions and perturbation expansions of the variables to reduce the problem to finite order at a time invariant geometry. In the present formulation terms are kept to second order with respect to the wave

<sup>1</sup>Department of Hydrodynamics and Water Resources, Technical University of Denmark, DK-2800 Lyngby, Denmark

<sup>2</sup>SIREHNA, 1 rue de la Noë, BP 42105, 44321 Nantes Cedex 3, France

<sup>3</sup>International Research Centre for Computational Hydrodynamics, Danish Hydraulic Institute, Agern Allé 5, DK-2970 Hørsholm, Denmark

steepness perturbation parameter and to first order with respect to the current speed perturbation parameter. Time integration is accomplished using the Adams-Bashforth-Moulton method. Further details can be found in Büchmann *et al.* (1997).

Since the boundary integral equations depends only on the geometry, the finite order model can apply LU-decomposition of the linear system at the onset and then use back-substitution to solve at each time step. This procedure represents an initial  $O(N^3)$  cost, where  $N$  is the number of collocation points, and an  $O(N^2)$  cost per time step, where the  $O(N^2)$  cost dominates for the values of  $N$  considered.

Using a fully non-linear model, the boundary geometry changes at each time step requiring both the construction and solution of a new linear system at each time step. Preconditioned GMRES is used to solve this system requiring  $O(N^2)$  cost per time step. Even though both methods use  $O(N^2)$  operations per time step, for the same number of nodes the lower order method is much faster. Also for the lower order model the wave steepness can be chosen in the post-processing procedure, and thus a whole range of wave steepnesses can be calculated in one computation. On the other hand the lower order model may require more nodes than the fully non-linear model to resolve the same physical problem. This is due to the fact that the scattered free second order waves may be much shorter than the incident waves, and is especially true for increasing Froude numbers. The increase in the number of nodes required in the finite order model is particular important since both models use  $O(N^2)$  memory, and for the finite order model, with a lower cost per time step, it turns out that it is memory rather than CPU time that limits the problem size.

## NUMERICAL RESULTS

The two models have been used to calculate the runup on a bottom mounted vertical circular cylinder in waves and current. Simulations have been made for  $kh = ka = 1$ , where  $k$  is the wave number,  $h$  is the water depth and  $a$  is the radius of the cylinder, and for incident wave heights  $H/h$  up to 0.300 (wave steepness  $H/L$  up to 0.0477, where  $L = 2\pi/k$  is the wave length). For this value of  $kh$  Stokes second order wave theory is invalid for  $H/h > 0.365$  ( $H/L > 0.058$ ). This means that the incident wave height should be well below this limit when the lower model is used. The runup profile has been found for a range of different Froude numbers,  $Fr = U/\sqrt{gh}$ , and wave heights,  $H$ .

The runup profile around the cylinder has been plotted on Figure 1 as function of the angle,  $\beta$ , for three different Froude numbers and two different wave heights. The agreement between the two models is very good for low Froude numbers (*e.g.*  $Fr = 0.025$ ), while for larger Froude numbers (*e.g.*  $Fr = 0.100$ ) some differences are observed. The analysis of these differences motivated the introduction of a correction to the finite order results, accounting for the steady wave elevation due to the current alone. Being of second or higher order in the current strength, steady waves due to the current were not taken into account in the original finite order formulation. Using the dynamic free surface boundary condition (the Bernoulli equation) the so-called "double body elevation" can be found to improve the results from the lower order model. The results from the lower order model with the double body elevations added are also shown on Figure 1. The correction due to "double body elevations" is seen to improve the agreement between the two models significantly. This is particularly true for low wave steepnesses, where the double body elevation is the dominant nonlinear contribution. For higher values of the wave steepness, both higher order diffraction effects and interactions between steady and oscillatory flows come into play. With the double body elevations added, however, the agreement between the models is good for a sensibly wider range of Froude numbers and wave steepnesses.

Even though the profiles compare well in all the cases shown, in Figure 1.d) some short wave features are observed in the lower order model results close to  $\beta = 0.7\pi$ . A convergence study has been made, and it has been shown that the second order solution is not fully converged in space. Also, it has not been possible to make a finer discretization without bringing the truncation boundaries too close to the cylinder. It should be noted also, that for waves in an opposing current of intermediate strength, say  $Fr = -0.100$ , the results from the two models differs significantly on the side of the cylinder near  $\beta = \pi/2$ .

Figure 2 shows the runup at the front of the cylinder,  $R = \max \eta(\beta = 0)$ , as function of wave height for different Froude numbers. This figure confirms the very good agreement of the models in the low Froude number - low wave steepness regime. For higher inputs, the increasing influence of nonlinear phenomena not included in the finite order model is clearly observed. Also it is clear from Figure 2 that the non-linear contributions to the runup are very significant.

## CONCLUSIONS

A comparison has been made between the fully non-linear BEM by Ferrant (1997) and the lower order BEM by Büchmann *et al.* (1997) with the focus on calculating runup on a bottom mounted vertical circular cylinder

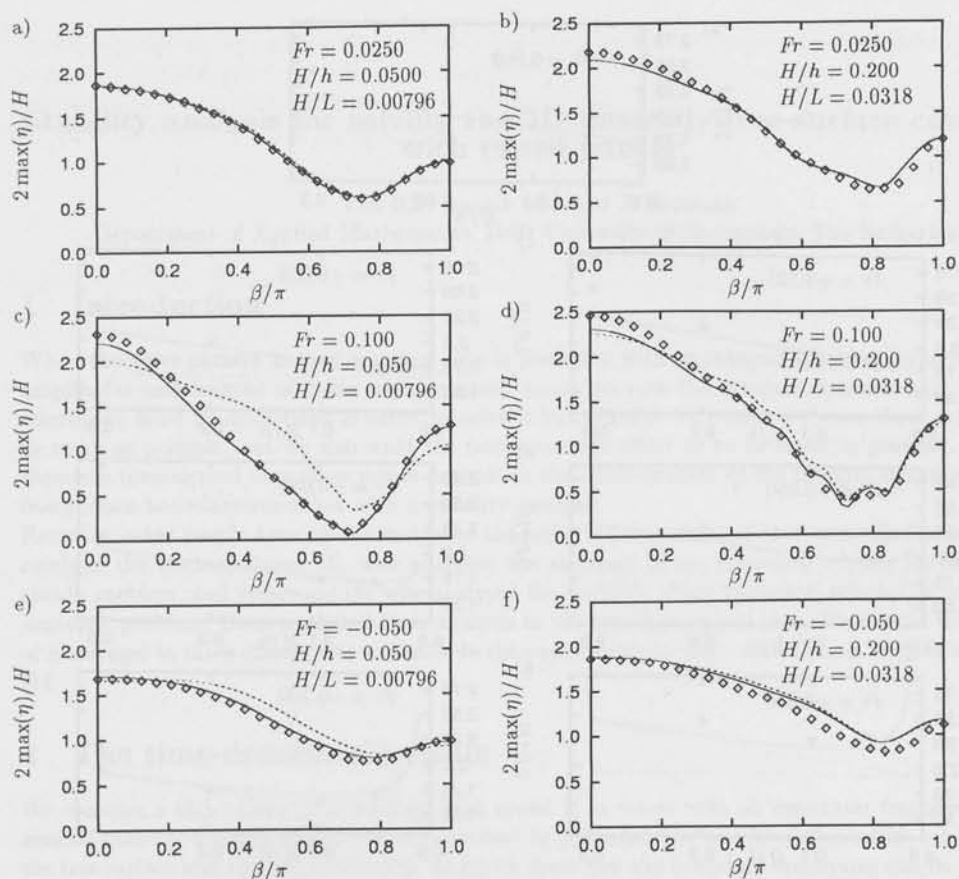


Figure 1: Examples of runup profiles on a cylinder for  $kh = ka = 1$ . Results from the fully non-linear model ( $\diamond$ ), the lower order model (---) and the lower order model with double body elevations added (—).

in waves and current. Runup results from these two models agree very well for low Froude numbers and up to medium wave steepness. For large wave steepness and Froude numbers the difference between the results from the two models increases. However, the correction due to "double body elevations" is seen to improve the agreement between the two models significantly.

Thus for low Froude numbers and small to medium wave steepness the lower order method represents an accurate and computationally fast alternative to the fully nonlinear approach, at least for the present geometry and wavenumber. For increasing Froude numbers the difference between the results from the two models becomes larger and the lower order method also becomes less efficient due to a demand of finer discretization than the non-linear method. For higher Froude numbers and wave steepnesses the fully non-linear approach should be used. Note also the versatility of the fully nonlinear model which can be applied to a variety of problems among which is wave-current interaction as presented here and calculation of higher order forces as presented by Ferrant (1996).

#### ACKNOWLEDGMENTS

Research on nonlinear wave-current-body interactions using ANSWAVE is part of a CLAROM project on: "Large amplitude wave amplifications in the vicinity of offshore structures", with Bureau Veritas, Doris Engineering, Bouygues Offshore, G.ESIM, Ifremer, Principia RD and Sirehna as partners.

The work on the WAVETANK model was funded in part by the Danish National Research Foundation. Their support is greatly appreciated.

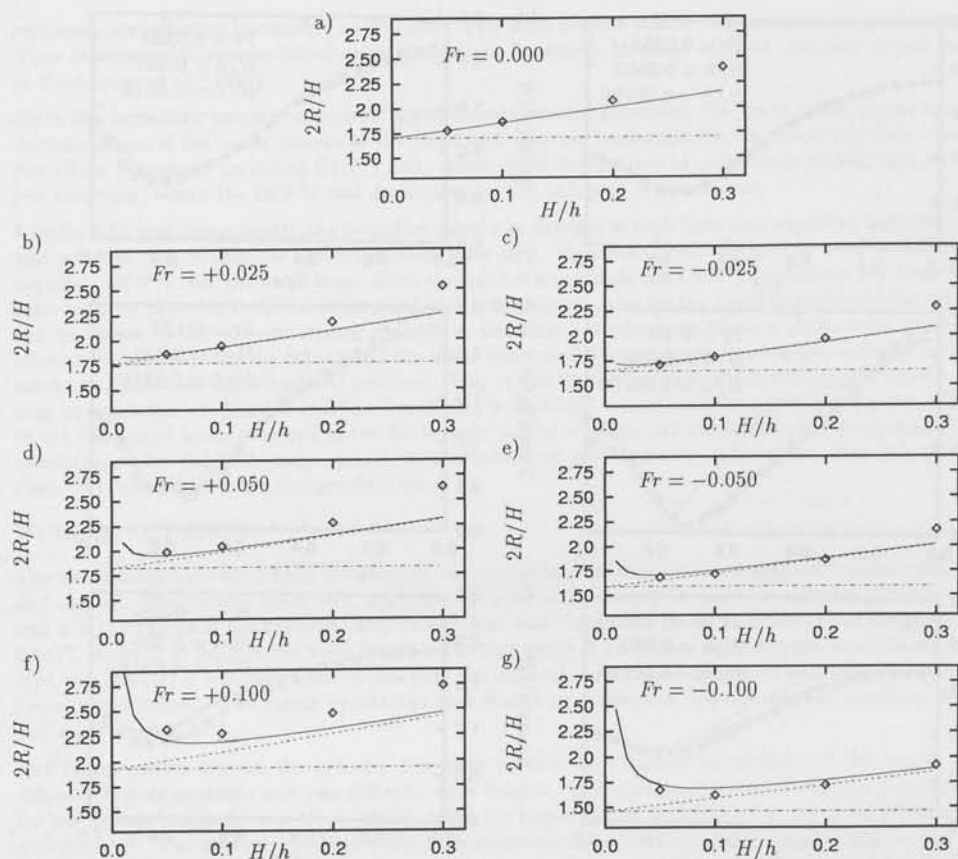


Figure 2: Runup at the front of the cylinder for  $kh = ka = 1$ . Results from the fully non-linear model ( $\diamond$ ), the lower order model to first order in  $H/h$  (---), to second order in  $H/h$  (····) and to second order in  $H/h$  with double body elevations added (—).

## REFERENCES

- Büchmann, B., Skourup, J. and Cheung, K. F., (1997). Runup on a structure due to waves and current. *Proceedings of the 7th International Offshore and Polar Engineering Conference*, vol. 3, 48-55, Honolulu, Hawaii, USA.
- Cheung, K. F., Isaacson, M. and Lee, J. W., (1996). Wave diffraction around a three-dimensional body in a current. *ASME Journal of Offshore Mechanics and Arctic Engineering*, **118**(4), 247-252.
- Ferrant, P., (1996). Simulation of strongly nonlinear wave generation and wave-body interactions using a 3-D MEL model. *Proceedings of the 21st ONR Symposium on Naval Hydrodynamics*, 93-109, Trondheim, Norway.
- Ferrant, P., (1997). Nonlinear wave-current interactions in the vicinity of a vertical cylinder. *Proceedings of the 12th International Workshop on Water Waves and Floating Bodies*, Marseille, France.
- Kring, D. C., (1994). Time Domain Ship Motions by a Three-Dimensional Rankine Panel Method. Ph.D. thesis, Department of Ocean Engineering, Massachusetts Institute of Technology, Cambridge, Massachusetts, USA.
- Malenica, S., Clark, P. J. and Molin, B., (1995). Wave and current forces on a vertical cylinder free to surge and sway. *Applied Ocean Research*, **17**, 79-90.
- Nakos, D. E., (1990). Ship Wave Patterns and Motions by a Three Dimensional Rankine Panel Method. Ph.D. thesis, Department of Ocean Engineering, Massachusetts Institute of Technology, Cambridge, Massachusetts, USA.
- Nossen, J., Grue, J. and Palm, E., (1991). Wave forces on three-dimensional floating bodies with small forward speed. *Journal of Fluid Mechanics*, **227**, 135-160.
- Sierevogel, L. M. and Hermans, A. J., (1996). Time-domain calculations on a sailing vessel in waves, study on increasing speed. *Proceedings of the 11th International Workshop on Water Waves and Floating Bodies*, Hamburg, Germany.
- Skourup, J., Büchmann, B. and Bingham, H. B., (1997). A second order 3D BEM for wave-structure interaction. *Proceedings of the 12th International Workshop on Water Waves and Floating Bodies*, Marseille, France.

## Stability analysis for solving the 3D unsteady free-surface condition with raised panels

Tim H.J. Bunnik and Aad J. Hermans

Department of Applied Mathematics, Delft University of Technology, The Netherlands

### 1 Introduction

When the wave pattern around a sailing ship is predicted with an integral equation formulation, the amplitudes and lengths of these waves contain errors because the integral equation and boundary conditions must be discretized in order to solve it numerically. Of course we want these errors to be as small as possible, but we also want the computational effort to be as small as possible. We have therefore investigated how these errors depend on the discretization of the integral equation and the free-surface boundary condition with a stability analysis.

Recently, other people have also investigated the stability or accuracy of their numerical schemes. We combine the work of Raven [3], who analysed the accuracy of his numerical scheme for solving the steady problem, and Sierrevogel [2], who analysed the stability of her numerical scheme for solving the unsteady problem. Both restricted their analysis to the two-dimensional case. We extend the analysis of Sierrevogel to three dimensions and include the opportunity to use a raised panel surface like Raven did.

### 2 The time-domain algorithm

We consider a ship sailing at a constant high speed  $U$  in waves with an encounter frequency  $\omega$ . We assume that the hydrodynamics can be described by potential flow and linear boundary conditions on the free surface and the hull of the ship. In [1] we show how the boundary conditions can be linearized about the flow and wave pattern caused by a steady moving ship in calm water. Far away from the ship, this flow can be approximated by a uniform flow. The boundary condition on the free surface then becomes

$$\frac{\partial^2 \phi}{\partial t^2} + 2U \frac{\partial^2 \phi}{\partial t \partial x} + U^2 \frac{\partial^2 \phi}{\partial x^2} + g \frac{\partial \phi}{\partial z} = 0 \quad \text{on } z = 0 \quad (1)$$

Because of simplicity we will use this condition, and not the complicated condition that we actually use, to analyse the accuracy and stability of our time-domain algorithm. The unknown potential is found by putting sources on the hull of the ship,  $\Omega_2$ , and on a surface,  $\Omega_1$ , at a short distance  $z_f$ , above the free surface. This raised surface has some advantages as we shall see. The potential is found to be

$$\phi(\vec{x}, t) = \iint_{\Omega_1} \sigma(\vec{\xi}, t) G(\vec{x}, \vec{\xi}) d\vec{\xi} + \iint_{\Omega_2} \sigma(\vec{\xi}, t) G(\vec{x}, \vec{\xi}) d\vec{\xi} \quad G = \frac{-1}{4\pi r} \quad (2)$$

If this expression is substituted in the boundary condition (1), a boundary integral equation for the source strength  $\sigma$  on the raised surface is found

$$W_1 \sigma = RHS \quad (3)$$

Integrals over the hull of the ship are shifted into a Right Hand Side, because in this abstract we only look at errors caused by discretizing the free surface. The raised surface is now divided into panels and on each panel the source strength is assumed to be constant. The integral (2) now turns into a summation over all panels of source strength times the integrated Green function. If we also

introduce difference schemes for the time derivatives and tangential space derivatives, we can solve the potential and corresponding wave pattern numerically. Because we solve discretized equations, the waves are different from the waves that would follow from the continuous equations (1) and (2). We will investigate the difference in wave length and wave amplitude by studying the linear operator  $W_1$  in Fourier space.

### 3 The continuous case

The Fourier transform of the continuous free surface condition (1) and the continuous integral equation (2) can be obtained with the following pair of transforms

$$\tilde{\phi}(k, \theta, \omega) = \int_{-\infty}^{\infty} \int_{-\infty}^{\infty} \int_{-\infty}^{\infty} \phi(x, y, t) e^{-i(\omega t - kx \cos \theta - ky \sin \theta)} dx dy dt \quad (4)$$

$$\phi(x, y, t) = \frac{1}{(2\pi)^3} \int_{-\infty}^{\infty} \int_{-\pi}^{\pi} \int_0^{\infty} \tilde{\phi}(k, \theta, \omega) e^{i(\omega t - kx \cos \theta - ky \sin \theta)} k dk d\theta d\omega \quad (5)$$

$k$  is the wave number;  $\theta$  the wave angle and  $\omega$  the wave frequency. After some calculations it can be shown that the Fourier transform of the linear operator  $W_1$  equals

$$\tilde{W}_1 = \tilde{G}(-\omega^2 + 2Uk\omega \cos \theta - U^2 k^2 \cos^2 \theta + gk) \quad (6)$$

After transforming back, the potential turns out to be

$$\phi(x, y, t) = \frac{1}{(2\pi)^3} \int_{-\infty}^{\infty} \int_{-\pi}^{\pi} \int_0^{\infty} \frac{R\tilde{H}\tilde{S} \tilde{G}}{\tilde{W}_1} e^{i(\omega t - kx \cos \theta - ky \sin \theta)} k dk d\theta d\omega \quad (7)$$

The zeros of the operator  $\tilde{W}_1$  give the wave-like contributions of this integral. The dispersion relation  $\tilde{W}_1(k, \theta, \omega) = 0$  therefore has to be solved. It can be shown that the behaviour of the solution depends on the Strouhal number  $\tau = \frac{\omega U}{g}$ . We will restrict our analysis to speeds and frequencies for which  $\tau > \frac{1}{4}$ . This can be done because we assume the speed of the ship, and therefore also the encounter frequencies of the incoming waves, to be high. When  $\tau > \frac{1}{4}$ , the solutions of the dispersion relation are

$$k_{\pm} = \begin{cases} \frac{g}{4U^2 \cos^2 \theta} (1 \pm \sqrt{1 + 4\tau \cos \theta})^2 & \text{if } 1 + 4\tau \cos \theta \geq 0, \\ \frac{g}{4U^2 \cos^2 \theta} (1 \pm i\sqrt{-1 - 4\tau \cos \theta})^2 & \text{if } 1 + 4\tau \cos \theta < 0 \end{cases} \quad (8)$$

So, if  $1 + 4\tau \cos \theta < 0$ , the wave number has a non-zero imaginary part, which means that these waves disappear rapidly when they propagate up- or downstream. If  $1 + 4\tau \cos \theta \geq 0$ , the integration contour in (7) can be chosen such, that the solution only contains waves that propagate downstream, see for example [4]. We therefore only concentrate on downstream wave angles i.e.  $-\frac{\pi}{2} \leq \theta \leq \frac{\pi}{2}$ .

### 4 The discrete case

We now discretize the raised surface and the time and space derivatives in the free surface condition (1). The raised surface is divided into rectangular panels of size  $\Delta x \times \Delta y$ . The height of this raised surface above the free surface  $z = 0$  is proportional to the area of these panels according to  $z_{fs} = \alpha \sqrt{\Delta x \Delta y}$ . The potential can now be written as an infinite sum over all panels:

$$\phi(x_m, y_n) = \sum_{i=-\infty}^{\infty} \sum_{j=-\infty}^{\infty} \sigma_{ij} \int_{(i-\frac{1}{2})\Delta x}^{(i+\frac{1}{2})\Delta x} \int_{(j-\frac{1}{2})\Delta y}^{(j+\frac{1}{2})\Delta y} \frac{-dx_0 dy_0}{4\pi \sqrt{(x_m - x_0)^2 + (y_n - y_0)^2 + z_{fs}^2}} \quad (9)$$

The collocation points  $(x_m, y_n)$  lie on the free surface at a vertical distance  $z_{fs}$  from the middle of a panel, so  $x_m = m\Delta x$  and  $y_n = n\Delta y$ .

The derivatives can be discretized as follows:

$$\frac{\partial^2 \phi}{\partial t^2}(t_{i+1}) = \frac{1}{(\Delta t)^2} \left( d_0^{(tt)} \phi(t_{i+1}) + d_{-1}^{(tt)} \phi(t_i) + d_{-2}^{(tt)} \phi(t_{i-1}) + d_{-3}^{(tt)} \phi(t_{i-2}) \right) \quad (10)$$

$$\frac{\partial^2 \phi}{\partial x^2}(x_{i+1}) = \frac{1}{(\Delta x)^2} \left( d_0^{(xx)} \phi(x_{i+1}) + d_{-1}^{(xx)} \phi(x_i) + d_{-2}^{(xx)} \phi(x_{i-1}) + d_{-3}^{(xx)} \phi(x_{i-2}) \right) \quad (11)$$

Similar formulae apply to the first order derivatives  $\frac{\partial \phi}{\partial t}$  and  $\frac{\partial \phi}{\partial x}$ . The coefficients  $d^{(tt)}$ ,  $d^{(xx)}$ ,  $d^{(x)}$  and  $d^{(t)}$  can be chosen such that a first or second order difference scheme is obtained. We use upwind differences for the space derivatives, which means that only points upstream from the collocation point in question are used in the difference scheme. We do this, because it is the only way to obtain a stable scheme for high speeds as shown in [2]. We now use the discrete Fourier transform to obtain the wave number in the discretized case. This transform and its inverse are defined by

$$\hat{\phi}(k, \theta, \omega) = \Delta x \Delta y \Delta t \sum_{m=-\infty}^{\infty} \sum_{n=-\infty}^{\infty} \sum_{p=-\infty}^{\infty} \phi(x_m, y_n, t_p) e^{-i(\omega p \Delta t - km \Delta x \cos \theta - kn \Delta y \sin \theta)} \quad (12)$$

$$\phi(x_m, y_n, t_p) = \frac{1}{(2\pi)^3} \int_{-\frac{\pi}{\Delta t}}^{\frac{\pi}{\Delta t}} \int_{-\frac{\pi}{\Delta y}}^{\frac{\pi}{\Delta y}} \int_{-\frac{\pi}{\Delta x}}^{\frac{\pi}{\Delta x}} \hat{\phi}(k, \theta, \omega) e^{i(\omega p \Delta t - km \Delta x \cos \theta - kn \Delta y \sin \theta)} d(k \cos \theta) d(k \sin \theta) d\omega \quad (13)$$

If we apply this transform to the discretized boundary condition and integral equation, we find the discrete Fourier transform of the operator  $W_1$ .

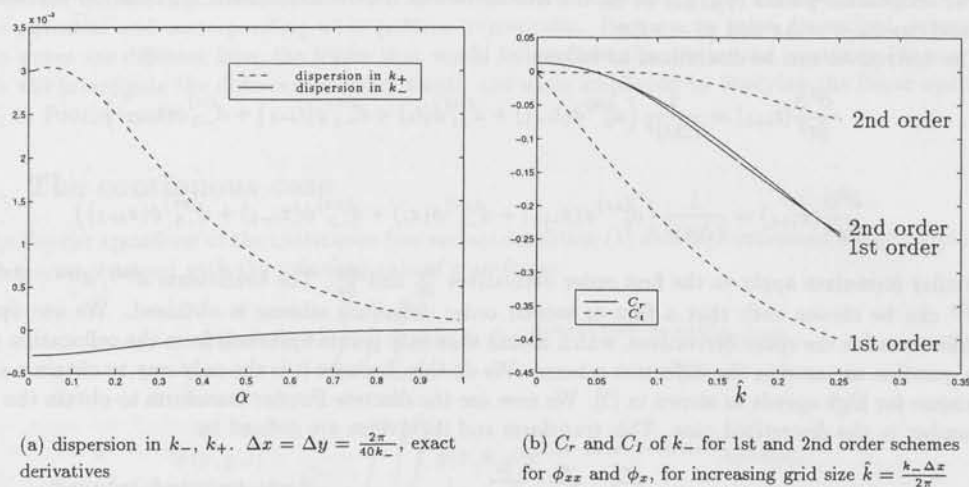
$$\begin{aligned} \hat{W}_1 = & \frac{\hat{G}}{\Delta x \Delta y} \left( \frac{1}{(\Delta t)^2} \left( d_0^{(tt)} + d_{-1}^{(tt)} e^{-i\omega \Delta t} + d_{-2}^{(tt)} e^{-2i\omega \Delta t} + d_{-3}^{(tt)} e^{-3i\omega \Delta t} \right) + \right. \\ & \frac{2U}{\Delta x \Delta t} \left( d_0^{(x)} + d_{-1}^{(x)} e^{ik \Delta x \cos \theta} + d_{-2}^{(x)} e^{2ik \Delta x \cos \theta} \right) \left( d_0^{(t)} + d_{-1}^{(t)} e^{-i\omega \Delta t} + d_{-2}^{(t)} e^{-2i\omega \Delta t} \right) + \\ & \left. \frac{U^2}{(\Delta x)^2} \left( d_0^{(xx)} + d_{-1}^{(xx)} e^{ik \Delta x \cos \theta} + d_{-2}^{(xx)} e^{2ik \Delta x \cos \theta} + d_{-3}^{(xx)} e^{3ik \Delta x \cos \theta} \right) + g \frac{\hat{Q}}{G} \right) \quad (14) \end{aligned}$$

$\hat{G}$  is the discrete Fourier transform of the integrated green function, and  $\hat{Q}$  the discrete Fourier transform of the integrated vertical derivative of the Green function,  $\frac{\partial G}{\partial z}$ . After some complicated manipulations it can be shown that these transforms equal

$$\hat{G} = \sum_{m=-\infty}^{\infty} \sum_{n=-\infty}^{\infty} \frac{e^{-z_{fs} \sqrt{\alpha_m^2 + \beta_m^2}}}{2\alpha_m \beta_m \sqrt{\alpha_m^2 + \beta_m^2}} \left( e^{-\frac{1}{2}i\Delta x \alpha_m} - e^{\frac{1}{2}i\Delta x \alpha_m} \right) \left( e^{-\frac{1}{2}i\Delta y \beta_n} - e^{\frac{1}{2}i\Delta y \beta_n} \right) \quad (15)$$

$$\hat{Q} = \sum_{m=-\infty}^{\infty} \sum_{n=-\infty}^{\infty} \frac{e^{-z_{fs} \sqrt{\alpha_m^2 + \beta_m^2}}}{2\alpha_m \beta_m} \left( e^{-\frac{1}{2}i\Delta x \alpha_m} - e^{\frac{1}{2}i\Delta x \alpha_m} \right) \left( e^{-\frac{1}{2}i\Delta y \beta_n} - e^{\frac{1}{2}i\Delta y \beta_n} \right) \quad (16)$$

where  $\alpha_m = k \cos \theta + \frac{2\pi m}{\Delta x}$  and  $\beta_n = k \sin \theta + \frac{2\pi n}{\Delta y}$ . Only a small number of terms has to be taken into account because these series converge very fast. The zeros of the discrete operator  $\hat{W}_1$  correspond with the discrete wave numbers and can be found numerically. They can be compared with the continuous ones and any differences indicate errors.

Figure 1: Results for  $U = 1.25$ ,  $\omega = 20$ ,  $\theta = 0$ 

## 5 Damping, dispersion and temporal stability

We can relate the continuous wave number  $k_c$  and the discrete wave number  $k_d$  by writing

$$k_d = k_c (1 + C_R(\omega, U, \theta, \Delta t, \Delta x, \Delta y, \alpha) + iC_I(\omega, U, \theta, \Delta t, \Delta x, \Delta y, \alpha)) \quad (17)$$

Non-zero  $C_r$  or  $C_l$  indicate an error in the discrete wave number. If  $C_R$  is negative, this means the wave number is too small, so the predicted wave length is too large. A positive  $C_R$  indicates an under estimation of the wave length. A positive  $C_I$  indicates numerical amplification, and a negative  $C_I$  numerical damping. We have investigated the dependence of these errors on the difference schemes, the time step, the grid size and the distance from panels to free surface for various speeds, frequencies and wave angles. It turned out that the use of second order difference schemes for the space derivatives reduces damping drastically compared to the use of first order difference schemes, as can be seen in figure 1(b). Furthermore, it was found that the use of raised panels reduces numerical dispersion. As can be seen in figure 1(a), the dispersion decreases if the distance from panels to free surface is increased. If this distance becomes too large, the time integration is not temporal stable anymore. This temporal stability can be investigated by rewriting the dispersion relation. If we substitute  $Z = e^{-i\omega\Delta t}$ , we obtain a third order complex relation for  $Z$ , which has three roots. If one or more of these roots is outside the unit circle in the complex plane, the numerical scheme is temporal unstable.

## References

- [1] T.H.J. Bunnik *Motions of a vessel at high speed*. Report 97-11, Delft University of technology.
- [2] L.M. Siervogel *Time-Domain Calculations of Ship Motions*. PhD Thesis, Delft University of Technology, 1998.
- [3] H.C. Raven. *A Solution Method for the Nonlinear Ship Wave Resistance Problem*. PhD Thesis, Delft University of Technology, 1996.
- [4] J.V. Wehausen and E.V. Laitone. *Surface waves*, volume 9 of *Encyclopedia of physics*. Springer-Verlag, Berlin, Germany, 1960.

## Super Green Functions for Generic Dispersive Waves

Xiao-Bo Chen (Bureau Veritas, France)  
Francis Noblesse (David Taylor Model Basin, USA)

### Green functions and super Green functions

In potential flows, a Green function  $G(\xi, \bar{x})$  defines the velocity potential of the flow created at a point  $\xi = (\xi, \eta, \zeta)$  by a source of unit strength located at a point  $\bar{x} = (x, y, z)$ . The Green function for an unbounded incompressible fluid is

$$4\pi G = -1/r$$

where  $r = \sqrt{(\xi - x)^2 + (y - \eta)^2 + (z - \zeta)^2}$  is the distance between the field point  $\xi$  and the singular point  $\bar{x}$ . In free-surface hydrodynamics, Green functions can be expressed as

$$G = G^S + G^F$$

where  $G^F$  accounts for free-surface effects and  $G^S$  is defined in terms of simple singularities. E.g., for time-harmonic ship waves in deep water, the simple-singularity component  $G^S$  is given by

$$4\pi G^S = -1/r + 1/r'$$

where  $r' = \sqrt{(\xi - x)^2 + (y - \eta)^2 + (z + \zeta)^2}$ . The free-surface component  $G^F$  is given by the Fourier superposition of elementary waves

$$4\pi^2 G^F = \lim_{\varepsilon \rightarrow +0} \int_{-\infty}^{\infty} d\beta \int_{-\infty}^{\infty} d\alpha \frac{e^{Zk - i(X\alpha + Y\beta)}}{D + i\varepsilon \text{sign}(D_f)} \quad (1a)$$

where  $k = \sqrt{\alpha^2 + \beta^2}$  is the wavenumber and

$$(X, Y, Z \leq 0) = (\xi - x, \eta - y, \zeta + z) \quad (1b)$$

Furthermore,  $D$  is the dispersion function

$$D = (f - F\alpha)^2 - k$$

and  $\text{sign}(D_f) = \text{sign}(\partial D / \partial f)$  is given by

$$\text{sign}(D_f) = \text{sign}(f - F\alpha)$$

The nondimensional frequency  $f$  and the Froude number  $F$  are defined as

$$f = \omega \sqrt{L/g} \quad F = U / \sqrt{gL}$$

where  $\omega$  is the encounter frequency of the regular ambient waves exciting the ship motions,  $L$  and  $U$  are the ship length and forward speed, and  $g$  is the acceleration of gravity.

Two fundamental difficulties greatly restrict the practical utility of free-surface Green functions.

A first major difficulty is that the singular double Fourier integral representation (1a) of free-surface effects is nearly impossible to compute accurately (except in very few relatively simple cases for which the near-field behavior of  $G^F$  can be determined analytically [1]) in the critically-important limit  $(X, Y, Z) \rightarrow 0$  where (1a) has a very complex singularity. A second major difficulty is that although Green functions provide valuable insights, they are not directly useful (except for idealized cases involving flows about a sphere) for practical applications, which require flows generated by *distributions* of singularities (sources and dipoles) over hull-panels and waterline-segments. Indeed, practical calculations involve *distributions* of singularities (rather than point singularities) of the form

$$\mathcal{G} = \int_{P_0} \left\{ \begin{matrix} G\sigma \\ \nabla G \cdot \delta \end{matrix} \right\} \quad (2)$$

where  $P_0$  stands for a hull-panel or a waterline-segment near a point<sup>1</sup>  $\bar{x}_0 = (x_0, y_0, z_0 \leq 0)$ , and  $\sigma$  and  $\delta = (\delta_x, \delta_y, \delta_z)$  are source and dipole densities, respectively. A function (2) associated with a *distribution* of singularities is called a *super Green function* to emphasize its similarities and differences with usual Green functions associated with *point* singularities. Evaluation of super Green functions  $\mathcal{G}$  for free-surface flows in the usual approach, in which  $G$  and  $\nabla G$  are evaluated using (1) and subsequently integrated over a panel or a segment as in (2), is a hopeless task which cannot be performed accurately (notably for time-harmonic ship waves) for field points near a waterline-segment or a hull-panel at the free surface.

### Fourier-Kochin representation of super Green functions

However, the super Green functions  $\mathcal{G}$  of main interest in free-surface hydrodynamics, and their first<sup>2</sup> derivatives  $\nabla \mathcal{G}$ , can be evaluated in a remarkably simple way using Kochin's formulation and the Fourier representation of free-surface effects summarized below. Within the Fourier-Kochin formulation [2], the free-surface-effect component

$$G^F = \int_{P_0} \left\{ \begin{matrix} G^F \sigma \\ \nabla G^F \cdot \delta \end{matrix} \right\} \quad (3)$$

<sup>1</sup>The reference point  $\bar{x}_0$  may be taken at (or near) the centroid of  $P_0$

<sup>2</sup>and indeed higher

of the super Green function

$$\mathcal{G} = \mathcal{G}^S + \mathcal{G}^F$$

is defined by substituting (1) into (3) and performing the space integration over the hull-panel or the waterline-segment before the Fourier integration. Thus, the free-surface component  $\mathcal{G}^F$  is given by the double Fourier integral representation

$$4\pi^2 \mathcal{G}^F = \lim_{\varepsilon \rightarrow +0} \int_{-\infty}^{\infty} d\beta \int_{-\infty}^{\infty} d\alpha \frac{S e^{Zk - i(X\alpha + Y\beta)}}{D + i\varepsilon \text{sign}(D_f)} \quad (4a)$$

where

$$(X, Y, Z \leq 0) = (\xi - x_0, \eta - y_0, \zeta + z_0) \quad (4b)$$

and  $S$  is the spectrum function defined as

$$S = \int_{P_0} \mathcal{E} \left\{ i\alpha \delta_x + i\beta \delta_y + k \delta_z \right\} \quad (5a)$$

$$\text{with } \mathcal{E} = e^{k(z-z_0) + i[\alpha(x-x_0) + \beta(y-y_0)]} \quad (5b)$$

The integral representations (1) and (4) of the free-surface components  $G^F$  and  $\mathcal{G}^F$  of the related Green function  $G$  and super Green function  $\mathcal{G}$  show that  $G^F$  is a special case of  $\mathcal{G}^F$  corresponding to

$$S=1$$

An essential property of the spectrum function (5) associated with a *distribution* of singularities is

$$S \rightarrow 0 \quad \text{as } k = \sqrt{\alpha^2 + \beta^2} \rightarrow \infty$$

As a result, the super Green function  $\mathcal{G}^F$  defined by (4) is not singular in the limit  $(X, Y, Z) \rightarrow 0$ , unlike  $G^F$  which has a complex singularity in this limit. Furthermore, space integration over a hull-panel or a waterline-segment is incomparably simpler in (5a), where the elementary wave-function (5b) is infinitely differentiable, than in (3) which involves functions  $G^F$  and  $\nabla G^F$  singular in the limit  $(X, Y, Z) \rightarrow 0$ . Thus, the Fourier-Kochin representation of super Green functions given by (4) and (5) effectively circumvents the two previously-noted fundamental difficulties restricting the utility of the classical approach based on (1) and (3). In this usual approach, *influence coefficients*<sup>3</sup> in fact cannot be evaluated with accuracy for field (control) points in the vicinity of a distribution of singularities over a waterline segment or a hull-panel at the free surface. However, the Fourier-Kochin representation (4) and (5) makes it possible to evaluate influence coefficients in all cases, including the

<sup>3</sup>which are super Green functions

most difficult and important<sup>4</sup> case involving a waterline segment or a hull-panel at the free surface.

The space integration (5) in the Fourier-Kochin representation of super Green functions is a trivial task, as was already noted. However, the Fourier integration (4a) is a nontrivial issue. This critical issue is considered in [3-5] and in a forthcoming study [6] for an arbitrary spectrum function  $S$  and an arbitrary dispersion function  $D$ , i.e. for generic dispersive waves generated by an arbitrary distribution of singularities. Indeed, while super Green functions are defined above for time-harmonic ship waves in deep water, a broad class of dispersive waves, including steady or time-harmonic water waves in finite water depth (with or without forward speed) and internal waves in a density-stratified fluid, are defined by the generic Fourier representation (4). The most important results given in [3] and [5] and in the unpublished study [6] are summarized here.

#### Far-field waves

The generic super Green function  $\mathcal{G}^F(X, Y)$  defined by the Fourier representation

$$\mathcal{G}^F = \lim_{\varepsilon \rightarrow +0} \int_{-\infty}^{\infty} d\beta \int_{-\infty}^{\infty} d\alpha \frac{A e^{-i(X\alpha + Y\beta)}}{D + i\varepsilon \text{sign}(D_f)} \quad (6)$$

is now considered for generic dispersion and amplitude functions  $D$  and  $A$ . We may assume that the amplitude function  $A(\alpha, \beta)$  in (6) vanishes as  $k \rightarrow \infty$  and does not oscillate rapidly, as follows from (5). We have

$$\mathcal{G}^F \sim \mathcal{G}^W \quad \text{as } H = \sqrt{X^2 + Y^2} \rightarrow \infty \quad (7)$$

where  $\mathcal{G}^W$  represents the far-field waves contained in  $\mathcal{G}^F$ . The far-field waves  $\mathcal{G}^W$  are given by single Fourier integrals along curves, called *dispersion curves*, defined by the dispersion relation<sup>5</sup>  $D=0$ :

$$\mathcal{G}^W = -i\pi \sum_{D=0} \int_{D=0} ds \frac{\Theta A}{\|\nabla D\|} e^{-i(X\alpha + Y\beta)} \quad (8a)$$

$$\text{with } \Theta = \text{sign}(D_f) + \text{erf}\left(\frac{k_*(X D_\alpha + Y D_\beta)}{\sigma \|\nabla D\|}\right) \quad (8b)$$

Here,  $\sum_{D=0}$  means summation over all the dispersion curves,  $ds$  is the differential element of arc length of a dispersion curve,  $\|\nabla D\|^2 = D_\alpha^2 + D_\beta^2$  with  $D_\alpha = \partial D / \partial \alpha$  and  $D_\beta = \partial D / \partial \beta$ , erf is the

<sup>4</sup>because free-surface effects are largest in this case

<sup>5</sup>The dispersion relation typically defines several distinct dispersion curves, although a single dispersion curve may exist in simple cases; e.g. wave diffraction-radiation without forward speed

usual error function,  $\sigma$  is a positive real constant whose role is explained further on, and  $k_*$  is a reference wavenumber. The reference wavenumber  $k_*$  may be taken equal to the local value of the wavenumber  $k$  at the dispersion curve, although other reference wavenumbers may be used. E.g., for free-surface flows,  $k_* = f^2$  and  $k_* = 1/F^2$  are proper choices for time-harmonic flows without forward speed and steady flows, respectively.

In the far-field limit  $H \rightarrow \infty$ , (8) yields

$$\mathcal{G}^W \sim -i\pi \sum_{D=0} \int_{D=0} ds [\text{sign}(D_f) + \text{sign}(\vec{X} \cdot \nabla D)] \\ A \exp[-i(X\alpha + Y\beta)] / \|\nabla D\| \quad (9)$$

Expressions (9) and (8), given in [3] and [5] respectively, are asymptotically equivalent Fourier representations of the far-field waves  $\mathcal{G}^W$  contained in  $\mathcal{G}^F$ . The radiation condition is satisfied via the sign function  $\text{sign}(D_f)$ , which stems from the  $\varepsilon \rightarrow +0$  limit in (6). Expression (9) is independent of the constant  $\sigma$  in (8). The far-field Fourier representation (9) is applied to the important case of time-harmonic ship waves in deep water in [7]. This Fourier integral representation of far-field waves in generic dispersive media can be further approximated using the method of stationary phase. The stationary-phase approximation of (9) yields simple relations, given in [8], between the dispersion curves associated with the dispersion relation  $D=0$  and important aspects (wavelengths, directions of wave propagation, phase and group velocities, and cusp angles) of the corresponding far-field waves.

#### Wave and local components

In the near field, the super Green function (6) can be expressed as the sum of a wave component  $\mathcal{G}^W$  and a local (near-field) component  $\mathcal{G}^N$ :

$$\mathcal{G}^F = \mathcal{G}^W + \mathcal{G}^N \quad (10)$$

where  $\mathcal{G}^W$  is given by (8). The positive real constant  $\sigma$  in (8) may be chosen so that the local component  $\mathcal{G}^N$  decays without oscillations, i.e. so that the wave component  $\mathcal{G}^W$  fully accounts for the waves included in  $\mathcal{G}^F$  in the near field (as well as in the far field where  $\mathcal{G}^N$  is negligible and  $\mathcal{G}^F \sim \mathcal{G}^W$ ). Thus, both the wave component  $\mathcal{G}^W$  and the local component  $\mathcal{G}^N$  in (10) involve the constant  $\sigma$ , although the sum  $\mathcal{G}^W + \mathcal{G}^N$  is of course independent of  $\sigma$ , like the representation (9) of the far-field waves contained in  $\mathcal{G}^F$ .

The decomposition (10) into wave and local components is nonunique. The wave component

$\mathcal{G}^W$  in (10) is taken as the representation (9) in [3] and [4], where a Fourier representation of the corresponding local component  $\mathcal{G}^N$  suited for numerical evaluation is given. In the present study, the wave component  $\mathcal{G}^W$  in (10) is taken as the representation (8) obtained in [5]. The wave component (9) used in [3] and [4] is a particular case<sup>6</sup> of the wave component (8). The integrand of the double Fourier integral representation of the local component  $\mathcal{G}^N$  given in [4] is continuous everywhere but varies rapidly across a dispersion curve. Here, the more general expression (8) for the wave component is used, and a remarkably simple Fourier representation of the corresponding local component  $\mathcal{G}^N$  is given. The near-field representation of  $\mathcal{G}^F$  given here is mathematically exact<sup>7</sup> and is quite well suited for accurate and efficient numerical evaluation. In particular, the integrand of the double Fourier integral representation of the local component  $\mathcal{G}^N$  given further on is continuous everywhere and varies slowly across a dispersion curve.

#### Local component

Practical Fourier representations, suited for accurate and efficient numerical evaluation, of the wave component  $\mathcal{G}^N$  associated with the Fourier representation of generic dispersive waves defined by (6), (10), (8) are given in [6] for generic dispersive waves and for the specific case of time-harmonic ship waves. A dispersion relation  $D=0$  may define several basic types of dispersion curves, including closed dispersion curves surrounding points  $(\alpha_j, \beta_j)$  in the Fourier plane and open dispersion curves. These various cases are considered in [6]. The case of a dispersion relation which yields open dispersion curves defined by single-valued functions  $\alpha = \alpha_j(\beta)$  with  $-\infty < \beta < \infty$  is considered here. Steady ship waves and wave diffraction-radiation by a ship for  $\tau = U\omega/g > \sqrt{2/27} \approx 0.272$ , are examples of this type of dispersion curves, called open dispersion curves of type A. In this case<sup>8</sup> the wave and local components in (10) are given by

$$\mathcal{G}^W = -i\pi \sum_j \int_{-\infty}^{\infty} d\beta [\text{sign}(D_f D_\alpha) + \text{erf}(\frac{k_* X}{\sigma})] \\ A \exp[-i(X\alpha + Y\beta)] / D_\alpha$$

Here  $\sigma$  and  $k_*$  are the positive real constant and the reference number already introduced in (8b). The

<sup>6</sup>Expression (9) corresponds to the far-field limit  $H \rightarrow \infty$  or the limit  $\sigma \rightarrow 0$  of (8)

<sup>7</sup>whereas the representation of  $\mathcal{G}^N$  given in [4] involves numerical approximations

<sup>8</sup>for which constant- $\beta$  lines intersect each dispersion curve only once

relation  $d\beta/|D_\alpha| = ds/|\nabla D|$  yields the alternative expression

$$\mathcal{G}^W = -i\pi \sum_j \int_{D=0} ds [\text{sign}(D_j) + \text{sign}(D_\alpha) \text{erf}(\frac{k_* X}{\sigma})] A \exp[-i(X\alpha + Y\beta)]/|\nabla D|$$

The local component  $\mathcal{G}^N$  is given by

$$\mathcal{G}^N = \int_{-\infty}^{\infty} d\beta e^{-iY\beta} \int_{-\infty}^{\infty} d\alpha e^{-iX\alpha} (\frac{A}{D} - \sum_j \frac{E_j^\alpha A_j}{(\alpha - \alpha_j) D_\alpha^j})$$

where  $A_j$  and  $D_\alpha^j$  stand for the values of the functions  $A$  and  $D_\alpha$  at the  $j^{\text{th}}$  dispersion curve<sup>9</sup>  $\alpha = \alpha_j(\beta)$ , and  $E_j^\alpha$  is the localizing function

$$E_j^\alpha = \exp[-\frac{\sigma^2}{4} (\frac{\alpha - \alpha_j}{k_j^*})^2]$$

Here  $k_j^*$  is the reference wavenumber attached to the  $j^{\text{th}}$  dispersion curve. The integrand of the double Fourier integral representation of the local component  $\mathcal{G}^N$  is finite at a dispersion curve. Specifically, we have

$$\frac{A}{D} - \frac{E_j^\alpha A_j}{(\alpha - \alpha_j) D_\alpha^j} \sim \frac{A_\alpha^j D_\alpha^j - A_j D_{\alpha\alpha}^j / 2}{(D_\alpha^j)^2} \text{ as } \alpha \rightarrow \alpha_j$$

where  $A_\alpha^j$  and  $D_{\alpha\alpha}^j$  are the values of  $A_\alpha$  and  $D_{\alpha\alpha}$  at the  $j^{\text{th}}$  dispersion curve. Furthermore, the localizing function  $E_j^\alpha$ , and consequently the integrand of the Fourier representation of  $\mathcal{G}^N$ , vary slowly across a dispersion curve because it is not necessary to use small values<sup>10</sup> of the constant  $\sigma$ .

As was already noted, the foregoing Fourier representation of the super Green function (6) may be used for open dispersion curves of type A. An analogous Fourier representation may be used if the dispersion function  $D$  yields one or more dispersion curve, called open dispersion curves of type B, defined by single-valued functions  $\beta = \beta_j(\alpha)$  with  $-\infty < \alpha < \infty$ . This Fourier representation of the super Green function (6) is given in [6], where similar expressions for the case of a closed dispersion curve and dispersion curves of arbitrary shape are also given. Applications of these Fourier representations of generic dispersive waves to the case of time-harmonic free-surface flows with forward speed may also be found in [6].

<sup>9</sup>E.g., for steady ship waves and wave diffraction-radiation by a ship for  $\tau > \sqrt{2/27} \approx 0.27$  we have two distinct dispersion curves, and therefore  $j = 1, 2$

<sup>10</sup>whereas the representation given in [4] requires thin dispersion strips, corresponding to very small values of  $\sigma$

## Conclusion

The foregoing Fourier representation of the generic super Green function (6) is remarkable in view of its generality<sup>11</sup>, its simplicity and elegance, and the fact that it is well suited for accurate and efficient numerical evaluation<sup>12</sup>. Also, the decomposition (10) into wave and local components yields a natural decomposition of hydrodynamic loads into added-mass and wave-damping components in which damping effects are defined by single Fourier integrals.

Thus, free-surface Green functions, which offer important built-in advantages<sup>13</sup>, can be used as effectively as simple Rankine sources. E.g., free-surface Green functions can be used in a calculation method based on linearization about the double-body flow<sup>14</sup>, and to couple a nonlinear and/or viscous near-field calculation method and a far-field potential-flow representation [9].

## References

- [1] B. Ponizy, F. Noblesse, M. Ba and M. Guilbaud (1994) *Numerical evaluation of free-surface Green functions*, JSR 38, 193-202
- [2] F. Noblesse and C. Yang (1995) *Fourier-Kochin formulation of wave-diffraction-radiation by ships or offshore structures*, STR 42, 115-139
- [3] F. Noblesse and X.B. Chen (1995) *Decomposition of free-surface effects into wave and near-field components*, STR 42, 167-185
- [4] F. Noblesse and C. Yang (1996) *Fourier representation of near-field free-surface flows*, STR 43, 19-37
- [5] F. Noblesse and X.B. Chen (1997) *Far-field and near-field dispersive waves*, STR 44, 37-43
- [6] X.B. Chen and F. Noblesse (1998) *Super Green functions*. To be presented at the 22nd Symposium on Naval Hydrodynamics
- [7] F. Noblesse, X.B. Chen and C. Yang (1996) *Fourier-Kochin theory of free-surface flows*, 21st Symposium on Naval Hydrodynamics, 120-135
- [8] X.B. Chen and F. Noblesse (1997) *Dispersion relation and far-field waves*, 12th WWWFB
- [9] F. Noblesse, C. Yang and X.B. Chen (1997) *Boundary-integral representation of linear free-surface potential flows*, JSR 41, 10-16

<sup>11</sup>The representation can be applied to a broad class of dispersive waves, including steady or time-harmonic water waves in finite water depth with forward speed and internal waves in a density-stratified fluid, generated by arbitrary distributions of singularities

<sup>12</sup>The integrands of the Fourier representations of both the wave component and the local component are continuous

<sup>13</sup>proper far-field behavior, radiation condition

<sup>14</sup>by distributing free-surface Green functions over the free surface in a finite, fairly small, region the vicinity of the ship since the Kelvin free-surface condition becomes nearly exact at a small distance from the ship

## Computation of impulse response function using differential properties of the time-domain Green function.

A.H. CLÉMENT

ÉCOLE CENTRALE de NANTES  
Laboratoire de Mécanique des Fluides - division Hydrodynamique Navale  
CNRS URA 1217, E.C.N., Nantes, FRANCE

In this paper, three methods for evaluating the time-domain Green function during BEM computations of impulse response functions of floating bodies are compared, in terms of cpu time performances. The impulsive wave radiation problem is solved in the general frame of linear free-surface potential flow. The comparison is made by considering a single degree of freedom, say heave motion, without loss of generality.

A body of wetted surface  $C$ , in equilibrium on the fluid at rest, is given at  $t=0$  an impulsive motion defined by a step velocity. We shall work here on the heave motion:  $V_e = zH(t)$ . The resulting velocity potential is the solution of the Fredholm-Volterra integral equation :

$$\frac{\Phi(M, T)}{2} - \iint_C \Phi(M', T) \frac{\partial}{\partial n'} G_0(M', M) dC = -H(T) \iint_C G_0(M', M) n_z(M') dC$$

$$- \int_0^T dT' \iint_C F(M', T', M, 0) n_z(M') dC + \int_0^T dT' \iint_C \Phi(M', T') \frac{\partial}{\partial n'} F(M', T', M, T) dC \quad (1)$$

where the Green function is given by :

$$G(M', t', M, t) = -\frac{1}{4\pi} [\delta(t-t') G_0(M', M) + H(t-t') \mathcal{F}(M', t', M, t)] ; G_0(M', M) = \left( \frac{1}{R} - \frac{1}{R_1} \right) \quad (2-a/b)$$

$$\text{and : } \mathcal{F}(M', t', M, t) = F(r, (z+z'), (t-t')) = 2 \int_0^\infty J_0(Kr) e^{K(z+z')} \sqrt{K} \sin \sqrt{K}(t-t') dK \quad (2-c)$$

The term (2-b) is the impulsive part of the function, whereas (2-c) is generally referred to as the memory part.

Since the early eighties, several authors have proposed numerical algorithms for the solution of the above 3D problem, or some variant (Liapis 1986, King 1987, Kormeyer 1988, Magee 1991, Bingham 1994,...). In his program, Ferrant (1988) used a zeroth order direct BEM method. His computer code was used as a basis in the present study; it was adapted to take into account the new computational techniques for the Green function. Let us briefly summarize here the main features of the code. The body surface  $C$  is discretized into plane triangular or quadrilateral panels  $C_j$ . Sources of constant density  $\sigma = \partial\Phi/\partial n$ , and dipoles of constant density  $\mu (= -\Phi)$  are distributed over the panels. The source strength  $\sigma_j$  on each panel is known through the body no-flux boundary condition. Denoting :

$$D_{ij} = \iint_{C_j} \frac{\partial}{\partial n_j} G_0(M_i, M_j) dC_j \quad S_{ij} = \iint_{C_j} G_0(M_i, M_j) dC_j \quad (3)$$

$$s_{ij}(T) = \iint_{C_j} F(M_j, 0, M_i, T) dC_j \quad d_{ij}(T) = \iint_{C_j} \frac{\partial}{\partial n_j} F(M_j, 0, M_i, T) dC_j \quad (4)$$

the continuous integral equation (1) degenerates into a discrete finite order algebraic system :

$$[D_{ij}] [\mu_j(T)] = -H(T) [S_{ij}] [\sigma_j(0)] - \int_0^T dT' [s_{ij}(T')] [\sigma_j(0)] + \int_0^T dT' [d_{ij}(T-T')] [\mu_j(T')] \quad (5)$$

Coefficient matrices  $[D_{ij}]$  and  $[S_{ij}]$  (3) are computed by the classical Hess et Smith formula. Since they are time independent, they are evaluated once for all, and the first one is inverted at the onset by a gaussian procedure. The solution at each time step is then obtained by a simple matrix product after updating the RHS. It requires the computation of convolution products of the past solution with the Green function and its gradient [see (5)]. The matrices  $s_{ij}$  and  $d_{ij}$  must be evaluated at each time step, and stored in order to compute the kernel of the convolution integral from 0 to the current time  $t$ . This is the main burden in this kind of time-domain computations, and the most time consuming.

The original expression (2) is not well suited for numerical evaluation; then, in the eighties, several authors (Jami 1981, Liapis 1986, King 1987, Newman 1985-1992,...) developed numerical procedures based on: series or asymptotic expansions, Filon quadratures, recursive relations,... The first method to be implemented in our code was based on these formulas (King (1987)); it will be referred to as "series expansions method" in the sequel.

The second numerical method for the evaluation of the Green function memory term (2-c) is based on a bi-linear interpolation in a pre-computed table. (Ferrant 1988b, Magee & Beck 1989). This is made possible by the change of variable  $\lambda = KR_1$  in (2-c) yielding:

$$F(r, z, t) = 2R_1^{-3/2} \int_0^\infty J_0(\lambda \sqrt{1-\mu^2}) e^{-\lambda \mu} \sqrt{\lambda} \sin(\sqrt{\lambda} \tau) d\lambda, \quad (6)$$

where the integral is a function of only two "natural variables":  $\mu = -z/R_1$ ,  $\tau = t/\sqrt{R_1}$ . This second method, which was already implemented in the original code, will be denoted: "tabulation method" in the following.

At the last Workshop in Marseille (Clément 1997), we gave a third alternative way to compute the time-domain Green function and its gradient. It is based on a general lemma (Clément 1998) which establishes that these functions satisfy very simple fourth order Ordinary Differential Equation (ODE). It was shown for instance that  $F(r, Z, t)$ , is a solution of:

$$(r^2 + Z^2) \frac{\partial^4 F}{\partial t^4} - Zt \frac{\partial^3 F}{\partial t^3} + \left( \frac{t^2}{4} - 4Z \right) \frac{\partial^2 F}{\partial t^2} + \frac{7t}{4} \frac{\partial F}{\partial t} + \frac{9}{4} F = 0 \quad (7)$$

The spatial derivatives of  $F$  satisfy similar ODE, differing only by their numerical coefficients. Then, since the time grows monotonously in the time stepping methods considered, these functions may be computed "in-line" by integrating the ODE with respect to the time variable using standard algorithms like Runge-Kutta or predictor-corrector. In the present study, second and fourth order Runge-Kutta methods were tested. (see Fig.3).

The integrals over the panels (4) may then be computed by Gauss point quadratures rules. Both the one point and the four points rules were tested; it was found that, for a given final accuracy, the single point algorithm which requires a finer meshing, was relatively more efficient than the four points, due to a better approximation of the Rankine part of the solution. We therefore kept this one point integration rule in all the computations reported herein.

The impulsive hydrodynamic forces are finally computed as:

$$M_{ij}(T) = \iint_C \Phi_i(M', T) n_j(M') dC \quad L_{ij}(T) = \iint_C \frac{\partial}{\partial T} \Phi_i(M', T) n_j(M') dC \quad (8)$$

### IRF of a heaving hemisphere.

As a test case to compare the three above mentioned methods, we began with the simple problem of the heaving hemisphere.

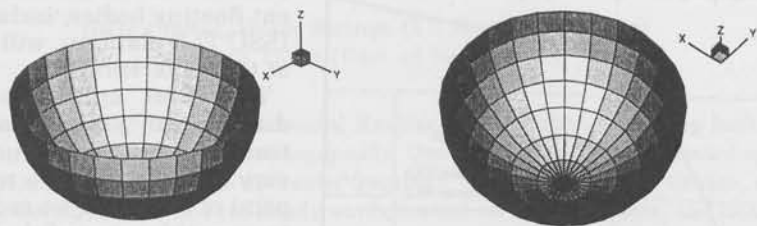


Fig 1: Floating hemisphere : a 4x49 panels mesh.

The responses functions  $M_{33}(T)$  and  $L_{33}(T)$  resulting from a step vertical velocity are computed. A typical result for  $0 < t < 20$  is plotted in figure 2. Convergence with the mesh size was investigated by varying systematically the number of panels. It was found that the mesh illustrated by Figure 1 above (*i.e.* 4x7x7 panels) gave results converged to within 1% in the vicinity of  $t=1.475$ , where  $L_{33}(T)$  reaches its maximum value.

The oscillations observed in the tail of the response, for  $t > 6$ , are the time-domain counterpart of the well known "irregular frequencies", and arise from the same origin. Since we were mainly interested here in *cpu* time statistics, we did not try to suppress this phenomenon by the help of the usual dedicated methods. This point is left for a further study.

Let us now compare the *cpu* time required by the three methods of Green function evaluation (Fig.3). The numerical process of the convolution integral suggests a quadratic growth of the computing time. Such a behaviour was observed with both the tabulation and the ODE methods, whereas the series expansion method presents two different regimes. For  $t < 18$ , we observe a quasi-linear growth of the *cpu*-time. In this area, the Green function is evaluated by series expansion or by Filon quadrature, according to the relative position of source and field points. These methods are far more time consuming than the asymptotic expansion which is used when  $\tau > 14$ . When all the couples of points satisfy this conditions, the program speeds up and a quadratic behaviour is recovered. The benefit of using the ODE method is clearly illustrated by Figure 3. One should notice that these curves correspond to quite long simulations. In the present case of the heaving hemisphere, a simulation up to  $t=20$  should be sufficient from a practical point of view (see Fig.2). It would result in the computing time shown in the table below, when using a DEC Alpha 500 workstation, at 330MHz.

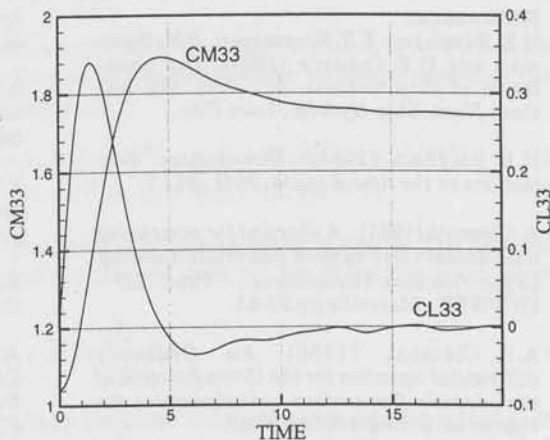


Fig.2: time-domain "added mass"  $M_{33}(T)$ , and impulse response function  $L_{33}(T)$ .  $dt=0.025$ , 4x49 panels.

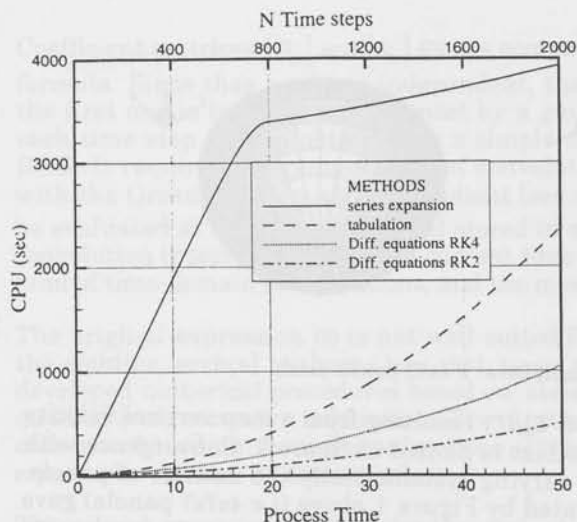


Fig.3 : Floating hemisphere. (4x49 panels): *cpu* time requirement

Method	<i>cpu</i> -time (sec.)
series	3398
tabulation	413 (=1/8)
ODE RK4	211 (=1/16)
ODE RK2	104 (=1/33)

#### References :

H.B. Bingham, F.T. Korsmeyer, J.N. Newman and G.E. Osborne (1993), The simulation of ship motions. In : *Proc. 6th Intl Conf. Num. Ship Hydrol.*, Iowa City.

H.B. Bingham (1994), *Simulating ship motions in the time domain*. PhD. M.I.T

A. Clément (1997) : *A shortcut for computing time-domain free-surface potentials avoiding Green function evaluations*. - *Proc. 12<sup>th</sup> IWWWFB* ; Marseille pp.37-43.

A.H. Clément (1998), *An Ordinary differential equation for the Green function of time-domain free-surface hydrodynamics*. (to appear in) *J. Engineering Math.*

P. Ferrant (1988a), *Radiation d'ondes de gravité par les déplacements de grande amplitude d'un corps immergé : comparaison des approches fréquentielles et instationnaires*. Thèse de Doctorat de l'Université de Nantes.

P. Ferrant (1988b), A fast computational method for transient 3D wave-body interaction *Proc Int. Conf. Comp. Model. Ocean Engng.* Venice.

A. Jami (1981), *Etude théorique et numérique de phénomènes transitoires en*

hydrodynamique navale. Thèse de Doctorat ès Sciences. ENSTA, Paris.

Further results for other different floating bodies, including the ISSC TLP platform, will be given at the conference.

This first application of the differential properties of the time-domain Green function is very encouraging, in a numerical point of view, and we recommend to use this powerful approach whenever a numerical evaluation of this function, or its spatial derivatives, is needed.

Other applications of the above mentioned Green function ODE, in the time-domain and in the frequency domain as well, are under consideration and will be presented in further communications.

**Acknowledgements :** This work was financially supported by the *Direction des Recherches, Études et Techniques* of the French Ministry of Defense (DGA). The author is thankful to Dr Pierre Ferrant who developed the initial version of the computer code.

B.W. King (1987) Time-domain analysis of wave exciting forces on ships and bodies. PhD Univ. Michigan.

F.T. Korsmeyer (1988), The first- and second order transient free surface wave radiation problem. PhD Diss. M.I.T.

S.J. Liapis (1986), Time-domain analysis of ship motions. PhD Diss. Univ. Michigan.

A.R. Magee and R.F. Beck (1989). Vectorized Computation of the Time-Domain Green Function. *4th Workshop Water Waves & Floating Bodies*. Oystese.

A.R. Magee, (1991). Large amplitude ship motions in the time domain. PhD Thesis. Univ. Michigan.

J.N. Newman (1985). The evaluation of free-surface Green functions. *Proc. 4th Intl Conf. Numer. Ship Hydrol.* Washington.

J.N. Newman (1992). The approximation of free-surface Green functions. in: *Wave Asymptotics*. P.A. Martin & G.R. Wickham ed, pp. 107-135. Cambridge University Press.

## A Fully 3-d Rankine Method for Ship Seakeeping

Heike Cramer, Volker Bertram (TU Hamburg-Harburg)  
Gerhard Thiart (Univ. of Stellenbosch)

We will present here a 'fully' three-dimensional Rankine panel method, capturing both the steady and the time-harmonic potentials three-dimensionally. Our method captures all forward-speed effects, namely – in addition to the change in encounter frequency – dynamic trim and sinkage, steady wave profile (average wetted surface) and the steady wave elevation on the free surface, and local the steady flow field

We consider a ship with average speed  $U$  in a regular wave of small amplitude  $h$ . The boundary conditions will be linearized with respect to  $h$ . The method will only be outlined here. Bertram (1996,1998) give more details. We limit ourselves to cases where  $\tau > 0.25$ . Then only downstream waves will be created by the ship. We solve the problem in the frequency domain using an indirect Rankine singularity method, i.e. solving for source strengths as unknowns. The elements are first-order elements (plane and constant strength).

The problem is formulated in right-handed Cartesian coordinate systems. The inertial  $Oxyz$  system moves uniformly with velocity  $U$ .  $x$  points forward,  $z$  downwards. The  $Ox\bar{y}\bar{z}$  system is fixed at the ship and follows its motions. When the ship is at rest position,  $\bar{x}$ ,  $\bar{y}$ ,  $\bar{z}$  coincide with  $x$ ,  $y$ ,  $z$ . The rigid body motion expressed in the motion vector  $\vec{u} = \{u_1, u_2, u_3\}^T$  and the rotational motion vector  $\vec{\alpha} = \{u_4, u_5, u_6\}^T = \{\alpha_1, \alpha_2, \alpha_3\}^T$ . All motions are assumed to be of first order small.

A perturbation formulation for the potential is used omitting higher-order terms:

$$\phi^t = \phi^{(0)} + \phi^{(1)} \quad (1)$$

$\phi^{(0)}$  is the steady contribution and  $\phi^{(1)}$  the time-harmonic contribution proportional to  $h$ . We describe the elevation of the free surface  $\zeta$  in a similar form as the potential where we specify explicitly that quantities are time-harmonic in encounter frequency  $\omega_e$ :

$$\phi^t(x, y, z; t) = \phi^{(0)}(x, y, z) + \phi^{(1)}(x, y, z; t) = \phi^{(0)}(x, y, z) + \text{Re}(\hat{\phi}^{(1)}(x, y, z)e^{i\omega_e t}) \quad (2)$$

$$\zeta^t(x, y; t) = \zeta^{(0)}(x, y) + \zeta^{(1)}(x, y; t) = \zeta^{(0)}(x, y) + \text{Re}(\hat{\zeta}^{(1)}(x, y)e^{i\omega_e t}) \quad (3)$$

The symbol  $\hat{\cdot}$  denotes generally the complex amplitude of a time-harmonic quantity. The harmonic potential  $\phi^{(1)}$  is decomposed into the potential of the incident wave  $\phi^w$ , the diffraction potential  $\phi^d$ , and 6 radiation potentials:

$$\phi^{(1)} = \phi^d + \phi^w + \sum_{i=1}^6 \phi^i u_i \quad (4)$$

The steady potential  $\phi^{(0)}$  can be computed by a 'fully nonlinear' wave resistance program which yields also second derivatives of the potential using higher-order panels on the hull. The potential of the incident wave  $\phi^w$  is also known as usual. So the remaining unknowns are the diffraction and (unit motion) radiation potentials. These are determined by solving the Laplace equation subject to the boundary conditions:

At the average free surface ( $z = \zeta^{(0)}$ ):

$$(-\omega_e^2 + Bi\omega_e)\hat{\phi}^{(1)} + ((2i\omega_e + B)\nabla\phi^{(0)} + \vec{a}^{(0)} + \vec{a}^g)\nabla\hat{\phi}^{(1)} + \nabla\phi^{(0)}(\nabla\phi^{(0)}\nabla)\nabla\hat{\phi}^{(1)} = 0 \quad (5)$$

$$\vec{a} = (\nabla\phi^{(0)}\nabla)\nabla\phi^{(0)}, \vec{a}^g = \vec{a} - \{0, 0, g\}^T, B = -(1/a_3^2)\frac{\partial}{\partial z}(\nabla\phi^{(0)}\vec{a}^g).$$

On the ship hull  $S(\vec{x}) = 0$ , using  $\vec{m} = (\vec{n}\nabla)\nabla\phi^{(0)}$ :

$$\vec{n}\nabla\hat{\phi}^{(1)} + \vec{u}(\vec{m} - i\omega_e\vec{n}) + \hat{\vec{\alpha}}(\vec{x} \times (\vec{m} - i\omega_e\vec{n}) + \vec{n} \times \nabla\phi^{(0)}) = 0 \quad (6)$$

The 'shifting' technique developed originally for the steady wave-resistance case can be adapted without problems to the time-harmonic problem and fulfills also automatically the open-boundary condition (no reflection at the downstream boundary).

Incident wave and diffraction potentials are decomposed into symmetrical and antisymmetrical components. Boundary conditions (4) and (5) then form systems of linear equations in the source strengths for the 8 unknown potentials ( $\hat{\phi}^{d,s}$ ,  $\hat{\phi}^{d,a}$ ,  $\hat{\phi}^i$ ,  $i = 1..6$ ). The four symmetrical (likewise the four antisymmetrical) systems of equations share the same coefficient matrix with only the r.h.s. being different. All four cases are solved simultaneously using Gauss elimination. Then the computation of all potentials and their derivatives at all collocation points is straight-forward. But for the total potential, the so-far unknown motion amplitudes still need to be determined. The expressions for this final step are derived in principle from 'force = mass · acceleration' to:

$$m(\ddot{\vec{u}} + \ddot{\vec{\alpha}} \times \vec{x}_g) = -\vec{\alpha} \times \vec{G} + \int_{S^{(0)}} (p^{(1)} - \rho(\vec{u}\vec{a}^g + \vec{\alpha}(\vec{x} \times \vec{a}^g)))\vec{n} dS \quad (7)$$

$$m(\vec{x}_g \times \ddot{\vec{u}}) + I\ddot{\vec{\alpha}} = -\vec{x}_g \times (\vec{\alpha} \times \vec{G}) + \int_{S^{(0)}} (p^{(1)} - \rho(\vec{u}\vec{a}^g + \vec{\alpha}(\vec{x} \times \vec{a}^g)))(\vec{x} \times \vec{n}) dS \quad (8)$$

$p^{(1)}$  is the total unsteady pressure.  $\vec{G} = \{0, 0, mg\}^T$  is the ship's weight,  $m$  the displacement mass,  $\vec{x}_g$  the center of gravity,  $I$  the matrix of mass inertia moments with respect to the origin of the ship-fixed system. Eqs.(7) and (8) yield a system of linear equations for  $u_i$  ( $i = 1, \dots, 6$ ) which is quickly solved by Gauss elimination.

We added recently an ad hoc correction to account for the propulsion characteristics. Thrust and resistance forces acting on the ship are affected by the motions. One could include thrust and resistance vectors similar to the weight vector  $\vec{G}$  to account for all motions. However, the main effect comes from surge motions in long waves and this allows a somewhat simpler treatment. Surge motions change the longitudinal velocity of the ship. Correspondingly changed resistance and propulsion characteristics of the ship will induce considerable damping of surge motions especially for long waves. Also the local orbital velocity of the waves may have some influence. Inclusion of these effects yields, Bertram and Thiaert (1998):

$$(1-t)T_h - R = ((1-t)(i-w)T_h' - R')\dot{u}_1 - (1-t)(1-w)T_h'(\phi_x^w(\vec{x}_p) + \phi_x^d(\vec{x}_p)) + \bar{v}_{dif}R' \quad (9)$$

$T_h'$ ,  $R'$  are derivatives of thrust and resistance with respect to speed,  $t$  thrust deduction fraction,  $w$  Taylor wake fraction. These are approximated by empirical formulas.  $\bar{v}_{dif}$  approximates the influence of the orbital velocity averaging over the wetted surface of the ship:

$$\bar{v}_{dif} = \frac{1}{S^{(0)}} \int_{S^{(0)}} (\phi_x^w + \phi_x^d) dS \quad (10)$$

Eq.(9) is added as correction on the r.h.s. of the first component of vector eq.(7). The  $\dot{u}_1$  term can be interpreted as surge damping, the remaining terms contribute to the exciting surge force.

We present results for the S-175 ITTC containership at  $F_n = 0.275$ . The hull was discretized by 631 elements. The hull was modified in the aft region by integrating the rudder into the hull. For symmetric motions, this will have only negligible effect, but for antisymmetric motions this should capture the physics better than omitting the rudder totally. In a first step, the nonlinear wave-resistance problem was solved to determine the steady potential and its derivatives. The same discretized hull model was used for the seakeeping computations. The grid on the free surface had then about 1300 elements for each case. Fig.1 shows the RAOs for motions in head waves. The results of our panel method agree generally very well with experiments. The surge motions for low frequencies are still computed somewhat higher than measured. The reason is unclear, but could lie in nonlinear effects or

margins of errors in the experiments. We also show results for the same grids, but with the classical steady-flow approximation, i.e. no trim and sinkage, flat free surface, uniform flow, and integration only to the calm-waterline. This approximation yields differences in the heave and pitch motions of up to 20% for medium wave lengths. Similar effects were observed for a Series-60 ship by Bertram (1997).

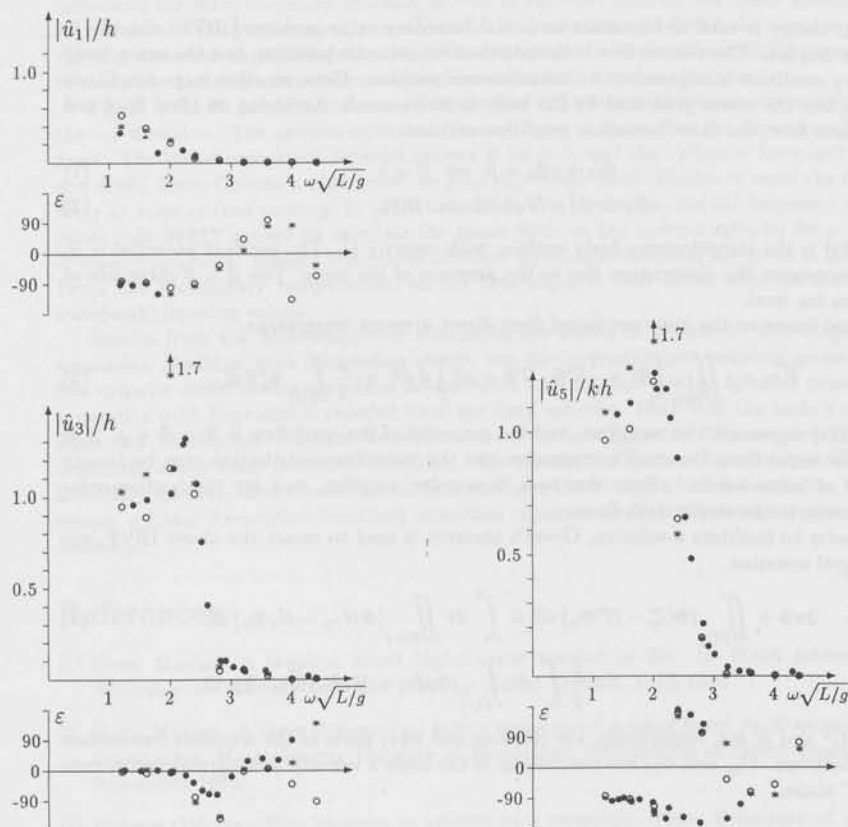


Fig.1: RAOs for S-175,  $\mu = 180^\circ$ ,  $F_n = 0.275$ ; ● experiment, ○ Rankine panel method (RPM) with all forward-speed effects, \* RPM with classical uniform flow approximation.

#### References

- BERTRAM, V. (1996), *A 3-d Rankine panel method to compute added resistance of ships*, IfS Report 566, Univ. Hamburg
- BERTRAM, V. (1997), *Vergleich verschiedener 3D-Verfahren zur Berechnung des Seeverhaltens von Schiffen*, Jahrbuch Schiffbautechn. Gesellschaft, Springer
- BERTRAM, V. (1998), *Numerical investigation of steady flow effects in 3-d seakeeping computations*, 22th Symp. on Naval Hydrodyn., Washington
- BERTRAM, V.; THIART, G. (1998) Fully three-dimensional ship seakeeping computations with a surge-corrected Rankine panel method, submitted to JMST

## Multiple-body Simulations using a Higher-Order Panel Code

Donald Danmeier<sup>1</sup>

### Formulation

Potential theory is used to formulate an initial-boundary value problem (IBVP) directly in the time domain. The free-surface is linearized about its calm position, but the exact body boundary condition is imposed on its instantaneous position. Thus, we allow large-amplitude motions, but the waves generated by the body must be small. Assuming an ideal fluid and irrotational flow, the these boundary condition and are:

$$\Phi_{tt} + g\Phi_z = 0 \quad \text{on } Z = 0 \quad (1)$$

$$\Phi_n = (\vec{U} - \nabla\varphi) \cdot \vec{n} \quad \text{on } B(t). \quad (2)$$

Here,  $B(t)$  is the instantaneous body surface, with velocity  $\vec{U}$ . The incident potential is  $\varphi$ , and  $\Phi$  represents the disturbance due to the presence of the body. The  $Z = 0$  plane lies at the mean sea level.

Global forces on the body are found from direct pressure integration.

$$\vec{F} = -\rho \iint_{B(t)} \left( \Psi_t + \frac{1}{2} \nabla\Psi \cdot \nabla\Psi + gZ \right) \vec{n} dS + \frac{\rho}{2} \int_{\Gamma(t)} \Psi_t^2 \vec{n} dl \quad (3)$$

where,  $\Gamma(t)$  represents the waterline, and the potential of the total flow is  $\Psi = \Phi + \varphi$ . The quadratic terms from Bernoulli's expression and the waterline contribution may be loosely thought of 'second-order' effects due to a 'first-order' solution, and are the leading-order contributors to the steady drift force.

In order to facilitate a solution, Green's theorem is used to recast the above IBVP into an integral equation.

$$2\pi\Phi + \iint_{B(t)} (\Phi G_n^o - G^o \Phi_n) dS = \int_0^t d\tau \iint_{B(\tau)} (\Phi H_{\tau n} - H_\tau \Phi_n) dS \quad (4)$$

$$+ \frac{1}{g} \int_0^t d\tau \int_{\Gamma(\tau)} (\Phi H_{\tau\tau} - H_\tau \Phi_\tau) \vec{U}_{2d} \cdot \vec{n}_{2d} dl$$

where,  $G^o$  and  $H$  are, respectively, the Rankine and wave parts of the transient free-surface Green function.  $\vec{U}_{2d}$  and  $\vec{n}_{2d}$  are projections of the body's velocity and normal vector onto the  $XY$  plane.

### Numerical Solution

We use higher-order panel methods to efficiently solve the integral equation. The body surface and velocity potential are mapped to a square parametric plane via the B-spline basis. A Galerkin procedure gives a linear system of equations. The success of this B-spline based panel method in the frequency domain has been demonstrated by Maniar [1] [2]. A major advantage of the method is the ability to analytically differentiate the solution, and we exploit this by including the  $(\nabla\Phi \cdot \nabla\Phi)$  term in the Bernoulli pressure.

The results presented in this abstract only include horizontal modes, however, if our finite-amplitude simulations include vertical motion, the body needs to be remeshed at every time step. In these cases, an automated marching algorithm detects the body/free-surface intersection in the parametric plane. We then produce new B-spline coefficients for the portion of the body below the mean free-surface by a least-square fit.

<sup>1</sup>Department of Ocean Engineering, MIT, USA (danmeier@mit.edu)

## N-body Simulation

Hydrodynamic interactions may greatly change wave loads when multiple bodies operate in close proximity. Ohkusu [3] examined the motions of a ship in the neighborhood of an offshore structure. His ship-structure system included a large moored cylindrical structure with a horizontal axis. The floating ship lies parallel to the structure's longitudinal axis and is subject to monochromatic beam waves. Ohkusu looked at how the fixed structure influenced the wave-frequency motions, as well as the drift force on the freely floating ship. At certain wavelength/separation conditions, his calculations predicted the upwave drift of the ship observed during model testing. We will use the finite-amplitude IBVP formulation to study the hydrodynamic interactions of two truncated circular cylinders.

Figure 1 shows two identical truncated circular cylinders, with planar waves incident in the  $-x$  direction. The upwave cylinder is free to move in surge, but the downwave body is fixed. The initial separation between centers is  $2d = 5$ , and the cylinders have unit radius and draft. From Ohkusu's experience, we may expect the fixed cylinder to repel the floating body at some critical spacing. In order to confirm this prediction, the 3D frequency domain panel code WAMIT is used to calculate the mean force on the upwave cylinder for a variety of wave frequencies. Results from three different separation distances are given in Figure 2. From this preliminary computation, we see that negative drift forces arise for a range of wavelength/spacing values.

Results from the finite-amplitude simulation are shown in Figure 3. The large initial separation produces weak interaction effects, but the hydrodynamic coupling grows as the free cylinder drifts downwave. After several wave periods, the upwave cylinder experiences a negative drift force and is repelled from the fixed cylinder. Note that the body's acceleration and velocity are  $O(\epsilon)$ , but its motions are  $O(1)$  in magnitude. This requires an exact treatment of the body boundary condition. The steady flow induced by the slow drift is of secondary interest, since the diffraction field produces the strong interactions effects. For this reason, a linear free-surface boundary condition captures the hydrodynamics to the desired accuracy.

## References

- [1] Hiren Maniar. A B-spline based higher-order method in 3D. In *Tenth International Workshop on Water Waves and Floating Bodies*, Oxford, April 1995.
- [2] Hiren Maniar. *A three dimensional higher order panel method based on B-splines*. PhD dissertation, Massachusetts Institute of Technology, Department of Ocean Engineering, September 1995.
- [3] Makoto Ohkusu. Ship motions in vicinity of a structure. *Proc. Behaviour of offshore structures*, Trondheim, August 1976.

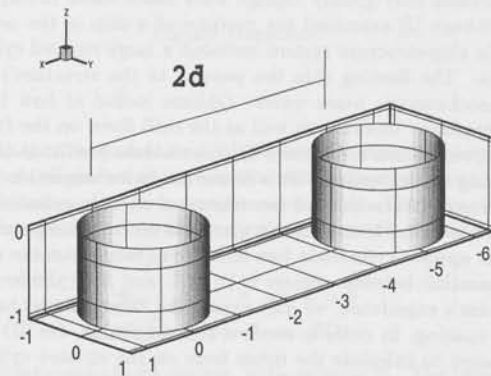


Figure 1: Two interacting cylinders with unit radii and draft. Distance between centers is 5. Waves in  $-x$  direction. Upwave cylinder is free in surge, downwave body is fixed.

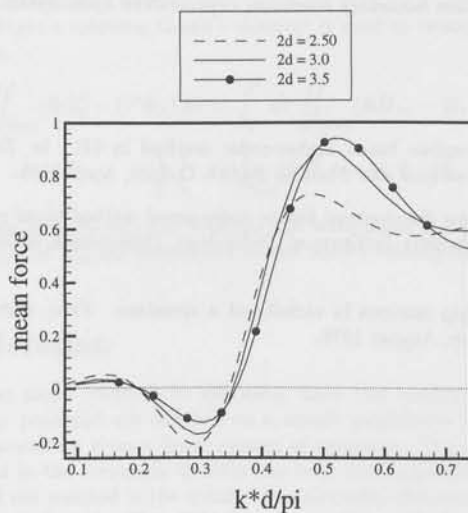


Figure 2: Mean drift force on upwave cylinder calculated from WAMIT. Non-dimensional force is  $\bar{F} = \frac{F}{\rho g A^2 R}$ , where  $A$  is incident wave amplitude and  $R$  is radius of cylinder.

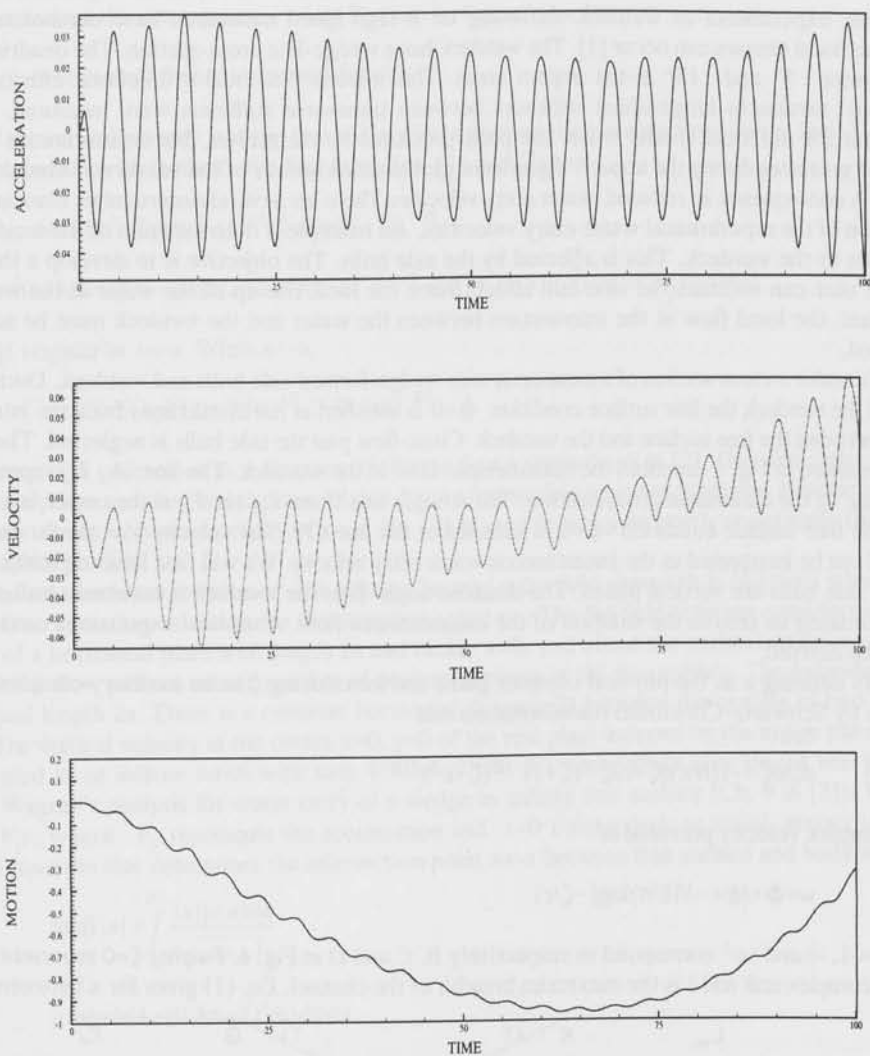


Figure 3: Time histories of upwave cylinder from finite-amplitude simulation. Incident waves are monochromatic, with wavenumber  $K = 2$  and amplitude  $A = 0.1$ . Non-dimensional length and time are:  $\bar{x} = \frac{x}{R}$ ,  $\bar{t} = t(R/g)^{(1/2)}$

## WATER ENTRY OF A WEDGE INTO A CHANNEL

Odd M. Faltinsen<sup>1</sup> and Rong Zhao<sup>2</sup><sup>1</sup> Norw. Univ. of Science and Techn., N-7034 Trondheim, Norway<sup>2</sup>MARINTEK, 7002 Trondheim, Norway

Full scale experiments of wetdeck slamming on a high-speed catamaran have demonstrated that significant local stresses can occur [1]. The wetdeck has a wedge-like cross-section. The deadrise angles are between  $5^\circ$  and  $15^\circ$  in the impact areas. This implies that local hydroelastic effects are not dominant. Strains in longitudinal stiffeners between transverse stiffeners were measured. What is important for the local strains is not the peak pressures by themselves, but representative spatially averaged pressures during the impact. Significant global accelerations of the vessel occurred during the impact. A consequence is reduced water entry velocities. There are several uncertainties associated with estimation of the experimental water entry velocities. An example is determination of the incident flow velocities to the wetdeck. This is affected by the side hulls. The objective is to develop a theoretical method that can estimate the side-hull effect. Since the local rise up of the water at the wetdeck is important, the local flow at the intersection between the water and the wetdeck must be accurately described.

Consider a cross-section of a catamaran with wedge-formed side hulls and wetdeck. During water entry of the wetdeck the free surface condition  $\phi=0$  is satisfied at horizontal lines from the intersection points between the free surface and the wetdeck. Cross-flow past the side hulls is neglected. The channel flow presented in Fig. 1 describes the instantaneous flow at the wetdeck. The line  $A_\infty E_\infty$  represents the centerline of the catamaran cross-section. The straight line from  $L_\infty$  to  $F_\infty$  is the center line of a side hull. The free surface condition  $\phi=0$  is satisfied at the line  $CH$ . The velocity  $V$  at the far ends of the channel can be interpreted as the instantaneous water entry velocity. We will first limit ourselves to  $\gamma=0$ , i.e. the side hulls are vertical plates. The deadrise angle  $\beta$  of the wetdeck is assumed small.  $\beta$  can be approximated as zero in the solution of the instantaneous flow. Analytical expressions can to a large extent be derived.

By defining  $z$  as the physical complex plane and introducing  $\zeta$  as an auxiliary complex plane, it follows by Schwartz-Christoffel transformation that

$$dz/d\zeta = -i(\ell/\pi)(\zeta+c)\zeta^{-1}(\zeta+1)^{-1/2}(\zeta+c^2)^{-1/2} \quad (1)$$

The complex velocity potential is

$$w = \phi + i\psi = -V(\ell/\pi)\log(-\zeta/c) \quad (2)$$

Here  $\zeta=-1$ ,  $-c$  and  $-c^2$  correspond to respectively  $B$ ,  $C$  and  $D$  in Fig. 1. Further  $\zeta=0$  represents  $E_\infty F_\infty$ .  $i$  is the complex unit and  $\ell$  is the maximum breadth of the channel. Eq. (1) gives for  $x$  between  $B$  and  $C$

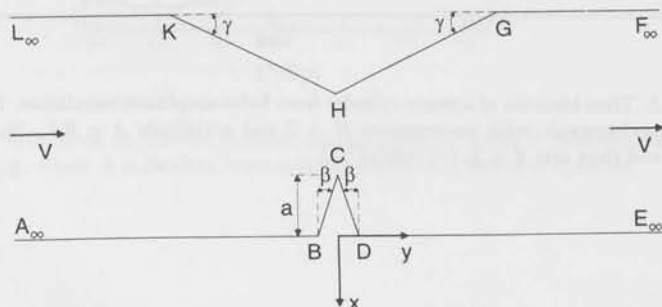


Fig. 1 Channel flow representing instantaneous flow during water entry of the wetdeck.

$$x = \frac{\ell}{\pi} \left\{ \sin^{-1} \left( \frac{-\zeta - 0.5(1+c^2)}{0.5(1-c^2)} \right) - \sin^{-1} \left( \frac{0.5(1+c^2) + c^2/\zeta}{0.5(1-c^2)} \right) \right\}, \quad -1 < \zeta < -c \quad (3)$$

The corresponding velocity potential is given by Eq. (2). It follows from Eq. (3) that the half beam  $a$  of the wetdeck at the instantaneous water line can be related to  $c$  by

$$c = (1 - \sin(0.5\pi a/\ell)) / (1 + \sin(0.5\pi a/\ell)) \quad (4)$$

We need the vertical velocity  $v$  at the free surface in predicting the instantaneous water line. The water line is at  $\zeta = ce^{i\theta}$  with  $0 < \theta < \pi$ . We find from Eqs. (1) and (2) that

$$v = V(c^2 + 2c\cos\theta + 1)^{1/2} (2c(\cos\theta + 1))^{-1/2} \quad (5)$$

$$\cos\theta = -\left\{ 0.25(1-c)^2/c + \sin(\pi(x+a)/\ell)(1-c) c^{-1/2} + (1-0.25(1-c)^2/c)\cos(\pi(x+a)/\ell) \right\} \quad (6)$$

Eq. (5) is singular at  $x=-a$ . When  $x \sim -a$ ,

$$v = V(0.5(1-c)/c)^{1/2} (\pi)^{1/2} (-(x+a))^{-1/2} \quad (7)$$

The intersection point  $x=-a$  as a function of time is found similarly as in [2]. One first determine the intersection points and then find the time it takes for the free surface to move from one intersection point to the next. In the very near vicinity of  $x=-a$ , Eq. (7) is used to integrate partly analytically the path of a free surface particle.

The solution is inconvenient if  $\ell/a$  is large. Instead a far-field approach is followed when  $\ell/a > 3$  and used as a starting condition for the complete solution. The far-field solution considers an image system of a horizontal plate with length  $2a$  and centre  $x=0, y=0$  about the vertical walls  $x=\pm\ell$ . This means cross-flow past an infinite number of horizontal plates in the free surface. The individual plates have equal length  $2a$ . There is a constant horizontal distance  $2\ell$  between the centres of two adjacent plates. The vertical velocity at the centre  $x=0, y=0$  of the real plate induced by the image plates can be represented as an infinite series with sum  $V(0.5\pi a/\ell)^2/6$ . We concentrate now on the real plate and follow Wagner's analysis for water entry of a wedge in infinite free surface (Ch. 9 in [3]). We write  $V = V_0 + V_1 t$ , where  $V_1$  represents the acceleration and  $t=0$  corresponds to initial impact time. The integral equation that determines the intersection point  $x=-a$  between free surface and body surface is

$$\tan\beta|x| = \int_0^{|x|} \frac{|x|\mu(a)da}{\sqrt{x^2 - a^2}} \quad (8)$$

Further

$$\mu(a) = V(1 + (0.5\pi a/\ell)^2/6) dt/da \quad (9)$$

Since solution of Eq. (8) is  $\mu(a) = 2\tan\beta/\pi$ , solution of Eq. (9) is

$$2k\tan\beta \tan^{-1}(a/k) = \pi(V_0 t + 0.5V_1 t^2) \quad (10)$$

where  $k = 2\sqrt{6}\ell/\pi$ . Eq. (10) determines  $a$  as a function of time. The free surface elevation  $\eta$  and vertical free surface velocity  $v$  are

$$\eta = 2|x|\tan\beta \sin^{-1}(a/|x|)/\pi \quad (11)$$

$$v = V(1 + (0.5\pi a/\ell)^2/6)|x|(x^2 - a^2)^{-1/2} \quad (12)$$

When the complete theory is started, Eqs. (11) and (12) are used as initial conditions.

The pressure  $p$  on the wedge is found from  $\rho \partial \phi / \partial t$ , where  $\rho$  is the mass density of water. The far-field solution gives

$$p/\rho = V_1(V/V)(a^2 - x^2)^{1/2} + V(da/dt) a((0.5\pi a/\ell)^2(a^2 - x^2)^{1/2}/3 + (V/V)(a^2 - x^2)^{-1/2}) \quad (13)$$

where  $V/V = 1 + (0.5\pi a/\ell)^2/6$ . Eq. (13) can be analytically integrated to obtain space-averaged pressures and total force. The space-averaged pressure in the complete theory is obtained by first numerically integrating  $\phi$  from  $x_i$  to  $x_{i+1}$  for each time step and then numerically time differentiate this expression. The total vertical force  $F$  can also be expressed as  $d(a_{22}V)/dt$  where  $a_{22}$  is the vertical added mass of the plate.  $a_{22}$  can be analytically expressed [4]. It follows that

$$F/\rho = -V_1 4\ell^2 \pi^{-1} \ln \cos(0.5\pi a/\ell) + 2\ell V^2 C_w \tan(0.5\pi a/\ell) \tan \beta \quad (14)$$

where the wetting factor  $C_w = a \cdot \tan \beta / d(t)$  and  $d(t) = V_0 t + 0.5V_1 t^2$ . Non-dimensional force, space-averaged pressure and time are introduced.  $F \tan^2 \beta / (\rho V^2 d(t))$  and  $p_{av} \tan \beta / (0.5\rho V^2)$  are presented as function of  $d(t)/(a_{max} \tan \beta)$ .  $a_{max}$  means maximum value of  $a$ . When  $V = V_0$ , non-dimensional force and pressure will only depend on  $\ell/a_{max}$ . Results are shown in Fig. 2 for  $\ell/a_{max}$  between 1.2 and 2.0

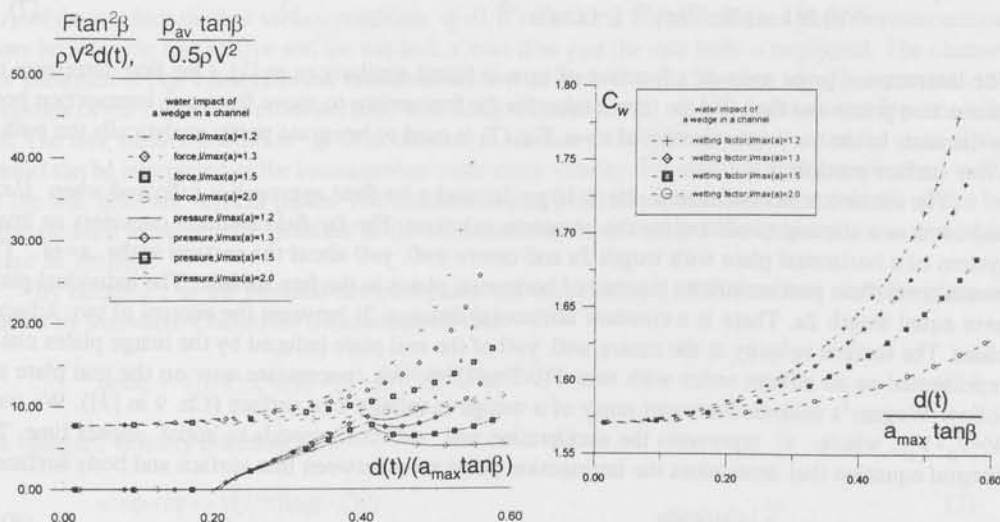


Fig. 2 Non-dimensional force  $F$ , space-averaged pressure  $p_{av}$  and wetting factor  $C_w$  as a function of non-dimensional time during water entry of a wedge. Constant entry velocity  $V$ .

together with the wetting factor  $C_w$ . The pressure is averaged from  $x = a_{max}/3$  to  $2a_{max}/3$ . There is a small jump in the force when the complete theory is started. This is not noticeable in the figure. The similar behaviour of the far-field solution and the complete theory represents a good verification test. When time goes to zero, the non-dimensional force is  $\pi^3/4$ . When  $\ell/a_{max} \rightarrow 1$  and the water is at  $a_{max}$ , the force goes to infinity. This can be seen from the last term in Eq. (14). The factor  $\tan(0.5\pi a/\ell)$  behaves like  $(\ell - a)^{-1}$  when  $a \rightarrow \ell$ . The singular behaviour of the force will be stronger since  $C_w$  increases when  $a \rightarrow \ell$ . The increase of  $C_w$  is caused by increased fluid velocities at the free surface when  $a \rightarrow \ell$ . A large force on the wetdeck means a large acceleration of the catamaran and a subsequent drop in the impact velocities. This implies that the actual force is not infinite. The space-averaged pressure has a peak, then drops and increases again. The peak occurs when the spray root of the jet ( $x = \pm a$ ) is at  $x = x_{i+1}$ . The far-field solution is then a good approximation. The later increase is caused by decreased

$\ell/a$ -values. The first peak of the non-dimensional pressure is of main concern in the structural analysis. The reasons are the decreasing entry velocity during the water entry and that maximum pressure can be approximated by the pressure term presented in Fig. 2. There is an additional pressure term proportional to the acceleration  $V_1$ . Since  $V_1$  is negative, this "added mass" pressure causes a pressure reduction and can as time goes on provide a negative total pressure.

The presented expressions do not describe the jet flow (spray) at the body surface. However, since the velocity potential has a square root singularity, we can match with the inner 2-D jet flow solution by Wagner [5]. The far-field solution gives a jet thickness  $\delta = 0.5a \tan^2 \beta / \pi$ . The complete theory gives  $\delta = (V \ell / da dt)^2 (1-c) \ell / (8\sqrt{c})$ . Fig. 2 gives  $a$  and  $da/dt$  from  $C_w$ . Eq. (5) determines  $c$ .

The previous procedure cannot be used for finite interior half angle  $\gamma$  of the side hulls.  $\gamma$  was about  $25^\circ$  at one of the tested impact areas. The side hull effect can be examined by setting  $\beta = \pi/2$  in Fig. 1 and using a Schwartz-Christoffel transformation.  $G$ ,  $H$  and  $K$  in Fig. 1 correspond to respectively  $c^2$ ,  $c$  and  $1$  in the  $\zeta$ -plane. On the free surface  $\zeta = ce^{i\theta}$  ( $0 < \theta < \pi$ ),  $dx/d\theta = (\ell/\pi)(2c(1-\cos\theta)/(c^2-2c\cos\theta+1))^{1/2}$  and the vertical velocity  $v = V(\ell/\pi)d\theta/dx$ .  $c$  can be related to the  $x$ -value of  $H$  by integrating  $dx/d\theta$  from  $\theta=0$  to  $\pi$ .  $v$  at  $x=0$  is a good measure of the incident velocity to the wetdeck. The instantaneous draft  $D(t)$  of the side hull was about  $\ell$  at initial time of impact. Results of  $v_1/V$  are presented in Fig. 3 and show the importance of the side hulls for finite  $\gamma$ -values.  $v_1$  means  $v$  at  $x=0$ . If the wetdeck is introduced into the analysis, the flow around the wetdeck is influenced by the side hulls. The results in the first part of the paper can be used to judge the importance of this effect. However, all effects can be combined simultaneously. The Schwartz-Christoffel transformation requires then four parameters that have to be related to physical coordinates. A complete solution will be presented and verified with the more analytically based results presented in this paper.

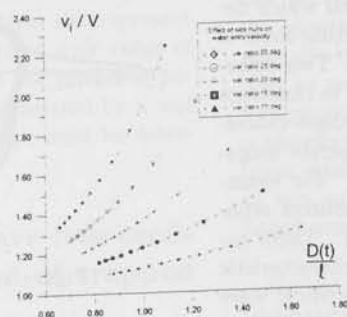


Fig. 3 Influence of side hulls on water entry velocity.

A simplified procedure where the instantaneous flow picture for  $\gamma=0$ ,  $\beta=0$  and finite  $\gamma$ ,  $\beta=\pi/2$  were combined, has been used to predict the structural loads in the wetdeck. A procedure like this can predict similar maximum strains as measured by [1]. However, since the flow was not measured, errors in estimates of incident wave velocities cause errors in water entry velocities and structural loads. A numerical method that should predict also the water entry velocities must include the non-linear effects due to side hulls and the wetdeck on global vessel accelerations.

## References

1. Aarsnes, J.V., Hoff, J.R., 1997, Full scale test with Ulstein Test Vessel, Marintek report
2. Zhao, R., Faltinsen, O., Aarsnes, J.V., 1996, Water entry of arbitrary two-dimensional sections with and without flow separation, Proc. 21st Symp. on Naval Hydrodynamics, Trondheim.
3. Faltinsen, O.M., Sea Loads on Ships and Offshore Structures, Cambridge University Press, 1990.
4. Sedov, L.I., 1965, Two-dimensional problems in hydrodynamics and aerodynamics, New York: Interscience
5. Zhao, R., Faltinsen, O., 1993, Water entry of two-dimensional bodies, J. Fluid Mech., Vol. 246, pp. 593-612.

# On the generation of wave free oscillatory bodies and of trapped modes

E. Fontaine and M.P. Tulin

University of California, Ocean Engineering Laboratory, Santa Barbara CA 93106-1080.

## 1 Introduction

The motion of bodies piercing a free surface in the presence of gravity usually leads to the formation of waves on the surface, which propagate away from the body. In this paper, we explore within the framework of first order potential flow theory, the existence of wave-free two dimensional flows past surface piercing oscillating bodies. The shape of the body is found by constructing a wave free potential which decays to zero at infinity and interpreting some of its streamlines as body boundaries. Two different general techniques can be used to construct such a potential. First, through phase cancellation of the wave fields due to discrete singularities with appropriate spacings. For example, McIver (1997) considers two sources separated by half a critical wavelength. There exists then a relation between the characteristic length of the body shape and the critical wave frequency. The use of this method is thus limited to higher frequencies. Another technique, introduced by Tulin (1976, 1982) in connection with ship waves, is based on the use of wave-free compound singularities. It has been successfully applied in three-dimensions for the minimization of ship wave resistance by Tulin & Oshri (1994). A portion of Tulin's results were re-discovered and applied by Tuck (1992). In this paper, we apply this technique to the seakeeping problem in order to find shapes of bodies that do not generate waves while oscillating at a given frequency. It is also shown how body shapes that generate the so called "trapped modes" can be derived using this theory. Simple examples are considered here using a single wave-free compound singularity, but results for singularity distributions, which can be interpreted in terms of body volume and verti-

cal force distributions, can also be derived using the same basic ideas. These results can also be extended in three-dimensions as carried out by Tulin in the case of bodies in uniform streams.

## 2 Wave-free compound singularities

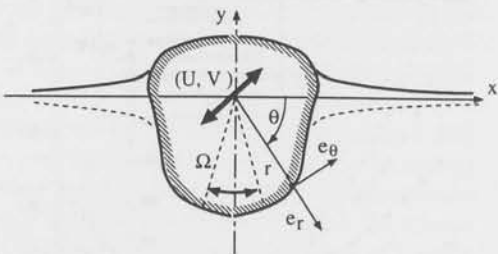


Figure 1: Geometric definitions.

We consider the two-dimensional case of a surface piercing body oscillating with pulsation  $\omega$  in heave, sway and roll (see. fig.1). The variables are non-dimensionalized using  $1/\omega$  as the time scale and  $g/\omega^2$  as the length scale, where  $g$  is the acceleration due to gravity

$$\begin{aligned} \bar{x} &= \frac{\omega^2 x}{g}, & \bar{y} &= \frac{\omega^2 y}{g}, & \bar{t} &= \omega t, \\ \bar{\eta} &= \frac{\omega^2 \eta}{g}, & \bar{\phi} &= \frac{\omega^3 \phi}{g^2} \end{aligned} \quad (1)$$

The complex potential

$$\Psi = [\bar{\phi} + i\bar{\psi}] e^{i\bar{t}} = [\Psi_h(\bar{z}) + \Psi_s(\bar{z})] e^{i\bar{t}} \quad (2)$$

is considered as the sum of a *hard* singularity system,  $\Psi_h$ , generating only horizontal velocities on the free surface, and a *soft* system  $\Psi_s$

which generates only vertical velocities on the free surface.  $\Psi_h$  and  $\Psi_s$  are defined so that<sup>1</sup>  $\Im([\Psi'_h]_{y=0}) = \Im([\Psi'_s]_{y=0}) = 0$  and  $\Re([\Psi'_s]_{y=0}) = \Re([\Psi'_h]_{y=0}) = 0$ . It follows that the complex potential  $\Psi$  will satisfy the linearized free surface boundary condition

$$\Re([\Psi - i\Psi']_{y=0}) = 0 \quad (3)$$

provided that  $\Re([\Psi_h - i\Psi'_s]_{y=0}) = 0$ . This last relation is verified by simply choosing

$$\Psi_h = i\Psi'_s \quad (4)$$

Finally, the compound singularity defined by  $\Psi = (\Psi_s + i\Psi'_s)e^{i\tilde{t}}$  satisfies the free surface boundary condition and is wave free. Simple wave-free compound systems can be constructed directly using soft systems based on standard singularities such as sources and vortices, centered about a fixed point and its image (see Tulin, 1994). On the other hand, soft systems can be obtained from the hard ones, and vice et versa, by using (4). It can also be checked that if  $\Psi_s$  is a soft system, then its derivatives also represent soft systems. There is therefore a wide range of possibilities for the choice of the wave-free potential. Given the potential generated by a real oscillating body, the body shape must be determined.

### 3 Generation of wave-free oscillating bodies and of trapped modes

We now look for body shapes that would generate, while oscillating, the wave-free flow described by a given complex potential  $\Psi$ . The oscillations of the body are given by  $V = g\tilde{V}_0/\omega e^{i\tilde{t}}$  for heave,  $U = g\tilde{U}_0/\omega e^{i\tilde{t}}$  for sway and  $\Omega = \omega\tilde{\Omega}_0 e^{i\tilde{t}}$  for roll. Using  $\tilde{r} = f(\theta)$  as a parameterization for the shape of the body, the body boundary condition is written as

$$\frac{\partial\phi}{\partial n} = (U\tilde{e}_x + V\tilde{e}_y + \Omega\tilde{e}_z \times \tilde{r}) \cdot \tilde{n} \quad (5)$$

where  $\tilde{n} = -\tilde{e}_r + 1/f \cdot df/d\theta \tilde{e}_\theta$  is the normal to the body. This leads to the following differential

<sup>1</sup>the notation  $\Re$  and  $\Im$  stands for real and imaginary parts of a complex number.  $\Psi'$  indicate a derivation of analytic function  $\Psi$  with respect to the complex variable  $\tilde{z} = \tilde{x} + i\tilde{y} = \tilde{r}e^{i\theta}$ .

equation for  $f$

$$\frac{1}{f} \frac{df}{d\theta} = \frac{N(f, \theta)}{D(f, \theta)} \quad (6)$$

where

$$N(\tilde{r}, \theta) = \cos\theta(\tilde{\phi}_{\tilde{x}} - \tilde{U}_0 + \tilde{r}\tilde{\Omega}_0 \sin\theta) + \sin\theta(\tilde{\phi}_{\tilde{y}} - \tilde{V}_0 - \tilde{r}\tilde{\Omega}_0 \cos\theta), \quad (7)$$

and

$$D(\tilde{r}, \theta) = -\sin\theta(\tilde{\phi}_{\tilde{x}} - \tilde{U}_0 + \tilde{r}\tilde{\Omega}_0 \sin\theta) + \cos\theta(\tilde{\phi}_{\tilde{y}} - \tilde{V}_0 - \tilde{r}\tilde{\Omega}_0 \cos\theta). \quad (8)$$

Families of body shapes that do not generate waves at a given frequency while oscillating with velocities  $\tilde{U}_0, \tilde{V}_0, \tilde{\Omega}_0$  can therefore be constructed by numerical integration of equation (6), starting from different initial conditions. Of course in our linear approximation, the amplitude of body motion must remain small when compared to the characteristic length describing the body shape.

On the other hand, bodies which would not oscillate in the presence of an oscillating free surface perturbation must obey the same differential equation (6) with  $\tilde{U}_0 = \tilde{V}_0 = \tilde{\Omega}_0 = 0$ , which may also be recognized as the equation of stream lines in polar coordinates. These bodies therefore generate the so called "trapped modes". It is therefore expected that resonance phenomena occur while oscillating these bodies. This leads to non-uniqueness of the solution and infinite added mass, McIver (1997).

For the examples presented below, the integration has performed using a standard fourth order Runge Kutta algorithm with adaptation of the incremental step to the solution.

### 4 Simple examples

As an illustration of the previous ideas, we now look for symmetric bodies that do not generate waves while oscillating at a given frequency in heave. The velocity field has to satisfy the symmetry condition  $\tilde{\phi}_{\tilde{x}}(\tilde{r}, \pi - \theta) = -\tilde{\phi}_{\tilde{x}}(\tilde{r}, \theta)$  and  $\tilde{\phi}_{\tilde{y}}(\tilde{r}, \pi - \theta) = \tilde{\phi}_{\tilde{y}}(\tilde{r}, \theta)$  so that the shape of the body obtained by integrating (6) remains symmetric. A simple wave-free compound singularity centered at  $z = 0$  which satisfies this condition is given by

$$\Psi = -\alpha \left( \frac{i}{z} + \frac{1}{z^2} \right) \Re(e^{i\tilde{t}}) \quad (9)$$

which leads for the free surface elevation  $\bar{\eta} = -\alpha \sin(\bar{t})/\bar{x}^2$ . The oscillations of the body therefore generate an evanescent free surface deformation.

Considering  $\alpha$  as a parameter, a family of flat bottom bodies can be found (see fig. 2) starting from initial conditions  $\theta = -\pi/2$ ,  $f = -\bar{y}_0$  where  $\bar{y}_0$  is the only real root of equation  $-(\bar{V}_0/\alpha)\bar{y}^3 + \bar{y} + 2 = 0$  ( $\alpha > 0$ ). Let us denote  $\bar{x}_0$  the half width of the flat body at the waterline. For each value of  $\alpha$ , two additional one parameter families can be obtained, starting from initial conditions  $\theta = 0$ ,  $f = f_0$ . For  $f_0 > \bar{x}_0$ , body shapes are wine glass like and extend down to  $-\infty$  (see fig. 3) while for  $f_0 < \bar{x}_0$ , twin hull closed bodies are obtained. For the resonant problem, a family of twin hull bodies is obtained (fig. 4).

We now consider the case of a forced roll motion, i.e.  $\bar{U}_0 = \bar{V}_0 = 0$ . In order to respect the symmetry condition, the velocity field has to satisfy  $\bar{\phi}_{\bar{x}}(\bar{r}, \pi - \theta) = \bar{\phi}_{\bar{x}}(\bar{r}, \theta)$  and  $\bar{\phi}_{\bar{y}}(\bar{r}, \pi - \theta) = -\bar{\phi}_{\bar{y}}(\bar{r}, \theta)$ . A simple wave-free compound singularity centered at  $z = 0$  satisfying this condition is given by

$$\Psi = \alpha \left( \frac{1}{\bar{z}} - \frac{i}{\bar{z}^2} \right) \Re(e^{i\bar{t}}) \quad (10)$$

Starting the integration of eq. (6) from  $\theta = 0$ ,  $f = f_0$  leads to the definition of two families of bodies (see fig. 5 and 6). For large values of  $f_0$ , bodies are very close to circular since eq. (6) leads to  $df/d\theta = 0$  as  $r$  goes to infinity. For small values of  $f_0$  a family of twin hull bodies is found. The resonant problem also leads to a family of twin hull bodies (fig. 7).

## 5 Summary & conclusions

A method is presented using compound wave-free singularities for the determination of families of two dimensional body shapes that do not produce waves while oscillating at a given frequency in heave, sway or roll. Body shapes that generate trapped modes are also derived. Examples are given showing that a wide range of shapes can be generated even with a simple singularity system.

In view of the Haskind formula relating radiation damping and wave excitation, Newman (1977), bodies which are wave free when oscillated will be force free in the same mode when

placed in an incident wave field at the same frequency. The latter can be chosen, for example, as the natural resonant frequency of the body, suggesting an application for this theory.

Using distributed compound singularities, a wide variety of wave-free realistic bodies can be developed, and the method can be extended to the axially symmetric case.

**Acknowledgement:** The authors are grateful for the support of ONR Ocean Technology Program, Dr Tom Swean, Program Manager.

## References

- [1] McIver, M., 1997, "Resonance in the unbounded water wave problem", *12th International Workshop on Water Waves and Floating Bodies, Marseille*.
- [2] Newman, N., 1977, *Marine Hydrodynamics*. MIT Press., pp. 304.
- [3] Tuck E.O., Tulin, M.P. 1992, "Submerged bodies that do not generate waves", *Abstract for the 7th International Workshop on Water Waves and Floating Bodies*.
- [4] Tulin, M.P., 1976, "Free surface flows without waves", *Abstract and Lecture, 13th IUTAM Congress, Delft*.
- [5] Tulin, M.P., 1982, "Free surface flows without waves", *HYDRONAUTICS, Incorporated Technical Report 8035-2*.
- [6] Tulin, M.P., Oshri, O., 1994, "Free Surface Flows without Waves; Applications to Fast Ships with Low-Wave Resistance", *Proceedings of the 20th Symposium on Naval Hydrodynamics (Santa Barbara)*, pp.157-169.

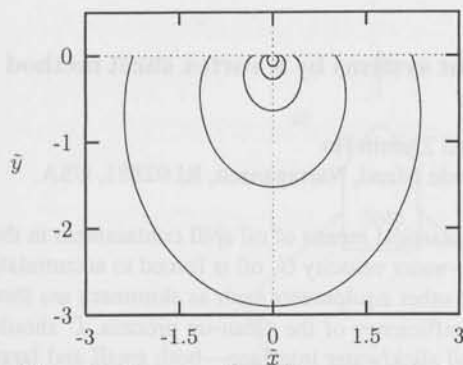


Figure 2: Heave motion. One parameter family of wave free flat bottom bodies for  $\alpha/\bar{V}_0$  varying from  $10^{-3}$  (smallest body) to 5.

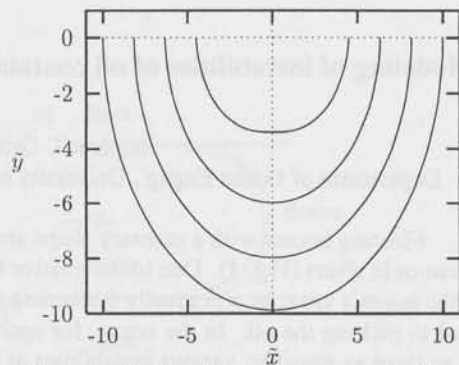


Figure 5: Roll motion. One parameter family of wave free flat bottom bodies for  $\alpha/\bar{\Omega}_0 = 10$ .

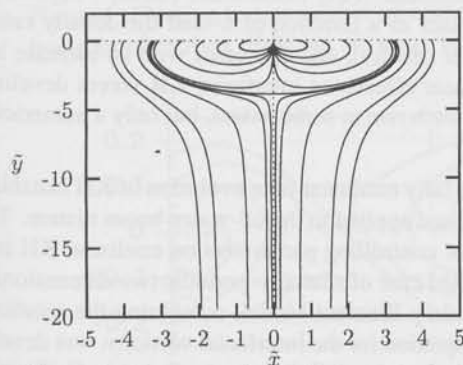


Figure 3: Heave motion. For  $\alpha = 1$ , inside and outside families of body shapes.

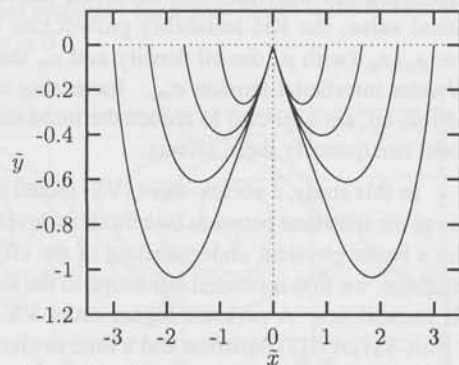


Figure 6: Roll motion. One parameter family of wave free twin hull bodies ( $\alpha/\bar{\Omega}_0 = 10$ ).

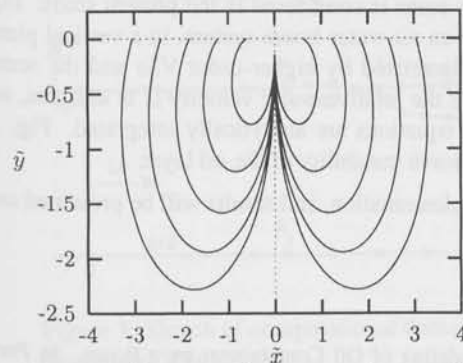


Figure 4: Heave motion, resonant case. One parameter family of body shapes that generate trapped modes.

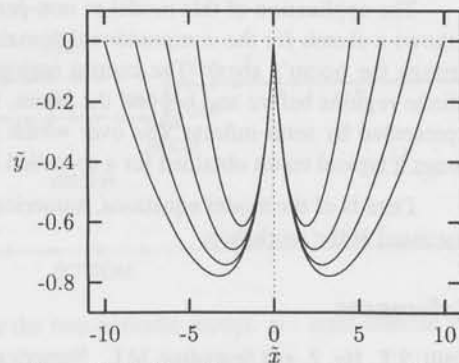


Figure 7: Roll motion, resonant case. One parameter family of body shapes that generate trapped modes ( $\alpha/\bar{\Omega}_0 = 10$ ).

## Modeling of instabilities of oil containment systems by a vortex sheet method

Stéphan T. Grilli<sup>1</sup> and Zhimin Hu

Department of Ocean Engng., University of Rhode Island, Narragansett, RI 02881, USA.

Floating booms with a catenary shape are the classical means of oil spill containment in the ocean or in rivers (Fig. 1). Due to the relative boom-water velocity  $U$ , oil is forced to accumulate in the boom's apex, as a gradually thickening slick; other equipments such as skimmers are then used to pick-up the oil. In the ocean, for optimum efficiency of the clean-up process,  $U$  should be as large as possible; various instabilities at the oil slick/water interface—both small and large scale—however, put a low practical limit to this velocity at about  $U_{cr} \simeq 0.5$  m/s (see Grilli *et al.* (1996) (GHS) for details and literature review).

Experiments have shown that such instabilities are triggered by small scale shear instabilities at the oil/water interface, i.e., so-called Kelvin-Helmholtz (KH) instabilities (GHS) : beyond a critical value, the KH instability growth rate increases as a function of  $U$  and the density ratio  $\varphi = \rho_o/\rho_w$  (with  $\rho_o$  the oil density and  $\rho_w$  the water density), and decreases with an increase in oil/water interfacial tension  $\sigma_{ow}$ . Increasing nonlinear effects, as interfacial KH waves develop and roll-up, are expected to reduce the instability growth rate to some extent, but only a numerical model can quantify these effects.

In this study, a vortex-sheet (VS) model of the fully nonlinear time evolution of KH instabilities at the interface between two fluids is developed and applied to the oil-water-boom system. To gain a better physical understanding of the effects of controlling parameters on nonlinear KH instabilities, we first restricted our scope to the simplified case of spatially-periodic two-dimensional KH instabilities. A periodic higher-order VS Boundary Element Model, combining the solution of Biot-Savart (BS) equation and a time evolution equation for the interfacial vorticity, was developed. Details of model development, implementation, and validation can be found in Grilli and Hu (1997). This model accurately predicts the fully-nonlinear growth rate of periodic interfacial KH instabilities, including situations where intense roll-up of interfacial VSs occurs (Fig. 2).

The application of this model to non-periodic cases is considered in the present study. Fig. 3 shows a sketch for the computational domain for an oil-water-boom system, in a vertical plane through the boom's apex. The central region is discretized by higher-order VSs and the semi-infinite regions before and beyond the boom, where the relative water velocity  $U$  is uniform, are represented by semi-infinite VSs over which BS's equations are analytically integrated. Fig. 4 shows a typical result obtained for a so-called headwave instability of the oil layer.

Details of the model equations, numerical implementation, and results will be presented and discussed at the workshop.

## References

Grilli, S.T., Hu, Z. and Spaulding, M.L. Numerical Modeling of Oil Containment by a Boom. In *Proc.*

<sup>1</sup>Ph.Nb.: (401)874-6636; Fax : (401)874-6837; email : grilli@mistral.oce.uri.edu; http://www.oce.uri.edu/~grilli

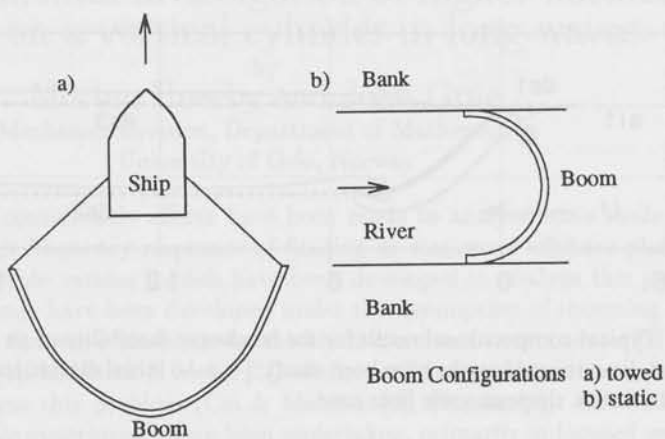


Figure 1: Floating booms used in oil containment systems : (a) towed boom in the ocean; (b) fixed boom across a river. Relative oil-water velocity is  $U$ .

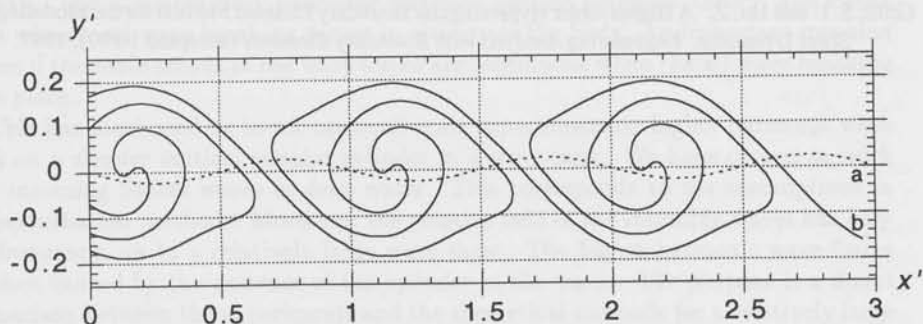


Figure 2: Typical computational result for the periodic KH instability at the interface between two fluids. a: initial sinusoidal perturbation; b: computational profile at some later time.

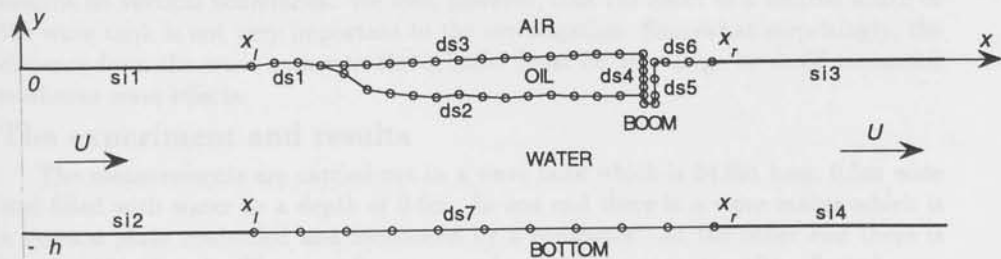


Figure 3: Sketch of computational domain for the non-periodic model. si : semi-infinite VSs; ds : discretized VSs.

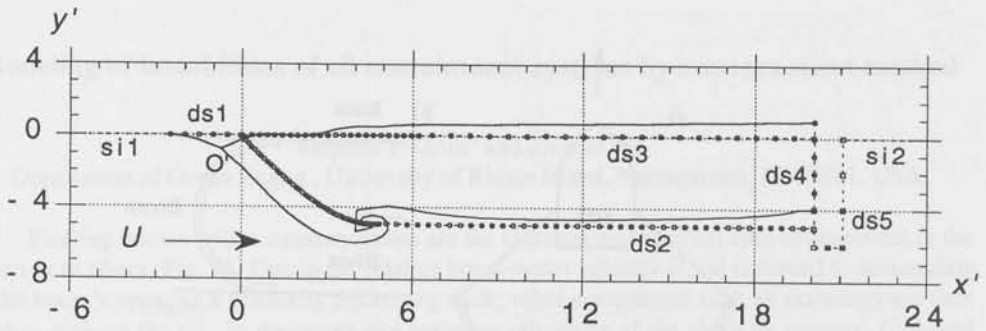


Figure 4: Typical computational result for the headwave instability of an oil slick contained by a boom (non-dimensional lengths have been used). (—○—) initial discretized oil slick shape; (—) computed oil slick shape at some later time.

19th Arctic and Marine Oil spill Prog. Tech. Seminar (AMOP), pps. 343-376. Environment Canada, 1996.

Grilli, S.T. and Hu, Z. A Higher-order Hypersingular Boundary Element Method for the Modeling of Vortex Sheet Dynamics. *Engineering Analysis with Boundary Elements* (accepted 10/97), 1997.

## An experimental investigation of higher harmonic forces on a vertical cylinder in long waves

by

Morten Huseby and John Grue

Mechanics Division, Department of Mathematics  
University of Oslo, Norway

In recent time considerable efforts have been made to analyze wave loads which lead to sudden high frequency responses of floating or stationary offshore platforms. On the theoretical side various models have been developed to analyze this problem. Perturbation methods have been developed under the assumption of incoming Stokes waves, to capture the wave loads up to the third harmonic component (Faltinsen, Newman & Vinje [1], Malenica & Molin [2]). Fully nonlinear methods have also been developed to analyze this problem (Cai & Mehlum [3], Ferrant [4]). Several model tests and small scale experiments have been undertaken, primarily in focused waves or irregular waves. A thorough understanding of this problem is still lacking, however. With regard to the perturbation methods, it is uncertain what are their domain of validity. The available fully nonlinear methods assume potential theory, and break down when local wave breaking occurs in vicinity of the body. An important question is then if the main trends of the wave forces are continuous when (local) wave breaking takes place.

This has motivated us to set up small scale experiments on higher harmonic wave loads on a slender vertical circular cylinder in a wave tank. We have chosen to work with incoming Stokes waves in deep water. This corresponds to the assumptions in the perturbation methods. Moreover, the velocity field of the incoming waves has only one frequency, up to a relatively large wave slope. The higher harmonic wave forces are then caused by the presence of the cylinder in the waves. The purpose is a direct comparison between the experiments and the theoretical methods for a relatively large range of wave amplitude to cylinder diameter ratio, at several non dimensional wave numbers. While the experiments are carried out in a relatively narrow wave tank, with a ratio of about 8 between the tank width and the cylinder diameter, the theories assume no vertical boundaries. We find, however, that the effect of a limited width of the wave tank is not very important to the investigation. Somewhat surprisingly, the distance from the wave maker to the cylinder must be very large to avoid unwanted nonlinear wave effects.

### The experiment and results

The measurements are carried out in a wave tank which is 24.6m long, 0.5m wide and filled with water to a depth of 0.6m. In one end there is a wave maker which is a vertical plate controlled and monitored by a computer. At the other end there is an absorbing beach. The recordings are performed before any (small) reflected wave has reached the cylinder. The waves are generated by periodic motions of the wave maker. After a leading transient part the wave train becomes periodic, to a good approximation. Recordings of the incoming waves confirm a shape corresponding to Stokes waves for wave slopes less than 0.19, which is the largest wave slope in the experiment.

The cylinder is  $R = 3\text{cm}$  of radius and is extending throughout the entire water

depth. The non dimensional wavenumber in the presented results is  $kR = 0.245$ . The wave amplitude,  $A$ , is varying so that  $Ak$  is ranging from  $Ak = 0.06$  to  $Ak = 0.19$ , and the ratio of the wave amplitude and the radius of the cylinder is ranging from  $\frac{A}{R} = 0.24$  to  $\frac{A}{R} = 0.78$ . The distance from the wave maker to the cylinder is ranging from 6.33m to 15.45m. The total force  $F(t)$  in the horizontal direction is recorded by two force transducers. The first four harmonic components of  $F$  are obtained by Fourier transform over 10 wave periods, i.e.

$$F(t) = \text{Re}(F_1 e^{i\omega t} + F_2 e^{i2\omega t} + F_3 e^{i3\omega t} + F_4 e^{i4\omega t} + \dots) \quad (1)$$

For the first harmonic force we find an excellent agreement between the measurements and linear theory for all wave amplitudes. We have taken into account the effect of the laminar boundary layer at the cylinder.

In figure 1 we compare our measurements on  $|F_2|$  with second order theory (Newman [5], figure 5 and Molin [6]). The experiments are in good agreement with the theory for small  $Ak$ . For moderate wave slope the measured  $|F_2|$  becomes smaller than the theoretical value. We find, on the other hand, good agreement between theory and experiment for the phase of the second harmonic force for all  $A$  (results not shown).

In figure 2 we compare our results with the third order theories of Malenica & Molin [2] (figures 6 and 8) and FNV [1]. We see that both theories are in good agreement with our measurements of the amplitude  $|F_3|$ . For the phase of the third harmonic, the results of Malenica & Molin are in excellent agreement with the measurements. The theory of FNV predicts a value of the phase that are roughly speaking 180 degrees out of phase with our measurements. We notice that the third harmonic force seems to be well predicted by third order theory up to wave slopes as large as  $Ak = 0.19$ .

For the fourth harmonic component we give data for  $Ak$  exceeding 0.1, since this force is too small to be measured at smaller wave slopes. We find that  $|F_4|R/\rho g A^4$  is approximately 3.3. The phase of  $F_4$  is about 2.5.

When we place the cylinder too close to the wave maker, an oscillation as function of the wave amplitude appears in the higher harmonic forces. An example is displayed for  $|F_2|$  in figure 1. This effect disappears when the distance to the wave maker is increased.

At the workshop more results for various wave numbers will be presented.

This work was conducted under the DEEPER JIP with financial support from the Research Council of Norway and a consortium of industrial sponsors.

## References

- [1] FALTINSEN, O. M., NEWMAN, J. N. AND VINJE, T. (1995) Nonlinear wave loads on a slender vertical cylinder. *J. Fluid Mech.* **289**, 179-199.
- [2] MALENICA, S. AND MOLIN, B. (1995) Third-harmonic wave diffraction by a vertical cylinder. *J. Fluid Mech.* **302**, 203-229.
- [3] CAI, X. AND MELUM, E. (1996) Two fragments of a method for fully nonlinear simulation of water waves. In: *Waves and nonlinear processes in hydrodynamics*. Grue, J., et al (Editors). Kluwer 1996. pp 37-50.
- [4] FERRANT, P. (1996) Computation of higher order diffraction effects using a fully nonlinear simulation method. *Proc. 11th W.W.W.F.B.*, Hamburg, 1996.
- [5] NEWMAN, J. N. (1996) The second-order wave force on a vertical cylinder. *J. Fluid Mech.* **320**, 417-443.
- [6] MOLIN, B. (1979) Second-order diffraction loads upon three dimensional bodies. *Appl. Ocean Res.* **1**, 197-202.

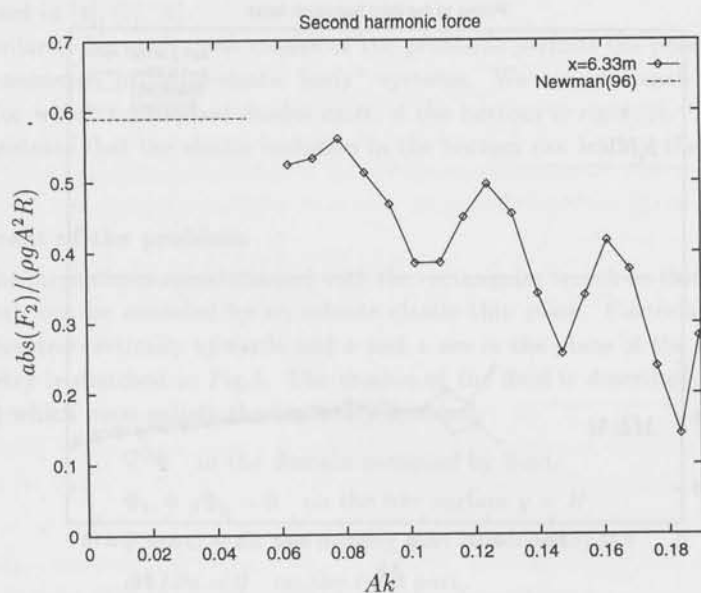
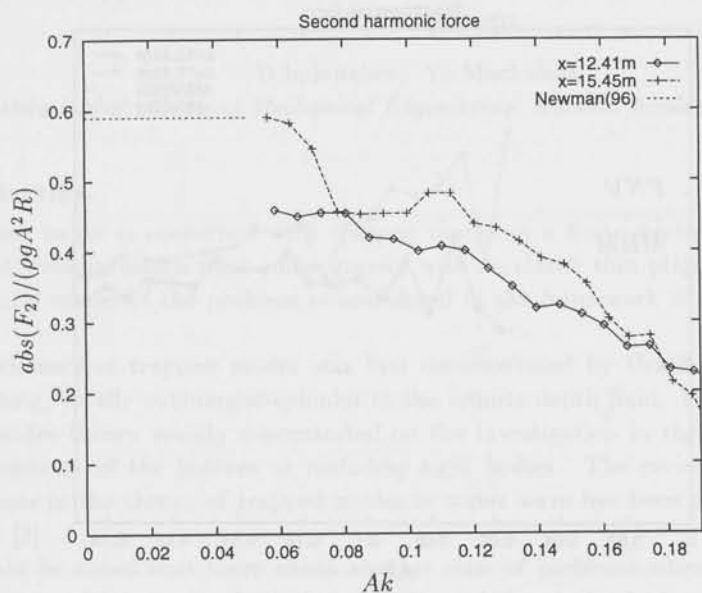


Figure 1: The second harmonic force calculated taking the Fourier transform over 10 wave periods. Upper figure: The distance from the cylinder to the wave maker is 12.41m and 15.45m from. Bottom figure: The distance from the cylinder to the wave maker is 6.33m.

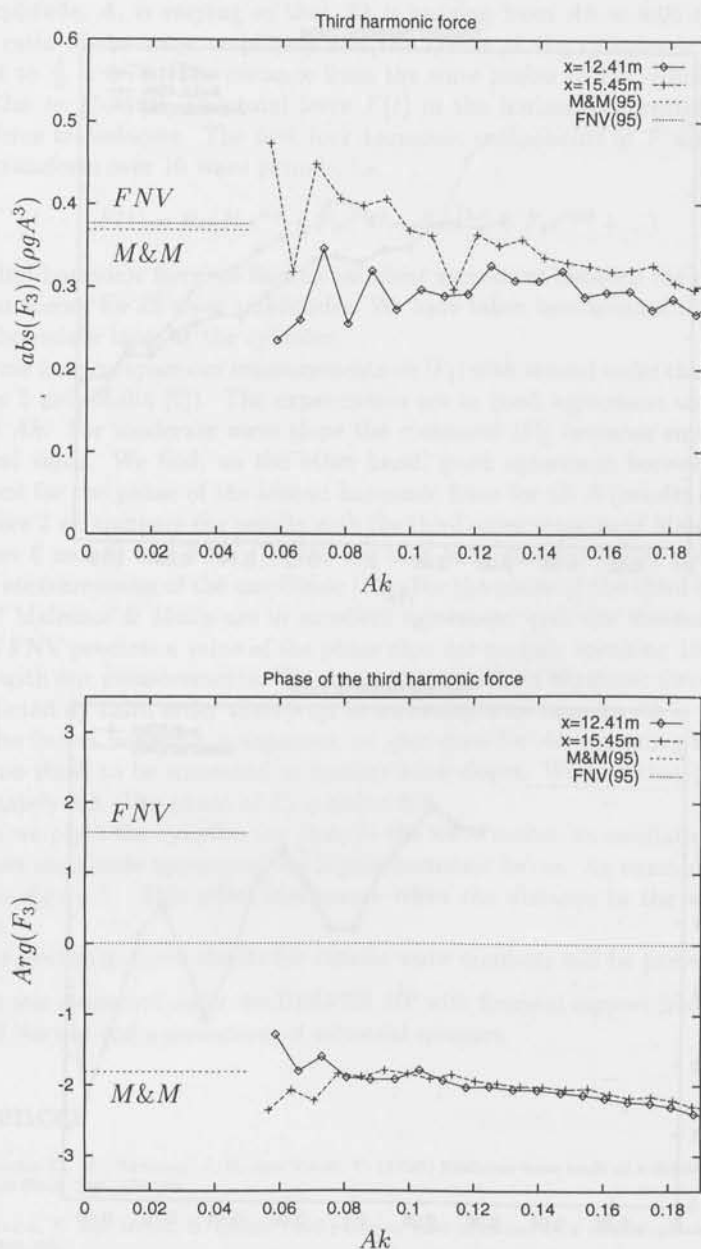


Figure 2: The third harmonic force calculated taking the Fourier transform over 10 wave periods. The distance from the cylinder to the wave maker is 12.41m and 15.45m. Upper figure: The amplitude of the third harmonic force. Bottom figure: The phase of the third harmonic force.

## Trapped modes in wave channel with an elastic plate on the bottom

D.Indejtchev, Yu.Mochalova

*Institute of Problems of Mechanical Engineering, Russian Academy of Sciences*

### 1. Introduction

This present paper is concerned with trapped modes in a finite depth channel occupied by an inviscid, incompressible fluid under gravity with an elastic thin plate on the bottom. The mathematical model of the problem is considered in the framework of linearized water-wave theory.

The existence of trapped modes was first demonstrated by Ursell [1] in the case of an infinitely long, totally submerged cylinder in the infinite depth fluid. Further research in the trapped modes theory mainly concentrated on the investigation in the fluid either having a specific geometry of the bottom or including rigid bodies. The review of the more recent developments in the theory of trapped modes in water wave has been presented by Evans & Kuznetsov [2].

It should be noted that there exists another class of problems where the trapped modes phenomenon can also occur. It is the oscillation of the elastic body with inclusion having at least one infinite boundary. The possibility of trapped modes in the elastic systems was demonstrated in [4], [5], [6].

The similarity between these classes of the problems permits the possibility of the trapped modes phenomenon in "fluid-elastic body" systems. We consider such types of the bottom geometry for which no trapped modes exist, if the bottom is rigid [3]. The aim of the paper is to demonstrate that the elastic inclusion in the bottom can lead to the existence of trapped modes.

### 2. Statement of the problem

Consider the three-dimensional channel with the rectangular trench on the bottom. The bottom of the trench can be modeled by an infinite elastic thin plate. Cartesian axes are chosen so that  $y$  is directed vertically upwards and  $x$  and  $z$  are in the plane of the unperturbed bottom. The geometry is sketched in Fig.1. The motion of the fluid is described by velocity potential  $\Phi(x, y, z, t)$  which must satisfy the boundary problem:

$$\nabla^2 \Phi \quad \text{in the domain occupied by fluid,} \quad (1)$$

$$\Phi_{tt} + g\Phi_y = 0 \quad \text{on the free surface } y = H, \quad (2)$$

$$\Phi_y = w_t \quad \text{on the moving part of boundary,} \quad (3)$$

$$\partial\Phi/\partial n = 0 \quad \text{on the rigid part,} \quad (4)$$

where  $H$  is the depth of the channel,  $g$  is the acceleration due to gravity,  $w$  is the small plate displacement determined by the equation

$$Dw_{zzzz} + kw + Mw_{tt} = \rho \int_{-a}^a (\Phi_t + gw) dx \quad (5)$$

on the moving part of the boundary. Here  $M$  is the elastic construction mass per unit length,  $D$  is the cylindrical rigidity,  $k$  is the elastic foundation rigidity,  $\rho$  is the liquid density. Trapped



$\xi_k$  is the positive root of the equation below

$$g\xi \tan h\xi = -\omega^2, \quad \zeta_k = \sqrt{\xi_k^2 + m^2}, \quad k \geq 1.$$

It should be mentioned for the rigid bottom,  $w_0 = 0$ , our spectral problem has only continuous spectrum beginning with the cut-off frequency  $\omega_b$ , where  $\omega_b = \sqrt{gm \tanh mH}$ .

The solution of the problem (7)-(9) has the following form

$$\varphi(x, y) = -i\omega w_0 \int_{-a}^a G(|x - \eta|, y, \omega) d\eta. \quad (13)$$

Setting  $m, k, M, D$  arbitrary parameters, on which the spectral parameter  $\omega$  (fundamental frequency) depends, and substituting (13) into (10) we can have the following transcendental equation to determine the fundamental frequencies

$$\bar{k}_m - M\omega^2 = M_\rho(\omega)\omega^2, \quad M_\rho(\omega) = -\rho \int \int_{-a}^a G(|x - \eta|, 0, \omega) d\eta dx. \quad (14)$$

Analyzing the frequency equation (14) one can come to the following results.

- For  $\omega < \omega_b$ ,

the unique fundamental frequency  $\omega_1$  exists, if and only if  $Dm^4 + k > 2apg$ ;

the following estimate  $0 < \omega_1 < \min\{\omega_b, \sqrt{\bar{k}_m/M}\}$  holds for the fundamental frequency and the corresponding trapped mode is

$$\varphi(x, y) = -2i\omega_1 w_0 \begin{cases} \sum_{k=0}^{\infty} B_k(y, \omega_1) [1 - e^{-\zeta_k a} \cosh \zeta_k x], & |x| < a, \\ \sum_{k=0}^{\infty} B_k(y, \omega_1) e^{-\zeta_k |x|}, & |x| > a; \end{cases}$$

if  $ma \gg 1$ , the fundamental frequency can be given by the following approximation

$$\omega_1^2 \approx \frac{\bar{k}_m}{M + \frac{2a\rho}{m} \coth mH}.$$

- For  $\omega = \omega_b$ , the problem has only trivial solution  $\varphi = 0$ .

• For  $\omega > \omega_b$ , the Green function is the complex, with a consequent formation of surface travelling waves carrying the energy to infinity. The condition (11) is fulfilled when  $\omega = \omega_{11n}$ ,

$$\omega_{11n}^2 = g\sqrt{m^2 + \pi^2 n^2/a^2} \tanh(H\sqrt{m^2 + \pi^2 n^2/a^2}), \quad n \geq 0. \quad (15)$$

The frequency  $\omega_{11n}$  (15) is fundamental one, if and only if the generalized rigidity  $k_m$  is defined in terms of another parameters as  $k_m = (M + M_\rho(\omega_{11n}))\omega_{11n} + 2apg$ , and the corresponding trapped mode is expressed by

$$\varphi(x, y) = -2i\omega_{11n} w_0 \begin{cases} B_0(y, \omega_{11n}) [1 - \cos \zeta_0 a \cos \zeta_0 x] + \sum_{k=1}^{\infty} B_k(y, \omega_{11n}) [1 - e^{-\zeta_k a} \cosh \zeta_k x], & |x| < a, \\ \sum_{k=1}^{\infty} B_k(y, \omega_{11n}) e^{-\zeta_k |x|}, & |x| > a. \end{cases}$$

#### 4. The case of a rectangular trench with an elastic bottom

Let us consider the channel with an uneven bottom. We divide the infinite domain  $W$  into to parts  $W = \overline{W^{(+)}} \cup \overline{W^{(-)}}$  (see Fig.1). We give equivalent formulation of our problem (7)-(10) that is set only in the bounded domain  $W^{(-)}$

$$\nabla^2 \varphi = m^2 \varphi \text{ in } W^{(-)}, \quad \varphi = B_1 \varphi \text{ when } |x| < a, \quad y = 0, \quad (16)$$

$$\varphi_y = -\lambda B_2 \varphi \text{ when } |x| < a, \quad y = -h, \quad \varphi_x = 0 \text{ when } x = \pm a. \quad (17)$$

where  $B_1 \varphi = \int_{-a}^a \varphi_y(\eta, 0) G(x - \eta, 0, \omega) d\eta$ ,  $B_2 \varphi = \frac{\omega^2}{k_m/M - \omega^2} \int_{-a}^a \varphi(x, -h) dx$  and  $G$  is the

Green function (12). Further the solution of the problem (16)-(17) will be sought for  $\omega < \omega_b$ . We treat the parameter  $\lambda = \frac{\rho}{M}$  as a spectral parameter. The potential  $\varphi$  is expressed by the unknown function  $\psi$  in the following way

$$\varphi(x, y) = -\lambda\psi(x, y)B_2\varphi, \quad (18)$$

where  $\psi$  is the solution of the following problem

$$\nabla^2\psi = m^2\psi \text{ in } W^{(-)}, \quad \psi = B_1\psi \text{ when } |x| < a, \quad y = 0, \quad (19)$$

$$\psi_y = 1 \text{ when } |x| < a, \quad y = -h, \quad \psi_x = 0 \text{ when } x = \pm a. \quad (20)$$

Separating of variables in the problem (19)-(20) yields the nonhomogeneous infinite system of algebraic equations. It can be shown that the system has the unique bounded solution and the solution of the problem (19)-(20) exists and is unique. Integrating (18) with respect to  $x$  from  $-a$  to  $a$  we determine the spectral parameter

$$\frac{1}{\lambda} = \frac{\omega^2}{\omega^2 - \tilde{k}_m/M} \int_{-a}^a \psi(x, -h) dx. \quad (21)$$

It can be shown by analysis of the problem (19)-(20) that  $\int_{-a}^a \psi(x, -h) dx < 0$ . Then we obtain the following results

• For  $\omega < \omega_b$ , if the frequency satisfying the inequalities  $0 < \omega < \min\{\omega_b, \sqrt{\tilde{k}_m/M}\}$ , there exists only one spectral parameter  $\lambda$  and the corresponding trapped mode is given by (18). If  $ma \gg 1$ , the fundamental frequency can be expressed by

$$\frac{1}{\lambda} \approx \frac{\tilde{k}_m}{\rho\omega^2} - 2a \frac{\coth mH + \tanh mh}{m(1 + \tanh mh \coth mH)}$$

• For  $\omega = \omega_b$ , there exists only one spectral parameter  $\lambda$  which is given by

$$\frac{1}{\lambda} = \frac{1}{mg\rho} [k_m \coth mH + 2ag\rho(\coth mH - \coth mh)]$$

and the corresponding eigenfunction is  $\varphi(x, y) = 0$  in  $W^{(+)}$  and  $\varphi(x, y) = \varphi(y)$  in  $W^{(-)}$ .

Then we have the interesting phenomenon. The fluid oscillations occur only in the bounded domain,  $W^{(-)}$ , and the fluid is rest in the infinite domain  $W^{(+)}$ .

## 5. Conclusion

The possibility of the trapped modes phenomenon in the finite depth channel with elastic inclusion on the bottom has been demonstrated. Two cases of the geometry of the rigid bottom for which no trapped modes exist has been considered. We have obtained the conditions of the existence trapped modes for the different ranges of the frequency.

**Acknowledgments.** This work was done in collaboration with N.G. Kuznetsov.

## References

- [1] Ursell, F.: *Proc. Camb. Phil. Soc.* 47 No. 3 (1951), 347-358.
- [2] Evans, D.V., Kuznetsov, N.: *Gravity waves in water of finite depth.* (1997), 127-168.
- [3] Bonnet-Ben Dhia, A-S., Joly, P.: *SIAM J. Appl. Math.* 53 No. 6 (1993), 1507-1550.
- [4] Bobrovnikskii, Yu.I., Korotkov M.P.: *Acoustic J.* 35 No. 5 (1991),
- [5] Abramyan, A. Andreev, V. Indeitchev, D.: *J. of Tech. Physics.* 2 No. 3 (1996), 3-17.
- [6] Indeitchev, D.A., Osipova E.V.: *J. of Tech. Physics.* 3 No. 8 (1996), 124-132.

## Influence of the Steady Flow in Seakeeping of a Blunt Ship through the Free-Surface Condition

Hidetsugu IWASHITA

Engineering Systems, Hiroshima University  
Kagamiyama 1-4-1, Higashi-Hiroshima 739, JAPAN

### Introduction

The accurate estimation of the wave pressure locally acting on a ship in a seaway is an important topic for the practical ship design besides general estimations of total hydrodynamic forces and/or ship motions. In the last workshop [1] we presented some numerical results based on the 3-D Green function method (GFM) and investigated numerically the influence of the steady flow in seakeeping, especially in the wave pressure on a blunt ship (HSVA tanker). There we obtained a conclusion that the influence of the steady Kelvin-wave field through the body boundary condition seems not so remarkable in the local wave pressure distributions against our experimental data for a blunt VLCC [2], where the experimental wave pressure indicates considerably larger value than the theoretical estimation of the GFM at the bow part although some numerical improvements are observed by taking into account the steady Kelvin-wave field instead of the double-body flow through the body boundary condition. Then it is suspected that another influence of the steady flow through the free-surface condition might affect more strongly the local wave pressure especially at the bow part.

In this paper we develop a Rankine panel method (RPM), which was originally presented by Jensen [3] and Ando [4] for the steady wave-making problem and extended to the unsteady problem by Bertram [5], mixing a numerical technique to make the method effective even for the blunt ship. The numerical method developed here is applied to a blunt VLCC advancing in oblique short waves. Numerical results are compared with the experiments and another numerical results of GFM or strip theory, and the influence of the steady flow in the wave pressure through the free-surface condition is discussed.

### Formulation

We consider a ship advancing at constant forward speed  $U$  in oblique regular waves encountered at angle  $\chi$ , Fig.1. The ship motion  $\xi_j e^{i\omega_e t}$  ( $j = 1 \sim 6$ ) around its equilibrium position and the wave amplitude  $A$  of the incident wave are assumed to be small.  $\omega_0$  is the circular frequency and  $K$  the wave number of the incident wave. The encounter circular frequency is  $\omega_e (= \omega_0 - KU \cos \chi)$ . The linear theory is employed for this problem assuming ideal (potential) flow.

The velocity potential  $\Psi$  governed by Laplace's equation can be expressed as

$$\Psi(x, y, z; t) = U[\Phi(x, y, z) + \varphi(x, y, z)] + \Re[\phi(x, y, z)e^{i\omega_e t}] \quad (1)$$

where

$$\phi = \frac{gA}{\omega_0}(\phi_0 + \phi_T) + i\omega_e \sum_{j=1}^6 \xi_j \phi_j, \quad \phi_0 = ie^{Kz - iK(x \cos \chi + y \sin \chi)} \quad (2)$$

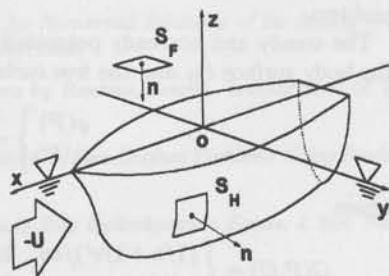


Fig. 1 Coordinate system

$\Phi$  means the double-body flow,  $\varphi$  the steady wave field and  $\phi$  the unsteady wave field. Assuming small disturbance due to the ship, we can linearize the free-surface conditions for  $\varphi$  and  $\phi$  in several forms. In this paper we adopted the following free-surface conditions derived by Yasukawa [6] and corresponding body boundary conditions. For  $\varphi$  it becomes

$$\frac{1}{2K_0} \nabla \Phi \cdot \nabla (\nabla \Phi \cdot \nabla \Phi) + \frac{1}{K_0} \nabla \Phi \cdot \nabla (\nabla \Phi \cdot \nabla \varphi) + \frac{1}{2K_0} \nabla (\nabla \Phi \cdot \nabla \Phi) \cdot \nabla \varphi + \frac{\partial \varphi}{\partial z} = 0 \quad \text{on } z = 0 \quad (3)$$

$$\frac{\partial \varphi}{\partial n} = 0 \quad \text{on } S_H \quad (4)$$

and for  $\phi_j$

$$-K_e \phi_j + 2i\tau \nabla \Phi \cdot \nabla \phi_j + \frac{1}{K_0} \nabla \Phi \cdot \nabla (\nabla \Phi \cdot \nabla \phi_j) + \frac{1}{2K_0} \nabla (\nabla \Phi \cdot \nabla \Phi) \cdot \nabla \phi_j + \frac{\partial \phi_j}{\partial z} = 0 \quad \text{on } z = 0 \quad (5)$$

$$\frac{\partial \phi_j}{\partial n} = n_j + \frac{U}{i\omega_e} m_j \quad (j = 1 \sim 6), \quad \frac{\partial \phi_7}{\partial n} = -\frac{\partial \phi_0}{\partial n} \quad \text{on } S_H \quad (6)$$

where

$$\begin{aligned} (n_1, n_2, n_3) &= \mathbf{n}, & (m_1, m_2, m_3) &= -(\mathbf{n} \cdot \nabla) \mathbf{V}, \\ (n_4, n_5, n_6) &= \mathbf{r} \times \mathbf{n}, & (m_4, m_5, m_6) &= -(\mathbf{n} \cdot \nabla)(\mathbf{r} \times \mathbf{V}), \end{aligned}$$

$\mathbf{r} = (x, y, z)$ ,  $\mathbf{V} = \nabla \Phi$ ,  $K_0 = g/U^2$ ,  $K_e = \omega_e^2/g$  and  $\tau = U\omega_e/g$ .  $m_j$  in eq.(6) derived by Timman & Newman [7] is an influence term from the steady flow to the unsteady flow on the body surface. Eq.(3) coincides with the Dawson's free-surface condition in the steady problem [8] and eq.(5) is a corresponding form in the unsteady problem.

If we put  $\Phi = -x$ ,  $\partial\varphi/\partial n = n_x$  and  $\mathbf{V} = \nabla[-x + \varphi]$ , the formulation (3) ~ (6) leads to the Neumann-Kelvin formulation which is applied to the GFM.

## Numerical methods

The RPM applied in this study is a collocation method developed by Jensen [3] and Ando [4] for the steady problem and extended to the unsteady problem by Bertram [5]. The radiation condition is satisfied by shifting the collocation point one panel upward on the free surface. Recently Eguchi [9] and Nakatake [10] proposed its extended computation method which is quite robust and stable even for the blunt ship in the steady problem. We solve our problem applying this method to the unsteady problem.

The steady and unsteady potentials,  $\varphi$  and  $\phi_j$ , are both expressed by the source distributions on the body surface  $S_H$  and the free surface  $S_F$  as follows:

$$\left. \begin{matrix} \varphi(P) \\ \phi_j(P) \end{matrix} \right\} = - \iint_{S_H+S_F} \left\{ \begin{matrix} \sigma_s(Q) \\ \sigma_j(Q) \end{matrix} \right\} G(P, Q) dS \quad (7)$$

where

$$G(P, Q) = \begin{cases} (1/r + 1/r')/4\pi & \text{for } Q \text{ on } S_H \\ 1/4\pi r & \text{for } Q \text{ on } S_F \end{cases}, \quad \left. \begin{matrix} r \\ r' \end{matrix} \right\} = \sqrt{(x-x')^2 + (y-y')^2 + (z \mp z')^2}$$

The body surface and the free-surface are discretized into the finite number of constant panels, and numerical solutions for steady and unsteady problems are obtained such that a corresponding set of the free-surface condition and the body boundary condition are satisfied at collocation points. The collocation points on  $S_H$  coincides with the geometric center of each panel and those on  $S_F$  are shifted one panel upward in order to force the radiation condition numerically. This numerical radiation condition is valid only for  $\tau > 1/4$  in the unsteady problem where the waves do not propagate to the forward direction of the ship. Fig. 2 and 3 illustrate the computation grids on  $S_H$  and  $S_F$ . For the panels inside the waterline on  $S_F$ , source distributions are forced to be zero, or those panels are totally removed from the computation domain [9], [10].

The GFM is also attempted in this study for the blunt VLCC. The free surface and body boundary conditions for the steady and unsteady problems are reduced to the well known Neumann-Kelvin formulation as noted in the previous section. The computation domain is restricted only on  $S_H$  by introducing the Green function which satisfies the free-surface condition and the radiation condition analytically. Instead of this advantage we need to evaluate this complicated function accurately. The special algorithm presented by Iwashita & Ohkusu [11] is employed for evaluating this Green function, and the direct method incorporated with the spline element [2] is adopted for solving the boundary value problem. Although the influence of the non-uniform steady flow cannot be taken into account through the free-surface condition, the Kelvin wave field can affect through the body boundary condition,  $m_j$ .

## Numerical results

Fig. 4 shows the perspective view of the steady wave around the VLCC obtained by the present RPM with conditions (3) and (4). Fig. 5 is its 2-D profile along the ship-side. A large steady bow wave is simulated well compared with a picture of experiment, Fig. 6.

Fig. 7 and 8 show the comparison of  $m_3$  distribution on the ship surface evaluated from  $\Phi$  and  $-x + \varphi$ . The former is used in the computation of the RPM and the latter is in the GFM. The wavy distribution can be observed in Fig. 8.

Fig. 9 illustrates the diffraction wave around the VLCC at  $F_n = 0.2$ ,  $\lambda/L = 0.5$  and  $\chi = 180$  deg. So called  $k_2$ -wave system is simulated remarkably in the figure.

Fig. 10 is a wave pressure distribution on VLCC at ordinate 9. The present RPM estimates the wave pressure well among other computations by reflecting the influence of the steady flow around blunt bow part.

Further calculations are now in progress and the results will be presented in the workshop.

## References

- [1] Iwashita, H., Bertram, V.: *Numerical Study on the Influence of the Steady Flow in Seakeeping*, 12th WWWFB, Marseille (1997)
- [2] Iwashita, H., Ito, A., Okada, T., Ohkusu, M., Takaki, M., Mizoguchi, S.: *Wave Forces Acting on a Blunt Ship with Forward Speed in Oblique Sea (3rd Report)*, J. Soc. Naval Arch. Japan 176 (1994) (in Japanese)
- [3] Jensen, G., Mi, Z.-X., Söding, H.: *Rankine Source Methods for Numerical Solutions of the Steady Wave Resistance Problem*, 16th Symp. on Nav. Hydrodyn., Berkeley (1986)
- [4] Ando, J., Nakatake K.: *A Method to Calculate Wave Flow by Rankine Source*, Transactions of The West-Japan Soc. of Naval Arch. No. 75(1988) (in Japanese)
- [5] Bertram, V.: *Fulfilling Open-Boundary and Radiation Condition in Free-Surface Problems Using Rankine Sources*, Ship Technology Research, Vol. 37/2(1990)
- [6] Yasukawa, H.: *A Rankine Panel Method to Calculate Unsteady Ship Hydrodynamic Forces*, J. Soc. Naval Arch. Japan 168 (1990)
- [7] Timman, R., Newman, J.N.: *The Coupled Damping Coefficients of a Symmetric ship*, JSR 5/4 (1962)
- [8] Dawson, C. W.: *A Practical Computer Method for Solving Ship Wave Problems*, 2nd Int. Conf. on Numerical Ship Hydrodynamics, Berkeley (1977)
- [9] Eguchi, T.: *Numerical Analysis of Rankine Source Collocation Method for the Steady Wave Making Resistance Problem*, J. Soc. Naval Arch. Japan 177 (1995) (in Japanese)
- [10] Nakatake K., Ando, J.: *A Method to Calculate Wave Flow around a Wide Ship*, Transactions of The West-Japan Soc. of Naval Arch. No. 90(1995) (in Japanese)
- [11] Iwashita, H., Ohkusu, M.: *Hydrodynamic Forces on a Ship Moving with Forward Speed in Waves*, J. Soc. Naval Arch. Japan 166 (1989) (in Japanese)

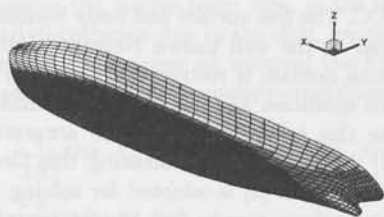


Fig. 2 Hull form and computation grids of VLCC  
(1200 panels)

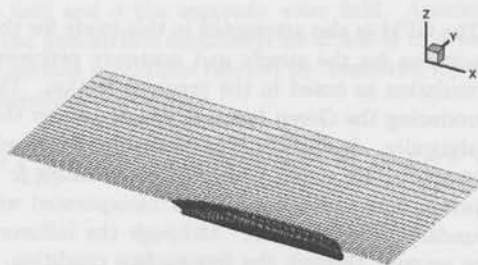


Fig. 3 Computation grids on  $S_H$  and  $S_F$   
(600 and 2666 panels on half)

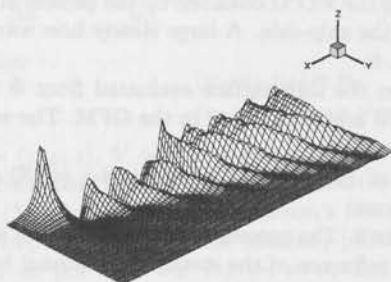


Fig. 4 Perspective view of the steady wave  
at  $F_n = 0.2$

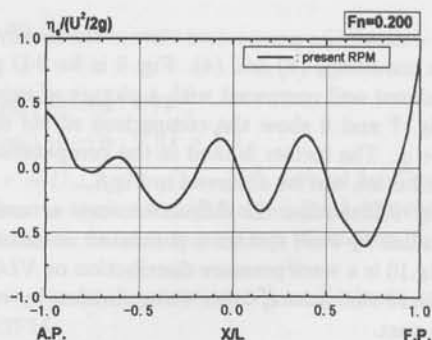


Fig. 5 Computed steady wave along ship-side  
at  $F_n = 0.2$

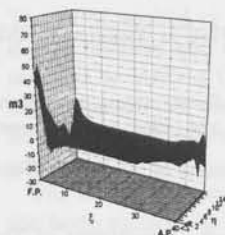


Fig. 7  $m_3$  distribution on  $S_H$   
(double-body flow)

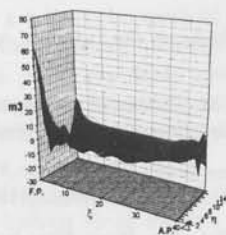


Fig. 8  $m_3$  distribution on  $S_H$   
(Kelvin wave flow)

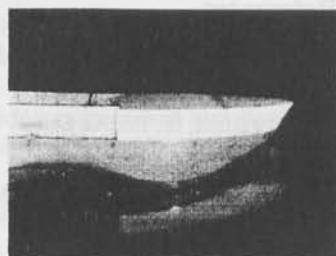


Fig. 6 Picture of the steady wave  
along ship-side at  $F_n = 0.2$

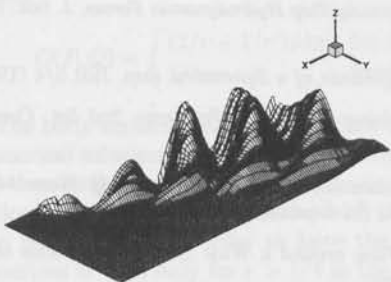


Fig. 9 Perspective view of the diffraction wave  
at  $t = 0$  ( $F_n = 0.2$ ,  $\lambda/L = 0.5$ ,  $\chi = 180$  deg.)

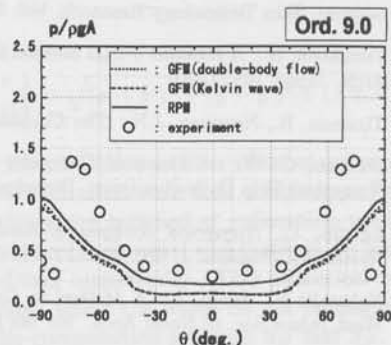


Fig. 10 Wave pressure distribution at ord.9  
( $F_n = 0.2$ ,  $\lambda/L = 0.5$ ,  $\chi = 180$  deg.)

## Wave decay characteristics along a long array of cylindrical legs

Hiroshi Kagemoto

University of Tokyo, Japan

### 1. Introduction

A very large floating structure (VLFS) of several kilometers in length and in width is now considered as a possible alternative of such land-based structures as an airport. Although there can be various types of structures that are used for such purposes, the structures proposed so far are roughly categorized into two types of structures. One is a simple thin box-shaped structure and the other one is a structure supported on a large number of cylindrical legs. For the design of a floating structure, we need to be able to estimate the hydrodynamic forces on the structure correctly. However, when the structure is so large as extends several kilometers horizontally, the computational burden for the analysis of hydrodynamic forces is so large that it is practically impossible to carry out. For a thin box-shaped structure, the author proposed an approximate but quite accurate method in exploiting the fact that the structure is far larger than the ambient wavelength and thus the flow field can be assumed with good approximation to be the same as that around the structure which extends infinitely in horizontal direction<sup>1</sup>). For a structure supported on a large number of legs, similar approximation can be applied in which the flow field around an array of a large number of legs is assumed to be the same as that around an array composed of an infinite number of legs (except at the vicinity of the ends of the array)<sup>2</sup>). When the structure is located in head waves, however, these approximations do not work well because waves actually decay as they propagate through the structure while, if we stick to the infinite-length or the infinite-leg assumptions described above, wave amplitudes can not decay since the approximations impose that there should be no way other than the phase to distinguish the wave at one place from that at another place. For a box-shaped structure, the decay characteristics of head waves have been found to be proportional to the inverse square-root of the distance along which the wave propagated from the up-wave end of the structure. This result coincides with that predicted by a slender-body theory. By exploiting this quantitative decay characteristics of waves, an approximate computation is still possible for the hydrodynamic analysis of a box-shaped structure in head waves<sup>1</sup>). If similar quantitative decay characteristics of head waves propagating along a structure supported on a large number of legs could be found, an approximate hydrodynamic analysis of the structure may be possible in a similar way as conducted for a box-shaped structure. This is the motivation of the present work.

### 2. Experiment

A 3×20 array of truncated composite cylinders were fixed in regular head waves as shown in Fig.1 and the surface elevations between the cylinders were measured. Fig.2 shows the results on the amplitude of the surface elevation in waves of 4 representative wave periods. 'Cal' in the legends stands for the results obtained by the calculations based on a linear potential theory. An interesting feature is that short waves decay as they propagate from the head of the array toward the end of the array (Fig.2(a)) whereas, as the wave period becomes longer, the distribution of the wave amplitudes begins to oscillate spacewise (Fig.2(b)) and even be enhanced rather than be decayed as the wave is further elongated (Fig.2(c),(d)).

### 3. Parametric numerical computation

Since, as is observed in Fig.2, the linear potential theory agrees well with the experimental results, de-

tailed computation was carried out for an array of  $1 \times 60$  vertical truncated cylinders ( $D/d=1.0, h/d=2.0, \ell/D=2.0$  where  $D$ :diameter,  $d$ :draft,  $h$ :water depth,  $\ell$ :distance between adjacent cylinders) while varying the wavelength systematically. Fig.3 shows some of the typical results of the computation. It should be noted that a tiny difference of the wavelength ( $\Delta\lambda/\ell = 0.002$ ) induces a big difference of the surface elevations as shown in Fig.3(b) and Fig.3(c). The large surface elevation that occurs at a certain particular wavelength ( $\ell/\lambda = 0.449$ ) may correspond to one of the resonant phenomena indicated by Maniar and Newman<sup>3</sup>). Another interesting feature is that as the wavelength becomes longer, the amplitude of the surface elevation begins to oscillate spacewise (Fig.3(d)) and the wavelength of the spacewise oscillation becomes shorter as the wavelength becomes still longer (Fig.3(e)). It is also noticeable that the wave amplitude is enhanced rather than be decayed as the wave propagates along the array. This enhancement of wave amplitudes persists up to the longest wavelength ( $\ell/\lambda = 0.359$ ) conducted in the present computation, although, in principle, it should converge to the amplitude of the incident wave ( $\zeta_a$ ) as the wavelength becomes very long. In order to extract some of the hidden features of these wave-decay (or wave-enhancement) characteristics, Fig.3 were replotted in log-log papers as in Fig.4. From this figure it can be known that, when waves decay, the decay rate is roughly proportional to the inverse square-root of the traveled distance of waves measured from the head of the array, which is also the case for a box-shaped very long structure. On the other hand, if we examine the relationship between the consecutive difference of  $\zeta_i$  (amplitude of the surface elevation measured at  $i$ -th measured point) as shown in Fig.5, we now know that

$$\zeta_{i+1} - \zeta_i \sim \alpha(\zeta_i - \zeta_{i-1}) \quad (1)$$

in the vicinity of the head of the array, which implies that the waves decay exponentially there.

#### Acknowledgement

The experimental results shown in Fig.3 were obtained by M.Saito and H.Ioku of the University of Tokyo as part of their graduation project.

#### Reference

- (1) H.Kagemoto, M.Fujino, and T.Zhu: *J. Applied Ocean Research*, **19**, 49-60, 1997.
- (2) H.Kagemoto and D.K.P.Yue: *Proc. 5th OMAE*, Vol1, 206-211, 1986.
- (3) H.D.Maniar and J.N.Newman: *J. Fluid Mech.*, **339**, 309-330, 1997.

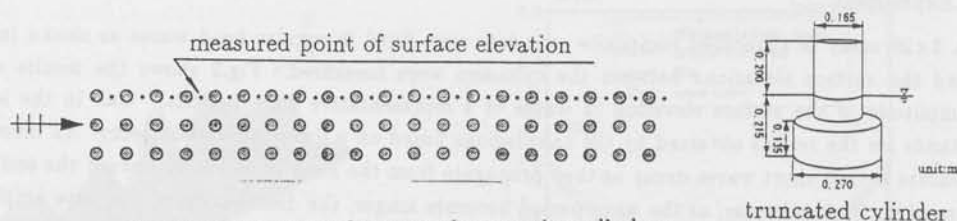


Fig.1 A  $3 \times 20$  array of truncated composite cylinders  
(center to center distance: 0.540m)

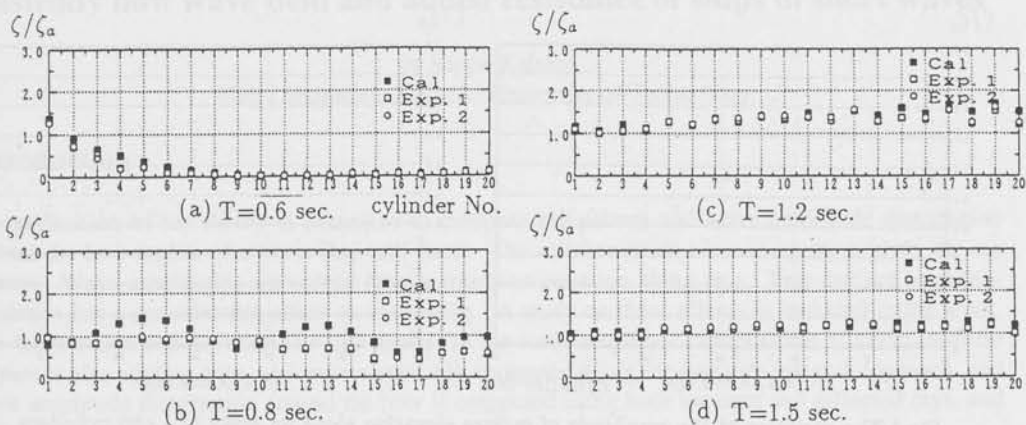


Fig.2 Comparisons of the measured amplitude of surface elevation with numerical calculations

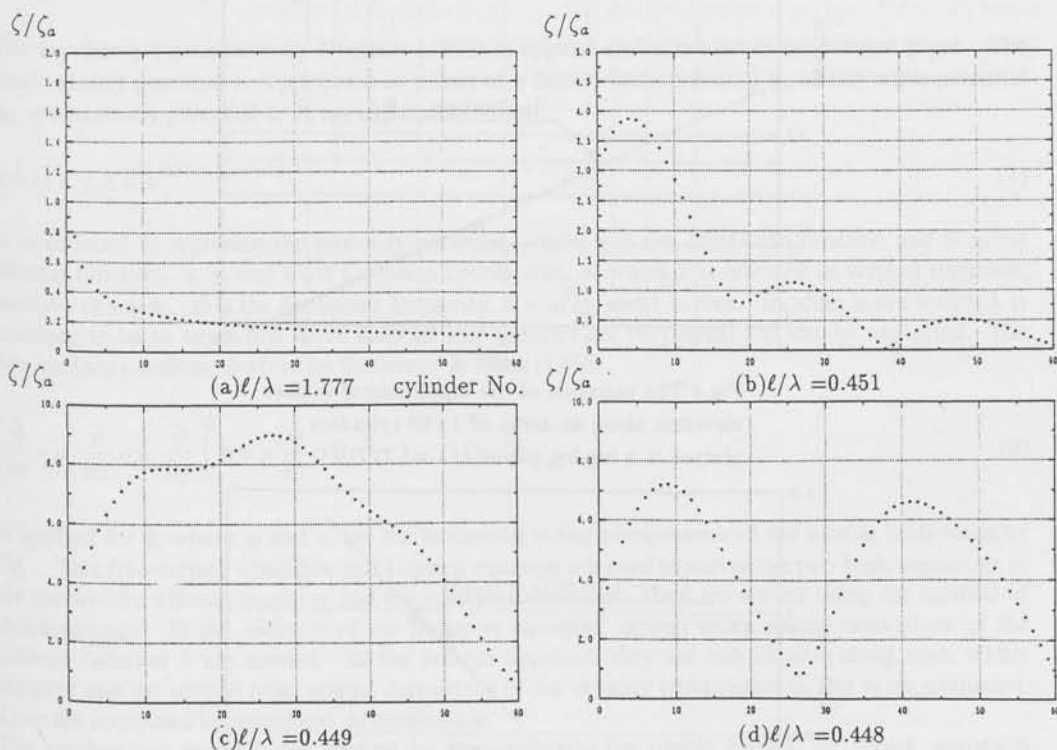


Fig.3 The variation of the amplitude of surface elevation along an array of  $1 \times 60$  cylinders

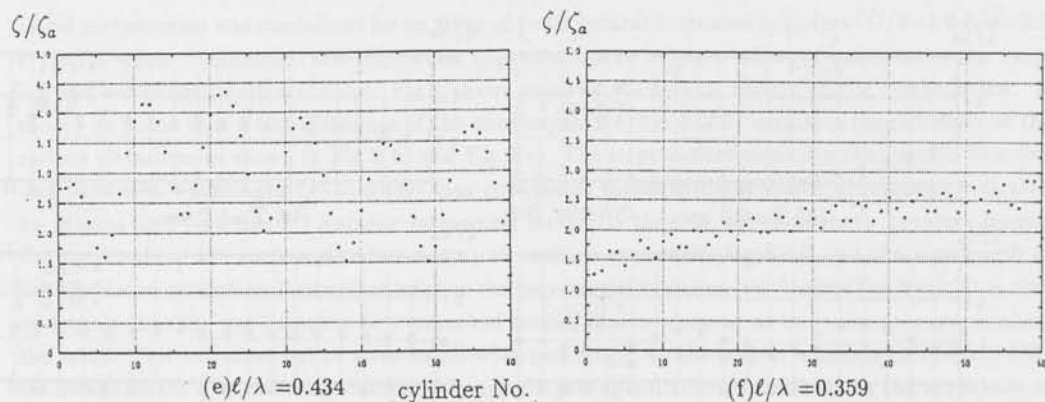


Fig.3 The variation of the amplitude of surface elevation along an array of  $1 \times 60$  cylinders

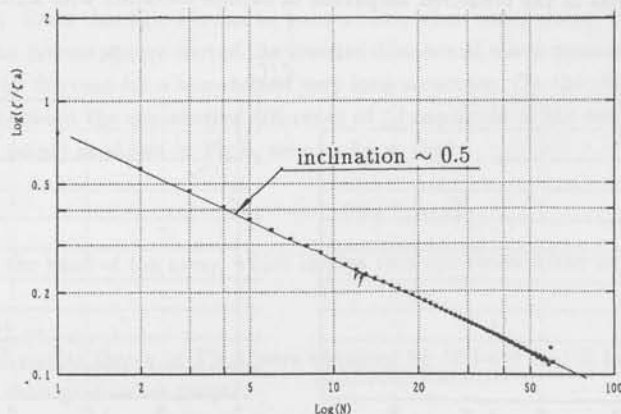


Fig.4 The variation of the amplitude of surface elevation along an array of  $1 \times 60$  cylinders plotted in a log-log paper ( $l/\lambda = 1.777$ )

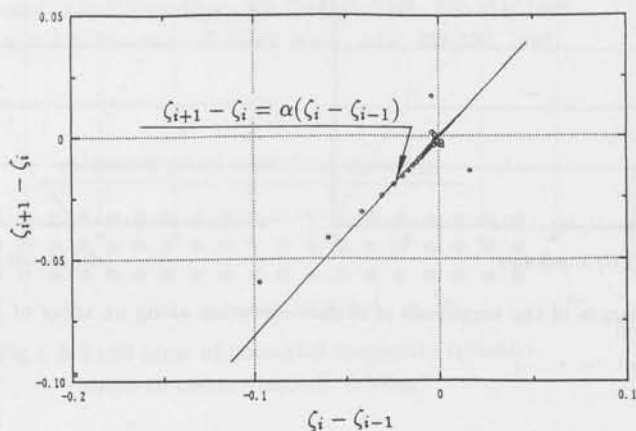


Fig.5  $\zeta_{i+1} - \zeta_i$  vs  $\zeta_i - \zeta_{i-1}$  ( $l/\lambda = 1.777$ )

## Unsteady bow wave field and added resistance of ships in short waves

by Seppo Kalske

Ship Laboratory, Helsinki University of Technology

### Introduction

An application of ray theory is presented to compute ray pattern and wave amplitude distribution around the bow region of a blunt ship hull form. The solution of an eikonal equation gives the ray pattern. Wave amplitudes are solved from a transport equation along rays. Free-surface boundary condition has a considerable effect on the results. A study on these effects is included in the work. The wave action conservation law that applies to the wave amplitude computation in a non-uniform current is also applied here. Added resistance is computed using the pressure integral approach, and wave amplitude distribution around the bow is computed using both incident and reflected rays, and taking their interaction into account.

### The extended ray theory

The ray theory formulation by Hermans (1993) is applied and extended in the present paper. The total velocity potential is represented as a sum of a double-body potential  $\phi_r$ , steady wave potential  $\phi_0$ , and unsteady potential  $\phi$ . A ray expansion

$$\phi = a(x, y, z; k) e^{ikS(x, y, z) - i\omega t} \quad (1)$$

is introduced to represent the unsteady potential, where  $a$  is the amplitude function and  $S$  is the eikonal function.  $x$ ,  $y$ , and  $z$  are Cartesian coordinates, of which  $z$  is oriented in vertical direction, positive upwards.  $\omega$  is the encounter frequency,  $k = \omega^2/g$ , and  $t$  is time. Incident wave length  $\lambda$  is assumed to be so small that wave induced ship motions are very small and can be neglected. The free-surface condition derived by Sakamoto & Baba (1986)

$$\left( \frac{\partial}{\partial t} - u_r \frac{\partial}{\partial x} - v_r \frac{\partial}{\partial y} \right)^2 \phi + g \frac{\partial \phi}{\partial z} = 0 \quad (2)$$

is applied for  $\phi$ , where  $u_r$  and  $v_r$  are the horizontal scalar components of the double body velocity  $\nabla \phi_r$ . This free-surface condition and Laplace equation are used to derive the two basic equations in ray theory: the eikonal equation and the transport equation. They are solved using the method of characteristics. In the solution of the transport equation, second order spatial derivatives of the eikonal function  $S$  are needed. In the present approach they are solved also along rays, which requires that the second order spatial derivatives of the velocity components  $u_r$  and  $v_r$  are evaluated. They are computed by numerical differentiation.

The original ray method was applied by Hermans only for simple bodies, for which analytical evaluation of  $u_r$  and  $v_r$  is possible. In this work, the ray method is extended to practical ship hull forms in two ways. In the first way, the velocity field is computed by a two-dimensional panel method using only the geometry of the waterline of a body. This corresponds to a ship with a very large draft. In the second way, the velocity field is computed by a three-dimensional panel method, where the total underwater part of the ship hull is modelled, and finite draft effects are correctly taken into account in computing  $u_r$  and  $v_r$ . The three-dimensional approach was accomplished by using the velocity field output from the Shipflow computer program package (Larsson et al., 1990).

### Free surface boundary condition

The above free surface condition, Eq. 2, makes a pair with the free surface condition in the low speed theory for steady ship motion. Other free surface conditions can in principle also be used. One example is the so-called low speed free surface condition that can be derived from slightly different assumptions than used by Sakamoto & Baba (1986) for the unsteady potential  $\phi$ . By assuming that the wave length of the unsteady motion is larger than for the steady motion, namely

$$\left(\frac{\partial}{\partial x}, \frac{\partial}{\partial y}, \frac{\partial}{\partial z}\right)\phi = O(U^{-1}\phi), \quad (3)$$

where  $U$  is speed of advance of the ship, and taking into account only linear terms in  $\phi$ , the following low speed free surface condition on  $z = 0$  can be derived

$$\frac{\partial^2 \phi}{\partial t^2} + 2u_r \phi_{xt} + 2v_r \phi_{yt} + g \frac{\partial \phi}{\partial z} = 0. \quad (4)$$

When Eq. 4 is compared with Eq. 2, it can be seen that the non-linear terms in  $\nabla\phi$  are ignored. This free-surface condition yields a slightly different ray pattern than the other free-surface condition. Added resistance values differ more, especially when the reduced frequency  $\tau = U\omega/g$  increases. Wave amplitude can be also computed by using the wave action conservation law that can be applied in the steady form in the present case. It can be shown that the application of the wave action conservation law reduces to the transport equation derived by Hermans (1993) when a two-dimensional double body flow approximation is used. This corresponds to an infinite draft assumption. When a more realistic three-dimensional double body flow approximation is used, an additional term remains in the wave action equation compared with Hermans' transport equation. This additional term affects the wave amplitude and added resistance results but not the ray pattern.

### Unsteady wave elevation around a blunt bow

Measured data exist for the unsteady wave elevation for the Series 60  $C_B = 0.8$  model near the bow region in short waves (Ohkusu, 1996). An approximate approach to compute also the wave elevation with ray theory is developed in this work. First, a set of points is selected where the total unsteady wave elevation is to be computed. For each point the values of the wave elevation and eikonal function of the nearest incident ray passing the point are saved. These values are stored also for the nearest passing reflected ray, and the total wave elevation at each point can be computed.

In ray theory, computation of wave elevation along a reflected ray is in many cases difficult and very small steps in integration of the ray and transport equations are required. In addition, there are caustic curves, where wave amplitudes tend to infinity, and no realistic wave amplitude results can be obtained. Caustics are defined as envelopes of reflected rays, and their location can be predicted numerically. Thus, the caustic curves can be avoided in the wave elevation computation.

In physical terms, waves become steeper and tend to break when they approach a caustic curve. Naito et al. (1987) explain that this breaking happens when a complex valued wave number is obtained as a solution of the local dispersion relation. In the present method, the eikonal equation is equivalent to the dispersion relation, and ray tracing gives the solution for the local wave number. When the reflected rays are traced with the present method, no complex valued solutions for the local wave number are obtained when an adaptive stepsize control is used in the integration. If too large values for the step are used, reflected rays do not bend enough, and complex valued wave numbers are obtained. This fact does not support the use of Naito's breaking criterion.

Hermans (1993) derived a uniform expansion for wave elevation computation in an essentially one-dimensional case, where he is able to reduce the transport equation to a simple form well-known in optics. A boundary-layer solution near the caustic point is presented, but only very few numerical results are given. It is difficult to extend this approach to a practical ship hull form.

## Results and discussion

At present stage, results are available for the Series 60  $C_B = 0.8$  hull form at full and ballast draft and for a bulk carrier hull form OHS with a bulbous bow at ballast condition. Examples of result for ray patterns near ship bows are given in Figures 1 and 2.

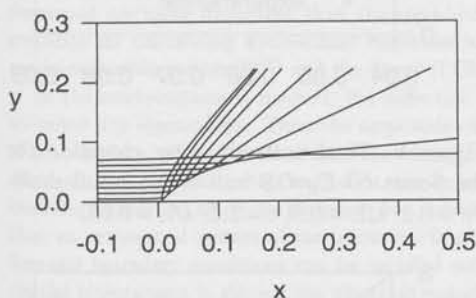


Figure 1. Ray pattern for Series 60  $C_B=0.8$  hull form at ballast draft.  $F_n=0.1$ ,  $\lambda/L=0.5$ .

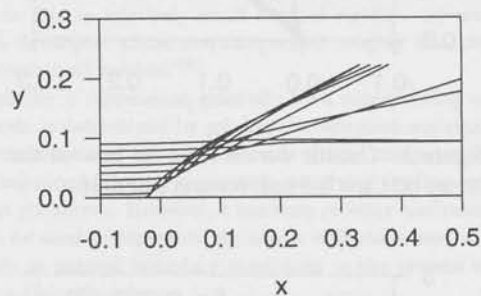


Figure 2. Ray pattern for the OHS hull form at ballast draft.  $F_n=0.17$ ,  $\lambda/L=0.5$ .

Wave elevation results are most interesting in the region around the bow, where both incident and reflected rays exist. This region lies between the ship hull and the caustic curve, and examples of caustic location computed numerically are shown in Figure 3 as a function of reduced frequency  $\tau$ . Computed wave elevations with comparison of measured results are shown in Figure 4 for an example case. The results are divided with the far field amplitude values. The agreement is good especially near the ship hull and near the bow.

Added resistance is computed with the pressure integral approach using an equation derived by Hermans (1993). Results for the Series 60  $C_B = 0.8$  hull at  $F_n = 0.10$  at full draft are shown in Figure 5. The results with a two-dimensional velocity field computation are shown in Figure 6 for the so-called blunt ship model (Nakamura et al., 1983), which has an extremely blunt bow form. In this case, results by the method of Sakamoto & Baba (1986) are also included. It can be concluded that the low speed free-surface condition, Eq. 4, can be applied for relatively small values of reduced frequency  $\tau$ . When  $\tau$  increases, overestimation of added resistance occurs. The use of wave action equation gives in most cases improved results especially as  $\tau$  increases. For an extremely blunt bow form ray theory results are in good agreement with experimental results.

Additional computations will be made to validate the method further.

## References

- Hermans, A.J., 1993. The Diffraction of Short Free-Surface Water Waves, a Uniform Expansion. *Wave Motion* 18 (1993) 103 - 119.
- Larsson, L., Broberg, L., Kim, K.-J. & Zhang, D.-H. 1990. A Method for Resistance and Flow Prediction in Ship Design. *Transactions of SNAME*, 98 (1990) 495 - 535.

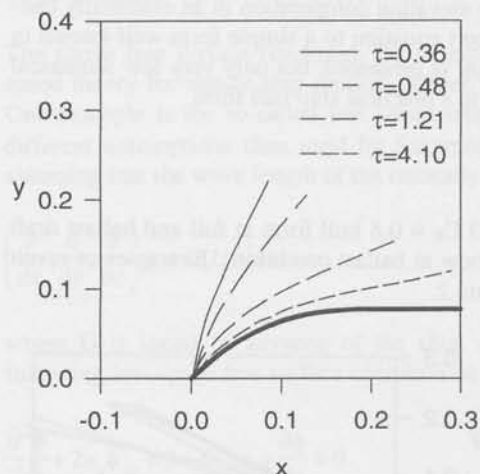


Figure 3. Caustic curves near the bow of the Series 60  $C_B = 0.8$  hull form at full draft.

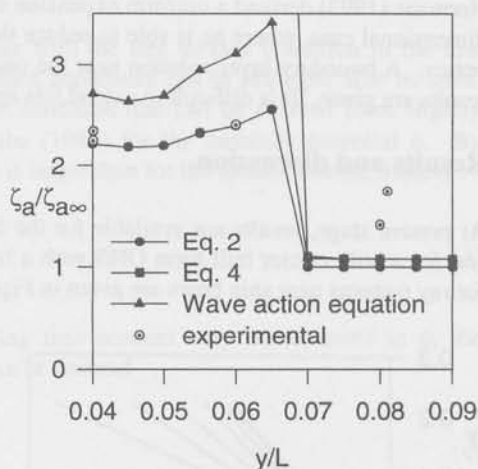


Figure 4. Total unsteady wave elevation for the Series 60  $C_B = 0.8$  hull form at full draft.  $Fn = 0.2$ ,  $\lambda/L = 0.5$ ,  $\tau = 1.2$ ,  $x/L = 0.05$ .

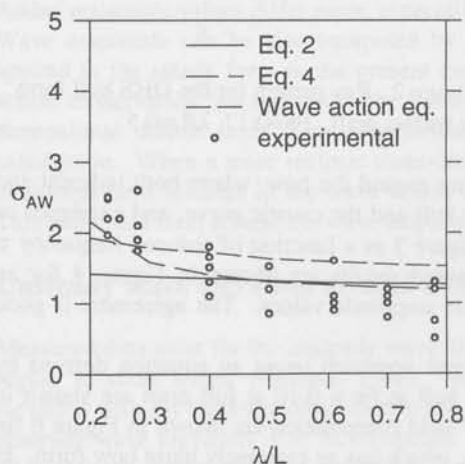


Figure 5. Added resistance for the Series 60  $C_B = 0.8$  hull form at full draft.  $Fn = 0.10$ ,  $0.36 \leq \tau \leq 0.87$ .  $\sigma_{AW} = R_{AW} / (\rho g B^2 / L)$ .

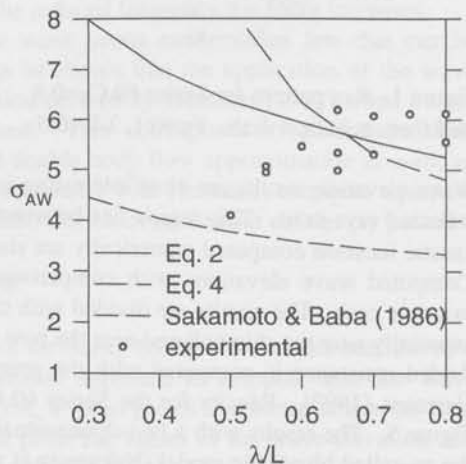


Figure 6. Added resistance for the blunt ship model with two-dimensional velocity computation.  $Fn = 0.15$ ,  $0.60 \leq \tau \leq 1.16$ .

Naito, S., Nakamura, S. & Nishiguchi, A. 1987. Added Resistance in Regular Head Waves of a Ship with Blunt Bow. Proc. of Prads '87 Conference, Trondheim, 22 - 26 June, 1987, pp. 291 - 301.  
 Nakamura, S., Naito, S., Matsumoto, K., Susukida, K. & Nishiguchi, A. 1983. Experimental Study on Resistance Increase in Regular Head Waves of a Ship with Blunt Bow. Journal of the Kansai Society of Naval Architects, No. 190, pp. 73 - 81.

Ohkusu, M. 1996. Private communication.

Sakamoto, T. & Baba, E. 1986. Minimization of Resistance of Slowly Moving Full Hull Forms in Short Waves. Proceedings of 16th Symposium on Naval Hydrodynamics, Berkeley, Ca. July 13 - 18, 1986, pp. 598 - 612.

## A New Direct Method for Calculating Hydroelastic Deflection of a Very Large Floating Structure in Waves

by Masashi KASHIWAGI

Research Institute for Applied Mechanics, Kyushu University  
6-1 Kasuga-koen, Kasuga-city, Fukuoka 816-8580, Japan

### 1. Introduction

Very large floating structures with shallow draft, considered as an airport, are featured in that the hydroelastic responses are more important than the rigid-body motions due to relatively small flexural rigidity. Several methods for calculating hydroelastic responses have been developed; those are categorized roughly into the mode-expansion method<sup>1)~3)</sup> and the direct (FEM-BEM combined) method.<sup>4)5)</sup>

In the mode-expansion method, the deflection of a structure is represented generally by a superposition of so-called dry eigenmodes. Then the amplitude of each mode is determined by solving the vibration equation of a thin plate, with the added mass and damping force corresponding to specified mode shapes computed in advance. One problem in this method is that an analytical solution of the dry eigenmode, satisfying the free-end boundary condition along the periphery of a structure, is not yet known. However, it has been recently confirmed that an orthogonal system of mathematical functions can be used to represent the elastic deflection, and the free-end boundary conditions can be satisfied subsequently as natural boundary conditions in the process of partial integrations in solving the vibration equation with a Galerkin scheme.

If our interest is placed not on the contribution of each mode function but on the elastic deflection as a whole, the direct method is more lucid than the mode-expansion method. However, the direct method is generally time consuming, because the vibration equation must be solved simultaneously with the integral equation for the pressure distribution beneath a structure. In most prior works<sup>4)5)</sup> based on the direct method, the vibration equation has been solved using a commercial software of FEM, and the pressure at nodal points used in FEM analyses has been determined by means of BEM. Therefore, the relation between the direct method and the mode-expansion method seems not clear, from a viewpoint of numerical calculation scheme.

The present paper is intended to develop a new direct solution method, which does not rely on the FEM, and to make clear the relation of the new method with Kashiwagi's numerical scheme<sup>1)</sup> based on the mode-expansion method.

### 2. Mathematical Formulation

Cartesian coordinates are defined with  $z = 0$  as the plane of the undisturbed free surface and  $z = h$  as the horizontal sea bottom. The incident regular wave comes from the negative  $x$ -axis with incidence angle  $\beta$ .

Time-harmonic motions of small amplitude are considered, with the complex time dependence  $e^{i\omega t}$  applied to all first-order oscillatory quantities. The boundary conditions on the body and free surface are linearized, and the potential flow is assumed. The plan view of the structure is rectangular with length  $L$  and width  $B$ , and the draft is regarded as zero because of its very small value relative to  $L$  and  $B$ .

We express the velocity potential,  $\phi(x, y, z)$ , the pressure distribution,  $p(x, y)$ , the vertical displacement of the free surface,  $\zeta(x, y)$ , and the elastic deflection of a structure,  $w(x, y)$ , in nondimensional form as follows:

$$\left. \begin{aligned} \phi(x, y, z) &= i\omega a(L/2)\phi'(x, y, z), & p(x, y) &= \rho g a p'(x, y) \\ \zeta(x, y) &= a\zeta'(x, y), & w(x, y) &= a w'(x, y) \end{aligned} \right\} \quad (1)$$

where  $a$  is the amplitude of incident wave,  $\omega$  the circular frequency,  $\rho$  the fluid density, and  $g$  the gravitational acceleration. The prime denotes nondimensional quantities, but it will be omitted for brevity in what follows.

The coordinates  $(x, y, z)$  are also made nondimensional in terms of  $L/2$ , and thus the structure exists in the region of  $|x| \leq 1$  and  $|y| \leq b \equiv B/L$  on  $z = 0$ .

Hydrodynamically, the disturbance due to the presence of a structure can be expressed by the pressure applied on the free surface. Then the dynamic and kinematic free-surface boundary conditions are given by

$$p = K\phi + \zeta, \quad \frac{\partial\phi}{\partial z} = \zeta \quad \text{on } z = 0 \quad (2)$$

where  $K = \omega^2/g$ . Note that  $p = 0$  outside of a structure and  $\zeta = w$  beneath a structure.

Since the velocity potential can be given by the convolution integral of the pressure,  $p(x, y)$ , and the Green function,  $G(x, y, z)$ , satisfying (2) with  $p = 0$ , it is of relative ease to show that the integral equation for the unknown pressure takes the form

$$p(x, y) - K \iint_{S_H} p(\xi, \eta) G(x - \xi, y - \eta, 0) d\xi d\eta = w(x, y) \quad (3)$$

where  $S_H$  denotes the bottom of a structure with zero draft.

The body boundary condition can be satisfied by writing the deflection of a structure in the following form:

$$w(x, y) = w_S(x, y) + w_R(x, y) = -\zeta_I(x, y) + w_R(x, y) \quad (4)$$

where

$$\zeta_I(x, y) = \exp\{-ik_0(x \cos \beta + y \sin \beta)\} \quad (5)$$

is the elevation of incident wave, and subscripts  $S$  and  $R$  mean the scattering and radiation components, respectively.

Substituting (4) in (3) gives the equation to be solved:

$$p(x, y) - K \iint_{S_H} p(\xi, \eta) G(x - \xi, y - \eta, 0) d\xi d\eta - w_R(x, y) = -\zeta_I(x, y) \quad (6)$$

The radiation component of the deflection,  $w_R(x, y)$ , is unknown and subject to the vibration equation of a thin plate:

$$-MK\Lambda w_R(x, y) + D\left(\frac{\partial^4}{\partial x^4} + 2\frac{\partial^4}{\partial x^2 \partial y^2} + \frac{\partial^4}{\partial y^4}\right) w_R(x, y) = -p(x, y) \quad (7)$$

where  $M$  is the mass of a structure (divided by  $\rho L B d$ ),  $D$  is the flexural rigidity (divided by  $\rho g(L/2)^4$ ), and  $\Lambda = 2d/L$  with  $d$  being the draft.

Since the structure is freely floating,  $w_R(x, y)$  must satisfy the free-end boundary conditions along the periphery of the structure. Those conditions can be written as

$$\frac{\partial^2 w_R}{\partial n^2} + \nu \frac{\partial^2 w_R}{\partial s^2} = 0, \quad \frac{\partial}{\partial n} \left\{ \frac{\partial^2 w_R}{\partial n^2} + (2 - \nu) \frac{\partial^2 w_R}{\partial s^2} \right\} = 0 \quad (8)$$

where  $n$  and  $s$  denote the normal and tangential directions, respectively, and  $\nu$  is Poisson's ratio.

In the case of a rectangular plate, a concentrated force, stemming from the replacement of the torsional moment with an equivalent shear force, acts at four corners, which must be also zero. Namely

$$R = 2D(1 - \nu) \frac{\partial^2 w_R}{\partial x \partial y} = 0 \quad \text{at } x = \pm 1, y = \pm b \quad (9)$$

In summary, (6) and (7) are the simultaneous equations for the two unknowns: the pressure distribution  $p(x, y)$  and the vertical elastic deflection  $w_R(x, y)$ . Solving (6) and (7) at the same time while satisfying (8) and (9) is referred to as the direct method<sup>5)6)</sup>

If  $w_R(x, y)$  is expressed in terms of a system of appropriate known functions,  $w_j(x, y)$  ( $j = 1, 2, \dots$ ), in the form

$$w_R(x, y) = \sum_{j=1}^{\infty} X_j w_j(x, y), \quad (10)$$

the corresponding pressure can be sought from (6) in the form

$$p(x, y) = p_S(x, y) + \sum_{j=1}^{\infty} X_j p_j(x, y) \quad (11)$$

Here the amplitude  $X_j$  is unknown, but can be determined subsequently by solving (7) with free-end boundary conditions, (8) and (9), satisfied in an appropriate manner. This solution method is referred to as the mode-expansion method and featured in solving (6) and (7) separately.

### 3. A New Numerical Method

In the mode-expansion method developed by Kashiwagi<sup>1)</sup>, the pressure distribution is represented using bi-cubic B-spline functions. It may be natural in the direct method to express the elastic deflection,  $w_R(x, y)$ , with the same B-spline functions. Therefore we try to obtain numerical solutions in the following form:

$$\left. \begin{aligned} p(x, y) &= \sum_{k=0}^{NX+2} \sum_{\ell=0}^{NY+2} \alpha_{k\ell} B_k(x) B_\ell(y) \\ w_R(x, y) &= \sum_{k=0}^{NX+2} \sum_{\ell=0}^{NY+2} \gamma_{k\ell} B_k(x) B_\ell(y) \end{aligned} \right\} \quad (12)$$

where  $B_k(x)$  and  $B_\ell(y)$  are the cubic B-spline functions.  $NX$  and  $NY$  are the number of panel division in the  $x$ - and  $y$ -directions, respectively. Since one cubic spline function extends its influence over four panels, the number of total unknowns in each of  $p(x, y)$  and  $w_R(x, y)$  is  $(NX + 3) * (NY + 3)$ .

Substituting (12) into (6) and (7) and applying a Galerkin scheme with  $B_p(x)B_q(y)$  ( $p = 0 \sim NX + 2$ ,  $q = 0 \sim NY + 2$ ) as the weight function, we obtain a linear system of simultaneous equations, in the form

$$\sum_{k=0}^{NX+2} \sum_{\ell=0}^{NY+2} \left[ \alpha_{k\ell} \left\{ \mathcal{L}_{pq, k\ell}^{(1)} - K \mathcal{L}_{pq, k\ell}^{(2)} \right\} - \gamma_{k\ell} \mathcal{L}_{pq, k\ell}^{(1)} \right] = \mathcal{R}_{pq} \quad (13)$$

$$\sum_{k=0}^{NX+2} \sum_{\ell=0}^{NY+2} \left[ \alpha_{k\ell} \mathcal{L}_{pq, k\ell}^{(1)} + \gamma_{k\ell} \left\{ -MK\Lambda \mathcal{L}_{pq, k\ell}^{(1)} + D \mathcal{L}_{pq, k\ell}^{(3)} \right\} \right] = 0 \quad (14)$$

where

$$\mathcal{L}_{pq, k\ell}^{(1)} = \iint_{S_H} B_p(x) B_q(y) B_k(x) B_\ell(y) dx dy \quad (15)$$

$$\mathcal{L}_{pq, k\ell}^{(2)} = \iint_{S_H} B_p(x) B_q(y) \left[ \iint_{S_H} B_k(\xi) B_\ell(\eta) G(x - \xi, y - \eta, 0) d\xi d\eta \right] dx dy \quad (16)$$

$$\mathcal{L}_{pq, k\ell}^{(3)} = \iint_{S_H} B_p(x) B_q(y) \nabla^4 \{ B_k(x) B_\ell(y) \} dx dy \quad (17)$$

$$\mathcal{R}_{pq} = - \iint_{S_H} B_p(x) B_q(y) \zeta_I(x, y) dx dy \quad (18)$$

The stiffness matrix, (17), must be transformed by partial integrations to incorporate the free-end boundary conditions, (8) and (9). The procedure is the same as that used in the mode-expansion method of Kashiwagi<sup>1)</sup>, and the result takes the form

$$\begin{aligned} \mathcal{L}_{pq, k\ell}^{(3)} &= \iint_{S_H} \nabla^2 B_{pq} \nabla^2 B_{k\ell} dx dy \\ &- (1 - \nu) \iint_{S_H} \left\{ \frac{\partial^2 B_{pq}}{\partial x^2} \frac{\partial^2 B_{k\ell}}{\partial y^2} + \frac{\partial^2 B_{pq}}{\partial y^2} \frac{\partial^2 B_{k\ell}}{\partial x^2} - 2 \frac{\partial^2 B_{pq}}{\partial x \partial y} \frac{\partial^2 B_{k\ell}}{\partial x \partial y} \right\} dx dy \end{aligned} \quad (19)$$

where  $B_{pq} = B_p(x)B_q(y)$  and  $B_{k\ell} = B_k(x)B_\ell(y)$ .

The mass matrix,  $\mathcal{L}_{pq, k\ell}^{(1)}$ , serves also as the cross-coupling matrix between the pressure and elastic deflection, which has been computed using Clenshaw-Curtis quadrature with absolute error less than  $10^{-7}$  required. The integral  $\mathcal{L}_{pq, k\ell}^{(2)}$  given by (16) is the most time-consuming part but the same as that appearing in Kashiwagi's mode-expansion method. Therefore, by taking advantage of 'relative similarity relations', it can be computed with less computational time.

### 4. Numerical Results

It is confirmed that the present method gives substantially the same results as those by the mode-expansion method using products of one-dimensional free-free beam modes to represent the elastic deflection.

Since the present method uses only the B-spline functions as a basis function, the computer code is simpler than the mode-expansion method. However, in the present method, the symmetry relation is not used, and thus the number of unknowns and the computational time are greater than that in the mode-expansion method of Kashiwagi.<sup>1)</sup>

Various computations have been performed, including the comparison with the experiments conducted at Ship Research Institute in Japan using a 1/30.8 scale model for a floating structure of  $L \times B \times d = 300\text{m} \times 60\text{m} \times 0.5\text{m}$ . Those results will be presented at the Workshop. Here, instead, we show one example of the wave profile around a structure of  $L/B = 4$ . Since the pressure is zero on the free surface, the total wave elevation can be computed from (2) and (5) by the equation:

$$\zeta_T(x, y) = \zeta_I(x, y) - K \iint_{S_H} p(\xi, \eta) G(x - \xi, y - \eta, 0) d\xi d\eta \quad (20)$$

Figure 1 is the result computed for  $L/\lambda = 10$  and  $\beta = 30^\circ$  in deep water, with  $NX = 40$  and  $NY = 10$ . The flexural rigidity was taken equal to  $1.875 \times 10^{-6}$ , which might be stiffer than a realistic floating airport. For comparison, Fig. 2 shows the wave profile around a rigid structure with the same dimensions. We can see that the wave reflection from an elastic plate is small near the bow and the transmitted wave is visible even downstream. The pattern of elastic deflection on the plate is different from that of water wave both in the wave length of fluctuation and the propagation angle.

## References

- 1) Kashiwagi, M. (1998): A B-Spline Galerkin Scheme for Calculating Hydroelastic Response of a Very Large Floating Structure in Waves, *J. Marine Science and Technology* (to be published)
- 2) Takaki, M. and Gu, X. (1996): Motions of a Floating Elastic Plate in Waves, *J. Soc. Nav. Arch. Japan*, Vol. 180, pp. 331-339
- 3) Ohmatsu, S. (1997): Numerical Calculation of Hydroelastic Responses of Pontoon Type VLFS (in Japanese), *J. Soc. Nav. Arch. Japan*, Vol. 182 (to be published)
- 4) Yago, K. and Endo, H. (1996): On the Hydroelastic Response of Box-Shaped Floating Structure with Shallow Draft (in Japanese), *J. Soc. Nav. Arch. Japan*, Vol. 180, pp. 341-352
- 5) Yasuzawa, Y. *et al.* (1997): Dynamic Response of a Large Flexible Floating Structure in Regular Waves, *Proc. 16th Int. Conf. on Offshore Mech. and Arctic Eng.*, Vol. 6, pp. 187-194

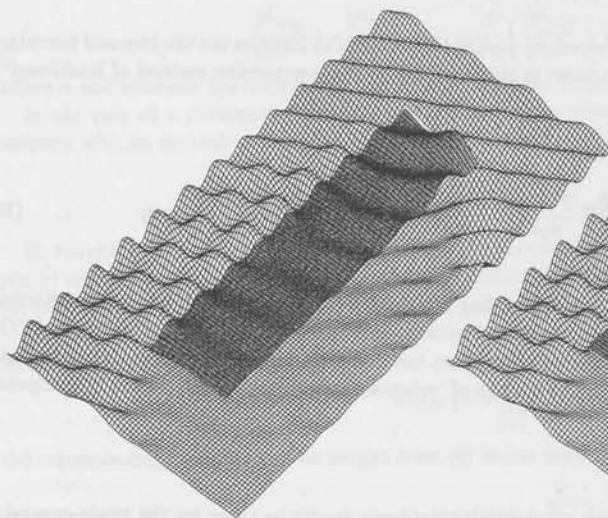


Fig. 1: Wave pattern around an elastic plate of  $L/B = 4$  and  $D = 1.875 \times 10^{-6}$ .  $L/\lambda = 10$  and  $\beta = 30^\circ$  in deep water.

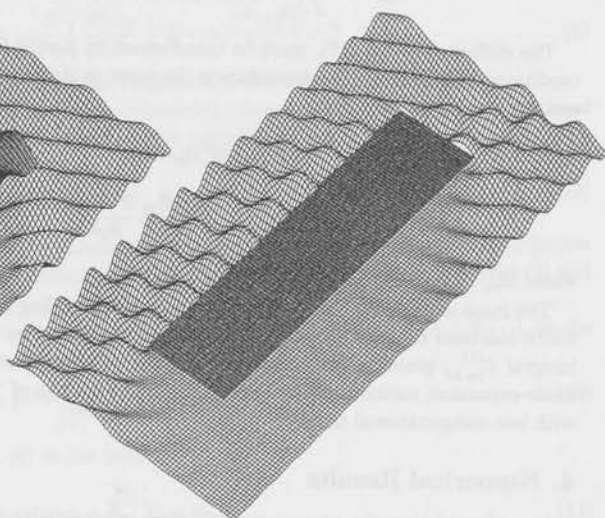


Fig. 2: Wave pattern around a rigid plate. Geometrical dimensions and wave data are the same as Fig. 1.

## One-side inequalities in the problem of wave impact

T.I.Khabakhpasheva, A.A.Korobkin

Lavrentyev Institute of Hydrodynamics,  
Novosibirsk, 630090, RUSSIA

The plane unsteady problem of wave impact onto an elastic beam is considered. Initially a wave crest touches the horizontal and beam at its left edge and hits the beam from below thereafter at a constant velocity. The problem is coupled, the beam deflection is determined by the hydrodynamic loads, which themselves depend on velocities of beam elements. The wetted part of the beam, where the hydrodynamic loads are applied, is unknown and has to be found together with the liquid flow and the beam deflection. The original formulation of the impact problem contains not only equations of motion and boundary conditions but one-side inequalities as well. The first inequality implies that the liquid particles cannot penetrate the plate and the second one that the pressure in the contact region cannot be less than a limiting value  $p_{adh}$ , which depends on adhesive forces between liquid and the plate surface. The additional limitations make us to control both the pressure distribution along the wetted area and the free surface elevation at every time step and to change the boundary conditions when and where the mentioned one-side inequalities fail.

If the pressure on the plate drops down to the limiting value  $p_{adh}$ , a new 'inner' free surface has to be introduced. After that we shall consider the wave impact onto the plate with attached cavity. Within the framework of incompressible liquid we do not know any approach to describe the asymptotic behaviour of the 'inner' free surface just after its appearance. Separation of compressible liquid from the surface of a rigid plate under its impact onto the liquid was described by Korobkin (1994). In this case the formation of the 'inner' free surface is due to relief wave interaction, which come from the periphery of the plate. For elastic-plate impact the pressure in the contact region can drop down to the limiting value owing to the plate flexibility, which reduce the local impact velocities. The numerical codes available to deal with the elastic plate impact is mainly to evaluate the plate deflection and the stress distribution in the plate but not the pressure distribution along the wetted area. Moreover, experiments on elastic plate impact indicate great scattering of the measured pressure which does not encourage us to treat the problem in a deterministic way. In order to evaluate the pressure on the contact region, it is suggested to proceed as follows: (i) determine the beam deflection and its velocity; (ii) evaluate the pressure from the hydrodynamic part of the problem taking the beam deformation as given and taking into account the singularity of the pressure close to the contact points. This approach makes it possible to distinguish low-pressure zones, where liquid can separate from the beam surface (see Korobkin (1996)). But a model to describe the initial stage of the liquid separation and the cavity evolution thereafter is still not available. This is a reason why at present the one-side inequality for the pressure cannot be incorporated into computer codes.

The one-side inequality for the surface elevation implies that the shape of the free surface has to be evaluated at every time step together with the beam deflection and we need to check that the free surface does not intersect the surface of the entering body. The moment  $t_*$ , when the free boundary of the liquid touches the body surface outside the contact region, has to be distinguished, and the scheme of the flow has to be changed at this instant of time. At this instant a new part of the contact region appears, which is started from the point of the first contact. These two parts of the contact region are separated by the cavity filled

with air. At stage where  $t > t_*$  the interaction between the body and the liquid continues but in presence of the cavity. This effect is similar to the air-cushion effect well-known in the impact theory but it has also its own peculiarities. Namely, at the moment of time, when the cavity has been formed, a part of body is already submerged in the liquid and the value  $t_*$  is determined by both the body deformations and the liquid flow at  $t < t_*$ .

This effect was discovered in the problem of wave impact onto an elastic beam at its edge. Parameters of the beam and the wave responsible for this effect were distinguished. In particular, the cavity formation was detected for impact of the wave with the initial radius of curvature at its top  $R = 10\text{m}$  at the velocity  $V = 3,5\text{m}$  onto the elastic plate of mild steel with its length  $2L$  and thickness  $h$  being  $1\text{m}$  and  $1\text{cm}$  respectively. The wave hits the plate from below at its left-hand side edge. The plate is assumed simply supported at its edges. Numerical calculations were performed within the framework of the Wagner approach with 5 and 10 "dry" modes of the beam taken into account. The numerical method was described by Khabakhpasheva and Korobkin (1997). In the case under consideration the shape of the free surface was controlled and it was revealed that the free surface touches the right edge of the plate when only about  $75\text{cm}$  of the plate is wetted. Therefore the initial dimension of the cavity is about  $15\text{cm}$ . The formation of the cavity is due to the strong interaction of the plate with the liquid. The plate deformations are not great but they are sufficient to decrease the rate of the contact region expansion so much that the beam edge touches the liquid surface before the whole plate is wetted.

There are two dimensionless parameters  $\alpha, \beta$ , which determine the peculiarities of elastic plate impact. Two regions in the plane of the parameters  $(\alpha, \beta)$ , where the Wagner approach fails, were distinguished without taking into account the one-side inequalities. In the first region, the size of the contact region is not monotonic function of time, which is prohibited by the classical Wagner theory. In the second region, the rate of the contact region expansion is unlimited, which indicates very high hydrodynamic loads. These loads cannot be described correctly with the incompressible liquid model and acoustic effects have to be taken into account. Within both regions the numerical calculations were performed using the numerical code described by Khabakhpasheva and Korobkin (1997). The second region of the parameters  $\alpha, \beta$  is of great interest because it distinguishes the impact conditions with very high loads. It should be noted that these loads are much higher than those for a rigid plate and are due to the plate flexibility. The high hydrodynamic loads increase the beam deflection and make it possible that the beam edge touches the liquid free surface well before the beam is totally wetted or the Wagner approach fails.

## 1 Formulation of the problem

Until the time moment  $t_*$  the problem of wave impact onto an elastic plate at its edge is solved within the framework of classical Wagner approach. At the next stage,  $t > t_*$ , the liquid flow and the beam deflection are governed by the following equations

$$\varphi_{xx} + \varphi_{yy} = 0 \quad (y < 0), \quad (1)$$

$$\varphi_y = -1 + w_t(x, t) \quad (y = 0, \quad 0 < x < c(t), \quad d(t) < x < 2), \quad (2)$$

$$\varphi = 0 \quad (y = 0, \quad x < 0, \quad x > 2, \quad c(t) < x < d(t)), \quad (3)$$

$$\varphi \rightarrow 0 \quad (x^2 + y^2 \rightarrow \infty), \quad (4)$$

$$p(x, y, t) = -\varphi_t(x, y, t), \quad (5)$$

$$\alpha \frac{\partial^2 w}{\partial t^2} + \beta \frac{\partial^4 w}{\partial x^4} = p(x, 0, t) \quad (0 < x < 2, \quad t > t_*), \quad (6)$$

$$w = 0, \quad w_{xx} = 0 \quad (x = 0, \quad x = 2), \quad (7)$$

$$w(x, t_*) = w_0(x), \quad w_t(x, t_*) = w_1(x) \quad (0 < x < 2, \quad t = t_*). \quad (8)$$

Here  $c(t)$  indicates the position of the left end of the cavity and  $d(t)$  the position of its right end. It is assumed that the air in the cavity is absent, which leads to the boundary condition  $\varphi = 0$ , where  $y = 0$ ,  $c(t) < x < d(t)$ . The function  $w_0(x)$  and  $w_1(x)$  are determined by the solution of the problem at the initial stage,  $0 < t < t_*$ . The shape of the elastic surface  $y_b(x, t)$  is given by  $y_b(x, t) = x^2/2 - t + w(x, t)$  in the both parts of the contact region,  $0 < x < c(t)$  and  $d(t) < x < 2$ . Condition (3) shows that outside the contact region,  $y = 0$ ,  $x < 0$ ,  $x > 2$  and  $c(t) < x < d(t)$ , the liquid particle can move only vertically. The function  $c(t)$  and  $d(t)$  are unknown in advance and have to be determined together with the liquid flow.

## 2 Hydrodynamic problem

The hydrodynamic part of the problem (1)-(4) provides the deformation of the free surface. In particular,

$$Y(x, 0, t) = \frac{1}{\pi W(x)} \left[ \int_0^c \frac{y_b(\tau, t) W(\tau)}{\tau - x} d\tau - \int_d^2 \frac{y_b(\tau, t) W(\tau)}{\tau - x} d\tau \right] + \frac{D(t)}{\pi W(x)}, \quad (9)$$

where  $c(t) < x < d(t)$ ,  $W(\tau) = \sqrt{\tau(c-\tau)(2-\tau)(d-\tau)}$  for  $0 < \tau < c(t)$  and  $d(t) < x < 2$ ,  $W(x) = \sqrt{x(x-c)(2-x)(d-x)}$ ,  $D(t)$  is an arbitrary function of time,  $X - iY$  is the analytical function of the complex variable  $z = x + iy$  in the lower half-plane,  $X(x, y, t)$  is the horizontal displacement of a liquid particle and  $Y(x, y, t)$  is its vertical displacement. The one-side inequality

$$Y(x, 0, t) < y_b(x, t) \quad (c(t) < x < d(t))$$

leads to the following two equations with respect to the unknown functions  $c(t)$  and  $d(t)$

$$\int_0^c y_b(\tau, t) \sqrt{\frac{\tau(2-\tau)}{(c-\tau)(d-\tau)}} d\tau - \int_d^2 y_b(\tau, t) \sqrt{\frac{\tau(2-\tau)}{(\tau-c)(\tau-d)}} d\tau = 0,$$

$$\int_0^c y_b(\tau, t) \sqrt{\frac{\tau(2-\tau)(d-\tau)}{c-\tau}} d\tau + \int_d^2 y_b(\tau, t) \sqrt{\frac{\tau(2-\tau)(\tau-d)}{\tau-c}} d\tau = D(t).$$

Differentiation of the last equations in time provides the system

$$a_{11}(c, d, t)\dot{c} + a_{12}(c, d, t)\dot{d} = b_1(c, d, t), \quad (10)$$

$$a_{21}(c, d, t)\dot{c} + a_{22}(c, d, t)\dot{d} = b_2(c, d, t) + \dot{D}(t). \quad (11)$$

Far away the contact region,  $|z| \rightarrow \infty$ , the asymptotic behaviours of the displacements and the liquid velocity are given as

$$X - iY \sim \frac{iD(t)}{\pi W(z)}, \quad \varphi_x - i\varphi_y \sim \frac{iC(t)}{\pi W(z)}$$

The asymptotic formulae imply

$$\dot{D} = C(t) \quad (12)$$

where dot stands for derivative in time. The value  $C(t)$  as function of  $c$  and  $d$  is determined by the condition that  $\varphi(x, 0, t) = 0$  where  $c(t) < x < d(t)$ .

### 3 Elastic problem

The beam deflection  $w(x, t)$  is sought in the form

$$w(x, t) = \sum_{n=1}^{\infty} a_n(t) \sin(\pi n x / 2),$$

Where the coefficients  $a_n(t)$  are satisfied the system, which follows from (5) and (6),

$$\frac{d\vec{a}}{dt} = (\alpha I + \kappa S)^{-1} (\beta D \vec{q} + \vec{f}), \quad \frac{d\vec{q}}{dt} = -\vec{a}. \quad (13)$$

Here  $\vec{a} = (a_1, a_2, a_3, \dots)^T$ ,  $\vec{q}$  is the vector  $\vec{q} = (q_1, q_2, q_3, \dots)^T$ ,  $q_n = (\beta \lambda_n^4)^{-1} (\alpha \dot{a}_n + b_n)$ ,  $\vec{f} = (f_1(c, d), f_2(c, d), f_3(c, d), \dots)^T$ ,  $I$  is the unit matrix,  $D$  is the diagonal matrix,  $D = \text{diag}\{\lambda_1^4, \lambda_2^4, \lambda_3^4, \dots\}$ .  $S = (S_{nm})_{n,m=1}^{\infty}$  is the matrix with the elements

$$S_{nm}(c, d) = \int_0^c \varphi_n(x, 0, c, d) \sin(\pi m x / 2) dx + \int_d^2 \varphi_n(x, 0, c, d) \sin(\pi n x / 2) dx,$$

where  $\varphi_n$  is the solution of the following boundary value problem

$$\begin{aligned} \Delta \varphi_n &= 0 \quad (y < 0) & \varphi_n &= 0 \quad (y = 0: x < 0, c < x < d, x > 2) \\ \frac{\partial \varphi_n}{\partial y} &= \sin(\pi n x / 2) \quad (y = 0: 0 < x < c, d < x < 2) \end{aligned}$$

The initial conditions for the system (10)-(13) are

$$\vec{a} = 0, \quad \vec{q} = 0, \quad c = c_*, \quad d = 0 \quad (t = t_*). \quad (14)$$

The initial-value problem (10)-(14) is solved numerically by the fourth-order Runge-Kutta method with uniform step  $\Delta c$ . The variable  $c$  was chosen as independent variable instead of time  $t$ .

### 4 Numerical results

The calculations were performed for  $\alpha = 0.157, \beta = 0.03$ , with 2, 5 and 10 modes. The presence of air in the cavity is not taken into account. It was found that the cavity is very thin and localized near the right edge of the plate. The hydrodynamic pressures during the cavity collapse are very high but are of short duration. Main effect of the high pressures is on the stresses, which grow significantly close to the edge. It was revealed that the value  $t_*$  has to be evaluated very precisely to make the numerical scheme stable. This condition is not easy to fulfil. But it was proved that system (10), (11) provides  $\dot{d}(t_*) = 0$ . Therefore, in order to make the scheme stable, we can keep  $\dot{d}(t) = 0$  at several initial steps in time. The equality  $\dot{d}(t_*) = 0$  demonstrates that we cannot consider the impact of the right edge of the beam onto free surface independently on the total geometry of the beam even just after the impact occurs. This conclusion shows that "local effects" have to be treated very carefully and that our intuition can give us wrong ideas.

#### References

- Korobkin A. A.** Low-pressure zones under a liquid-solid impact // Bubble Dynamics and Interface Phenomena, Kluwer Academic Publishers, Netherlands, 1994. P. 375-381.
- Korobkin A. A.** Wave impact on the centre of an Euler beam // J.Appl.Mech.Tech.Phys. 1997 (In press).
- Khabakhpasheva T.I., Korobkin A.A.** Wave impact on elastic plates // Proc.12th Intern. Workshop on Water Waves and Floating Bodies, Carry-le-Rouet, France, 1997. P. 135-138.

# A Finite-Depth Unified Theory of Ship Motion

Yonghwan Kim, P.D. Sclavounos  
Massachusetts Institute of Technology

## 1 Introduction

In deep water strip theory has been refined to the unified theory of [1][2]. There are not many studies on the slender-body seakeeping in finite depth problem. In the present study, a new slender-body theory is introduced as the extension of unified theory to the finite-depth radiation problem with zero speed. Borresen[3] formulated a finite depth unified theory with forward speed, and he wrote the kernel of integral equation as the double integral in the Fourier domain. However, he was not successful to get the hydrodynamic coefficients or motions. In the present study, the series form of the kernel is derived, and the ship motion RAO is obtained. The computation extends to the second-order mean drift forces following the same idea of Kim & Sclavounos[4]. The results are compared with WAMIT's.

## 2 Theoretical Background

### 2.1 The Far-Field Solution

The far-field solution of heave and pitch motion is written as a distribution of the three-dimensional Green function  $G_{3D}$  along the center line of a ship.

$$\phi(x, y, z) = \int_L q(\xi) G_{3D}(\xi - x, y, z) d\xi = \frac{1}{2\pi} \int_{-\infty}^{\infty} du e^{iux} q^*(u) G^*(u; y, z) \quad (1)$$

where  $q(\xi)$  is the strength of Green function and

$$G^*(u; y, z) = -\frac{1}{2\pi} \int_{-\infty}^{\infty} dv e^{ivy} \frac{\cosh\{\sqrt{u^2 + v^2}(z+h)\}}{\cosh\{\sqrt{u^2 + v^2}h\}[\sqrt{u^2 + v^2} \tanh\{\sqrt{u^2 + v^2}h\} - \frac{\omega^2}{g}] } \quad (2)$$

The superscript \* means the Fourier transform, and  $G^*(u; y, z)$  recovers the infinite depth case of Ogilvie and Tuck when  $h \rightarrow \infty$ . When  $y$  is very small, this can be approximated as

$$\phi(x, y, z) \approx q(x) G_{2D}(y, z) + \int_L q(\xi) f(\xi - x, 0, 0) d\xi \quad (3)$$

with  $f^*(u; y, z) = G^*(u; y, z) - G^*(0; y, z) = G^*(u; y, z) - G_{2D}(y, z)$ .

### 2.2 The Near-Field Solution

The velocity potential of the near-field solution is written as the sum of a homogeneous solution  $\phi_H$  and a particular solution  $\phi_P$ .

$$\phi(x, y, z) = \phi_P(x, y, z) + C(x)\phi_H(x, y, z) \quad (4)$$

Adopting the same concept with the deep water theory, the outer expansion of the near-field solution can be written as

$$\phi(x, y, z) = \{\sigma(x) + C(x)[\sigma(x) + \bar{\sigma}(x)]\}G_{2D}(y, z) - C(x)\bar{\sigma}(x)[G_{2D}(y, z) - \bar{G}_{2D}(y, z)] \quad (5)$$

with

$$G_{2D}(y, z) - \bar{G}_{2D}(y, z) = 2i \frac{\cosh\{m_o(z+h)\}}{\cosh(m_o h)} \frac{m_o h}{\nu h + (\frac{m_o h}{\cosh(m_o h)})^2} \cos(m_o y) + O(\frac{1}{y}) \quad (6)$$

where  $\sigma(x)$ ,  $\bar{\sigma}(x)$  are the sectional strength and its complex conjugate of the two-dimensional Green function,  $G_{2D}$ . These can be obtained after solving the two-dimensional boundary value problem at each section. Besides,  $\nu = \frac{\omega^2}{g} = m_o \tanh(m_o h)$ .

### 2.3 Matching

Two matching conditions can be founded from Eq.(3) and (4), and an integral equation is derived from them.

$$q(x) + \frac{\nu h + (\frac{m_o h}{\cosh(m_o h)})^2}{2im_o h} [1 + \frac{\sigma(x)}{\bar{\sigma}(x)}] \int_L q(\xi) f(\xi - x, 0, 0) d\xi = \sigma(x) \quad (7)$$

This integral is the most important key in unified theory. To check the consistency of this integral equation with that of infinite depth, the kernel of the integral should be studied in more detail.

### 2.4 The Kernel of Integral Equation

The Fourier transformation of the kernel is written as follows:

$$\begin{aligned} f^*(u; y, z) &= G_{3D}^*(u; y, z) - G_{2D}(y, z) \\ &= -\frac{1}{2\pi} \int_{-\infty}^{\infty} dv e^{iv y} \left[ \frac{\cosh\{\sqrt{u^2 + v^2}(z+h)\}}{\cosh\{\sqrt{u^2 + v^2}h\}[\sqrt{u^2 + v^2}\tanh\{\sqrt{u^2 + v^2}h\} - \nu]} \right. \\ &\quad \left. - \frac{\cosh\{|v|(z+h)\}}{\cosh(|v|h)[|v|\tanh(|v|h) - \nu]} \right] \end{aligned} \quad (8)$$

The contour integral and inverse Fourier transformation lead to the series form of the kernel when  $(y, z) \rightarrow (0, 0)$ ,

$$\begin{aligned} f(x, 0, 0) &= \frac{1}{2\pi} \int_{-\infty}^{\infty} f^*(u; 0, 0) e^{iux} du \\ &= \frac{i}{2} \frac{m_o^2}{m_o^2 h - \nu^2 h + \nu} \{-iY_o(m_o x) + J_o(m_o x) - \frac{2}{m_o} \delta(x)\} \\ &\quad - \sum_{n=1}^{\infty} \frac{m_n^2}{m_n^2 h + \nu^2 h - \nu} \left\{ \frac{1}{\pi} K_o(m_n x) - \frac{1}{m_n} \delta(x) \right\} \end{aligned} \quad (9)$$

where  $-\nu = m_n \tan(m_n h)$ . The  $\frac{1}{r}$  singularity of the three-dimensional Green function cancels out with the logarithmic singularity of the two-dimensional Green function when it is integrated with respect to  $x$ . Also the Bessel function has a logarithmic singularity which is integrable. Fig.1 shows the Fourier-transformed kernel of the integral equation, and the kernel for finite depth approaches that of infinite depth as the depth becomes large.

## 2.5 Hydrodynamic Coefficients and Motions

The three dimensional correction terms on the added mass and damping coefficient can be added when the integral equation is solved [1][2]. To compute the wave excitation forces and moments, the far-field formula is applied in the present study [4]. Unified theory is applicable to heave-pitch coupled motion, but the finite-depth strip theory has to be used for sway-yaw-roll coupled motion.

## 2.6 The Second-Order Mean Drift Forces

The finite-depth mean drift forces and moment on surge, sway and yaw direction are computed using the formula in [5]. In particular, when there is no external work on a body, the formula which is positive definite provides more accurate results.

## 3 Computational Results

Fig.1 shows the added mass and damping coefficient of the heave motion. The ship model is a mathematical hull of parabolic shape. The beam(B) and length(L) ratio of hull is 0.15, and the draft(T) and length ratio is 0.1. As expected, unified theory is in very good agreement with WAMIT, especially in low frequency range. Fig.2 shows the wave excitation force for heave. The agreement with WAMIT is also favorable. Fig.3 shows the motion RAO of heave and pitch. It is interesting that the result of strip theory is not bad at low frequencies although strip theory is not accurate for the hydrodynamic coefficients. It is because the dominant force for motion at low frequency comes not from the mass and damping but the restoring force Fig.4 shows the longitudinal mean drift force at head sea. In order to get an accurate value of this parameter, the accurate computation of the Kochin function, i.e. the velocity potential, is essential as well as the motion RAO. Therefore Fig.4 indicates the accuracy of all solutions in the linear problem. As expected, unified theory provides the closer result to WAMIT than strip theory.

## 4 Acknowledgement

This work is supported by the Joint Industry Project, SWIM, at MIT.

## References

- [1] J.N. Newman, 1978, *The Unified Theory of Ship Motions*, Advances in Applied Mechanics, Vol.18
- [2] P.D. Sclavounos, 1981, *The Interaction of an Incident Wave Field with a Floating Slender Body at Zero Speed*, Proc. of the 3rd Int. Conf. on Numerical Ship Hydrodynamics
- [3] R. Borresen, 1984, *The Unified Theory of Ship Motions in Water of Finite Depth*, PhD Thesis, The Norwegian Institute of Technology
- [4] Y. Kim, and P.D. Sclavounos, 1996, *The Computation of the Second-Order Hydrodynamic Forces on a Slender Ship in Waves*, WWWFB'96
- [5] C.C. Mei, 1983, *The Applied Dynamics of Ocean Surface Waves*, Wiley Press

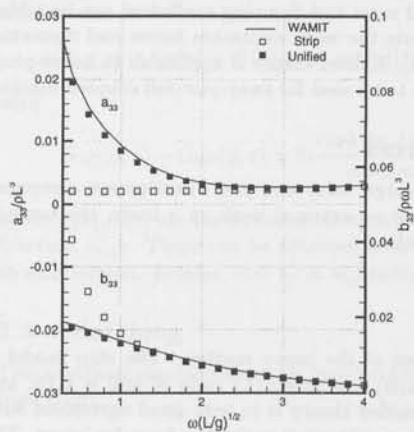


Figure 1: Added-Mass and Damping Coefficient : Heave,  $h/T=1.25$

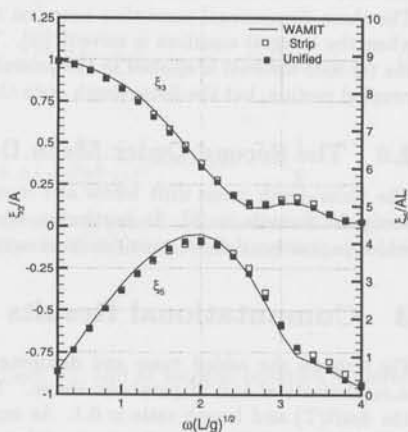


Figure 3: Motion RAO : Heave and Pitch, Head Sea,  $h/T=1.25$

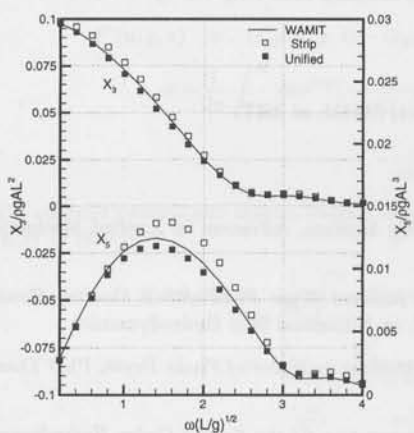


Figure 2: Wave Excitation : Heave and Pitch, Head Sea,  $h/T=1.25$

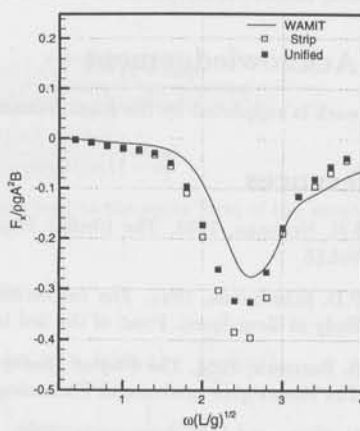


Figure 4: Longitudinal Mean Drift Force : Head Sea,  $h/T=1.25$

## Long time evolution of gravity wave systems

M. LANDRINI\*, O. OSHRI<sup>+</sup>, T. WASEDA<sup>+</sup> AND M. P. TULIN<sup>+</sup>  
\* INSEAN, Rome, Italy      + Ocean Engineering Lab, UCSB

### Introduction

Four main avenues for the non-linear prediction of conservative wave evolution exist: kinetic equations, the narrow banded cubic PDE of Schrödinger type (called here NLS), NLS plus (Dysthe), fully non-linear computational (FNL). The first three comprise the weakly non-linear family, based on truncation of expansions beyond third order in wave steepness,  $ka$ . Dysthe corrects a crucial shortcoming of the NLS, which predicts only symmetric wave envelopes. They are both derivable from kinetic equations. The latter permits evolution in both horizontal dimensions on the free surface and it is inherently free of narrow banded assumptions. It does, however require a pre-selection of the pertinent modes, a critical process. The preferred form of the kinetic equations which originated with Hasselman (1962) and Zakharov (1968), is that of Krasitskii (1994) preserving the Hamiltonian form of the free surface problem, discovered by Zakharov. These important Krasitskii equations have hardly been applied. Neither have these four major methods been previously compared with each other systematically, or with experiments. This was our purpose.

Recently at the OEL-UCSB we have carried out systematic experiments in a large wave tank<sup>1</sup> (50 m l, 4.2 m w, 2.1 m d) on the evolution of a carrier wave seeded with side bands, Tulin & Waseda (1997), as well as analytical-computational studies of evolution using various avenues, including Krasitskii (Oshri, 1996)

Meanwhile one of us (ML) has implemented a high resolution fully non-linear calculation method based on boundary integral equations. The method adopts the particular Eulerian-Lagrangian approach of Dold and Peregrine (1986). A significant speed up of the computations is obtained by coupling the spectral convergence properties of the Euler-Mclaurin quadrature formula with a fast summation multipole expansion technique allowing for an  $\mathcal{O}(N \log N)$  operation count and an  $\mathcal{O}(N)$  storage requirement. This development allows for the high resolution prediction of wave trains with  $\mathcal{O}(10^2)$  waves.

Here, in collaboration, we present some of our first results showing comparisons of the evolution of a system beginning as a carrier wave plus small closely spaced side-bands,  $(\omega_c \pm \delta\omega)$ , which begins as a Benjamin-Feir instability. Four different methods are used: FNL, Krasitskii, NLS; Dysthe. In particular, Krasitskii's four-waves reduced equations for discrete wave systems (Krasitskii, 1994) are solved and, for the first time using this model, the evolution of an arbitrary number of wave components is allowed for. More specifically, in the computations shown below, the number of waves is always large enough to achieve the invariance of the results under further refinement (in most of the computations at least 24 equally spaced wave components are used).

With FNL as a benchmark, the rank order of performance was: Krasitskii, Dysthe, NLS. The success of Krasitskii is due to the large number of waves allowed for: by reducing the number of waves Krasitskii fails and, eventually, NLS-like results are recovered.

### Results

The experiments, covering a range of  $ka_c$  and of  $\delta\omega$ , followed the evolution of a carrier plus seeded sidebands over about one cycle of modulation, usually ending in breaking (cfr. fig. 1). The lower sideband,  $-\delta\omega$ , always grew relative to the upper one,  $+\delta\omega$ , in contrast to well known results based on NLS but as predicted by Krasitskii (with a number of waves large enough) and Dysthe.

In particular, this behaviour is numerically studied for  $ka_c = 0.1$  (upper plot in fig. 2) where FNL, Krasitskii, Dysthe and NLS spectra are contrasted. The excellent performance of Krasitskii in predicting even the waveforms can be appreciated in the lower diagram.

The energy was markedly discretized in the experiments, with a spreading toward higher frequency modes, both free and bound. Only after breaking was widening of the major spectral peaks noticeable, probably due to breaking. This consistent discretization in the first cycle validates the kinetic equation approach, which considers only modes capable of interaction in the conservative theory of interaction. Breaking first occurs at a small value of  $ka_c$ , near 0.1, as observed in Su & Green (1985) and in the ocean.

<sup>1</sup>The OEL wavemaker is of plunging hydraulic type, computer controlled, designed and built-in-house and featuring an innovative plunger design

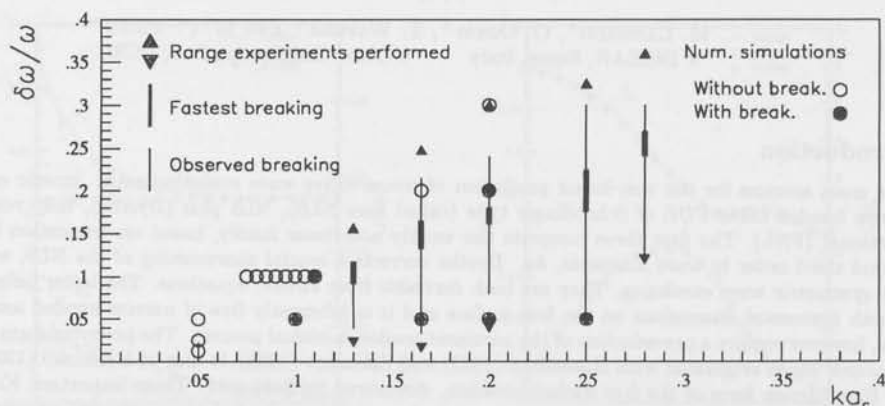


Figure 1: Summary of the experiments [4] and of the numerical computations performed. The experimental area where breaking events are observed is denoted by thin lines. Thicker lines indicate intense breaking close to the wave maker. Circles refer to numerical computations.

In the present computations, as breaking conditions are approached, differences appear in the predictions of weakly and fully non-linear methods. In particular, with small changes in  $ka_c$  the relative performance of Krasitskii, best of the weakly non-linear models, rapidly deteriorates in the second cycle of modulation (cfr. figures 3-4). We speculate that this is because, due to the weakly non-linear assumption, Krasitskii is unable to take into account the strong non-linearity at peak modulation that alters the energy exchange among wave modes, albeit in small quantity.

The high resolution of FNL is evidenced by its ability to follow waves through deformation to breaking; in figure 5,  $ka_c = 0.11$ , we note that the appearance of two simultaneous breakers may be very unusual. The general ability of FNL to predict the onset of breaking is shown by comparison with experiments (cfr. fig. 1). Clearly the FNL can prove very useful in the further study of evolution and breaking. The further development of Krasitskii may also prove worthwhile, as its use can be extended to two surface dimensions. In the long run, unfortunately, the use of any of these methods, even in one dimension, will fail after breaking. The experiments here clearly showed that breaking radically changes the evolution of the wave system. There have been attempts to deal with this using weakly non-linear theory, but no predictions have yet been tested by experimental comparison.

## References

1. HASSELMAN, K. On the nonlinear energy transfer in a gravity wave spectrum *J. Fluid Mech.* 12:481-500, 1962
2. ZAKHAROV, V.E. Stability of periodic waves of finite amplitude on the surface of deep fluid, *J. Appl. Mech. Tech. Phys.* 2: 190-194, 1968.
3. KRASITSKII, V.P. On reduced equations in the Hamiltonian theory of weakly nonlinear surface waves, *J. Fluid Mech.* 272: 1-20, 1994.
4. TULIN, M.P. AND WASEDA, T. Laboratory observations of wave group evolution, including breaking effects, OEL TR 97-160, submitted to *J. of Fluid Mech.*, 1997.
5. OSHRI, O. Theoretical study of the non-linear wave system, PhD dissertation thesis, University of California at Santa Barbara, 1996.
6. DOLD, J.W. AND PEREGRINE, D.H., Water-wave modulation., *Coast. Eng.*, 1986.
7. SU, M.Y. AND GREEN, A.W., Wave breaking and non-linear instability coupling in *The Ocean Surface* (Toba & Mitsuyasu eds.), 1985.

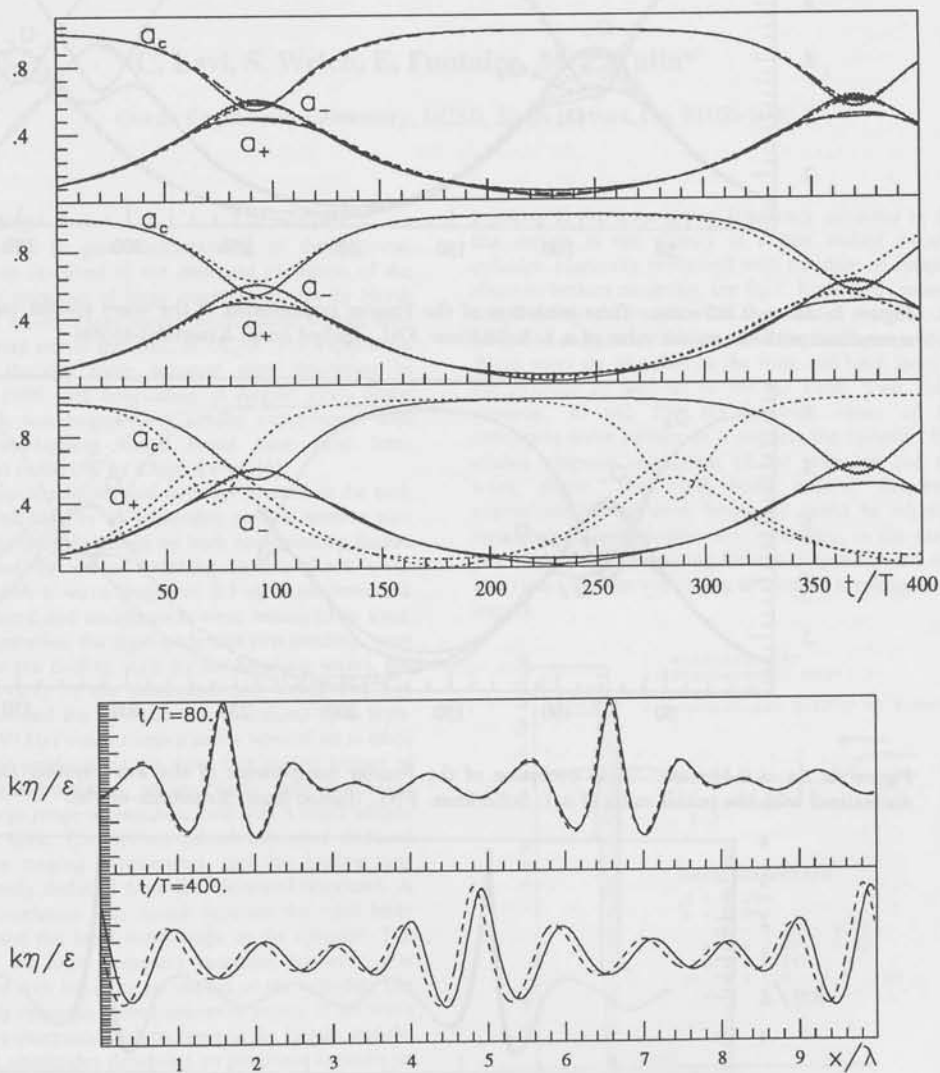


Figure 2:  $ka = 0.10$ -case. Top: time evolution of the Fourier components (amplitudes are normalized with the initial value of  $a_c$ ); from top down the FNL solution (solid lines) is contrasted with weakly non-linear predictions (dashed lines): Krasitskii-model (upper), Dysthe equation (middle) and non-linear Schrödinger equation. Bottom: wave patterns at the first (upper) and second (lower) maximum of the modulation cycle; FNL: solid lines, Krasitskii-model: dashed-lines.

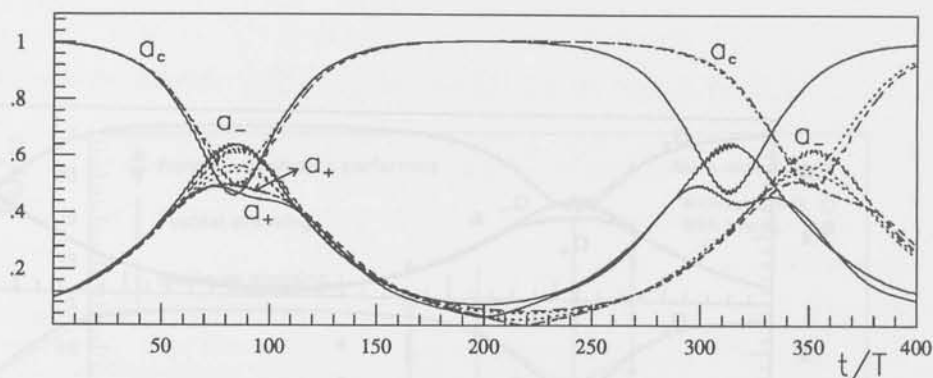


Figure 3:  $ka = 0.105$ -case. Time evolution of the Fourier components of the wave system (amplitudes are normalized with the initial value of  $a_c$ ). Solid lines: FNL, dashed lines: Krasitskii-model

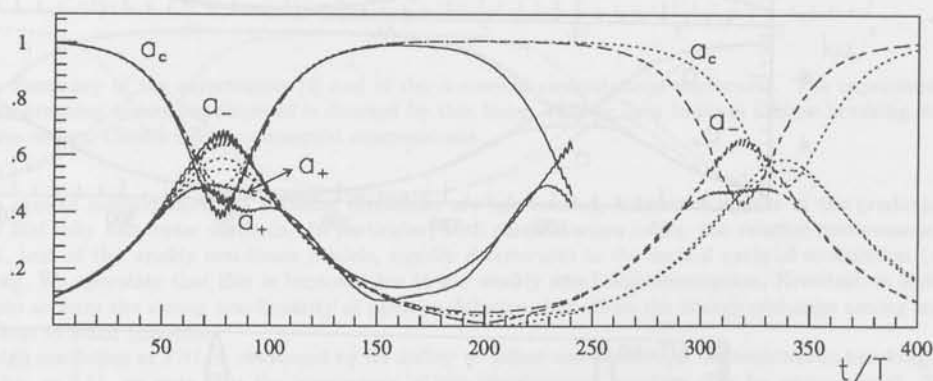


Figure 4:  $ka = 0.11$ -case. Time evolution of the Fourier components of the wave system (amplitudes are normalized with the initial value of  $a_c$ ). Solid lines: FNL, dashed lines: Krasitskii-model.

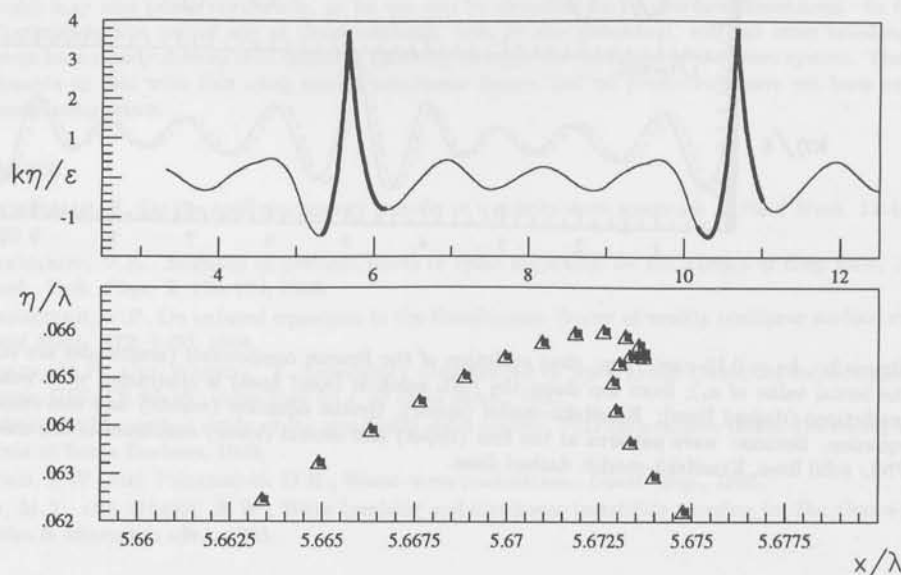


Figure 5: Final stage in the evolution of a perturbed wave train of initial steepness  $ka = 0.11$ . In the lower diagram the two plunging breakers are superimposed by translation and plotted in natural scale.

## Experiments on the Ringing Response of an Elastic Cylinder in Breaking Wave Groups

C. Levi, S. Welch, E. Fontaine, M. P. Tulin\*

Ocean Engineering Laboratory, UCSB, Santa Barbara, CA 93106-1080

### Summary

In order to gain understanding of the physical mechanism involved in the observed excitation of the structural response of large ocean structures by North Sea wind waves, experimental hydroelastic studies have been carried out in the OEL at UCSB. The experiment evolved through three separate tests beginning in October 1996, and concluding in August 1997. Since this work was begun very similar experiments with results overlapping those found here have been conducted in the UK by Chaplin et al. [1].

A thin-walled vertical cylinder pivoted at the tank bottom and held by an adjustable vertical tension wire was subjected to loadings by both non-breaking Stokes waves and by waves breaking in modulated wave groups, with a wave length of 2.3 m. Both down-tank displacement and acceleration were measured in time. Two frequencies, the rigid body and first bending, were excited in the ringing style by the breaking waves, but not observably by the monochromatic waves. The free surface around the cylinder was visualized by a high-speed (250 Hz) video camera and a vertical jet is often seen to be produced at the front face during impact of the deformed-breaking waves. Tests were conducted over a large range of variables, and only a small sample is given here. The system parameters were deduced from free ringing experiments, and the loading was subsequently deduced from the measured responses. A strong correlation was found between the rigid body loading and the local wave slope at the cylinder. The onset of the high frequency response, however, was correlated with breaking jet impact on the cylinder. The rigid body response at frequencies in excess of the wave frequency decreased with increase in the former, and the response amplitudes depended on the phase between jet initiation and impact of the wave on the cylinder. In general, the highest loads were obtained when the plunging jet impacted the cylinder. Accelerations as large as 0.25g were measured.

### The Experiments

Experimental techniques continuously evolved through a series of three different tests beginning in 1996. The present experiments were carried out during August 1997 in the large OEL wind-wave tank [150' L, 14' W, 8' D] using seeded side-bands [2,4], to generate groups of 2.3m waves, with initial steepness,  $ak_0$ , between 0.12 and 0.28. Periodic deformation and

breaking at the wave group frequency occurred in the test section in the vicinity of a thin walled circular cylinder, elastically restrained with freedom of rotation about its bottom mounting, see fig.1. Rigid body motion and bending deformation of the elastic cylinder are measured using accelerometer and displacement probes. Wave wires are disposed on the front and back faces of the cylinder as well as in the far field. Two video cameras, 30 and 250 Hz, provide views of the deforming wave surface as it impacts the cylinder; this allows temporal correlation of the response and the wave shape. The rigid body natural frequency normalized by the wave frequency could be adjusted through the upper tension wire mounting, in the range 1.5 - 5.5; and high bending flexural frequency, 20, was also typically observed during deforming breaking wave impact.

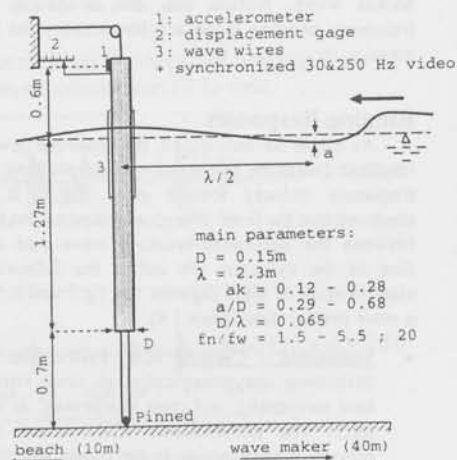


Figure 1: Experimental set-up.

### Monochromatic Response vs. Wave Groups

In tank tests with irregular waves, it has previously been reported, [3], that a correlation exists between ringing responses and impact by deformed breaking waves in wave groups. On the other hand, several studies have attempted to find the source of ringing response solely within the high frequency structure of Stokes waves. It was the chief purpose of these tests to compare monochromatic and wave group response in

\* To contact the authors: + 805-893-4937 ; mpt@vortex.ucsb.edu

order to clarify the physical cause of ringing, and the set-up described above is well able to do this. The loading is well in the inertial range (wave amplitude / cylinder diameter < 0.70 here), and the response in Stokes waves was found to be highly periodic and linear in the peak values up to the highest steepnesses tested,  $ak_0=0.28$ . Despite this linearity, the effect of harmonics on the temporal response is evident, see Figure 2a. For all rigid body frequencies tested, there was no clear evidence of "ringing" type behavior during the Stokes wave loading, i.e. suddenly large response decaying in time, until the next excitation. On the other hand, ringing responses were highly noticeable during loading in breaking wave groups, the excitation clearly originating during impact by the deformed or breaking wave, see fig. 3, but not in the other, smaller waves in the group. The period of ringing response is thus the period of the wave group, in this case six times the wave period. The temporal response for a discrete ringing event is shown in fig. 2b, where the height of the breaking wave just before 105s was chosen identical to the height of the Stokes wave with which it is compared, fig. 2a. The peak displacement is about twice those in the Stokes waves and the peak accelerations over 5 times as great. These factors would be even larger had the comparison been made with a wave group of the same time-averaged energy density as for the Stokes wave. Notice, too, the excitation of high frequency bending mode accelerations by the breaking wave.

### Ringling Responses

As might be anticipated, the observed level of the response increases as the normalized pitching resonant frequency reduces toward unity, fig. 3. It is also observed that the level of response depends on the phase between the deforming-breaking wave and the front face of the cylinder. We utilize the following brief classification of wave regimes, see fig. 5 and 6, based on a more precise description [4]:

- **Steepening - Cresting (CR, ECR).** The wave is deforming asymmetrically, its crest rising, front face steepening, and crest sharpening, as shown in fig. 5. The nomenclature (CR) means that this process is culminating in the immediate vicinity of the front face of the cylinder; (ECR) means that the process has not yet culminated there, but will before the crest reach the rear face of the cylinder.
- **Plunging Jet (JT).** A jet has formed at the crest of the deformed wave and is moving forward and downward, see fig. 6, while impacting the front face of the cylinder.
- **Splashing - Ploughing (SP).** The plunging jet has splashed into the front face of the wave, throwing water upwards as it ploughs forward and strikes the cylinder.

As shown in fig. 3, waves impacting during the plunging jet phase (JT) usually produce the highest response, for all natural frequencies; during the evolution of the breaking wave, the free surface becomes vertical in this regime.

### Wave Loads

Data from an example of a jetting breaker impacting the cylinder are presented in fig. 4a-c, showing, respectively, the displacement, acceleration, and wave induced moment. The latter, fig. 4c, has been deduced from the response data using a linear response equation of the mass-spring type; the added mass, damping, and restraint stiffness were determined from free oscillation tests in water, at the structural resonant frequency. The wave elevation measured at the front (#1) and the back (#2) of the cylinder are also shown in fig. 4d; their difference, which is proportional to the local wave slope at the cylinder is denoted by #3 in the same figure.

It is remarkable to note that the variation of the hydrodynamic moment on the cylinder, fig. 4c, is highly correlated with the local wave slope there, as measured by the cylinder mounted wave wires. This is simply seen by comparing the time at which both the peak hydrodynamic moment and its zero are reached, with the same times for the wave height difference. Perhaps this new experimental correlation can be used in the development of a useful engineering theory for the prediction of ringing loads in this frequency range. Incidentally, the same correlation between transverse loading and wave slope is predicted by Morison's formula when applied to cylinder wave loadings in waves of small steepness.

The excitation of the high frequency bending mode is indicated by the vertical arrows in fig. 4b-c, and this seems closely to coincide with a very rapid change in the slope of the longitudinal displacement of the system, i.e. to a "discontinuity" in the velocity. The equations of motion show that this requires the application of an impulse in momentum applied to the cylinder. The timing of this event indicates that the source of this impulse was the impact of the jet itself on the cylinder surface.

### References

- 1- Chaplin, J.R.; Rainey, R.C.T.; Yemm, R.W.- Ringing of a Vertical Cylinder in Waves- to be published.
- 2- Tulin, M.P.; Yao, Y.; Wang, P.- The Simulation of the Deformation and Breaking of Ocean Waves in Wave Groups- BOSS'94, Boston- Ma, 1994.
- 3- Davies, K.B., Leverette S.J., Spillane M.W., Ringing Response of TLP and GBS platforms, BOSS'94, Boston- Ma, 1994.
- 4- Tulin M.P. & Waseda T., Laboratory Observations of Wave Group Evolution Including Breaking Effects, 1997, submitted to JFM.

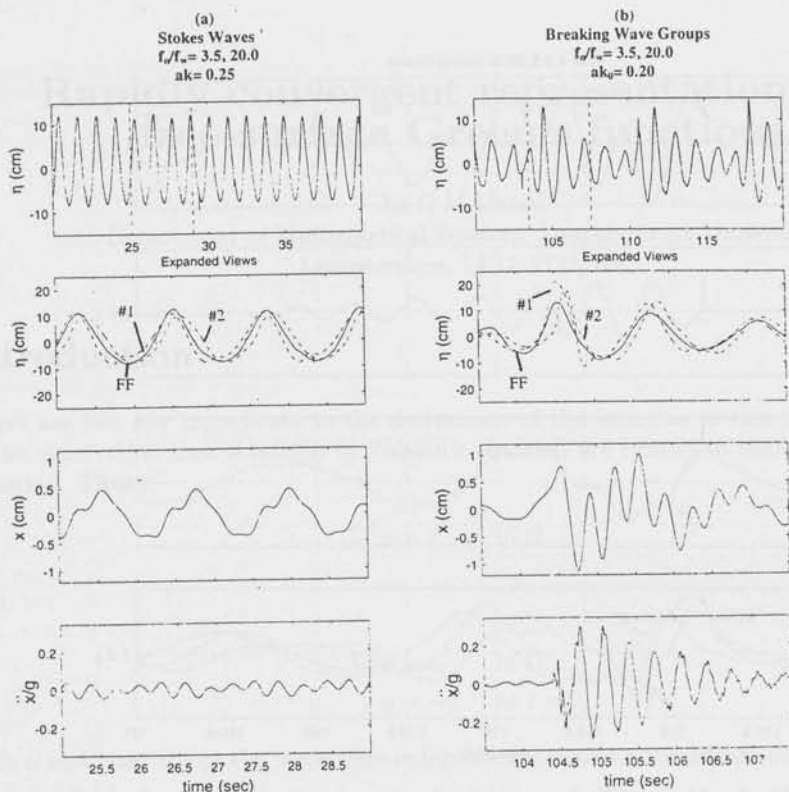


Figure 2: Displacement ( $x$ ) and Acceleration ( $\ddot{x}$ ) Responses Due to Stokes Waves (a) and Breaking Wave Groups (b).  $\eta$ , free surface elevation; #1 cylinder front; #2 cylinder rear; FF far field.

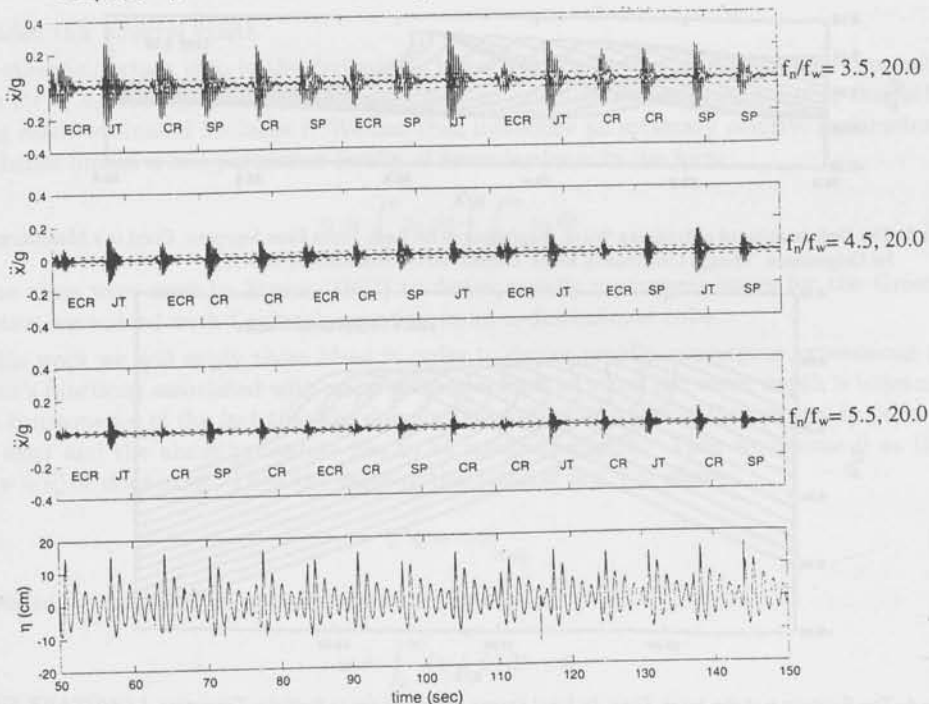


Figure 3: Acceleration Records Showing Ringing Responses Due to Breaking Wave Groups.

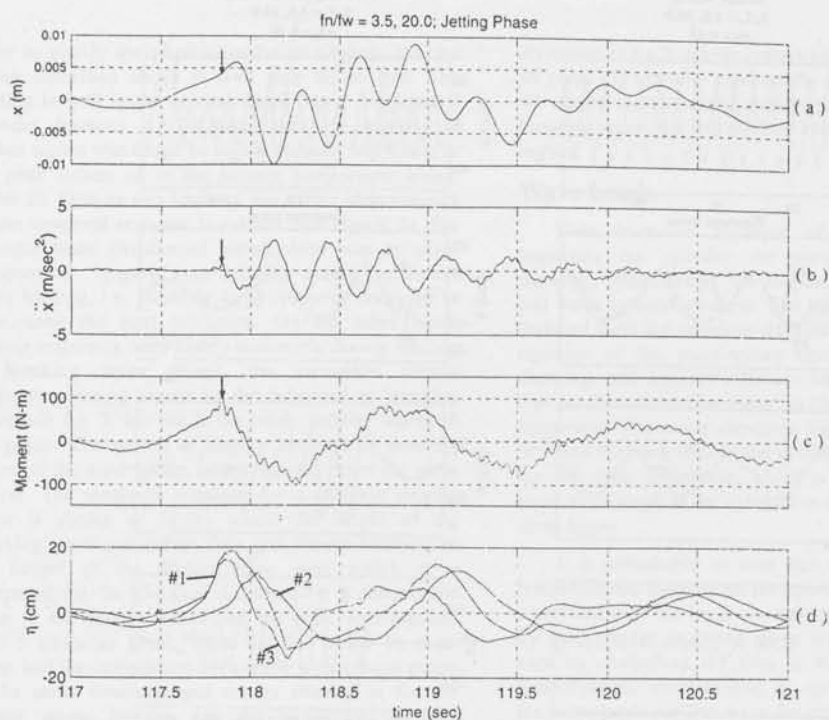


Figure 4: Moment (c) Based on Measured Displacement,  $x$ , (a) and Acceleration,  $\ddot{x}$ , (b). Free Surface Elevation,  $\eta$ , (d) as Measured on the Cylinder Front Face (#1), Cylinder Back Face (#2) and their Difference (#3).

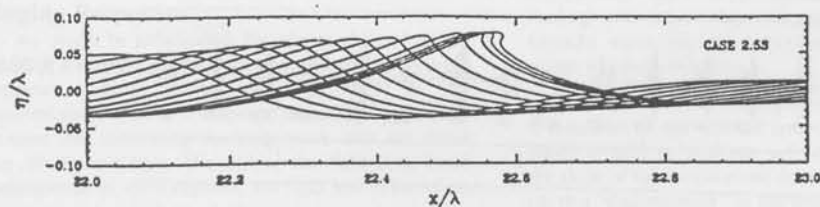


Figure 5: The Deformation of a Breaking Wave, Beginning at far Left. Front Face Steepens. Crest is a Maximum Near Jet Origination. Trough Continually Rises. LONGTANK Simulation (from [2]).

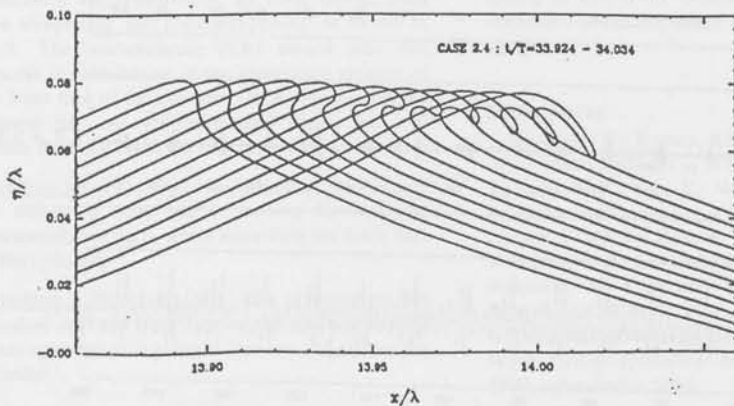


Figure 6: The Evolution of the Jet in Time. In Final Stages, Particles are in Ballistic Trajectory. LONGTANK Simulation (from [2]).

## Rapidly convergent representations for free-surface Green's functions

by C M Linton

Department of Mathematical Sciences, Loughborough University,  
Leicestershire, LE11 3TU, UK

### Introduction

There are two key ingredients to the derivations of the formulas in this paper. The first is the observation that solutions to Poisson's equation are related to solutions of the heat equation. Thus if

$$\nabla^2 u = f \quad \text{in } \Omega \quad (1)$$

and

$$\nabla^2 v = v_t \quad \text{in } \Omega, \quad (2)$$

$$v = -f \quad \text{at } t = 0, \quad (3)$$

with  $u$  and  $v$  satisfying the same time-independent boundary conditions on  $\partial\Omega$ , then

$$u = \int_0^\infty v \, dt, \quad (4)$$

provided this integral exists.

The other important step in the derivations below is to find two complementary representations for  $v$ ,  $v_1$  and  $v_2$ , the first of which is easy to calculate for small values of  $t$ , the latter being easily evaluated for large  $t$ . We can then introduce an arbitrary positive parameter  $a$  and hence obtain a one-parameter family of formulas for  $u$  in the form

$$u = \int_0^a v_1 \, dt + \int_a^\infty v_2 \, dt. \quad (5)$$

These ideas were used by Strain (1992) to derive rapidly convergent series for the Green's function associated with Laplace's equation in an  $n$ -dimensional cube.

In this work we will apply these ideas in order to derive rapidly convergent expressions for Green's functions associated with water-wave problems in which the water depth is constant. One consequence of the fact that the domain  $\Omega$  is unbounded is that the integral in (4) does not exist and the above procedure has to be modified slightly. Thus we choose  $\tilde{v}$  so that  $\int_0^\infty (v + \tilde{v}) \, dt$  does exist. Then the value of this integral is  $u + \tilde{u}$  where

$$\nabla^2 \tilde{u} = -\tilde{v} \Big|_{t=0}. \quad (6)$$

Provided we can solve this equation we then have

$$u = \int_0^\infty (v + \tilde{v}) \, dt - \tilde{u}. \quad (7)$$

## New representations for free-surface Green's functions

We will use the following definitions:

$$\begin{aligned} r &= [x^2 + y^2 + (z - \zeta)^2]^{1/2}, & r' &= [x^2 + y^2 + (2h + z + \zeta)^2]^{1/2}, \\ R &= [x^2 + y^2]^{1/2}, & \rho &= [x^2 + (z - \zeta)^2]^{1/2}, & \rho' &= [x^2 + (2h + z + \zeta)^2]^{1/2}, \\ \chi_n^{(1)} &= 2nh - \zeta - z, & \chi_n^{(2)} &= 2nh - \zeta + z, \\ \chi_n^{(3)} &= 2nh + \zeta - z, & \chi_n^{(4)} &= 2nh + \zeta + z. \end{aligned}$$

The exponential integral,  $E_1(x)$ , the incomplete Gamma function,  $\Gamma(a, x)$  and the complementary error function  $\text{erfc}(x)$  will also be used.

### Two dimensions

We consider the two-dimensional fluid domain  $-\infty < x < \infty$ ,  $-h < z < 0$  with the undisturbed free surface being  $z = 0$  so that the Green's function representing an oscillating point source at  $x = 0$ ,  $z = \zeta$  is  $\text{Re}(G \exp\{-i\omega t\})$  where  $G$  is the solution to

$$\nabla_{xz}^2 G = \delta(x)\delta(z - \zeta) \quad -h < z < 0, -h < \zeta < 0, \quad (8)$$

$$G_z = KG \quad \text{on } z = 0, \quad (9)$$

$$G_z = 0 \quad \text{on } z = -h, \quad (10)$$

and we require  $G$  to behave like outgoing waves as  $|x| \rightarrow \infty$ .

Numerous representations exist for this Green's function. In particular we have the eigenfunction expansion

$$G = - \sum_{m=0}^{\infty} \frac{\cos \mu_m(z+h) \cos \mu_m(\zeta+h)}{2\mu_m N_m} e^{-\mu_m|x|}, \quad (11)$$

where  $\mu_m$ ,  $m \geq 1$  are the positive solutions to  $\mu_m \tan \mu_m h + K = 0$ ,  $\mu_0 = -i\mu$  where  $\mu$  is the positive root of  $\mu \tanh \mu h = K$  and

$$N_m = \frac{h}{2} \left( 1 + \frac{\sin 2\mu_m h}{2\mu_m h} \right). \quad (12)$$

This series converges rapidly provided  $|x|$  is not too small.

Following the procedure outlined in the introduction we can derive the new representation for  $G$ ,

$$\begin{aligned} G = & - \frac{ie^{i\mu|x|}}{2\mu N_0} \cosh \mu(z+h) \cosh \mu(\zeta+h) - \sum_{m=0}^{\infty} \frac{\Lambda_m}{N_m} \cos \mu_m(z+h) \cos \mu_m(\zeta+h) \\ & - \frac{1}{4\pi} E_1 \left( \frac{\rho^2}{a^2 h^2} \right) - \frac{1}{4\pi} E_1 \left( \frac{\rho'^2}{a^2 h^2} \right) - \sum_{n=1}^{\infty} (-1)^n L_n, \end{aligned} \quad (13)$$

where  $a$  is an arbitrary positive parameter,

$$\Lambda_0 = - \int_0^{a^2 h^2 / 4} \frac{e^{-x^2/4t}}{(4\pi t)^{1/2}} e^{\mu^2 t} dt \quad (14)$$

$$= - \frac{1}{4\pi^{1/2}} \sum_{n=0}^{\infty} \frac{1}{n!} \left(\frac{\mu}{2}\right)^{2n} \left[ |x|^{2n+1} \Gamma\left(-\frac{1}{2} - n\right) - \sum_{m=0}^{\infty} \frac{(-1)^m x^{2m}}{m!(m-n-\frac{1}{2})(ah)^{2m-2n-1}} \right], \quad (15)$$

$$\Lambda_m = \int_{a^2 h^2 / 4}^{\infty} \frac{e^{-x^2/4t}}{(4\pi t)^{1/2}} e^{-\mu_m^2 t} dt \quad (16)$$

$$= \frac{1}{2\pi^{1/2} \mu_m} \sum_{n=0}^{\infty} \frac{(-1)^n}{n!} \left(\frac{x\mu_m}{2}\right)^{2n} \Gamma\left(\frac{1}{2} - n, \frac{\mu_m^2 a^2 h^2}{4}\right), \quad (17)$$

$$L_n = \int_0^{a^2 h^2 / 4} \frac{e^{-x^2/4t}}{(4\pi t)^{1/2}} \left( I_{n,n}(\chi_{n-1}^{(1)}) + I_{n,n}(\chi_n^{(2)}) + I_{n,n}(\chi_n^{(3)}) + I_{n,n}(\chi_{n+1}^{(4)}) \right) dt \quad (18)$$

and  $I_{n,n}(\chi)$  is a known function. If we set  $a = 0$  in (13) we recover the eigenfunction expansion (11).

For large values of  $|x|$  the integrals  $\Lambda_0$  and  $\Lambda_m$  are best evaluated numerically, whereas for small  $|x|$  the series representations can be used. The integrals  $L_n$  must be evaluated numerically but provided  $a$  is chosen small enough only  $L_1$  is required. We note that

$$\int_0^{a^2 h^2 / 4} \frac{e^{-x^2/4t}}{(4\pi t)^{1/2}} I_{1,1}(\chi) dt = - \frac{1}{4\pi} E_1\left(\frac{x^2 + \chi^2}{a^2 h^2}\right) - \frac{K e^{-K\chi}}{\pi^{1/2}} \int_0^{ah/2} e^{K^2 u^2 - x^2/4u^2} \operatorname{erfc}\left(\frac{\chi}{2u} - Ku\right) du. \quad (19)$$

Both the sums in (13) converge exponentially with the parameter  $a$  controlling the relative rates of convergence of the two series. For  $a = 0$  the eigenfunction expansion (11) is recovered. The second sum in (13) is exponentially localized in space and so we can think of it as representing local information whereas global low-frequency information is represented by the first sum. This type of decomposition is known as Ewald summation.

### Three dimensions

Next we consider the three-dimensional problem

$$\nabla^2 G = \delta(x)\delta(y)\delta(z - \zeta) \quad -h < z < 0, -h < \zeta < 0 \quad (20)$$

together with (9) and (10), and we require  $G$  to behave like outgoing waves as  $R \rightarrow \infty$ .

The eigenfunction expansion for  $G$  is

$$G = - \sum_{m=0}^{\infty} \frac{K_0(\mu_m R)}{2\pi N_m} \cos \mu_m(z+h) \cos \mu_m(\zeta+h). \quad (21)$$

Computations by Newman (1985), (1992) show that when  $R/h > 1/2$  this expansion is sufficient. Our new representation for  $G$  is

$$G = - \frac{i}{4N_0} H_0^{(1)}(\mu R) \cosh \mu(z+h) \cosh \mu(\zeta+h) - \sum_{m=0}^{\infty} \frac{\Lambda_m}{N_m} \cos \mu_m(z+h) \cos \mu_m(\zeta+h) - \frac{1}{4\pi r} \operatorname{erfc}\left(\frac{r}{ah}\right) - \frac{1}{4\pi r'} \operatorname{erfc}\left(\frac{r'}{ah}\right) - \sum_{n=1}^{\infty} (-1)^n L_n, \quad (22)$$

where

$$\Lambda_0 = - \int_0^{a^2 h^2 / 4} \frac{e^{-R^2 / 4t}}{4\pi t} e^{\mu^2 t} dt \quad (23)$$

$$= \frac{1}{4\pi} \left( \gamma + 2 \ln \frac{R}{ah} + \sum_{n=1}^{\infty} \frac{(-1)^n}{n n!} \left( \frac{R}{ah} \right)^{2n} \right) - \frac{1}{4\pi} \sum_{n=1}^{\infty} \frac{1}{n!} \left( \frac{\mu ah}{2} \right)^{2n} E_{n+1} \left( \frac{R^2}{a^2 h^2} \right), \quad (24)$$

$$\Lambda_m = \int_{a^2 h^2 / 4}^{\infty} \frac{e^{-R^2 / 4t}}{4\pi t} e^{-\mu_m^2 t} dt \quad (25)$$

$$= \frac{1}{4\pi} \sum_{n=0}^{\infty} \frac{(-1)^n}{n!} \left( \frac{R}{ah} \right)^{2n} E_{n+1} \left( \frac{\mu_m^2 a^2 h^2}{4} \right), \quad (26)$$

$$L_n = \int_0^{a^2 h^2 / 4} \frac{e^{-R^2 / 4t}}{4\pi t} \left( I_{n,n}(\chi_{n-1}^{(1)}) + I_{n,n}(\chi_n^{(2)}) + I_{n,n}(\chi_n^{(3)}) + I_{n,n}(\chi_{n+1}^{(4)}) \right) dt. \quad (27)$$

If we set  $a = 0$  in (22) we recover the eigenfunction expansion (21). The logarithmic singularity in  $\Lambda_0$  as  $R \rightarrow 0$  is, of course, exactly that required to cancel the singularity in the Hankel function. Hence, by writing  $-\frac{1}{4}H_0^{(1)}(\mu R) - \frac{1}{2\pi} \ln R$  as a power series, (22) is easily computed for small  $R$ .

For the evaluation of  $L_1$  we note that

$$\int_0^{a^2 h^2 / 4} \frac{e^{-R^2 / 4t}}{4\pi t} I_{1,1}(\chi) dt = -\frac{1}{4\pi\chi} \operatorname{erfc} \left( \frac{(R^2 + \chi^2)^{1/2}}{ah} \right) - \frac{Ke^{-K\chi}}{2\pi} \int_0^{ah/2} e^{K^2 u^2 - R^2 / 4u^2} \operatorname{erfc} \left( \frac{\chi}{2u} - Ku \right) du. \quad (28)$$

## Discussion

New representations have been derived for the finite-depth free-surface Green's function in two and three dimensions. These representations contain an arbitrary positive parameter  $a$  which can be varied so as to achieve the optimum convergence rate for the given physical parameters. Preliminary numerical calculations suggest that the method is very efficient. Numerical results showing the relative strengths and weaknesses of these new formulas compared with other techniques for calculating these Green's functions will be shown at the workshop.

The same techniques can be used to derive formulas for other Green's functions associated with water-wave problems and these will also be discussed.

## References

- NEWMAN, J. N. (1985). Algorithms for the free-surface Green function. *J. Engng. Math.*, **19**, 57-67.
- NEWMAN, J. N. (1992). Approximation of free-surface Green functions. In P. A. Martin and G. R. Wickham (Eds.), *Wave Asymptotics*. Cambridge University Press.
- STRAIN, JOHN (1992). Fast potential theory. II. Layer potentials and discrete sums. *J. Comput. Phys.*, **99**, 251-270.

## NUMERICAL SIMULATION OF SLOSHING WAVES IN A 3D TANK

Q.W. Ma\*, G.X. Wu\* and R. Eatock Taylor\*\*

+ Department of Mechanical Engineering, University College London, Torrington Place,  
London, WC1E 7JE, UK

++ Department of Engineering Science, University of Oxford, Parks Road, Oxford, OX1 3PJ,  
UK

### Introduction

Sloshing waves are associated with various engineering problems, such as the liquid oscillations in large storage tanks caused by earthquakes, the motions of liquid fuel in aircraft and spacecraft, the liquid motions in containers and the water flow on the deck of ships. These motions are often very large and their behaviour is strongly non-linear when the excitation is large or when the excitation is near to the natural frequencies. The wave pattern may behave like a standing wave, a travelling wave or a hydraulic jump. During the process, large pressures may be created. Here we consider the sloshing waves in a 3D rectangular tank undergoing translational motions in three directions. The numerical algorithm is based on the finite element method discussed in the last workshop (Ma, Wu & Eatock Taylor, 1997).

### Mathematical formulation

A Cartesian co-ordinate system,  $Oxyz$ , fixed with the tank is used. Its origin is located at the centre of the free surface, as shown in Figure 1. The displacement of the tank in  $x$ ,  $y$  and  $z$  directions are defined as:

$$(1) X_b = [x_b(t), y_b(t), z_b(t)]$$

The total velocity potential  $\phi$  can be split into:

$$(2) \phi = \varphi + xu + yv + zw$$

where  $u$ ,  $v$  and  $w$  are the components of  $U = \frac{dX_b}{dt}$  in the  $x$ ,  $y$  and  $z$  directions, respectively.  $\varphi$  in (2) satisfies the following equations:

$$(3) \nabla^2 \varphi = 0$$

in the fluid

$$(4) \frac{\partial \varphi}{\partial n} = 0$$

on the side walls

$$(5) \frac{\partial \zeta}{\partial t} = -\frac{\partial \varphi}{\partial x} \frac{\partial \zeta}{\partial x} - \frac{\partial \varphi}{\partial y} \frac{\partial \zeta}{\partial y} + \frac{\partial \varphi}{\partial z}$$

on the free surface

$$(6) \frac{\delta \varphi}{\delta t} = \frac{\partial \varphi}{\partial z} \frac{\partial \zeta}{\partial t} - \frac{1}{2} \nabla \varphi \cdot \nabla \varphi - g \zeta - x \frac{du}{dt} - y \frac{dv}{dt} - \zeta \frac{dw}{dt}$$

on the free surface

where  $\zeta$  is free surface elevation measured in  $Oxyz$  and  $\frac{\delta \varphi[x, y, \zeta(x, y, t), t]}{\delta t} = \frac{\partial \varphi}{\partial t} + \frac{\partial \varphi}{\partial z} \frac{\partial \zeta}{\partial t}$ . These equations are then combined with the initial conditions which can be given as:

$$(7) \zeta(x, y, 0) = 0 \quad \varphi(x, y, 0, 0) = -xu(0) - yv(0)$$

### Results

In the analysis below, some parameters are nondimensionalized as follows:

$$(x, y, z, L, B, a) \rightarrow (x, y, z, L, B, a)d, \quad t \rightarrow \tau \sqrt{d/g}, \quad \omega \rightarrow \omega \sqrt{g/d}$$

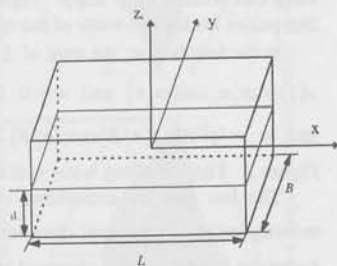


Figure 1 Tank and co-ordinate system

We first consider a 2D case in which  $L = 2$ ,  $B = 0.2$  and the motion of the tank is governed by  $u(\tau) = a\omega \cos(\omega\tau)$  and  $v = w = 0$ . Figure 2 shows the history of the wave elevation at  $x = -1.0$  with  $a = 0.00186$  and at four different frequencies either higher or lower than the natural frequency  $\omega_0 = \sqrt{(\pi/L)\tanh(\pi/L)}$ . It shows that the numerical results are in an excellent agreement with the linearised analytical solution (Faltinsen, 1978).

The second case considered is a 3D problem in a square tank of  $L = B = 4$ , which moves in a vertical direction with an initial horizontal disturbance defined by:

$$(8) \quad w(\tau) = \omega_z a_z \cos(\omega_z \tau), \quad u(\tau) = v(\tau) = \begin{cases} 0.0283 & \tau = 0 \\ 0 & \tau > 0 \end{cases}$$

We have made calculation for four different amplitudes and frequencies. The corresponding wave history recorded at one corner is presented in Figure 3 where  $\omega_0$  given above is also a natural frequency of this square tank. The wave elevation due to purely vertical motion is theoretically zero. It, however, can become quite large when a small initial horizontal perturbation exists, as can be seen from Figures 3b to 3d. Furthermore, these large responses are not in the forced frequency but in one near to  $\omega_0$ . A similar phenomenon was also reported by Su and Wang (1986) when they considered the motion at about twice the natural frequency.

In the third case, the tank of  $L = B = 8$  undergoes only horizontal motions defined as  $u(\tau) = v(\tau) = a\omega \cos(\omega\tau)$  with  $a = 0.0372$  and  $\omega = 0.9999\omega_0$ . A travelling wave can be observed in Figure 4 which shows the sequence of a wave crest moving from the corner  $(-L/2, -B/2)$  to the corner  $(L/2, B/2)$ . Figure 5 gives the wave history at the two corners. It can be seen that the wave can become very sharp. Figure 6 illustrates the pressure history at two points, which behaves like pulses hitting the walls of the tank repeatedly.

In the fourth case, the tank of  $L = 8$  and  $B = 4$  is moving with velocities  $u(\tau) = \omega_x a_x \cos(\omega_x \tau)$ ,  $v(\tau) = \omega_y a_y \cos(\omega_y \tau)$  and  $w = 0$  where  $a_x = 0.0372$ ,  $a_y = 0.0186$ ,  $\omega_x = 0.9999\sqrt{(\pi/L)\tanh(\pi/L)}$  and  $\omega_y = 0.9999\sqrt{(\pi/B)\tanh(\pi/B)}$ . Some typical snapshots of the wave profiles are illustrated in Figure 7. The travelling wave is also evident in this case.

The last case we considered corresponds to very shallow water. The tank of  $L = B = 25$  is moving only in horizontal directions with  $a_x = a_y = 1.2$  and  $\omega_x = \omega_y = 0.998\sqrt{(\pi/L)\tanh(\pi/L)}$ . A hydraulic jump has been observed in this case, as shown in Figure 8. It should be noted that there are some higher frequency waves superimposed on the wave system in our case. Huang and Hsiung (1996) also observed the hydraulic jump based on a shallow water formulation but no higher frequency waves seem to exist in their analysis. More results will be presented in the workshop.

## Acknowledgements

This work was sponsored by research Grant ref GR/K80372 from EPSRC, UK.

## References

- Faltinsen, O.M., 1978, A numerical non-linear method of sloshing in tanks with two dimensional flow, *J.S.R.*, Vol. 18, pp224-241.
- Huang, Z.J. and Hsiung, C.C. 1996, Nonlinear shallow-water flow on deck. *J.S.R.*, Vol. 40, pp303-315.
- Ma, Q., Wu, G.X. & R., Eatock Taylor, 1997, Finite element analysis of the non-linear transient waves in three dimensional long tank. *12th Workshop on Water Waves and Floating Bodies*.
- Su, T.C. and Wang, Y., 1986, Numerical simulation of three-dimensional large amplitude liquid sloshing in rectangular containers subjected to vertical excitation, *Seismic Engineering for Piping Systems, Tanks and Power Plant Equipment*, Vol. 108, ASME, pp. 149-154.

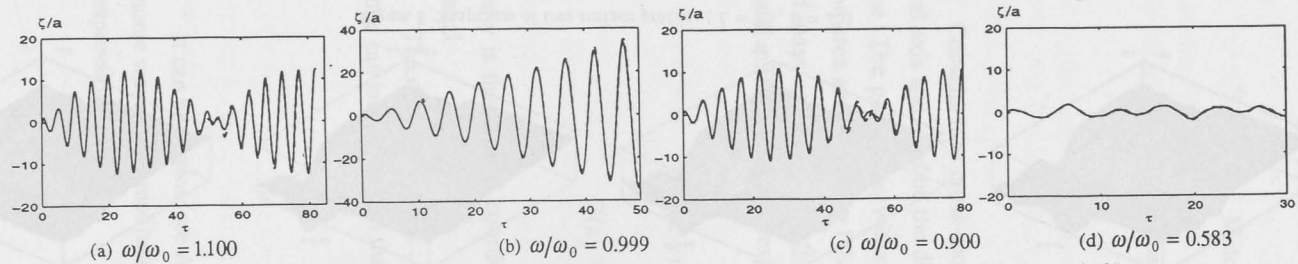


Figure 2 Wave history at  $x = -1.0$  for different frequencies (solid line: analytical; dashed line: numerical)

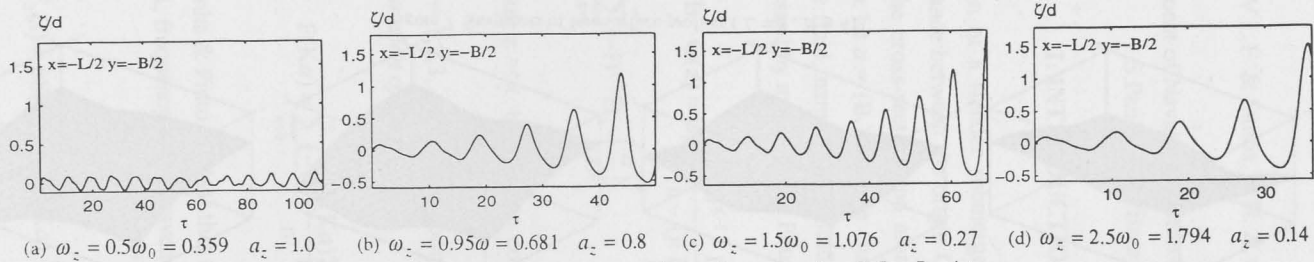


Figure 3 Wave history at a corner due to the motion of eq. 8 ( $L = B = 4$ )

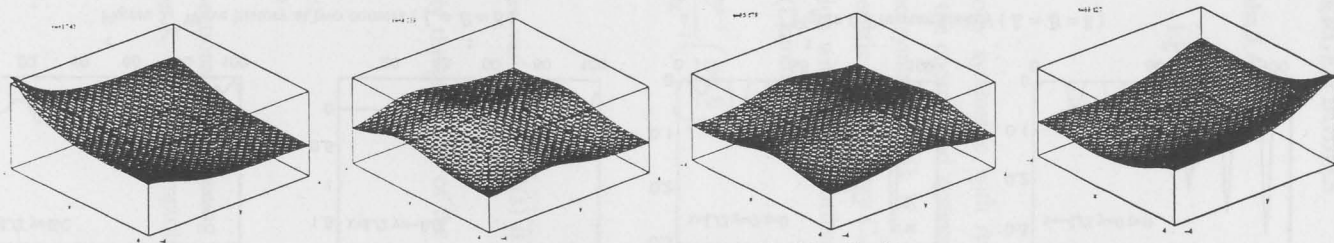
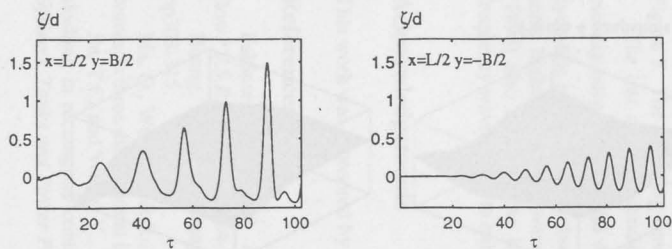
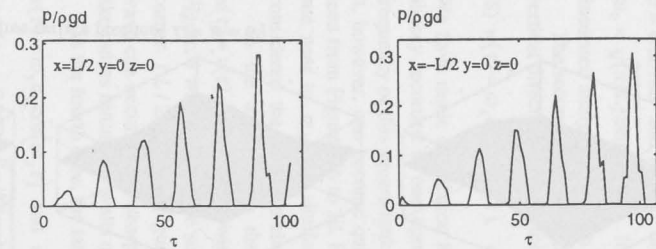
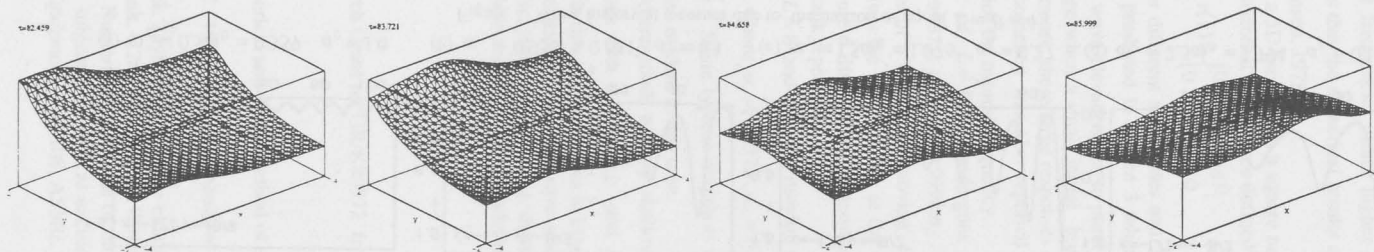
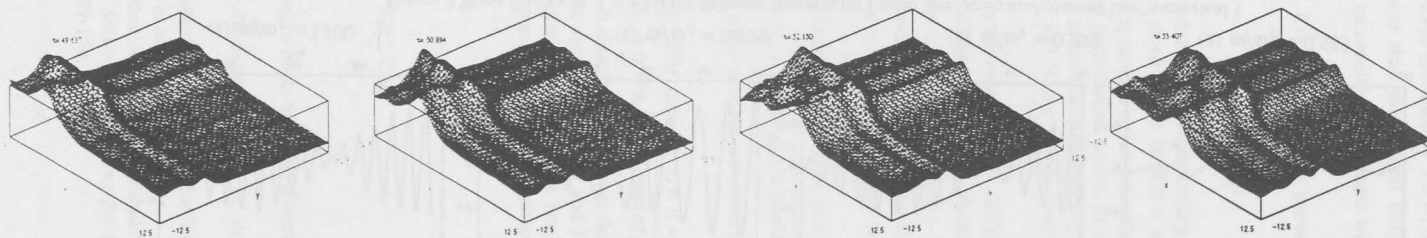


Figure 4 Snapshots of free surface profiles ( $L = B = 8$ )

Figure 5 Wave history at two corners ( $L = B = 8$ )Figure 6 Pressure history ( $L = B = 8$ )Figure 7 Snapshots of free surface profiles ( $L = 8, B = 4$ )Figure 8 Snapshots of free surface profiles ( $L = 25, B = 25$ )

## GEOMETRIC SYNTHESIS OF 2D SUBMERGED BODIES

Matos, V.L.F. & Simos, A.N. & Aranha, J.A.P.

Department of Naval and Ocean Eng. - EPUSP  
S. Paulo, S.P., Brazil

### 1. INTRODUCTION

Consider the cross-section of a slender submerged body symmetric with respect to the vertical axis and let  $d$  be the distance between the origin  $O$  of the coordinated system and the free surface. The point  $O$  is within the cross-section and along the symmetry axis. If  $S$  is the cross-section area and  $B_1 = (C_M + 1)S/2\pi$  let  $a = (B_1)^{1/2}$  be the characteristic length, where  $C_M$  is the heave added mass coefficient in *infinite* fluid, namely, in a fluid region without free surface. The heave potential in this case can be expressed by means of the Fourier (Laurent) series

$$\begin{aligned}\phi(x, y) &= B_1 \cdot G(z) = B_1 \sum_{n=1}^{\infty} \frac{a^{n-1}}{(n-1)!} \frac{D_n}{D_1} \frac{\partial^{n-1}}{\partial z^{n-1}} \left( \frac{\sin \theta}{r} \right); \\ G(z) &= - \sum_{n=1}^{\infty} (-i)^n \cdot D_n \cdot \left( \frac{a}{z} \right)^n,\end{aligned}\tag{1a}$$

where  $y$  is the vertical coordinate,  $z = x + i.y$  is the complex variable and  $G(z)$  is the complex potential.

The coefficients  $\{D_n ; n = 1, 2, 3, \dots\}$  define completely the geometry of the cross-section and one can introduce then the *function of form*

$$F(Ka) = \sum_{n=0}^{\infty} (-1)^n \frac{(Ka)^n}{n!} \frac{D_{n+1}}{D_1}.\tag{1b}$$

It can be shown (see Aranha & Pinto (1994)) that the sectional heave exciting force due to a harmonic wave with amplitude  $A$ , frequency  $\omega$  and wavenumber  $K = \omega^2/g$  is asymptotically given by the expression

$$\begin{aligned}f_3(t) &= \rho S (C_M + 1) \cdot F(Ka) \cdot \frac{dw_0}{dt}; \\ w_0(t) &= \left( \frac{\partial \phi_1}{\partial z} \right)_{x=z=0} = -i\omega A e^{-Kd} e^{-i\omega t},\end{aligned}\tag{2a}$$

with an error of the form  $[1 + O(\delta)]$  where

$$\delta = (C_M + 1) \cdot K^2 S \cdot F(Ka) \cdot e^{-2K(d-a_0)} \approx (Ka)^2 \cdot e^{-2Ka} \quad (2b)$$

In the above expression  $a_0$  is the radius of the circle that circumscribes the cross-section and since  $\delta \leq 0.135(a/d)^2$  the error is of order 3% when the equivalent cross-section radius  $a$  is half the distance  $d$  between the point O and the free surface.

Notice that  $F(Ka) \rightarrow 1$  when  $Ka \rightarrow 0$  and so (2a) recovers the inertia term of Morison formula in the low frequency limit; in this sense this expression represents an extension to the whole range of frequencies of this well known formula. Also,  $F(Ka) \equiv 1$  for a circle, indicating that Morison formula can be used in the whole range of frequencies for this geometry.

## 2. GEOMETRIC SYNTHESIS

The importance of such approximated solution is that it enables one to address, within certain limitations, the inverse problem, namely, the one where the behavior of the exciting force is defined and the geometry of the cross-section is then obtained. By defining a convenient *function of form*  $F(Ka)$  one can determine the coefficients  $\{D_n; n = 1, 2, 3, \dots\}$  and so the geometry of the cross-section that it is associated with the chosen  $F(Ka)$ . The purpose of this work is to present an example of this geometric synthesis and an experimental validation of the final result, by direct measurement of the exciting force in the wave tank. The example chosen was fitted to provide a simple geometry, that could be easily built and such that the final result could have been obtained by an ad hoc extension of Morison formula to the whole frequency range.

Consider then the *function of form*

$$F(Ka) = \cos^4(\alpha Ka) = \frac{3}{8} + \frac{4}{8} \cos(2\alpha Ka) + \frac{1}{8} \cos(4\alpha Ka) \quad (3a)$$

The geometry related to this one-parameter functions of form are such that the heave exciting force have a very flat zero at the frequency  $Ka = \pi/2\alpha$ . Expanding (3a) in power series one can determine the coefficients  $\{D_n; n = 1, 2, 3, \dots\}$  from (1b) and using them into the expression for  $G(z)$  the following complex potential is determined (see Simos (1997)):

$$G(z) = -\frac{3a^2 i}{8z} - \frac{a^2 i}{4z + 2\alpha a} - \frac{a^2 i}{4z - 2\alpha a} - \frac{a^2 i}{16z + 4\alpha a} - \frac{a^2 i}{16z - 4\alpha a} \quad (3b)$$

For  $\alpha = 0$  the complex potential  $G(z)$  represents a circle with radius  $a$  centered at the origin O; as  $\alpha$  increases this circle is continuously distorted and for  $\alpha$  large enough one obtains *five* circles

with centers placed at  $\{z = (0,0); z = (\pm 2\alpha a, 0); z = (\pm 4\alpha a, 0)\}$  and with radius  $\{(3/8)^{1/2}a; a/2; a/4\}$  respectively.

The figure below shows how the geometry changes with the increase of *tuning parameter*  $\alpha$ . Observing that the standard Morison formula can be used for a circle, irrespective of the value of the wavenumber, one obtains from this formula applied to the five circles exactly the expression (2a;3a). This result not only enhance the confidence in the proposed approximation but also displays a simple geometry that can be easily built in order to check experimentally expression (2a).

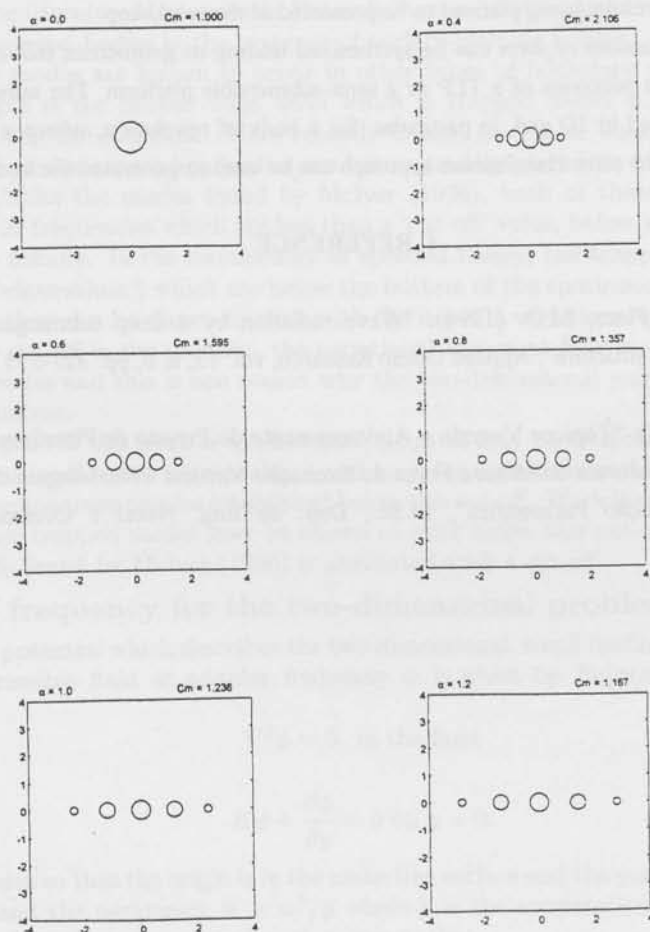


FIG.(1): Geometric synthesis of the function of form (3a) for different values of the parameter  $\alpha$ .

### 3. EXPERIMENTAL SET UP

Five cylinders with length  $l = 0.950$  m and with diameters  $\{0.150\text{m}; 0.122\text{m}; 0.061\text{m}\}$  were fixed in a rigid frame with the centers equidistant from each other by an adjustable distance  $b$ . The length  $l$  is a bit smaller than the wave tank width and if  $S = 0.047$  m<sup>2</sup> is the total cross section area, then  $\alpha = (S/\pi)^{1/2} = 0.122$  m and the parameter  $\alpha$  is defined by the equality  $b = 2\alpha a$ . So by changing  $b$  one can change the value of the *tuning parameter*  $\alpha$ . Two load cells were placed along the transversal arms of the frame, the line joining the load cells being coincident with the longitudinal axis of the wave tank. A low amplitude harmonic wave was then imposed by the wave maker and the resultant heave force was obtained by the sum of the forces in each load cell.

Preliminary experimental results seems to confirm the proposed approximation, a consistent set of experimental results being planned to be presented at the workshop.

Different *functions of form* can be synthesized leading to geometries that can be usefull as cross sections of the pontoons of a TLP or a semi-submersible platform. The same approximation can also be developed in 3D and, in particular, for a body of revolution, where a stream function can be introduced, the same Hamiltonian approach can be used to generated the body geometry.

### 4. REFERENCE

1. Aranha, J.P.A. & Pinto, M.O. (1994): "Wave radiation by a deep submerged cylinder with application to ocean structure", Applied Ocean Research, vol. 15, n. 6, pp. 327-335.
2. Simos, A.N. (1997): "Tópicos Visando o Aprimoramento do Projeto de Plataformas TLP: Estudo de Formas Bi-Dimensionais de Mínima Força de Excitação Vertical e Modelagem da Dinâmica dos Tendões sob Excitação Paramétrica", M.Sc., Dep. de Eng. Naval e Oceânica da EPUSP, Novembro de 1997;

## Uniqueness, trapped modes and the cut-off frequency

Maureen McIver

Loughborough University, Loughborough, Leicestershire, LE11 3TU, U.K.

### Introduction

For several years many authors tried to prove that the two-dimensional, linear water-wave problem was uniquely posed at all frequencies until McIver (1996) showed that trapped modes exist for pairs of special bodies placed in the free surface. Trapped modes are defined to be non-zero solutions of the homogeneous problem which have finite energy. Their existence at a specific frequency means that the forced problem does not have a unique solution at that frequency. The question of whether or not trapped modes exist for purely submerged bodies or variable sea-bed topography is still open. Uniqueness has been proved for some geometrical configurations of bodies and topography (see McIver 1996 for a review of the literature) but recently Evans & Porter (1998) showed that trapped modes exist for submerged bodies in the presence of surface-piercing bodies.

Trapped modes are known to occur in other types of boundary value problems. A classic example is the Stokes' edge wave which is trapped above a sloping beach and propagates along the shoreline. More recently Evans, Levitin & Vassiliev (1994) proved that trapped modes exist when bodies are symmetrically placed in water wave channels or guides. Unlike the modes found by McIver (1996), both of these types of trapped modes occur at frequencies which are less than a 'cut-off' value, below which waves cannot propagate to infinity. In the terminology of spectral theory, the trapped modes occur at frequencies ('eigenvalues') which are below the bottom of the continuous spectrum for the problem and they can be shown to exist with the use of a variational principle. However, if there is no cut-off in the problem, the variational argument fails to prove the existence of trapped modes and this is one reason why the two-dimensional water wave problem is difficult to analyse.

The purpose of this work is to show how a cut-off may be artificially introduced into the two-dimensional water-wave problem and how, for a wide class of bodies and variable topography, uniqueness may be established below this cut-off. Work is currently in progress to see whether trapped modes may be shown to exist below this cut-off and whether the trapped mode found by McIver (1996) is associated with a cut-off.

### A cut-off frequency for the two-dimensional problem

The velocity potential which describes the two-dimensional, small oscillations of an inviscid and incompressible fluid at angular frequency  $\omega$  is given by  $Re[\phi(x, y) e^{-i\omega t}]$  where  $\phi$  satisfies

$$\nabla^2 \phi = 0, \text{ in the fluid} \quad (1)$$

and

$$K\phi + \frac{\partial \phi}{\partial y} = 0 \text{ on } y = 0. \quad (2)$$

Axes are chosen so that the origin is in the mean free surface and the  $y$ -axis points vertically downwards and the parameter  $K = \omega^2/g$  where  $g$  is the acceleration due to gravity. In addition, no flow through any rigid surface means that

$$\frac{\partial \phi}{\partial n} = 0 \text{ on the sea-bed and any bodies.} \quad (3)$$

If trapped modes are sought then the radiation condition is replaced by

$$\phi \rightarrow 0 \text{ as } |x| \rightarrow \infty. \quad (4)$$

Uniqueness is established if the only solution to (1)-(4) is the trivial solution  $\phi = 0$ . Without loss of generality,  $\phi$  may be assumed to be real because if it were complex then the real and imaginary parts would separately satisfy the governing equations and boundary conditions. To be specific the problem in which there are no bodies in the fluid but there is a variable sea-bed which lies between  $x = \pm a$ , as illustrated in figure 1, is studied.

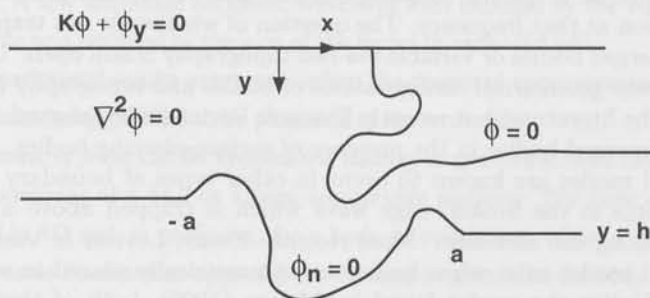


Figure 1 - Definition sketch and illustration of a nodal line

Greens theorem

$$\int_D \phi \nabla^2 \psi - \psi \nabla^2 \phi dV = \int_{\partial D} \phi \frac{\partial \psi}{\partial n} - \psi \frac{\partial \phi}{\partial n} dS \quad (5)$$

is applied to  $\phi$  and the harmonic function

$$\psi = \sin k(x - b) \cosh k(y - h) \quad (6)$$

in the region  $x \geq b \geq a$ ,  $0 \leq y \leq h$ , where  $h$  is the uniform depth of the layer in the region  $x \geq a$  and  $kh$  is the real, positive root of the dispersion relation  $Kh = kh \tanh kh$ . In this region, both  $\phi$  and  $\psi$  are harmonic and satisfy the same boundary conditions on the sea-bed and the free surface. As  $\phi \rightarrow 0$  as  $x \rightarrow \infty$  the only contribution to (5) comes from the line  $x = b$  and yields

$$\int_0^h \phi(b, y) \cosh k(y - h) dy = 0. \quad (7)$$

The function  $\cosh k(y - h)$  is strictly positive and as  $\phi(b, y)$  is a continuous function of  $y$ ,

$$\phi(b, y_0) = 0 \quad (8)$$

for some  $y_0(b)$  such that  $0 < y_0 < h$ . A value of  $y_0$  may be found for every  $b \geq a$  and so by continuity, there is a nodal line on which  $\phi = 0$  in the interior of the fluid which extends to infinity in the region  $x \geq a$ . Moreover in  $x \geq a$ ,  $\phi$  may be represented by an eigenfunction expansion, namely

$$\phi = \sum_{n=1}^{\infty} a_n \cos k_n(y - h) e^{-k_n(x-a)} \quad (9)$$

where  $\{k_n h\}$  is the monotonically increasing sequence of positive roots of the dispersion relation  $Kh = -k_n h \tan k_n h$ . If  $\phi$  is not identically equal to zero then for  $x \gg a$  it is dominated by the first non-zero term in this series, so for some  $j$

$$\phi = a_j \cos k_j (y - h) e^{-k_j (x - a)} + O(e^{-k_{j+1} x}) \text{ as } x \rightarrow \infty \quad (10)$$

and so there is a nodal line which asymptotes to the horizontal line  $y = d$  as  $x \rightarrow \infty$ , where  $k_j d$  is the smallest root of the equation  $\cos k_j (y - h) = 0$ . Furthermore, if the potential does correspond to a trapped mode, the other end of this line cannot lie on the sea-bed or go to either infinity. If it did then there would be a region in the fluid which was open to infinity and partially surrounded by lines on which either  $\phi$  or its normal derivative were zero and a simple application of the divergence theorem would mean that  $\phi = 0$  everywhere within that region and, by analytic continuation,  $\phi = 0$  everywhere in the fluid. Thus if  $\phi$  represents a trapped mode there is a nodal line which asymptotes to the line  $y = d$  as  $x \rightarrow \infty$  and whose other end lies on the free surface, as illustrated in figure 1. Although the precise position of the line is unknown, it defines the lower boundary of a subregion of the fluid contained between it and the free surface. In the next section it will be shown that there is a cut-off for this new region, below which waves cannot propagate to infinity and uniqueness will be established for  $Kh_{\max} \leq 1$  where  $h_{\max}$  is the maximum depth of the fluid.

### Uniqueness below the cut-off

The velocity potential for waves which propagate in a fluid layer of uniform depth  $d$  and which satisfies the condition  $\phi = 0$  on the lower boundary, is given by

$$\phi = \sinh k(y - d) e^{\pm i k x}, \quad (11)$$

where, to satisfy the free surface condition (2),  $kd$  is a root of the dispersion relation

$$Kd = kd \coth kd. \quad (12)$$

By examining the graph of  $y = x \coth x$  it is straightforward to show that there are no real roots of (12) if  $Kd < 1$ . Thus there is a cut-off frequency below which waves cannot propagate in a uniform layer and satisfy  $\phi = 0$  on the lower boundary.

The region  $D$  is defined to be the region contained between the nodal line and the free surface and the coordinate axes are redefined so that the origin is at the intersection of the nodal line and the free surface. Integration down a vertical line from any point  $b$  on the free surface of this new region gives

$$\phi(b, 0) = - \int_0^{d(b)} \frac{\partial \phi}{\partial y}(b, y) dy, \quad (13)$$

where  $d(b)$  is the smallest value of  $y$  such that the point  $(b, d(b))$  lies on the nodal line. (If there is only one such value then  $y = d(b)$  is the equation of the nodal line.) By squaring (13) and using the Cauchy-Schwarz inequality it may be shown that

$$\phi^2(b, 0) \leq \left[ \int_0^{d(b)} 1^2 dy \right] \left[ \int_0^{d(b)} \left( \frac{\partial \phi}{\partial y} \right)^2 dy \right] \leq d_{\max} \int_0^{d(b)} \left( \frac{\partial \phi}{\partial y} \right)^2 dy, \quad (14)$$

where  $d_{\max}$  is the maximum depth of the nodal line. An application of the divergence theorem with the use of (4) and (14) gives

$$\int_D (\nabla\phi)^2 dV = K \int_0^\infty \phi^2(x, 0) dx \leq K d_{\max} \int_0^\infty \int_0^{d(x)} \left( \frac{\partial\phi}{\partial y} \right)^2 dy dx \leq K d_{\max} \int_D (\nabla\phi)^2 dV. \quad (15)$$

If  $K d_{\max} < 1$  the inequality in (15) is only satisfied if  $(\nabla\phi)^2$  is identically equal to zero which means that  $\phi$  is a constant and this constant must be zero from the nodal line condition. So there are no trapped modes in the subregion for  $K d_{\max} < 1$ . As  $d_{\max} < h_{\max}$ , the maximum depth of the fluid, there are no trapped modes in the subregion and by analytic continuation, the whole fluid, if  $K h_{\max} \leq 1$ .

### Uniqueness for bodies and variable topography

The analysis of the previous section may be extended to the case where there are a finite number of nonbulbous, surface-piercing bodies in a fluid layer of variable depth. In this case, the nodal line may end on one of the bodies instead of the free surface. However, the nodal line and a portion of the body would still define the lower boundary of a subregion of the fluid and if the body is nonbulbous, vertical lines may be extended from every point on the free surface in the subregion to the nodal line and the analysis of the previous section will apply. In addition the proof of uniqueness for  $K h_{\max} \leq 1$  extends to the case where there is a single submerged or surface-piercing body of any shape. This is because there is also a nodal line which asymptotes to the line  $y = \text{const}$  as  $x \rightarrow -\infty$  and it is impossible for both nodal lines to end on the body unless the potential is identically equal to zero. Thus, at least one of the nodal lines must end on the free surface and this defines a subregion of the fluid in which the argument of the previous section may be applied.

### Conclusion

Uniqueness of potential for the two-dimensional, linear boundary value problem for water waves has been proved for general sea-bed topographies for  $K h_{\max} \leq 1$ . The result has also been extended to prove uniqueness for the same range of frequencies when there are any finite number of nonbulbous, surface-piercing bodies in the fluid or a single submerged or surface-piercing body of any shape. The numerical evidence is that the nodal line for the trapped mode potential obtained by McIver (1996) ends on one of the bodies. However, because the bodies found are bulbous it is not possible to extend vertical lines from every point on the free surface in the subregion to the nodal line and so there is no contradiction between the existence of this mode and the uniqueness results generated in this paper.

### References

- Evans, D.V., Levitin, M. & Vassiliev, D. 1994 'Existence theorems for trapped modes.' *J. Fluid Mechanics*, Vol. 261, pp 21 - 31.
- Evans, D.V. & Porter, R. 1998 'An example of non-uniqueness in the two-dimensional linear water wave problem involving a submerged body.' Submitted to *Proc. Roy. Soc. Lond. A*.
- McIver, M. 1996 'An example of non-uniqueness in the two-dimensional linear water wave problem.' *J. Fluid Mechanics*, Vol. 315, pp 257 - 266.

## On the completeness of eigenfunction expansions in water-wave problems

P. McIver

Department of Mathematical Sciences, Loughborough University, UK

### 1 Introduction

The method of eigenfunction expansions is a popular tool for the solution of the linear water-wave problem in constant depth water. The key result is that there exists a complete set of orthonormal vertical eigenfunctions so that any 'reasonable' function of the vertical coordinate may be expanded in terms of this complete set. This result comes from the theory of self-adjoint linear differential operators which is used extensively in many engineering applications of mathematics.

There are a number of problems involving wave interaction with a permeable breakwater or a perforated barrier for which the vertical eigenvalue problem is no longer self adjoint. A consequence of this is that the familiar theorems required to construct an eigenfunction expansion no longer apply and the 'obvious' eigenfunctions may not form a complete set. Perhaps the simplest problem of this type is examined in detail here, but first of all some aspects of the 'standard' water-wave problem are recalled.

### 2 The water-wave problem

Consider the linear water-wave problem for time-harmonic motion of angular frequency  $\omega$  in a region of constant depth  $h$ , and let  $y$  be the vertical coordinate with origin in the free surface and directed upwards. An attempt to find a solution in terms of vertical eigenfunctions leads to consideration of the differential equation

$$T\chi \equiv -\frac{d^2\chi}{dy^2} = \lambda\chi \quad \text{for} \quad -h < y < 0 \quad (1)$$

together with the boundary conditions

$$\frac{d\chi}{dy} = 0 \quad \text{on} \quad y = -h \quad \text{and} \quad \frac{d\chi}{dy} = K\chi \quad \text{on} \quad y = 0, \quad (2)$$

where  $K$  is the real number  $\omega^2/g$  and  $g$  is the acceleration due to gravity. It is well known that the solutions of this problem are of the form

$$\chi = \cos k(y+h) \quad (3)$$

where  $k = \lambda^{1/2}$  is a root of the dispersion relation

$$K = -k \tan kh. \quad (4)$$

This dispersion relation has two purely imaginary roots  $k = \pm k_0$  and an infinity of purely real roots  $\{k = \pm k_m; m = 1, 2, \dots\}$ . The set of vertical eigenfunctions

$$\chi_m = \frac{\cos k_m(y+h)}{N_m}, \quad m = 0, 1, 2, \dots, \quad (5)$$

with

$$N_m^2 = \frac{1}{2} \left( 1 + \frac{\sin 2k_m h}{2k_m h} \right), \quad (6)$$

form a complete orthonormal set satisfying

$$\frac{1}{h} \int_{-h}^0 \chi_m(y) \chi_n(y) dy = \delta_{mn} \quad (7)$$

where  $\delta_{mn}$  is the Kronecker delta.

It is convenient to introduce an inner product notation. Let  $u$  and  $v$  be any two functions that are square-integrable over the depth and define their inner product by

$$\langle u, v \rangle = \frac{1}{h} \int_{-h}^0 u \bar{v} dy \quad (8)$$

where the over bar denotes complex conjugate. In this notation, the orthogonality condition (7) is

$$\langle \chi_m, \chi_n \rangle = \delta_{mn}. \quad (9)$$

By the expansion theorem, any function  $f$  that is square integrable over the depth may be written

$$f = \sum_{m=0}^{\infty} \langle f, \chi_m \rangle \chi_m. \quad (10)$$

### 3 Wave motion in a permeable breakwater

A model for time-harmonic motion in a permeable breakwater<sup>1</sup> leads again to the consideration of the boundary-value problem (1-2) but with  $K$  now a complex number. This problem has been examined in some detail by Dalrymple, Losada & Martin<sup>2</sup>. In particular, they note that for certain values of the complex parameter  $K$  there are double roots of the dispersion relation (4) and, for these values of  $K$ , the eigenfunctions (5) no longer form a complete set. Dalrymple *et al.* obtain the missing eigenfunctions by an indirect argument based on the Green's function for the particular water-wave problem under consideration. Here, the problem is re-examined from the point of view of the general theory of non-self-adjoint linear differential operators.

An operator  $T$  is self adjoint if, for all suitable functions  $u$  and  $v$ ,

$$\langle Tu, v \rangle = \langle u, Tv \rangle. \quad (11)$$

Integration by parts shows that this relation is satisfied by the operator defined by (1-2) provided  $K$  is real. The corresponding breakwater problem, where  $K$  is complex, is not self adjoint and the familiar expansion theorems do not apply.

Fortunately, this particular problem falls into a class discussed in Chapter 12 of the text by Coddington & Levinson<sup>3</sup>. The eigenvalues of the problem (1-2) are given by  $\lambda = k^2$ , where  $k$  is a, now complex, root of the dispersion relation (4). Let  $C_n$  be a closed contour in the complex  $\lambda$  plane which encircles in an anticlockwise direction the eigenvalues  $\{\lambda_1, \lambda_2, \dots, \lambda_n\}$ , arranged in order of increasing modulus. The expansion theorem<sup>3</sup> says that, for suitable functions  $f$ ,

$$f(y) = - \lim_{n \rightarrow \infty} \int_{-h}^0 P_n(y, \eta) f(\eta) d\eta \quad (12)$$

where

$$P_n(y, \eta) = \frac{1}{2\pi i} \int_{C_n} G(y, \eta; \lambda) d\lambda, \quad (13)$$

$G$  is the Green's function for the particular problem under consideration, and provided suitable convergence criteria can be established. The Green's function for the problem (1-2) is

$$G(y, \eta; \lambda) = - \frac{(k \cos ky_{>} + K \sin ky_{>}) \cos k(y_{<} + h)}{k(K \cos kh + k \sin kh)}, \quad k = \lambda^{1/2}, \quad (14)$$

where

$$y_{<} = \min(y, \eta) \quad \text{and} \quad y_{>} = \max(y, \eta). \quad (15)$$

This Green's function has poles at values of  $\lambda$  corresponding to the roots of the dispersion relation (4) so that, by the residue theorem,

$$P_n(y, \eta) = \sum_{m=1}^n R_m(y, \eta) \quad (16)$$

where  $R_m$  is the residue of  $G$  at  $\lambda = \lambda_m$ . If the eigenvalues are known then the residues at the poles of the Green's function can be calculated and the form of the general expansion found. There are two difficulties with this, one numerical and one theoretical.

The numerical difficulty is in locating the eigenvalues in the complex plane. In the case of real  $K$  the roots of the dispersion relation lie on either the real or imaginary axis in the complex  $k$  plane and are therefore easily located. For complex  $K$ , Dalymple *et al.*<sup>2</sup> used a numerical scheme in which the roots are tracked individually as the imaginary part of  $K$  is increased from zero. Some new results have been obtained that should allow a more direct computation of these roots.

The theoretical problem is that for isolated values of  $K$  there is a double root of the dispersion relation and therefore a double pole of the Green's function. These double roots correspond to zeros in the complex  $k$  plane of the normalisation factor  $N_m$  defined in equation (6); the corresponding value of  $K$  follows from the dispersion relation (4). For almost all values of  $K$  there are no double roots.

The residue of the Green's function for a pole of order  $p_m$  at  $\lambda = \lambda_m$  is readily evaluated and may be written

$$R_m(y, \eta) = \sum_{q=1}^{p_m} \bar{\psi}_{m, p_m - q + 1}(\eta) \chi_{m, q}(y). \quad (17)$$

For the case of a simple pole,  $p_m = 1$ , the so-called 'generalised eigenfunctions' are given by

$$\chi_{m,1} = \frac{\cos k_m(y+h)}{N_m} \quad \text{and} \quad \psi_{m,1} = \bar{\chi}_{m,1} \quad \text{with} \quad \langle \chi_{m,1}, \psi_{m,1} \rangle = 1. \quad (18)$$

For the case of a double pole,  $p_m = 2$ , the generalised eigenfunctions are

$$\chi_{m,1} = -\frac{2 \cos k_m(y+h)}{\cos^2 kh} \quad \text{and} \quad \psi_{m,1} = \bar{\chi}_{m,1}, \quad (19)$$

$$\chi_{m,2} = \frac{1}{6}(4 \sin^2 kh - 3) \cos k_m(y+h) + k_m(y+h) \sin k_m(y+h) \quad \text{and} \quad \psi_{m,2} = \bar{\chi}_{m,2}, \quad (20)$$

with

$$\langle \chi_{m,1}, \psi_{m,1} \rangle = \langle \chi_{m,2}, \psi_{m,2} \rangle = 0 \quad \text{and} \quad \langle \chi_{m,1}, \psi_{m,2} \rangle = \langle \chi_{m,2}, \psi_{m,1} \rangle = 1. \quad (21)$$

In the double-pole case, although the residue is well defined, there is a degree of arbitrariness in the choice of the generalised eigenfunctions  $\{\chi_{m,q}, \psi_{m,q}; q = 1, 2\}$ . Generalised eigenfunctions corresponding to different eigenvalues are biorthogonal so that

$$\langle \chi_{m,q}, \psi_{n,r} \rangle = 0, \quad m \neq n. \quad (22)$$

With the above definitions, the general expansion theorem is

$$f = \sum_{m=1}^{\infty} \sum_{q=1}^{p_m} \langle f, \psi_{m, p_m - q + 1} \rangle \chi_{m, q} \quad (23)$$

For real  $K$ , all poles of the Green's function are simple and  $\psi_{m,1} = \chi_{m,1} \equiv \chi_m$  so that (23) reduces to (10), after a suitable relabelling of the eigenfunctions.

#### 4 Solutions of Laplace's equation

The expansion theorem (23) may be used to find solutions of water wave problems. For example, suppose that a solution  $\phi(x, y)$  of Laplace's equation is required satisfying the boundary conditions

$$\frac{\partial \phi}{\partial y} = 0 \quad \text{on } y = -h \quad \text{and} \quad \frac{\partial \phi}{\partial y} = K\phi \quad \text{on } y = 0. \quad (24)$$

The solution is sought in the form

$$\phi(x, y) = \sum_{m=1}^{\infty} \sum_{q=1}^{p_m} C_{m,q}(x) \chi_{m,q}(y) \quad (25)$$

which satisfies the Laplace equation provided

$$\sum_{m=1}^{\infty} \sum_{q=1}^{p_m} \{ C_{m,q}''(x) \chi_{m,q}(y) + C_{m,q}(x) \chi_{m,q}''(y) \} = 0. \quad (26)$$

Now

$$\chi_{m,1}'' = -k_m^2 \chi_{m,1} \quad \text{and} \quad \chi_{m,2}'' = -k_m^2 \chi_{m,2} - k^2 \cos^2 kh \chi_{m,1} \quad (27)$$

so that (22) may be used to isolate terms corresponding to distinct eigenvalues. For a simple pole

$$C_{m,1}'' - k_m^2 C_{m,1} = 0 \quad \text{and so} \quad C_{m,1}(x) = \alpha_m e^{k_m x} + \beta_m e^{-k_m x}. \quad (28)$$

For a double pole, application of the biorthogonality properties (21) yields

$$C_{m,2}'' - k_m^2 C_{m,2} = 0 \quad \text{and} \quad C_{m,1}'' - k_m^2 C_{m,1} = k^2 \cos^2 kh C_{m,2} \quad (29)$$

which have solutions

$$C_{m,2}(x) = \gamma_m e^{k_m x} + \delta_m e^{-k_m x} \quad (30)$$

and

$$C_{m,1}(x) = \alpha_m e^{k_m x} + \beta_m e^{-k_m x} + \frac{1}{2} k x \cos^2 kh (\gamma_m e^{k_m x} - \delta_m e^{-k_m x}). \quad (31)$$

#### 5 Conclusion

This work is concerned with a simple model for the propagation of water waves in a porous medium. The model has been extended to a two-layer flow by Yu & Chwang<sup>4</sup> and the problem is again not self adjoint. This modified problem involves additional matching conditions at an intermediate depth and the theorems given by Coddington & Levinson<sup>3</sup>, and others, do not apply to this case. Thus, it is not clear that the expansion theorem is valid even when there are no double roots of the dispersion relation. This and other models are currently under further investigation.

#### References

1. Sollitt, C. K. & Cross, R. H. 1972 Wave transmission through permeable breakwaters. In *Proceedings of the 13th Conference on Coastal Engineering, Vancouver, 1827-1846*. ASCE.
2. Dalrymple, R. A., Losada, M. A. & Martin, P. A. 1991 Reflection and transmission from porous structures under oblique wave attack. *Journal of Fluid Mechanics*, **224**, 625-644.
3. Coddington, E. A. & Levinson, N. 1955 *Theory of Ordinary Differential Equations*. McGraw-Hill.
4. Yu, X. & Chwang, A. T. 1994 Wave motion through porous structures. *Journal of Engineering Mechanics*, **120**, 989-1008.

## A procedure to remove secularity in third-order numerical wave tanks

B. Molin, ESIM & Y. Stassen, Ifremer

### Introduction

Many 2D numerical wave tanks have been developed worldwide. Most of them tackle the fully nonlinear problem, but some are based on the Stokes expansion procedure  $\Phi = \epsilon \Phi^{(1)} + \epsilon^2 \Phi^{(2)} + \dots$ , and are restricted to first (linear) or second-order effects. At the eleventh Workshop in Hamburg Büchmann presented a code with a third-order extension (Büchmann, 96). A similar model has been developed more recently by Stassen (Stassen et al, 1998).

In Büchmann and Stassen's codes successive boundary value problems are solved at orders  $i = 1, 2, 3$ , with the free surface conditions given as (at  $y = 0$ )

$$\Phi_t^{(i)} + g\eta^{(i)} = f^{(i)} \quad (1)$$

$$\eta_t^{(i)} - \Phi_y^{(i)} = h^{(i)} \quad (2)$$

where  $f^{(i)}$  and  $h^{(i)}$  are zero at order  $i = 1$  and depend on the solution(s) obtained at the previous order(s) for  $i = 2, 3$ .

When a regular wave is being produced in the numerical tank, a problem that has been observed is that the third-order component to the wave elevation, associated with  $\Phi^{(3)}$ , tends to increase steadily in amplitude as the wave travels down the tank. As a result when  $\eta = \epsilon \eta^{(1)} + \epsilon^2 \eta^{(2)} + \epsilon^3 \eta^{(3)}$  is being recomposed at a finite value of  $\epsilon$  (for comparison with experimental results for instance), the third-order term  $\epsilon^3 \eta^{(3)}$  gradually overruns the second-order and first-order ones, invalidating the perturbation procedure. This is illustrated in figure 2.

This phenomenon is due to secularity. In the frequency domain the remedy is well known and consists in slightly modifying the wave number, the frequency being imposed by the wave maker motion. In deep water regular waves the wave number correction is simply  $\Delta k = -\epsilon^2 k$ ,  $k$  being the wave number  $\omega^2/g$ .

In the time domain, with the wave front gradually advancing over still water (and the generated waves not necessarily being regular), a different procedure must be sought for. A possible one consists in stretching the coordinate system, as is proposed below.

### Theory

We consider two coordinate systems  $(x, y)$  and  $(X, Y)$ ,  $(x, y)$  corresponding to the physical domain, and  $(X, Y)$  to the computational domain. Both are centered at the free surface wave maker intersection.

The mapping between the computational domain and the physical domain is given by

$$x = X + \epsilon^2 P(X, Y, t) \quad (3)$$

$$y = Y + \epsilon^2 Q(X, Y, t) \quad (4)$$

with the following restrictions on  $P$  and  $Q$ :

$$\nabla P = O(1) \quad \nabla Q = O(1) \quad P(0, Y, t) = 0 \quad Q(0, 0, t) = 0 \quad kQ(X, 0, t) = O(1)$$

$kP(X, Y, t)$  being unrestricted.

For the sake of convenience we will also assume that the waterdepth  $h$  is rather shallow, or  $kQ(X, -h, t) = O(1)$ , but the problem can be worked out without this assumption. (As a matter of fact it is even simpler when the waterdepth is infinite).

As a result the boundaries of the physical domain correspond to the following curves in the computational domain:

$$\begin{aligned} x = 0 & \quad (\text{wavemaker}) \quad \rightarrow X = 0 \\ y = 0 & \quad (\text{free surface}) \quad \rightarrow Y = -\epsilon^2 Q(X, 0, t) \\ y = -h & \quad (\text{bottom}) \quad \rightarrow Y = -h - \epsilon^2 Q(X, -h, t) \end{aligned}$$

The following step is to formulate the BVP satisfied by  $\Phi(x, y, t)$  in the computational domain  $(X, Y)$ . Partial derivatives are transformed by

$$\frac{\partial}{\partial x} = (1 - \epsilon^2 P_X) \frac{\partial}{\partial X} - \epsilon^2 Q_X \frac{\partial}{\partial Y} \quad (5)$$

$$\frac{\partial}{\partial y} = (1 - \epsilon^2 Q_Y) \frac{\partial}{\partial Y} - \epsilon^2 P_Y \frac{\partial}{\partial X} \quad (6)$$

$$\frac{\partial}{\partial t} \rightarrow \frac{\partial}{\partial t} - \epsilon^2 P_t \frac{\partial}{\partial X} - \epsilon^2 Q_t \frac{\partial}{\partial Y} \quad (7)$$

the time derivative being the eulerian one, at  $x$  and  $y$  fixed.

At orders 1 and 2 the BVP's are unchanged. At order 3 the Laplace equation for  $\Phi^{(3)}$  is maintained provided  $P$  and  $Q$  verify the Cauchy-Riemann conditions  $P_X = Q_Y$ ,  $P_Y = -Q_X$ , or  $P(X, Y, t) + iQ(X, Y, t) = f(X + iY, t)$ .

The boundary conditions on the wave maker, bottom and free surface are transformed as follows.

### Wave maker

For the sake of simplicity we assume the wave maker to be vertical at  $x = 0$ . The no-flow condition in the physical domain is of the type

$$\Phi_x^{(3)}(0, y, t) = g^{(3)}(y, t)$$

with  $g^{(3)}$  depending on the solutions at orders 1 and 2.

The condition in the computational domain is then

$$\Phi_X^{(3)}(0, Y, t) = g^{(3)}(Y, t) + P_X \Phi_X^{(1)} + Q_X \Phi_Y^{(1)} = g^{(3)}(Y, t) + P_X \Phi_X^{(1)} \quad (8)$$

since  $Q_X = P_Y \equiv 0$  at  $x = X = 0$ .

### Bottom ( $y = -h$ )

Similarly the no-flow condition  $\Phi_y^{(3)}(x, -h, t) = 0$  becomes

$$\Phi_Y^{(3)} - Q_Y \Phi_Y^{(1)} - P_Y \Phi_X^{(1)} - Q \Phi_{YY}^{(1)} = 0$$

at  $Y = -h$ , or

$$\Phi_Y^{(3)} = -\frac{\partial}{\partial X}(Q \Phi_X^{(1)}) \quad (9)$$

**Free surface** ( $y = 0$ )

The new conditions at  $Y = 0$  are

$$\Phi_t^{(3)} - P_t \Phi_X^{(1)} - Q_t \Phi_Y^{(1)} - Q \Phi_{YY}^{(1)} + g \eta^{(3)} = f^{(3)}(X, t) \quad (10)$$

$$\eta_t^{(3)} - P_t \eta_X^{(1)} - \Phi_Y^{(3)} + Q_Y \Phi_Y^{(1)} + P_Y \Phi_X^{(1)} + Q \Phi_{YY}^{(1)} = h^{(3)}(X, t) \quad (11)$$

where  $\eta(X, t) = \epsilon \eta^{(1)}(X, t) + \epsilon^2 \eta^{(2)}(X, t) + \epsilon^3 \eta^{(3)}(X, t)$ .

Thanks to the free surface conditions verified by  $\Phi^{(1)}$  and  $\eta^{(1)}$ , these two equations can be rewritten as

$$\frac{\partial}{\partial t} [\Phi^{(3)} - P \Phi_X^{(1)} - Q \Phi_Y^{(1)}] + g [\eta^{(3)} - P \eta_X^{(1)}] = f^{(3)} \quad (12)$$

$$\frac{\partial}{\partial t} [\eta^{(3)} - P \eta_X^{(1)}] - \frac{\partial}{\partial Y} [\Phi^{(3)} - P \Phi_X^{(1)} - Q \Phi_Y^{(1)}] = h^{(3)} \quad (13)$$

that is the same equations as in the secular case are obtained with  $\Phi^{(3)}(x, 0, t)$  being replaced by  $\Phi^{(3)}(X, 0, t) - P \Phi_X^{(1)} - Q \Phi_Y^{(1)}$  and  $\eta^{(3)}(x, t)$  replaced by  $\eta^{(3)}(X, t) - P \eta_X^{(1)}$ .

This result would have been obtained readily if one had assumed both  $kP$  and  $kQ$  to be  $O(1)$  at the free surface, through Taylor developments in  $X$  and  $Y$ . Actually only  $kQ = O(1)$  is required (and to be checked later).

The procedure to get rid of secularity is now straight-forward. Be  $\Phi_S^{(3)}$  and  $\eta_S^{(3)}$  the (secular) solutions obtained when  $P = Q = 0$ . Then  $\eta_S^{(3)}$  contains a secular component at the same spatial frequencies as  $\eta^{(1)}$ . This suggests to take  $P(X, 0, t)$  equal to the slowly-varying part (in  $X$  and  $t$ ) of  $-\eta_S^{(3)}/\eta_X^{(1)}$ . Then, hopefully,  $\eta^{(3)}$  will reduce to the expected small, high frequency components.

Once  $P$  has been thus determined on the free surface,  $P$  and  $Q$  are obtained in the whole computational domain through

$$P + iQ(Z) = \frac{i}{\pi} \int_{-\infty}^{\infty} \left[ \frac{P(\zeta, 0, t)}{\zeta - Z} - \frac{P(\zeta, 0, t)}{\zeta} \right] d\zeta \quad (14)$$

with  $Z = X + iY$  and  $P(-\zeta, 0, t) = -P(\zeta, 0, t)$ . Then the modified boundary conditions, at the wave maker and on the bottom, can be accounted for.

Figures 1 through 4 show some preliminary results relating to experiments carried out in the towing tank of Ecole Centrale de Nantes. The length of the tank is 63 m, the waterdepth 2.8 m, the wave period 2.1 s and the wave amplitude 0.12 m.

Figure 1, 2 and 3 show, 35 s after the wavemaker got started, values of  $\eta_X^{(1)}$ ,  $\eta_S^{(3)}$  and  $-\eta_S^{(3)}/\eta_X^{(1)}$  along the tank. Figure 4 shows, at different instants, values obtained for  $P$  at the free surface, through low-pass filtering. All these results are dimensional, corresponding to  $\epsilon = ka = 0.11$ . It can be seen that  $P$ , which is nothing but the distance the first-order wave profile must be shifted forward, slowly adjusts to the steady state solution  $P = k^2 a^2 X$  as the wave system gets established in the tank.

**References**

- BÜCHMANN, B. (1996). 'A 2-D numerical wave flume based on a third order boundary element model', Proc. 11th Int. Workshop Water Waves & Floating Bodies, Hamburg.
- STASSEN, Y., LE BOULLUEC M. & MOLIN, B. (1998). 'A high order boundary element model for 2D wave tank simulation', ISOPE.

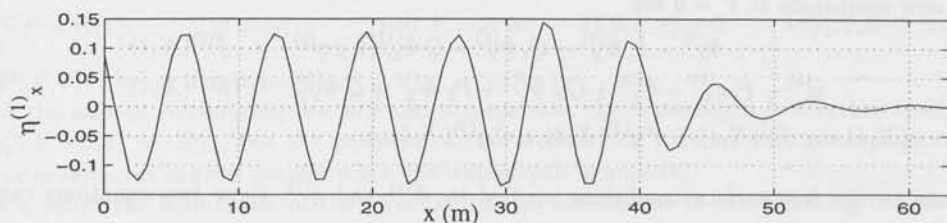


figure 1 :  $\eta_x^{(1)}$  along the tank at  $t=35$  s.

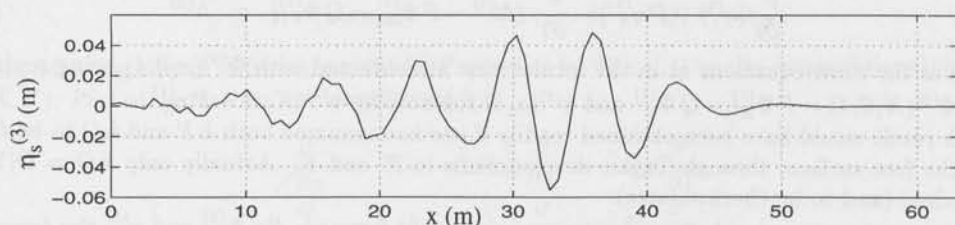


figure 2 :  $\eta_s^{(3)}$  along the tank at  $t=35$  s.

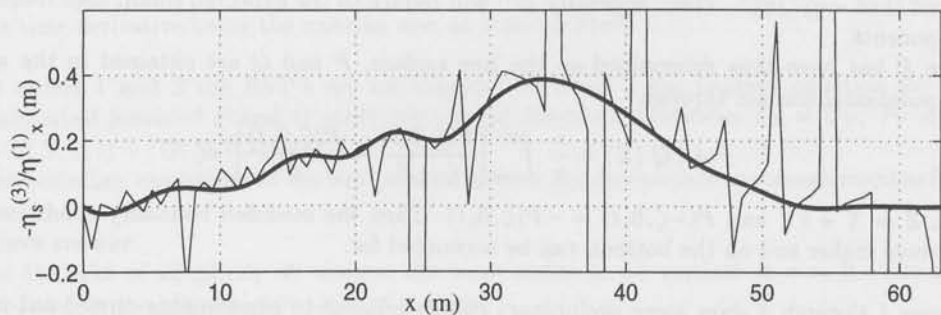


figure 3 :  $-\eta_s^{(3)}/\eta_x^{(1)}$  along the tank at  $t=35$  s.

The bold line shows results from low-pass filtering.

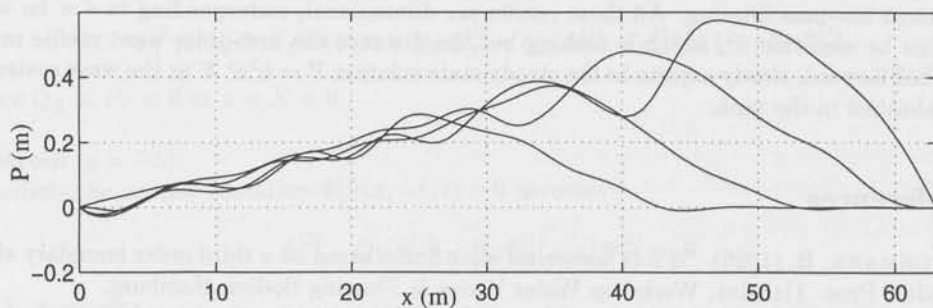


figure 4 :  $P$  obtained from low-pass filtering at  $t=30$  s,  $t=35$  s,  $t=40$  s and  $t=45$  s.

## Non-uniqueness in the water-wave problem: an example violating the inside John condition

by O. Motygin and N. Kuznetsov

*Laboratory for Mathematical Modelling of Wave Phenomena,  
Institute of Mechanical Engineering Problems, Russian Academy of Sciences*

### 1. Introduction

During the last decade uniqueness of the time-harmonic solution has been in the focus of much research in the linearized theory of water waves. A substantial breakthrough was the first example of non-uniqueness constructed by M. McIver (1996) in the two-dimensional water-wave problem. She applied the so-called inverse procedure which determines a physically admissible domain for a given solution instead of seeking a solution to the problem in a given domain. Developing this approach P. McIver & M. McIver (1997) obtained a non-uniqueness example for the axisymmetric water-wave problem, whilst Kuznetsov & Porter (1997) constructed a number of examples with different properties for the two-dimensional problem. Shortly after appearing the first non-uniqueness examples, one of the authors of the present work has proved the following uniqueness theorem for the two-dimensional problem (see Appendix in Linton & Kuznetsov 1997).

*Let two surface-piercing bodies be immersed symmetrically about the  $y$ -axis in deep water and satisfy the inside John (IJ) condition, that is, any vertical straight line through the portion of the free surface between the bodies, say  $F_0 = \{-b < x < b, y = 0\}$ , has no common points with the wetted bodies' contours.*

*Then the homogeneous water-wave problem has only trivial symmetric (antisymmetric) solution, if the inequality*

$$\pi \left( m + \frac{1}{4} \pm \frac{1}{4} \right) \leq \nu b \leq \pi \left( m + \frac{3}{4} \pm \frac{1}{4} \right) \quad (1)$$

*holds with the sign  $+$  ( $-$ ) for some  $m = 0, 1, \dots$*

This theorem means that the IJ condition is sufficient for uniqueness of symmetric/antisymmetric solution within the complementary intervals given by (1) for the non-dimensional spectral parameter  $\nu b$ . The examples constructed by Kuznetsov & Porter (1997), which include that of M. McIver (1996) as a particular case, show that this theorem can hardly be improved. The reason is that every interval where the symmetric solution is unique contains a subinterval of  $\nu b$ , for which there exists a two-body structure satisfying the IJ condition and trapping antisymmetric mode. The same result is shown to be true for the first three intervals where the antisymmetric solution is unique. Numerical calculations demonstrate that the same should be true for all intervals of  $\nu b$ , where (1) guarantees the uniqueness of antisymmetric solution.

The aim of the present work is to demonstrate that the IJ condition is not only sufficient, but also necessary for uniqueness in the intervals given by (1). We consider in detail the interval  $(\pi/2, \pi)$ , where the symmetric solution  $u^{(+)}$  is unique, and outline how our approach works for

other intervals. The idea of the proof is to construct a pair of bodies violating the IJ condition, trapping a symmetric mode and such, that  $\nu b \in (\pi/2, \pi)$  for them.

## 2. Statement of the problem

The small-amplitude two-dimensional motion of an inviscid, incompressible fluid under gravity is considered. We assume the motion to be  $\omega$ -periodic in time  $t$  and irrotational. Thus, it is described by a velocity potential  $\text{Re}\{u(x, y)e^{-i\omega t}\}$ , where  $(x, y)$  are Cartesian coordinates with the origin in the mean free surface and the  $y$ -axis directed vertically upwards.

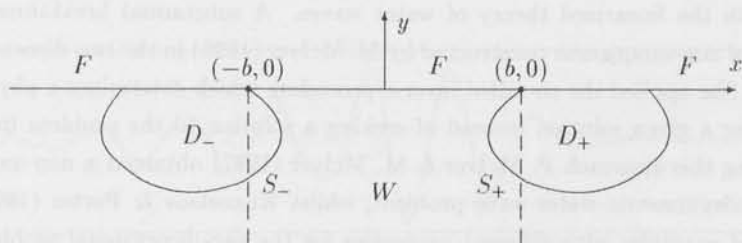


Figure 1: A definition sketch of the water domain.

Let  $W = \{-\infty < x < +\infty, y < 0\} \setminus (D_+ \cup D_-)$  denote the domain occupied by water. We assume  $W$  to have infinite depth and to be symmetric about the  $y$ -axis (see fig. 1). Two rigid surface-piercing bodies  $D_+$  and  $D_-$  are the mirror reflections of each other in the  $y$ -axis. The free surface is denoted by  $F$  and consists of three portions, two outside the bodies and one between them (it was referred to as  $F_0$ ); the wetted boundary of  $D_{\pm}$  is labelled  $S_{\pm}$ , and  $S = S_+ \cup S_-$ .

The eigenfunction  $u$  corresponding to a point eigenvalue  $\nu$  (usually referred to as trapped mode solution) must satisfy the following homogeneous boundary value problem:

$$\nabla^2 u = 0 \quad \text{in } W, \quad (2)$$

$$u_y - \nu u = 0 \quad \text{on } F, \quad (3)$$

$$\partial u / \partial n = 0 \quad \text{on } S, \quad (4)$$

and belong to the class of functions having the finite energy, that is,

$$\int_W |\nabla u|^2 dx dy + \nu \int_F |u|^2 dx < \infty. \quad (5)$$

Without loss of generality,  $u$  satisfying (2)–(5) may be considered to be real.

## 3. Trapped mode solution violating the IJ condition

To formulate the main result we need two functions. We define the first of them as follows:

$$u(x, y) = (2\nu)^{-1} [G_x(x, y; -\pi/\nu, 0) - G_x(x, y; \pi/\nu, 0)], \quad (6)$$

where the two-dimensional Green function is given by the usual formula (see Wehausen &

Laitone 1960)

$$G(x, y; \xi, \eta) = -\log |z - \eta| + \log |z - \bar{\zeta}| + 2 \int_{l_-} e^{k(y+\eta)} \frac{\cos k(x - \xi)}{k - \nu} dk,$$

$z = x + iy$ ,  $\zeta = \xi + i\eta$ , and  $l_-$  denotes the contour going along the positive half-axis and indented below at  $\nu$ . By the choice of the dipole points the integrals along indentations cancel in (6), and one immediately obtains that

$$u(x, y) = \frac{1}{\nu} \left[ \frac{x + \pi/\nu}{(x + \pi/\nu)^2 + y^2} - \frac{x - \pi/\nu}{(x - \pi/\nu)^2 + y^2} \right] + \int_0^\infty \frac{\sin k(\nu x - \pi) - \sin k(\nu x + \pi)}{k - 1} e^{k\nu y} dk,$$

where the integrand is bounded because the singularity in the denominator coincide with the zero of the numerator. Thus,  $u$  is a real harmonic function in the lower half-plane. Moreover,  $u(x, y)$  is even with respect to  $x$ , and the free surface boundary condition holds for it on  $\{x \neq \pm\pi/\nu, y = 0\}$ . The last integral is bounded as  $z \rightarrow \pm\pi/\nu$  as was shown by McIver (1996), and it decays as  $|z| \rightarrow \infty$  as follows from Bochner (1959) *Lectures on Fourier Integrals*, §§ 2.5, 8. Thus,  $u$  satisfies (5) in every fluid domain  $W$ , which does not contain a neighbourhood of the dipole points  $(\pm\pi/\nu, 0)$ .

The second required function is as follows:

$$v(x, y) = \frac{1}{\nu} \left[ \frac{y}{(x + \pi/\nu)^2 + y^2} - \frac{y}{(x - \pi/\nu)^2 + y^2} \right] + \int_0^\infty \frac{\cos k(\nu x - \pi) - \cos k(\nu x + \pi)}{k - 1} e^{k\nu y} dk,$$

that is,  $v$  is the streamfunction which corresponds to the velocity potential  $u$ , and has an arbitrary constant term to be equal to zero.

A family of fluid domains  $W$ , such that the IJ condition does not hold for  $W$  and  $u$  satisfies (2)–(5) in  $W$  can be constructed with the help of  $v$ . In fact, any streamline may be used

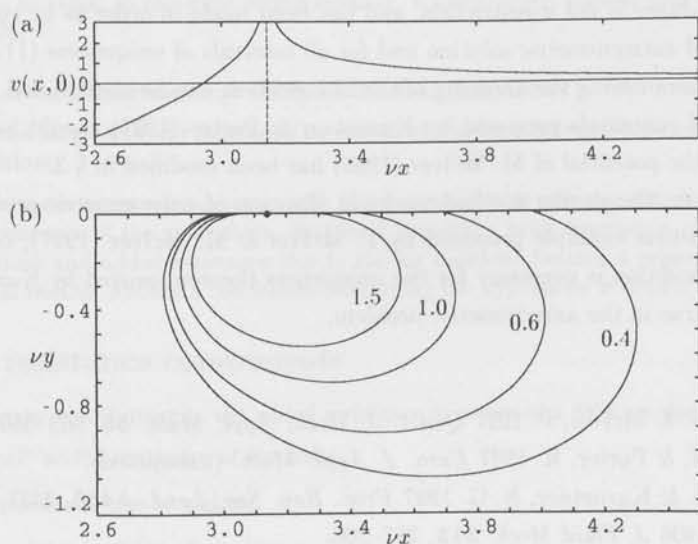


Figure 2: (a) the value of the streamfunction on  $y = 0$ , and (b) streamlines for  $v$ .

as  $S_+$ , if it has the following two properties. It connects with the positive  $x$ -axis on either side of the dipole point  $(\pi/\nu, 0)$ . The angle directed into  $W$  between the streamline and the positive  $x$ -axis is acute on the left of  $(\pi/\nu, 0)$ . On fig. 2(b) a number of streamlines defined by  $v(x, y)$  and having these properties are plotted, and on fig. 2(a) the graph of  $v(x, 0)$  is shown for convenience. Since  $v(x, y)$  is an odd function with respect to  $x$ , the reflection of  $S_+$  in the  $y$ -axis is also a streamline which we take as  $S_-$ . Now, let us formulate the main theorem concerning the existence of streamlines with these properties.

*For every level  $V > 0$  there exists only one streamline  $S_+(V) = \{(x, y) : v(x, y) = V\}$  with all internal points in  $\{x > 0, y < 0\}$  and the endpoints  $(x_V^{(\pm)}, 0)$ , such that  $x_V^{(\pm)} > 0$ ,  $\pm(x_V^{(\pm)} - \pi/\nu) > 0$ , and  $x_V^{(-)}\nu > 2\pi/3$ . For every streamline  $S_+(V)$  the IJ condition does not hold.*

We note that  $x_V^{(-)} = b$  for the water domain  $W$  having  $S_+(V)$  and its reflection in the  $y$ -axis as the wetted rigid contours. Thus, we have  $2\pi/3 < \nu b = \nu x_V^{(-)} < \pi$  for the defined  $W$ . Since  $u$  given by (6) delivers a symmetric eigenfunction satisfying (2)–(5) in this domain  $W$ , the immediate consequence of the main theorem is the following corollary:

*The IJ condition is necessary for the interval  $(\pi/2, \pi)$  to be free of non-dimensional point eigenvalues  $\nu b$  corresponding to symmetric eigenfunctions.*

#### 4. Concluding remarks

We restricted ourselves with the case of symmetric solution and of the uniqueness interval  $\pi/2 < \nu b < \pi$ , where  $2b$  is the distance between two surface-piercing bodies along the free surface. Our choice is not a restriction, and has been made in order to be specific. For either symmetric and antisymmetric solution and for all intervals of uniqueness (1) examples of non-uniqueness, guaranteeing the necessity of the IJ condition, can be constructed. For this purpose the non-trivial potentials proposed by Kuznetsov & Porter (1997) should be modified in the same way as the potential of M. McIver (1996) has been modified in § 3.

Furthermore, the similar method works in the case of axisymmetric problem. Modifying the non-uniqueness example proposed by P. McIver & M. McIver (1997), one easily obtains that the IJ condition is necessary for the uniqueness theorem proved by Kuznetsov & McIver (1997) to be true in the axisymmetric problem.

#### References

- Kuznetsov, N. & McIver, P. 1997 *Quart. J. Mech. Appl. Math.* **50**, 565–580.  
 Kuznetsov, N. & Porter, R. 1997 *Euro. J. Appl. Math.* (submitted).  
 Linton, C. M. & Kuznetsov, N. G. 1997 *Proc. Roy. Soc. Lond.* **A453**, 2437–2460.  
 McIver, M. 1996 *J. Fluid Mech.* **315**, 257–266.  
 McIver, P. & McIver, M. 1997 *Quart. J. Mech. Appl. Math.* **50**, 165–178.  
 Wehausen, J. V. & Laitone, E. V. 1960 *Handbuch der Physik* **9**, 446–778.

# Added Resistance of Surface Effect Ships

Joost Moulijn

Ship Hydromechanics Laboratory, Delft University of Technology

## 1 Introduction

This abstract presents some results from a PhD research project on seakeeping of Surface Effect Ships (SESs). The project is jointly sponsored by MARIN and the Royal Netherlands Navy.

A Surface Effect Ship is a hybridization of a catamaran and a hovercraft. An air cushion is enclosed by the side hulls, the deck, the water surface and flexible seals at the bow and stern (Figure 1). The bow seal is usually of the *finger*-type; a row of vertical loops of flexible material which are open to the cushion. The stern seal is usually of the *bag*-type; a horizontal loop of flexible material which is open to the sides, where the bag is closed by the side-hulls. Internal webs restrain the aft-side of the bag, and divide the bag into several (usually two or three) lobes. The bag is pressurized at a slightly higher pressure than the air cushion. Most of the vessel's weight is carried by the air cushion. The remainder is carried by the buoyancy of the hulls. The air cushion is pressurized by a system of fans. Air leaks under the seals from the cushion.

Up to now Surface Effect Ships were mainly operating in sheltered waters. In these days however there is an increasing interest in large SESs sailing in open seas. The design of these large vessels requires an accurate prediction method for motions and added resistance. The development and validation of such a method is the goal of this research project.

This abstract will focus on the topic of added resistance (i.e. the extra resistance of the vessel due to the ambient waves). SESs are found to have a large speed loss when sailing in waves, although Ehrenberg[1] states that an SES has much less speed loss than a catamaran. At MARIN an added resistance about as large as the calm water resistance was measured. For normal ships added resistance appears to be equal to the wave height squared. Kapsenberg[2] showed that this relation does *not* hold for SESs.

The aim of this extended abstract is to verify the following hypothesis:

**The origin of the large added resistance in waves of Surface Effect Ships can be attributed to the air cushion.**

The next section presents an argumentation for this hypotheses. It also presents a simple expression for the added resistance of the air cushion. Section 3 presents a brief description of a computational method for motions and added resistance due to the air cushion. Section 4 presents computational and experimental results. Finally a conclusion concerning the hypothesis is drawn.

## 2 Added resistance components

Several components contributing to the added resistance in waves of a SES are distinguished:

- the "normal" added resistance of the hulls
- the extra resistance due to sinkage
- the extra resistance of the air cushion

The "normal" added resistance of the hulls should be small because only a minor part of the vessel's weight is carried by the buoyancy of the hulls and because the hulls are very slender.

When an SES is sailing in a seaway, the amount of air leakage from the cushion increases as the ambient cause large air gaps under the seals. This causes a decrease of the excess pressure in the air cushion, so a larger part of the vessel's weight has to be carried by the buoyancy of the hulls. Therefore the vessel will sink into the water, and the resistance of the hulls will increase. Kapsenberg[2] showed that the extra resistance due to this sinkage is relatively small.

As the first two components are small, the major part of the large added resistance of SESs must be caused by the air cushion. The (normal) resistance of the air cushion follows from:

$$R_{ac} = p_c \cdot (\zeta_b - \zeta_s) \cdot B_c \quad (1)$$

where  $p_c$  is the excess pressure in the air cushion,  $\zeta_b$  and  $\zeta_s$  are the mean wave height at the bow and stern seal respectively, and  $B_c$  is the width of the cushion. The increase of the mean value of  $R_{ac}$  is the added resistance of the air cushion. The resistance due to the momentum of the air flows into and out of the cushion is neglected. This momentum drag is only small because of the low density of air.

As the added resistance of the air cushion is supposed to give the largest contribution to the total added resistance of SESs, it was decided to focus on this component first. It can be calculated easily using equation (1).

### 3 Computational method

In this section the computational method for motions and air cushion resistance is briefly described. A more complete description can be found in reference [3].

First some basic assumption of the method are presented. The excess pressures in the cushion and stern seal plena are constant in space. This implies that acoustic phenomena of the air in the cushion cannot be resolved (i.e. the cobblestone effect is neglected). Further, the motions of the vessel are assumed to be small. This implies that linear equations of motion and linear hydrodynamics can be used. The dynamics of the air cushion are highly non-linear. Therefore the motions and excess pressures have to be solved in a time simulation procedure. Up to now only heave and pitch displacement are considered.

Next to the unknown heave and pitch displacement two additional unknowns occur: the excess pressure in the cushion plenum  $p_c$ , and the excess pressure in the stern seal plenum  $p_s$ . Therefore two additional equations are needed. These equations follow from the combination of the equation of continuity for a plenum with the equation of state for the air in that plenum, which is taken to be the isentropic gas law. They represent the dynamical behavior of the air in the cushion and seal plena. Especially the terms representing the leakage of air from the cushion are highly non-linear. When the relative wave height at the seals is large, no air leakage will occur. When this relative wave height becomes smaller the seals may leave a gap. The air leakage flow is proportional to the area of this gap. The sudden opening of a leakage gap cannot be linearized.

The hydromechanical problem is solved using a 3-dimensional Rankine panel method. The boundary value problem was linearized around the undisturbed flow (i.e. Neumann-Kelvin linearization). The interaction of the air cushion with the wave surface is taken into account. Attention has been payed to the flow around the transom sterns. The problem is solved in the frequency domain. The frequency domain results of the panel method are transformed to the time domain using the theory of Cummins[4] and Ogilvie[5].

The stern seal geometry and force are computed using a two-dimensional model (longitudinal plane). The curvature of the wave surface is neglected, which is reasonable for not too short waves. Gravitational and inertial forces acting on the seal canvas are also neglected. The canvas is assumed to

have no bending stiffness. The dynamic pressure distribution which occurs under the seal due to air leakage is taken into account. The seal may either touch the water surface or leave a leakage gap.

## 4 Results

This section presents results for the HYDROSES target vessel; a large SES (cushion length is about 145m) which sails at a speed of 45 Kn. The computational results will be compared with experimental results of MARIN.

Figure 2 and Figure 3 present the RAOs for heave motions and cushion excess pressure. Results for several levels of wave steepness are shown. The agreement is good. The non-linear cushion dynamics appear to have only a small effect on the heave and pressure amplitude. The non-linear cushion dynamics manifest themselves most prominently as sinkage and drop of the mean cushion pressure.

Figure 4 presents the mean resistance of the air cushion in regular waves. Again results for several levels of wave steepness are shown. Contrary to expectations the resistance decreases in waves. This is caused by a drop of the mean cushion pressure. The smaller excess pressure in the air cushion causes a smaller (steady) wave resistance of the air cushion. This decrease of the air cushion resistance is counteracted by an increasing resistance of the hulls due to sinkage, which has not been computed.

Figure 5 presents the added resistance divided by the wave height squared. The computational data only include the added resistance of the air cushion, while the MARIN data include all added resistance components. There seems to be no correlation between the computational and experimental results at all. The experimental data show that the added resistance is not proportional to the wave height squared. Sometimes the measured added resistance is even negative. The hypothesis that the origin of the large added resistance in waves of SESs can be attributed to the air cushion cannot be confirmed.

## 5 conclusion

The origin of the large added resistance of Surface Effect Ships is not clear yet. According to the calculations the air cushion does not give a large contribution to added resistance. The other components are not likely to be large either. Therefore new model experiments will be carried out. These experiments will be focused on the origin and magnitude of added resistance of Surface Effect Ships.

## References

- [1] H.D. Ehrenberg. *Das Verhalten von Luftkissenkatamaranen (SES) im Seegang*. PhD thesis, Institut für Schiffbau der Universität Hamburg, 1996.
- [2] G.K. Kapsenberg. Seakeeping behaviour of a ses in different wave directions. In *Proc. Second International Conference on Fast Sea Transportation (FAST'93)*, 1993.
- [3] J.C. Moulijn. Non-linear motions of surface effect ships. In *RINA International Conference on Air Cushion Vehicles (ACVs)*, 1997.
- [4] W. E. Cummins. The impulse-response function and ship motions. *Schiffstechnik*, 9(47):101-109, 1962.
- [5] T. F. Ogilvie. Recent progress toward the understanding and prediction of ship motions. In *Proc. of 5th Symposium on Naval Hydrodynamics*, 1964.

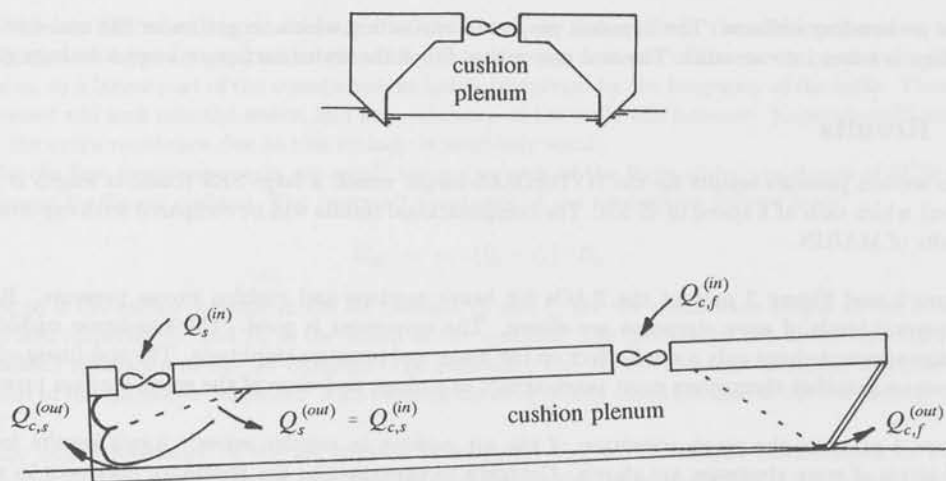


Figure 1: Longitudinal and transverse cut of a Surface Effect Ship

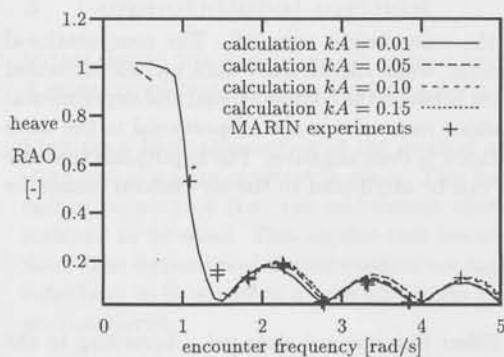


Figure 2: Heave motions of the HYDROSES target vessel

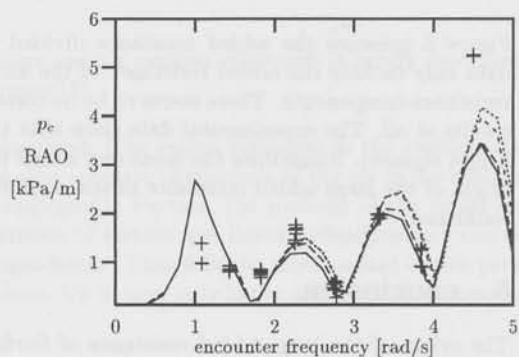


Figure 3: Cushion pressure response of the HYDROSES target vessel

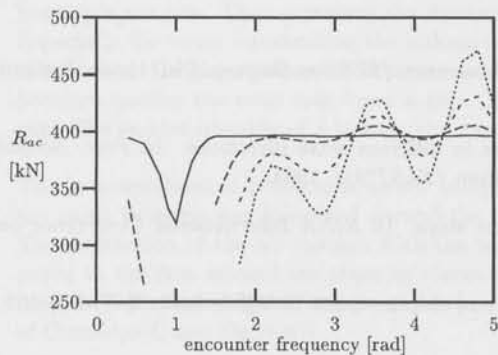


Figure 4: Resistance of the air cushion of the HYDROSES target vessel

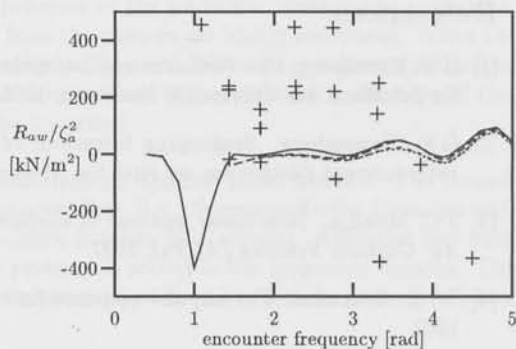


Figure 5: Added resistance operator of the HYDROSES target vessel

## Hydrodynamic analysis of the McIver toroid

J. N. Newman

Department of Ocean Engineering, MIT, Cambridge, MA 02139, USA

Recently M. & P. McIver have shown, for certain floating bodies of finite dimensions, that a homogeneous solution of the linear water-wave radiation problem exists at a particular frequency  $\omega_0$  and corresponding wavenumber  $k_0$ . In two dimensions the body is generated by a pair of point sources separated by an odd multiple of a half wavelength. In three dimensions the body is a toroid, generated by a ring source of radius  $r = c$ , where  $k_0 c$  is a zero of the Bessel function  $J_0$ . In both cases an interior free surface exists, similar to a 'moon pool'.

In discussions of two papers [1,2] at the last Workshop, questions were raised concerning (1) the local behavior of the added mass as  $k \rightarrow k_0$  (damping was not mentioned explicitly), and (2) the conjecture that standard numerical methods would fail in the same limit. The present work is intended to address these issues, in the three-dimensional context, by applying the radiation/diffraction panel code WAMIT to the McIver toroid.

### Geometrical construction

The first task is to consider the stream surface induced by a ring source of radius  $c$ . Nondimensional coordinates are used, with  $c = 1$ .

In [3] the velocity potential for a ring source is evaluated using analytic integration around the circle, but the remaining semi-infinite integral in wavenumber space is evaluated numerically with a truncation correction. A complementary procedure is followed here, using the subroutine for a point source based on the algorithms described in [4]. The Rankine singularity  $1/R$  is replaced by elliptic integrals. The remaining part of the free-surface point source is integrated around the ring using an adaptive Gauss-Chebyshev quadrature. The wavenumber is fixed, with  $k = j_{0,1} = 2.4048\dots$ , the first zero of  $J_0$ . The streamlines, defined by the relation  $\phi_r dz - \phi_z dr = 0$ , are traced by Runge-Kutta integration. This procedure is easily extended to a submerged ring source, or to a finite fluid depth, with typical results shown in Figure 1. For the case of zero submergence in a fluid of infinite depth the results agree within graphical precision with the body contours shown in [3].

### Radiation and diffraction analysis

The radiation and diffraction potentials on the body surface are evaluated from Green's theorem using the free-surface source potential as the Green function. The fluid depth is assumed infinite and the toroid is generated by rotating the outermost contour shown in Figure 1 about the vertical  $z$ -axis. Three different panelizations are used, with 512, 2048, and 8192 panels on the complete submerged surface. Except where otherwise noted, the irregular-frequency effects have been removed by imposing a Neumann condition on the plane  $z = 0$  inside the body. Figure 2 shows the discretization with 2048 panels on the submerged surface and 1600 additional panels on  $z = 0$  inside the body, giving a total of 3648 panels. Since two planes of symmetry are utilized, the total number of unknowns is reduced by a factor of 4.

The parameters evaluated include the heave added-mass, damping, and exciting-force coefficients, and the free-surface elevation at the center of the moon pool in the diffraction problem. The added-mass and damping coefficients are nondimensionalized by the factors  $\rho c^3$  and  $\rho c^3 \omega$ , respectively, where  $\rho$  is the fluid density and  $c$  the radius of the ring source. The exciting force is nondimensionalized by the factor  $\rho g c^2 A$ , where  $A$  is the incident-wave amplitude. The free-surface elevation is nondimensionalized by  $A$ . Approximately 200 closely-spaced wavenumbers have been used in the computations to define the details shown.

Figure 3 shows the added-mass and damping coefficients. Two sets of curves are included, where the effects of irregular frequencies are present (dashed) or removed (solid), to emphasize the distinction between the irregular frequencies and the physically relevant moon-pool resonance. The resonance, which occurs near the theoretical value  $k = 2.4048$ , is present in both sets of curves. The two extra singularities in the dashed curves are due to the irregular frequencies which exist in the vicinity of  $k = 1.51$  and  $2.81$ . Figure 4 compares the results based on the three different discretizations, in the vicinity of resonance. As  $k \rightarrow k_0$  the number of panels must be increased to achieve a given accuracy. The peak of the damping coefficient is relatively narrow, and within this resonant regime the numerical results are not reliable as indicated by the negative damping peak for the intermediate discretization.

The precise wavenumber where resonance occurs depends on the number of panels, and differs according as whether or not the irregular-frequency removal algorithm is used. Figure 5 shows the wavenumber at which resonance occurs in each case, determined from the values of  $k$  at which the added mass passes through zero and the other parameters achieve their maximum amplitudes. As the number of panels increases both resonant wavenumbers tend to the correct theoretical value, with errors which appear to be inversely proportional to the number of panels.

Figure 6 shows the results from the diffraction solution including the moon-pool elevation and exciting force. The exciting force is evaluated both directly from integration of the diffraction pressure, and indirectly using the Haskind relations. Differences between the two methods are noticeable in the vicinity of the resonant wavenumber, where the diffraction exciting force has a very sharp peak and the width of the Haskind peak is somewhat greater. The exciting force and damping vanish at  $k = 1.84\dots$

An explanation of the results in the resonant regime can be developed, along similar lines to the large added-mass and damping variations for bodies in channels, or submerged close to the free surface. Thus we assume that the solution matrix is singular, with a pole in the complex wavenumber plane. With the complex time factor  $e^{i\omega t}$  the pole is generally above the real axis, but for the McIver toroid the pole is on the real axis at  $k = k_0 = j_{0,1}$ . Each discretized body is a perturbation of the toroid, with the pole shifted above the real axis by a small distance  $\epsilon$ . As the number of panels tends to infinity,  $\epsilon \rightarrow 0$ . These assumptions imply that the added-mass and damping coefficients are approximated in the forms

$$A = \bar{A} + A_0 \frac{k - k_0}{(k - k_0)^2 + \epsilon^2}, \quad B = \bar{B} + B_0 \frac{\epsilon}{(k - k_0)^2 + \epsilon^2}. \quad (1)$$

where  $\bar{A}$  and  $\bar{B}$  are bounded near  $k = k_0$ ,  $B_0 > 0$ , and  $A_0 = -B_0$ . The numerical results in Figures 3-4 are consistent with these approximations. The singular behavior of the added mass occurs over a relatively broad band of wavenumbers, with the limiting form of the singularity proportional to  $(k - k_0)^{-1}$ , whereas the damping coefficient is similar to a delta-function. For an axisymmetric body the Haskind relations can be used to show that the damping coefficient is proportional to the square of the exciting force. Thus the singularity in the exciting force is weaker than for the damping coefficient, but with the same narrow width  $O(\epsilon)$ . Assuming that the diffraction pressure is singular in the same manner, the amplitude of the free-surface elevation in the moon pool is similar. These conjectures are consistent with the results shown in Figure 6.

Further details are given in a paper which has been submitted for publication in the Journal of Engineering Mathematics Special Edition on Ocean Mechanics. I am indebted to Dr. C.-H. Lee and Dr. P. McIver for substantive discussions and assistance.

## References

1. M. McIver, Resonance in the unbounded water wave problem. *Proceedings of the 12th IWWFEB, Carry-le-Rouet* (1996) 177-181.
2. P. McIver & N. Kuznetsov. On uniqueness and trapped modes in the water-wave problem for a surface-piercing axisymmetric body. *Proceedings of the 12th IWWFEB, Carry-le-Rouet* (1996) 183-187.
3. P. McIver and M. McIver, Trapped modes in an axisymmetric water-wave problem. *Quart. J. Mech. Appl. Math.* 50 (1997) 165-178.
4. J. N. Newman, Approximation of free-surface Green functions. In: P. A. Martin and G. R. Wickham (eds.), *Wave Asymptotics*. Cambridge, UK: Cambridge University Press (1992) 107-135.

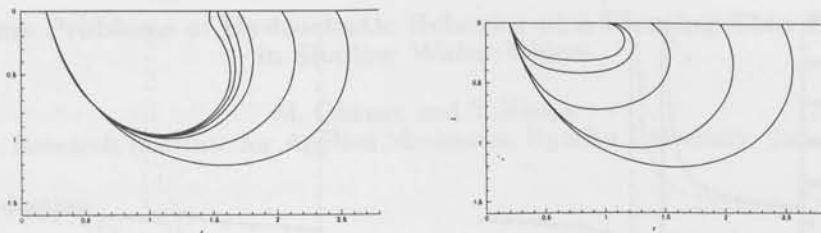


Figure 1: Contours of cross-sections generated by a ring source. In the left figure the source is submerged at the depths  $\zeta = 0, 0.2, 0.25, 0.26, 0.265, 0.269$ , respectively, proceeding from the outermost to the innermost section; the fluid depth is infinite. In the right figure the source is in the free surface and the fluid depths are  $h = \infty, 2.0, 1.0, 0.5, 0.36$ . In both cases the inner radius is fixed at 0.2.

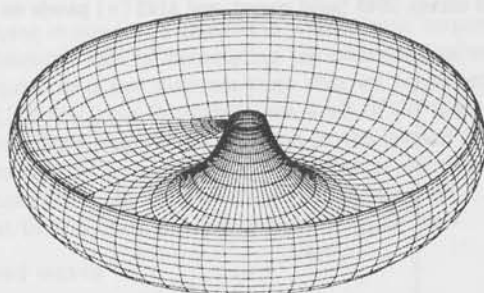


Figure 2: Perspective view of the body panelization, generated from the outermost contour in Figure 2, with 32 cosine-spaced segments along the contour and 64 equally-spaced azimuthal segments, giving a total of 2048 panels on the submerged surface. The 45°-sector of the interior free surface shows the additional panels used for the removal of irregular-frequency effects.

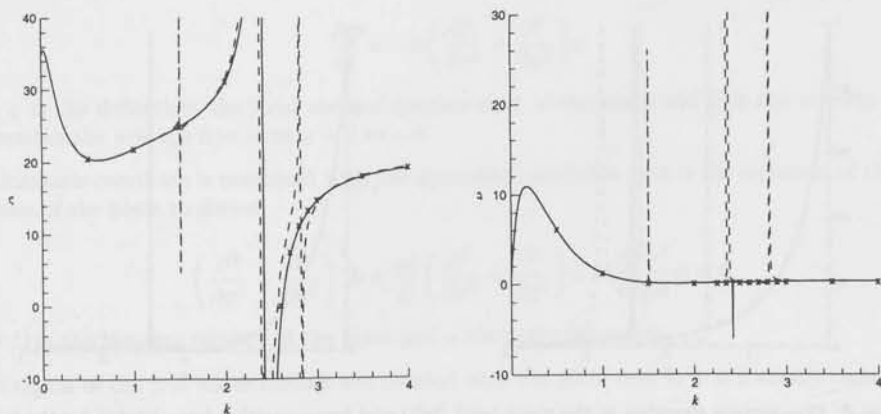


Figure 3: Heave added mass (left) and damping (right). The dashed curves include irregular-frequency effects, which are removed in the other results. The dashed and solid curves denote computations using 2048 panels on the body and 'x' represents computations with 8192 panels.

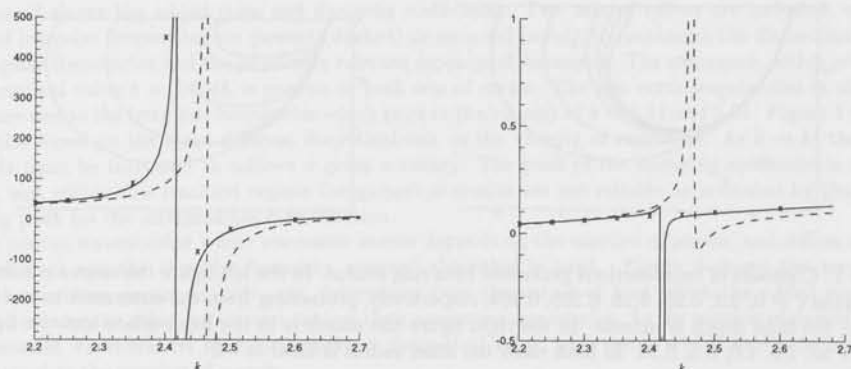


Figure 4: Added mass (left) and damping (right) in the vicinity of resonance, showing the convergence of results using 512 (dashed curve), 2048 (solid curve), and 8192 (x) panels on the submerged body surface.

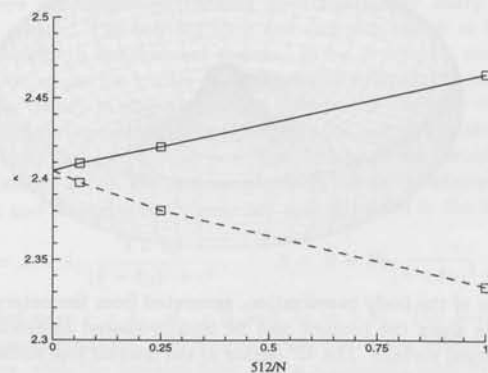


Figure 5: The resonant wavenumber for each discretization, showing the convergence to the theoretical limit  $j_{0,1} = 2.4048\dots$ . The dashed curve is based on computations including the irregular-frequency effects.

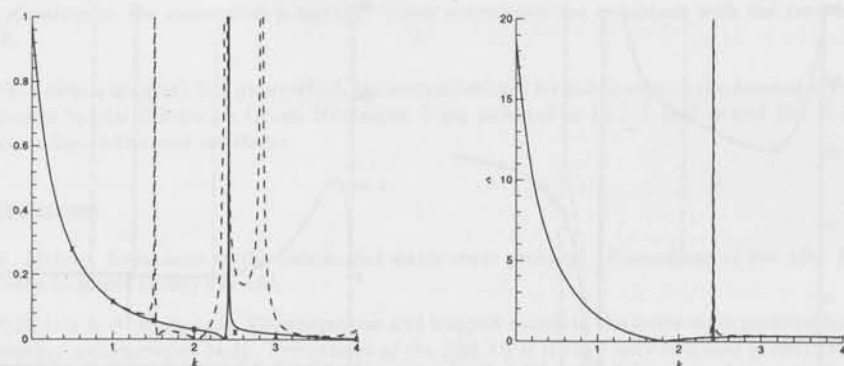


Figure 6: Free-surface elevation in the moon pool (left) and heave exciting force (right) for the body fixed in incident waves. The dashed curve in the left figure includes irregular-frequency effects, and the marks 'x' represent computations with 8192 panels. The dashed curve in the right figure represents the exciting force based on the Haskind relations.

## Some Problems of Hydroelastic Behavior of a Floating Thin Plate in Shallow Water Waves

M. Ohkusu and Y. Nanba

Research Institute for Applied Mechanics, Kyushu University, Japan

### 1. Introduction

Analysis of the vibration of a large but thin floating plate, a conceptual configuration of floating airports, when it is modeled as a membrane sheet of small bending rigidity on the water surface, is extremely simplified in the framework of linear shallow water theory. There is no reason that we do not use the linear shallow water theory to discuss the behaviors of floating airports in waves. The shallow water approximation is rather more realistic; very large structures like the floating airports are supposed to be located not offshore but near-shore. Consequently the horizontal size of them and wave length of our concern are very large compared with the water depth.

In this report we present some examples of analysis of hydroelastic response of a thin plate to waves in shallow water theory. Essential idea of formulating the boundary value problem to determine the plate deflection and the fluid flow is not different from that we presented in the papers (Ohkusu & Nanba (1996), (1997)) at 11th and 12th Workshop; the draft of the plate is assumed very small and the kinematic condition underneath the plate is imposed on the level of calm water surface. Equation of the plate vibration is combined with the kinematic condition to derive a quasi free surface condition for waves on the plate representing the vertical deflection of the plate. Difference is that all those formulations are carried out by the linear shallow water.

### 2. Elongate plate in head waves

Analysis of vibration of a thin plate of elongate form in waves at oblique incidence is straightforward in the linear shallow water theory. We present here the analysis not in oblique waves but in head waves. We assume the plate width  $2b$  is very small compared with the length  $L$  ( $\varepsilon = 2b/L$ ). Water depth  $h$  is constant and shallow compared with other length scale.  $z$  axis is vertically upward and the  $x-y$  plane coincides with calm water surface. The plate is on  $z = 0$  surface and occupies it at  $0 \leq x \leq L, -b \leq y \leq b$

Under the plate we have the kinematic condition

$$\frac{\partial \zeta}{\partial t} = -h \left( \frac{\partial^2}{\partial x^2} + \frac{\partial^2}{\partial y^2} \right) \phi \quad (1)$$

where  $\zeta$  is the deflection, the local vertical displacement of the plate and  $\phi$  is the velocity potential representing the average flow from  $z = 0$  to  $-h$ .

The kinematic condition is combined with the dynamical condition that is the equation of the vertical vibration of the plate to derive

$$\left( \frac{\partial^2}{\partial x^2} + \frac{\partial^2}{\partial y^2} \right)^3 \phi + \frac{\rho g}{D} \left( \frac{\partial^2}{\partial x^2} + \frac{\partial^2}{\partial y^2} \right) \phi + \frac{\rho g \omega^2}{D g h} \phi = 0 \quad (2)$$

where  $D$  is the bending rigidity of the plate and  $\omega$  the wave frequency.

In the region of the free water surface not covered with the plate over it  $\phi$  will satisfy the equation

$$\left( \frac{\partial^2}{\partial x^2} + \frac{\partial^2}{\partial y^2} \right) \phi + \frac{\omega^2}{g h} \phi = 0 \quad (3)$$

The kinematic condition at this part is identical to the equation (1)

We consider the case that incident wave of wave number  $k(=\omega/\sqrt{gh})$  are head on the plate from the direction of the positive  $x$ . When we assume the plate is elongate in the  $x$  direction and  $kb = O(1)$ , the following form of the solution will be reasonable.

$$\phi(x, y) = \psi(x, y)e^{-ikx} \quad (4)$$

Sufficiently away from the front edge at  $x = 0$ ,  $\psi$  is a slowly varying function of  $x$ . Hereafter we suppress the time-dependent term  $e^{i\omega t}$  in the formulation.

To the lowest order of approximation equation (4) in the region  $|y| = O(\varepsilon^{1/2})$  is rewritten as

$$-2ik \frac{\partial \psi}{\partial x} + \frac{\partial^2 \psi}{\partial y^2} = 0 \quad (5)$$

Substitute (4) into the plate equation (2) and retain the lowest order terms considering  $\partial/\partial y = O(\varepsilon^{-1})$  on the plate, we have

$$\left(-k^2 + \frac{\partial^2}{\partial y^2}\right)^3 \psi = 0 \quad (6)$$

Solution of equation (6) is straightforward. It will be written in the form

$$\psi = [a_1(x) + a_3(x)y + a_5(x)y^2]e^{ky} + [a_2(x) + a_4(x)y + a_6(x)y^2]e^{-ky} \quad (7)$$

$\psi$  given by (7) must satisfy the edge condition representing zero shear force and zero bending moment at  $y = \pm b$ . The edge conditions to the same order of approximation as equation (5) are the following four linear equations of  $a_j$

$$[a_1(x)P_1(y) + a_3(x)P_3(y) + a_5(x)P_5(y)]e^{ky} + [a_2(x)P_2(y) + a_4(x)P_4(y) + a_6(x)P_6(y)]e^{-ky} = 0 \quad (8)$$

at  $y = \pm b$

$$[a_1(x)Q_1(y) + a_3(x)Q_3(y) + a_5(x)Q_5(y)]e^{ky} + [a_2(x)Q_2(y) + a_4(x)Q_4(y) + a_6(x)Q_6(y)]e^{-ky} = 0 \quad (9)$$

at  $y = \pm b$

Here

$$P_{1,2}(y) = k^4, P_{3,4}(y) = \pm 4k^3 + k^4 y, P_{5,6}(y) = 12k^2 \pm 8k^3 y + k^4 y^2 \quad (10)$$

$$Q_{1,2}(y) = \pm k^5, Q_{3,4}(y) = 5k^4 \pm k^5 y, Q_{5,6}(y) = \pm 20k^3 + 10k^4 y \pm k^5 y^2 \quad (11)$$

$\psi$  on the plate given by equation (7) must match with the solution of (5) on the free water surface. The solution of (5) symmetrical in  $y$  for the head waves (Tuck (1965), Mei & Tuck (1980)) is

$$\psi = 1 - \frac{1+i}{2\sqrt{\pi k}} \int_0^x d\xi \frac{V(\xi)}{\sqrt{x-\xi}} e^{iky^2/2(x-\xi)} \quad (12)$$

Matching condition will be formulated following Mei & Tuck (1980). When  $y$  approaches zero (the breadth of the plate is of the order  $O(\varepsilon)$ ),  $\psi$  of (12) will become

$$\psi = \psi_0(x) + V(x)|y| \quad (13)$$

where

$$\psi_0(x) = 1 - \frac{1+i}{2\sqrt{\pi k}} \int_0^x d\xi \frac{V(\xi)}{\sqrt{x-\xi}} \quad (14)$$

Matching conditions are that mass flux and energy flux given by (7) and (13) must be equal respectively at  $y = \pm b$ . They are

$$[a_1(x) + a_3(x)y + a_5(x)y^2]e^{ky} + [a_2(x) + a_4(x)y + a_6(x)y^2]e^{-ky} = \psi_0(x) \quad \text{at } y = \pm b \quad (15)$$

$$\begin{aligned} & [a_1(x)k + a_3(x)(ky + 1) + a_5(x)(ky^2 + 2y)]e^{ky} \\ & - [a_2(x)k + a_4(x)(ky - 1) + a_6(x)(ky^2 - 2y)]e^{-ky} = \pm V(x) \quad \text{at } y = \pm b \end{aligned} \quad (16)$$

Our solution must be symmetrical in  $y$  and therefore  $a_1 = a_2$ ,  $a_3 = -a_4$ ,  $a_5 = a_6$ . Four linear equations (8), (9), (15) and (16) for  $y = +b$  determine four constants  $a_j$  ( $j = 1, 3, 5$ ) and  $\psi_0(x)$ , which are linear to  $V(x)$  such as  $a_j(x) = A_j V(x)$  and  $\psi_0(x) = \alpha V(x)$ .  $A_j$  and  $\alpha$  are independent of  $x$ . Their algebraic expression is lengthy and not given here. Those solutions and equation (14) give an Abel integral equation

$$\frac{1+i}{2\sqrt{\pi k}} \int_0^x d\xi \frac{V(\xi)}{\sqrt{x-\xi}} = 1 - 2V(x)[(A_1 + A_5 b^2) \cosh kb + A_3 b \sinh kb] \quad (17)$$

The solution  $V(x)$  of (17) is given in the form of the complementary error function and eventually determines the deflection  $\zeta$  of the plate.

### 3. Wide plate in head waves

Floating airports are generally of elongate form. Their width is, however, very large compared with the length of incident waves. The assumption of  $kb = O(1)$  as employed in the previous section is not always practical. In this section we consider a plate extending from  $x = 0$  to  $x = +\infty$  and from  $y = 0$  to  $y = -\infty$ ; the plate occupies a quarter of the whole water plane. Other 2/3 of the plane is the free water surface. Incident waves uniform in  $y$  direction of the wave number  $k$  come from  $x = -\infty$ . Here we are concerned with the plate deflection away from the front edge at  $x = 0$ .

Effect of the waves propagating in the region of the free water surface  $y \geq 0$  to the plate deflection is analyzed almost the same way as in the previous section. The solution is given in the form (4) and  $\psi$  on the plate part is given by (7) with  $a_2 = a_4 = a_6 = 0$  for the deflection to vanish far away ( $y \sim -\infty$ ) from the edge at  $y = 0$ . (7) can be matched with the solution on the free water part given in the form of (12) in the same manner as in the previous section.

The incident waves will come into the plate through the front edge at ( $x = 0, y \leq 0$ ). They are given by

$$\phi = A_0 e^{-ik_0 x} \quad (18)$$

where  $k_0$  is positive one of two real roots of the equation

$$k_0^6 + \delta k_0^2 - \delta k^2 = 0 \quad (19)$$

and  $A_0$  is determined by the edge conditions at  $x = 0$ . Other wave components are all zero because we are away from the edges and no waves come from  $x = \infty$ .

Though it is straightforward to have  $\psi e^{-ik_0 x}$  close to the  $y = 0$  edge of the plate to be matched with (18) and the waves on the free water part  $y > 0$  of the form  $e^{-i\sqrt{k^2 - k_0^2}y}$ , the matching of them are not completed. Details of the difficulty will be presented in the Workshop.

#### 4. Trapped waves on the plate

Existence of eigenfrequencies will be possible which correspond to modes of waves trapped over the plate. It was suggested by Prof. Evans at 12th IWWFBB.

We assume a solution of the form

$$\phi = \psi(y)e^{i\gamma x} \quad (20)$$

as in the section 2, while here we consider the case of  $\gamma > k (= \omega^2/gh)$ . Governing equation for  $\psi$  under the plate of infinite length in  $x$  direction and finite width in  $y$  direction will be

$$\left[ \left( -\gamma^2 + \frac{\partial^2}{\partial y^2} \right)^3 + \frac{\rho g}{D} \left( -\gamma^2 + \frac{\partial^2}{\partial y^2} \right) + \frac{\rho g}{D} k^2 \right] \psi = 0 \quad (21)$$

A solution is

$$\psi = \sum_{j=1}^6 b_j e^{\lambda_j y} \quad (22)$$

Here  $b_j (j = 1, 2, \dots, 6)$  are constants and  $\lambda_j$  are six roots of the equation

$$(-\gamma^2 + \lambda_j)^3 + \delta(-\gamma^2 + \lambda_j^2) + \delta k^2 = 0 \quad (23)$$

On the free water part with no plate over it the equation (3) is rewritten as

$$\frac{\partial^2 \psi}{\partial y^2} + (k^2 - \gamma^2) \psi = 0 \quad (24)$$

Solutions with no progressive wave are possible with this equation:

$$\psi = A e^{\sqrt{\gamma^2 - k^2}(y-b)} \quad \text{at } x < -b \quad (25)$$

$$\psi = B e^{-\sqrt{\gamma^2 - k^2}(y-b)} \quad \text{at } x > b \quad (26)$$

If the solutions given by equation (22) happen to match with the solutions (25) and (26) at  $y = \pm b$ , then they are trapped modes over the plate. Matching condition is obtained by imposing the conditions similar to (8), (9), (15) and (16) as:

$$M \cdot \mathbf{x}^T = 0 \quad (27)$$

where  $\mathbf{x}$  is the vector  $\mathbf{x} = (b_1, b_2, b_3, b_4, b_5, b_6, A, B)$  and  $M$  is a matrix.

If the frequencies exist at which the determinant of the matrix  $M$  is zero, the solutions will be the trapped modes. Simple algebraic expression of the determinant seems not possible and the frequency of zero determinant is numerically searched.

The condition of  $\gamma > k (= \omega^2/gh)$  is never realized with water waves and those trapped modes, if they exist, will be induced by other causes such as some wave impact force or wind effect. Practical implication of this phenomenon with the floating airports is to be discussed in future study.

#### References

- Mei, C.C., Tuck, E.O.: Forward scattering by long thin bodies, SIAM J. Appl. Math. vol.39, no.1 (1980)  
 Ohkusu, M., Nanba, Y.: Hydroelastic behavior of a very large floating platform in wave, 11th IWWFBB, Hamburg (1996)  
 Ohkusu, M., Nanba, Y.: Hydroelastic response of a floating thin plate in very short waves, 12th IWWFBB Carry-le-Rouet (1987)  
 Tuck, E.O.: Some theoretical results on diffraction of short waves by thin obstacles, J. Acoust. Soc. America 37 (1965)

# On the Wave Field due to a Moving Two-Dimensional, Submerged Body Oscillating Near the Critical Frequency

E. Palm and J. Grue

Department of Mathematics, University of Oslo,  
P.O.Box 1053 Blindern, N-0316 Oslo, Norway

## 1 Introduction

The problem of a body translating on or beneath a free surface while performing an oscillating motion, is of fundamental interest in marine fluid dynamics. It is of practical importance in the seakeeping of ships, and in the studying of offshore structures and devices for exploiting wave energy. The oscillations are often of small amplitudes such that the conditions required for linearization of the problem is fulfilled. It is then appropriate to solve the problem by using a Green function. For a body moving with a constant velocity  $U$ , or equivalently, a body embedded in a uniform current  $-U$ , the Green function generated by an oscillating, concentrated source is well-known.

This Green function is, however, unbounded for a certain value of the frequency  $\omega$ , corresponding to the non-dimensional number  $\tau = U\omega/g = 1/4$ . Here  $g$  is the acceleration of gravity. Physically speaking, in the two-dimensional case four waves are generated in the far-field when  $\tau$  is less than  $1/4$ . Three of these waves have negative group velocities and are located downstream. One wave has positive group velocity and are located upstream. When  $\tau \rightarrow 1/4$ , two of the waves merge into one wave which has zero group velocity. This wave is not able to transport wave energy upstream and we get a wave cut-off such that the two merged waves do not exist for  $\tau > 1/4$ . The singularity in the Green function for  $\tau = 1/4$  has therefore two causes: two of the waves merge into one which is expected to give a resonance situation, and the resulting wave is not able to transport wave energy.

The motion generated by a body of non-zero volume, oscillating or exposed to an incoming wave, may be found by using a distribution of sources located at the body surface. Since a single source is unbounded at  $\tau = 1/4$ , it was long believed that this is so also for a body. Grue & Palm [1] found, however, for a submerged circular cylinder in two dimensions that the motion and physical forces are bounded as  $\tau \rightarrow 1/4$ . The result was shown numerically as well as from the mathematical equations. Similar numerical results were obtained by Mo & Palm [2] for a submerged elliptical cylinder and by Grue, Mo & Palm [3] for a submerged foil.

This result was generalized by Liu & Yue [4] who were able to show that in two dimensions the motion at  $\tau = 1/4$  is bounded for a submerged body of arbitrary form, provided that the body has a non-zero cross-section area. They also extended their theory to floating two-dimensional bodies and three-dimensional submerged bodies. The paper was followed up by a new paper, Liu & Yue [5] where their result on the motion being finite at  $\tau = 1/4$ , is applied to the study of the time dependence of the wave resistance of a body accelerating from rest. It is known that if the motion is started impulsively from rest to a constant translating velocity, the transient Green function decays slowly, viz. as  $t^{-1/2}$  in two dimensions (and  $t^{-1}$  in three dimensions), where  $t$  is time. The reason for this slow decay is the occurrence of the

singularity at the frequency corresponding to  $\tau = 1/4$ . It was shown that for bodies with non-zero volumes the transient motion decays an order faster: as  $t^{-3/2}$  in two dimensions (and  $t^{-2}$  in three dimensions). For bodies of zero volumes they find that the decay is the same order as for the single source, however.

There are still shortcomings with the mathematical description of the physical problem at  $\tau$  close to  $1/4$ . The first relates specifically to the work [4] in which it is claimed that a finite solution exists if and only if the cross-section area is non-zero. We prove here that a finite solution of the problem exists for the motion near the singularity also when the body has zero cross-section area, namely for a thin two-dimensional foil. The result is independent of the value of the velocity circulation around the foil. Secondly, for a body with finite submergence the mathematical solution of the physical problem is bounded for  $\tau = 1/4$ . This solution tends, however, to infinity as the submergence of the body tends to infinity, as noted by Zhang & Zhu [6]. Such a behaviour is of course meaningless from a physical point of view.

## 2 Mathematical Formulation

### a. Bodies of non-zero cross-section

We consider a body in two dimensions embedded in a uniform current beneath a free surface, performing small oscillations in heave or sway. There may in general also be an incoming wave of the same frequency. It is assumed that a velocity potential  $\varphi$  exists, satisfying the Laplace equation.  $\varphi$  is properly divided into two parts:  $\varphi = \varphi_0 + \varphi_1$  where  $\varphi_0$  is the potential of the incoming wave.  $\varphi_0$  and  $\varphi_1$  may be written

$$\varphi_0 = \text{Re}_j \text{Re}_i f_0(z) \exp(j\omega t), \quad \varphi_1 = \text{Re}_j \text{Re}_i f_1(z) \exp(j\omega t) \quad (2.1)$$

where  $f_0(z)$  and  $f_1(z)$  are analytic functions of  $z = x + iy$  with  $x$  and  $y$  being the horizontal and vertical coordinates, respectively. Origin is in the undisturbed free surface and  $y$  is positive upwards.  $f_1(z)$  is written as

$$f_1(z) = \int_S \sigma(s) G_\sigma(z, \zeta(s)) ds \quad (2.2)$$

where  $G_\sigma(z, z_0)$  is the Green function for the problem (concentrated source at  $z = z_0$ ). The contour of the body is determined by  $z = \zeta(s)$  where  $s$  is the arclength, and  $\sigma(s)$  is the source strength. The integral equation for  $\sigma$  is singular for  $\tau = 1/4$ . Near this singularity the integral equation takes the form

$$\begin{aligned} \sigma(s') + \frac{2k}{\delta} [(n_x(s') + jn_y(s')) \exp(-jk\zeta(s'))] \int_S \sigma(s) \exp(jk\bar{\zeta}(s)) \\ + \int_S \sigma(s) M(s, s') ds + O(\delta) = H(s') \end{aligned} \quad (2.3)$$

Here

$$\delta = (1 - 4\tau)^{1/2}, \quad k = \omega/U,$$

$n_x$  and  $n_y$  are the  $x$ - and  $y$ -components of the normal vector of the body, and  $M$  and  $H$  are non-singular functions. A bar indicates the complex conjugate.

In [4] (2.3) was transformed into the following form

$$\sigma(s') - \frac{2k(n_x + in_y) \exp(-jk\zeta(s'))}{\delta + 2jk\Gamma} \int_S \sigma(s) ds \int_S M(s, s') \exp(jk\bar{\zeta}(s')) ds'$$

$$+ \int_S \sigma(s) M(s, s') ds = H(s') - \frac{(n_x + in_y) \exp(-jk\zeta(s'))}{\delta + 2jk\Gamma} \int_S H(s') \exp(jk\bar{\zeta}(s')) ds' \quad (2.4)$$

where

$$\Gamma = 2k \int_B \exp(2ky) dB \quad (2.5)$$

and  $B$  denotes the body section. Since  $\Gamma \neq 0$ , all the terms in (2.4) are finite and hence  $\sigma$  is finite also for  $\delta = 0$ .

## b. Bodies of zero cross section (the foil)

We consider now a thin oscillating foil submerged in a uniform current under a free surface [3]. A thin moving foil may be used to extract wave energy. It is assumed that the foil has a small camber and angle of attack. For the oscillatory part of the flow the effects of camber and thickness are only secondary and the foil may mathematically be replaced by a flat plate. The boundary conditions at the free surface may be linearized, even if the foil is placed close to the free surface.

The velocity circulation around the foil oscillates in time. Hence vortices are shed at the trailing edge and an infinite long vortex wake will be formed behind the foil.  $f_1(z)$  may now be written

$$f_1(z) = \int_{-\infty}^{\ell} \gamma(\xi) G_\gamma(z, \xi - id) d\xi \quad (2.6)$$

where  $G_\gamma(z, z_0)$  is the Green function for the problem (concentrated vortex at  $z = z_0$ ) and  $d$  is the depth of the foil.  $\gamma$  is now given by an integral equation of the form

$$\gamma(x) = \frac{1}{\pi^2} (\ell^2 - x^2)^{-1/2} \left[ -\frac{AR}{\delta} \int_{-\ell}^{\ell} \frac{(\ell^2 - \eta^2)^{1/2}}{x - \eta} \exp(-jk\eta) d\eta + \int_{-\ell}^{\ell} \frac{\ell^2 - \eta^2}{x - \eta} \left( -\int_{-\ell}^{\ell} \gamma(\xi) K_1(\eta, \xi) d\xi + H(\eta) + F_0(\eta) - \hat{F}(\eta) \right) d\eta - \pi\Gamma_s \right] \quad (2.7)$$

Here

$$\frac{R}{\delta} = \frac{T_1 + \Gamma_s [J_0(k_1\ell) - k \exp(-jk_1\ell)/(k + k_1)]}{\delta + jg_1(k_1\ell)} \quad (2.8)$$

with  $k_1$  denoting the wave number for one of the two waves which merge at  $\tau = 1/4$ .  $\Gamma_s$  is the velocity circulation and  $J_0$  denotes Bessel function of the first kind of order zero. It is proved that  $g_1(k_1\ell)$  is always positive. The other functions involved are all regular.

## Discussion

It is noted that (2.7) and (2.8) define an integral equation where all terms are finite for  $\delta \rightarrow 0$ , even though the cross-section is zero. It is easily shown that also  $f_1(z)$  is finite at this limit. The result is true independent of the value of the velocity circulation.

It should also be noted that the equations (2.4) and (2.7) are singular at  $\delta \rightarrow 0$ , even though  $\sigma$  and  $\gamma$  are finite at this limit. Physically this may be explained by the fact that for  $\tau < 1/4$  four waves are present, while two of these disappear for  $\tau > 1/4$ . It will be shown that some

of the physical forces may have infinite derivatives with respect to  $\omega$  at  $\tau = 1/4$ . This is also true for the source strengths  $\sigma$  and  $\gamma$ .

It is seen from (2.4) that for  $\delta = 0$  the second term becomes for large submergence proportional to  $\exp(kd)$  ( $d$  the depth). Also the velocities become proportional to  $\exp(kd)$ , which is a meaningless result from a physical point of view. A similar behaviour is also found for the foil. It was proposed in [6] to solve the problem by introducing non-linear effects. They exploit a quasi-linear model using a Green function, originally derived by Dagan & Miloh [7], which satisfies the free surface conditions up to third order in the small parameter  $\epsilon$ . By this they obtain that the wave motion set up at the free surface by a deeply situated body *decays* exponentially with the submergence of the body at  $\tau = 1/4$  which is a reasonable result. However, we believe that any other Green function may be used, having the merit that for  $\epsilon \rightarrow 0$  the classical Green function is recovered, and for deeply submerged bodies the wave motion at the free surface decays rapidly with the depth of the body.

We conclude that there are three different routes which may be taken to solve the problem. The first one is to integrate the integral equation directly through the singularity ([1], [2], [3]) which can be performed without difficulty. The second one is to develop the integral equation to a form where the source strength is finite at  $\tau = 1/4$  [4], and the third one is to use a Green function which is non-singular at  $\tau = 1/4$  [6]. Each of these methods have their advantages and disadvantages.

## References

- [1] J. Grue, and E. Palm, Wave radiation and wave diffraction from a submerged body in a uniform current. *J. Fluid Mech.* 151 (1985) 257-278.
- [2] A. Mo, and E. Palm, On radiated and scattered waves from a submerged elliptic cylinder in a uniform current. *J. Ship Res.* 31 (1987) 23-33.
- [3] J. Grue, A. Mo, and E. Palm, Propulsion of a foil moving in water waves. *J. Fluid Mech.* 186 (1988) 393-417.
- [4] Y. Liu, and D.K.P. Yue, On the solution near the critical frequency for an oscillating and translating body in or near a free surface. *J. Fluid Mech.* 254 (1993) 251-266.
- [5] Y. Liu, and D.K.P. Yue, On the time dependence of the wave resistance of a body accelerating from rest. *J. Fluid Mech.* 310 (1996) 337-363.
- [6] Y. Zhang, and S. Zhu, Resonant interaction between a uniform current and an oscillating object. *Appl. Ocean Res.* 17 (1995) 259-264.
- [7] G. Dagan, and T.M. Miloh, Free-surface flow past oscillating singularities at resonant frequency. *J. Fluid Mech.* 120 (1982) 337-363.

## Prediction of resonances due to waves interacting with finite linear arrays of cylinders

R. Porter and D. V. Evans

School of Mathematics, University of Bristol, Bristol, BS8 1TW, UK

### 1 Introduction

In this abstract we show how information concerning the trapped modes in the vicinity of an infinite array of bottom-mounted cylinders can be used to make accurate predictions of the frequencies at which large forces will occur on finite arrays of cylinders. Results are given here for circular cylinders, and it is hoped further results will be presented at the Workshop. Recently Maniar & Newman (1997) have shown how the interaction between an incident wave field and a long periodic array of vertical circular cylinders extending throughout the depth can generate large free-surface amplitudes and forces on the cylinders. They found that the frequencies at which these large resonances occurred corresponded to frequencies at which trapped modes exist for the corresponding *infinite* array of cylinders. Trapped modes represent a localised oscillation of finite energy which does not propagate away to infinity and they are simply the non-trivial solutions to the homogeneous problem. Using symmetry arguments in the trapped mode problem, the infinite array can be regarded as being equal to the problem of a single cylinder placed symmetrically in a channel with parallel walls having either Neumann or Dirichlet condition imposed upon them. Furthermore, it is also necessary to place a Dirichlet (antisymmetry) condition on the channel centreplane in order to generate a cut-off frequency. For the channel with Neumann conditions on the walls, this cut-off is given by  $kd = \frac{1}{2}\pi$  where  $k$  is the wavenumber and the channel is of width  $2d$ . For the channel having Dirichlet conditions on the walls, the cut-off is at  $kd = \pi$ . In each case, provided that the wavenumber is below its respective cut-off and provided that the motion is antisymmetric about the channel centreline, any oscillation localised about the cylinder is unable to propagate to infinity along the channel and is therefore trapped. The Neumann trapped mode was first shown to exist for circular cylinders of all sizes  $0 < a/d \leq 1$ , with  $a$  the cylinder radius, by Callan *et al* (1991). The Dirichlet trapped modes computed by Maniar & Newman (1997) only exist if  $0 < a/d < 0.678$ , that is for sufficiently small cylinders. Evans *et al* (1994) proved that all symmetric obstacles placed symmetrically in a channel having Neumann conditions on the walls exhibit a trapped mode below the cut-off  $kd = \frac{1}{2}\pi$ . The same is not true for a channel having Dirichlet conditions on the walls (as demonstrated, for example, by the circular cylinder), though the techniques used in Evans *et al* (1994) can be adapted to the Dirichlet case to provide a powerful result for the existence of Dirichlet trapped modes. More recently, Evans & Porter (1997) have shown that further isolated trapped modes exist *above* the cut-off for the circular cylinder in both the Neumann and Dirichlet case. In each case, they only exist at a precise wavenumber and for a precise cylinder size.

All the resonances appearing for a finite periodic array of cylinders in waves can be attributed to the presence of one of these trapped modes for the infinite array (see figure 1(a)). However, the values of  $kd$  at which maximum response occurs for the finite array is dependent on the number of elements,  $N$ , in the array and only tends to the trapped mode wavenumber as  $N \rightarrow \infty$ . Similarly, the amplitude of resonance increases (roughly linearly with  $N$ ) as  $N$  increases, though for an infinite array the response would be infinite. In the present paper we attempt to go further by predicting the value of  $kd$  and the amplitude of resonance for a finite array of  $N$  elements using only information from an infinite array. Though this appears on the face of it to be a step backwards, an infinite array

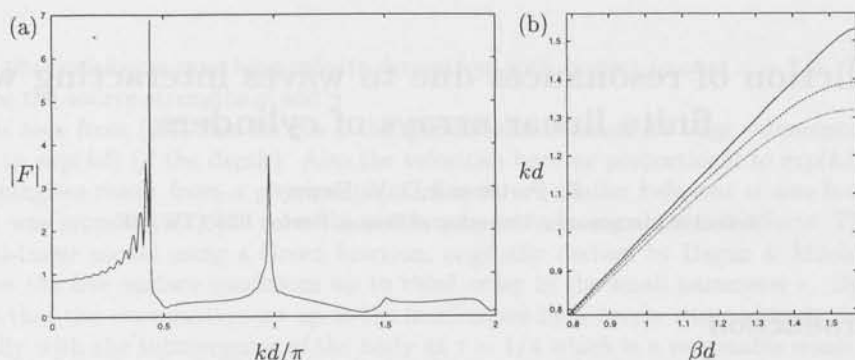


Figure 1: (a) Maximum exciting force on the middle cylinder in array of 25 cylinders in head seas with  $a/d = \frac{1}{2}$ . (b)  $kd$  versus  $\beta d$  for Rayleigh-Bloch waves along an array of circular cylinders with  $a/d = \frac{1}{4}$  (—),  $\frac{1}{2}$  (---),  $\frac{3}{4}$  (···).

is simpler to deal with analytically and so this concept provides a useful tool for predicting forces and frequencies on finite arrays of cylinder with general cross sections.

The trapped modes described above are just special cases of a more generalised trapped mode motion which are usually referred to as Rayleigh-Bloch waves (sometimes also called guided waves or edge waves).

Briefly, Rayleigh-Bloch waves describe oscillations in the vicinity of a periodic array or grating which do not radiate energy away from the grating but, in general, have some transport of energy along the array. They are characterised by a dominant wavenumber  $\beta$  in the direction of periodicity, the wavenumber  $k$  then having to satisfy the cut-off criterion  $k < \beta$  so as to ensure no outgoing waves. Thus  $\beta d = \frac{1}{2}\pi$  and  $\beta d = \pi$  are equivalent to the Neumann and Dirichlet trapped modes described earlier. Rayleigh-Bloch waves are explained in more detail in the following section.

## 2 Rayleigh-Bloch waves along periodic gratings

Consider an infinite periodic linear array of cylinders each of arbitrary cross section, having boundary  $\partial D$ , uniform throughout the depth. The generators of the cylinders are aligned with the depth coordinate,  $z$ , and positioned at  $(x, y) = (0, 2jd)$ , where  $j$  is an integer running from  $-\infty$  to  $\infty$ . According to classical linearised theory and assuming time harmonic motion whilst also removing the depth variation through a term proportional to  $\cosh k(z-h)$  where  $h$  is the constant fluid depth, the two-dimensional complex velocity potential describing the flow satisfies the Helmholtz equation,

$$\phi_{xx} + \phi_{yy} + k^2\phi = 0 \quad (1)$$

everywhere in the field apart from on the boundaries of the cylinders where

$$\phi_n = 0, \quad (2)$$

and  $n$  denotes the normal derivative with respect to the cylinder surface. Because the geometry has periodicity of  $2d$  in the  $y$ -direction, we may relate the potential through

$$\phi(x, y + 2jd) = e^{i\beta 2dj} \phi(x, y), \quad -\infty < j < \infty \quad (3)$$

which simply expresses that there is a change in phase of  $e^{i\beta 2d}$  from the field point at  $y$  to the field point at  $y + 2d$  in the adjacent 'cell'. Thus the total field can be obtained by referring to a single strip of width  $2d$  containing the cylinder. We therefore restrict our attention to the strip  $(x, y) \in (-\infty, \infty) \times [-d, d]$  and impose appropriate periodicity conditions on the lines  $y = \pm d$  of

$$\phi(x, d) = e^{i\beta 2d} \phi(x, -d), \quad \phi_y(x, d) = e^{i\beta 2d} \phi_y(x, -d), \quad (4)$$

with (3) providing the extension to all  $(x, y)$ . The Green's function for the problem defined by (1), (2) with (4) may be written as the integral representation

$$G_{\beta}(x, y; \xi, \eta) = -\frac{1}{2\pi} \int_0^{\infty} \frac{e^{i\beta d \operatorname{sgn}(y-\eta)} \sinh k\gamma|y-\eta| + \sinh k\gamma(d-|y-\eta|)}{\gamma(\cosh k\gamma d - \cos \beta d)} \cos k(x-\xi)t dt \quad (5)$$

where  $\gamma = (1-t^2)^{1/2} = i(t^2-1)^{1/2}$  and  $r = ((x-\xi)^2 - (y-\eta)^2)^{1/2}$ . See Linton (1998) for its derivation and other representations of the periodic Green's functions in (5). Applying Greens theorem to  $G_{\beta}$  and  $\phi$  in the rectangle  $(x, y) = (-X, X) \times [-d, d]$ ,  $X \rightarrow \infty$  yields the following integral equation for  $\phi$ :

$$\int_{\partial D} \phi(p) \frac{\partial}{\partial n_q} G_{\beta}(p; q) ds_q = \begin{cases} \frac{1}{2}\phi(p), & p \in \partial D, \\ \phi(p), & p \notin \partial D. \end{cases} \quad (6)$$

Following Linton & Evans (1992), we use a polar parametrisation for  $\partial D$  of  $\rho(\theta)$ ,  $0 \leq \theta \leq 2\pi$  and write  $(\theta, \psi)$  for  $(p, q)$ . Discretising the integral equation into  $M$  segments over the interval  $(0, 2\pi)$ , writing  $\theta_j = (2j-1)\pi/M$ ,  $j = 1, \dots, M$  and collocating reduces the above to the following algebraic system of equations:

$$\frac{2\pi}{M} \sum_{j=1}^M \phi(\theta_j) K_{ij} w_j = \frac{1}{2}\phi(\theta_i), \quad i = 1, \dots, M \quad (7)$$

where

$$K_{ij} = \partial G_{\beta}(\theta_i; \theta_j) / \partial n_q, \quad w_j = (\rho^2(\theta_j) + \rho'^2(\theta_j))^{1/2}. \quad (8)$$

It turns out that if we are below the cut-off,  $k < \beta$ , the above system can be recast as a real system despite the apparent complex nature of  $G_{\beta}$  in (5). Rayleigh-Bloch modes correspond to the non-trivial solutions to (7) or, equivalently, the vanishing of the determinant of the system, for which the realness of the system is vital.

For example, when the infinite array consists of circular cylinders of radius  $a$ , the Rayleigh-Bloch solutions in  $\beta d \leq \frac{1}{2}$  are shown in figure 1(b). Notice that  $\beta d = \frac{1}{2}\pi$  corresponds to a Neumann trapped mode, whence the well-known results of Callan *et al* (1991) are recovered.

### 3 Near-trapping by a finite linear array

In figure 1(a) we show the variation of the maximum exciting force on the middle cylinder in an array of 25 cylinders of non-dimensional radius  $a/d = \frac{1}{2}$  with non-dimensional wavenumber  $kd/\pi$ . We are interested in predicting the values of  $kd$  at which large peaks in forces occur. Maniar & Newmann (1997) made the connection between the Neumann and Dirichlet trapped modes in an infinite array ( $\beta d = \frac{1}{2}\pi$  and  $\beta d = \pi$  respectively) and these peaks. In fact, for 25 cylinders, the peak resonance occurs at a value of  $kd = 1.3820$  as opposed to the corresponding Neumann trapped mode wavenumber of  $kd = 1.3913$ . In what follows, we allow ourselves to consider general  $\beta d$  and the resulting Rayleigh-Bloch waves in the infinite array to improve upon the estimate to  $kd$  at which resonance occurs for a finite array. Our motivation comes from the form of the wave field along the finite array, shown for 25 cylinders at the resonant wavenumber  $kd = 1.3820$  in figure 2(b). In each 'cell' containing a cylinder, the wave field is similar to that for a trapped mode in a Neumann channel, but is modulated by a cosine-type envelope along the array. We can construct a similar solution for the Rayleigh-Bloch waves by choosing  $\beta d = \frac{1}{2}\pi(1-\epsilon)$ . Then from (3),

$$\phi(x, y + 2jd) = e^{ij\pi(1-\epsilon)} \phi(x, y) = e^{-ij\epsilon} [(-1)^j \phi(x, y)]. \quad (9)$$

The term in the square brackets represents the standing wave component of the solution whilst the exponential term contains a modulation of one half wavelength given by  $j\epsilon = 1$ . Matching this modulation with the finite array of  $N$  elements gives  $N\epsilon = 1$ , and so

$$\beta d = \frac{1}{2}\pi(1 - 1/N) \quad (10)$$

and the corresponding Rayleigh-Bloch wavenumber  $kd(\beta d)$  can be computed using the method outlined in the preceding section. This resulting value of  $kd$  provides the estimate to the wavenumber at which

$N$ (no. of cylinders)	$\beta d = \frac{1}{2}\pi(1 - 1/N)$	$kd(\beta d)$	$kd(\text{peak force})$
100	1.5550	1.3907	1.3907
50	1.5394	1.3889	1.3889
25	1.5080	1.3818	1.3820
20	1.4923	1.3767	1.3775
15	1.4661	1.3659	1.3680
10	1.4137	1.3376	1.3470

Table 1: Table showing the values of  $kd$  at which large forces occur in a linear array of  $N$  cylinders,  $a/d = \frac{1}{2}$  and the wavenumbers predicted using Rayleigh-Bloch theory.

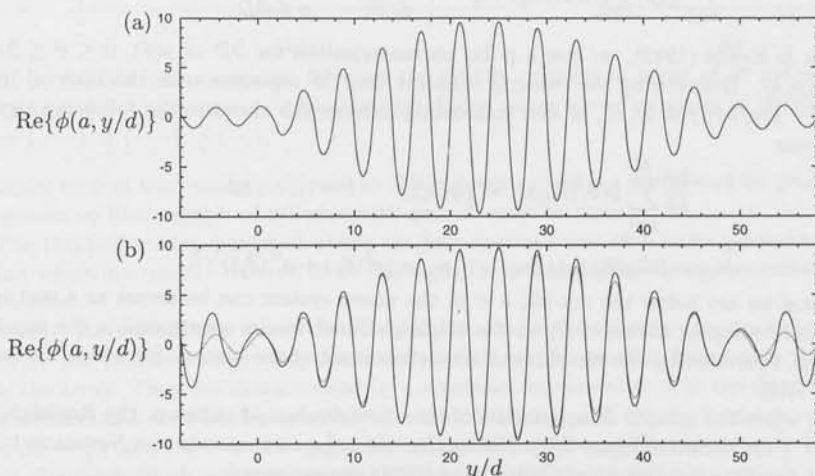


Figure 2: (a) The free-surface elevation along  $N = 25$  cylinders at the near-trapping frequency ( $a/d = \frac{1}{2}$ ), and (b) overlaid ( $\cdots$ ) on the Rayleigh-Bloch surface profile ( $-$ ) along a corresponding infinite array with  $\beta d$  given by (10).

the peak resonance occurs in the finite array and a comparison between the two is shown in table 1. For  $N \geq 25$  the agreement is excellent and even for  $N = 10$ , the discrepancy is only 1%. Figure 2(b) shows an overlay of the wave profile along the finite array of  $N = 25$  cylinders and the corresponding Rayleigh-Bloch wave profile computed using (10). In the range occupied by cylinders, the agreement is excellent, confirming the connection between near-trapping or resonance in finite linear arrays and Rayleigh-Bloch waves in infinite arrays.

### References

- CALLAN, M., LINTON, C. M. & EVANS, D. V. 1991 Trapped modes in two-dimensional waveguides. *J. Fluid Mech.* **229**, 51-64.
- EVANS, D. V. & PORTER, R. 1998 Trapped modes embedded in the continuous spectrum. To appear in *Q. J. Mech. Appl. Maths.*
- EVANS, D. V., LEVITIN, M. & VASSILIEV, D. 1994 Existence theorems for trapped modes. *J. Fluid Mech.* **261**, 21-31.
- LINTON, C. M. 1998 The Green's function for the two-dimensional Helmholtz equation in periodic domains. Submitted to *J. Eng. Maths.*
- LINTON, C. M. & EVANS, D. V. 1990 The interaction of waves with arrays of vertical circular cylinders. *J. Fluid Mech.* **215**, 549-569.
- LINTON, C. M. & EVANS, D. V. 1992 Integral equations for a class of problems concerning obstacles in waveguides. *J. Fluid Mech.* **245**, 349-365.
- MANIAR, H. D. & NEWMAN, J. N. 1997 Wave diffraction by a long array of cylinders. *J. Fluid Mech.* **339**, 309-330.

## Wave pattern analysis applied to nonlinear ship wave calculations

Hoyte C. Raven and Henk J. Prins

Maritime Research Institute Netherlands (MARIN), P.O.Box 28, 6700AA Wageningen, Netherlands.

Calculation methods for the steady wave pattern of a ship in still water usually suppose potential flow, and today often impose nonlinear free surface boundary conditions. Advantages of including all nonlinear effects have been demonstrated before [1]. One of these is that an accurate prediction of the wave resistance in principle becomes possible: Unlike Dawson-type linearisations, the full nonlinear free-surface conditions theoretically ensure full agreement between the resistance found from a far-field momentum balance and that from pressure integration over the hull. Thereby they rule out the occurrence of negative wave resistance predictions and similar problems.

Even so, computing wave resistance by hull pressure integration remains less attractive, having significant sensitivity to the hull panelling, in particular at low Froude numbers. The predicted wave pattern, however, is much less sensitive to the hull panelling. This suggests to evaluate the wave resistance from the calculated wave pattern, using a wave pattern analysis technique as developed in the past for towing tank experiments. For use in a computational method a transverse cut technique is most suitable, and has been applied before. Nakos [2] used it successfully for a linearised wave pattern calculation. Busch [3] used wave pattern analysis in a nonlinear method, obtained good results for a very slender hull form but did not pursue the application to other cases.

### The RAPID method

The method used in the present study is RAPID [4, 5]. It solves the steady potential flow problem with fully nonlinear free-surface boundary conditions by an iterative technique. Each iteration linearises with respect to the free-surface shape and velocity field found in the previous iteration. The solution is generated by source distributions on the hull surface and on a plane at a small distance above the free surface. The free-surface collocation points are on the wave surface itself, and are distributed over a finite domain around the ship. The method is quite efficient, converging usually in 8 to 15 iterations; each iteration asks some 6 sec. at 2500 panels, 50 sec. at 8000 panels, on a CRAY 916 vector computer. It is in routine use at MARIN since 1994, several hundreds of calculations being made each year; and besides is used at a few shipyards.

### Transverse cut analysis

Transverse cut analysis (see e.g. [6]) uses an expression for the wave resistance in terms of the amplitude of the wave components proceeding in all directions:

$$R_{wpat} = \frac{1}{8\pi} \int_0^\infty (F^2(u) + G^2(u)) \frac{\sqrt{1+4u^2}}{1+\sqrt{1+4u^2}} du, \quad (1)$$

for a wave pattern represented by :

$$\eta(x, z) = \frac{1}{4\pi} \int_{-\infty}^{+\infty} [F(u) \sin(sx + uz) + G(u) \cos(sx + uz)] du, \quad (2)$$

where the dispersion relation is  $s = \sqrt{(1 + \sqrt{1 + 4u^2})/2}$ . The amplitudes  $F$  and  $G$  can be found by applying a particular Fourier analysis to the wave height distribution along two transverse lines far behind the ship. In [3] it is shown that a larger number of wave cuts is preferable to provide redundancy and increase the accuracy of the result. In our study 8 cuts appeared to work well. The overdetermined system is solved in a least-squares sense.

The transverse cuts must be located far enough aft of the hull, they must extend laterally to outside the Kelvin wedge, they must be free of reflection effects, and the free-surface panel width must be small enough to resolve all wave components of interest. With some adjustments the ensuing requirements to the free-surface panelling can easily be met.

### Dependence on longitudinal position

Evidently, the wave pattern resistance is supposed to be independent of the longitudinal position of the cuts. But without further precautions it is not, as Fig.1 illustrates for the case of a slender vessel at  $F_n = 0.33$ . In general we observe that:

- Close to the stern, there is a rather quick variation of the resistance found;
- The resistance displays wavy variations around a mean line, with a slowly decreasing amplitude;
- The wave pattern resistance gradually decreases with distance of the cuts behind the stern;
- All values found are significantly lower than the pressure integration resistance level.

The first point is an expected symptom of the near-field disturbance around the hull, which violates the basic assumptions of the analysis. As far as our experience goes, further than 0.3 to 0.5  $L$  aft of the stern this effect is mostly negligible. The second effect was unexpected and is studied below. The last two points are discussed in the last section.

### Effect of nonlinearities on transverse cut analysis

To detect the cause of the wavy variations we go back to the derivation of transverse cut analysis. The starting point is a momentum or energy balance for a control volume surrounding the ship hull, bounded by the wave surface, an inlet plane and lateral boundaries at infinity, and a transverse outlet plane at any distance behind the stern. This provides the wave resistance in terms of an integral over the outlet plane, plus a line integral along its intersection with the wave surface:

$$Rw_{far} = \frac{1}{2} \int_D (-u^2 + v^2 + w^2) dS + \frac{1}{2} \int_{l_0} \eta^2 dz. \quad (3)$$

Here,  $u$ ,  $v$  and  $w$  are disturbance velocity components relative to the undisturbed flow.

The first term is not easily evaluated accurately and therefore is recast in an expression in terms of wave heights only. To this purpose, the far-field wave pattern is assumed to have the form (2), i.e. to be a superposition of simple sinusoidal wave components that satisfy the dispersion relation for the steady wave pattern. Substituting the corresponding potential field into (3) provides the expression (1) for the wave resistance in terms of the amplitude of the wave components.

If fully nonlinear boundary conditions are imposed, the resistance from (3) of course is independent of the position of the outlet plane, as there is no energy flux through the wave surface. Therefore, the wavy variations of the resistance must be due to an incorrect approximation of the integral over the outlet plane, in particular the assumed linearity of the wave components. This is confirmed by the fact that for a Neumann-Kelvin result (obtained with the same numerical method) the wavy variations of the wave pattern resistance are almost absent, as Fig. 1 shows: in that case the expression (2) is consistent with the linear free-surface boundary condition imposed, so the approximation of the outlet plane energy flux is exact. However, using a full Bernoulli expression for the wave height in the Neumann-Kelvin result disturbs this consistency and already introduces a pronounced waviness. We conclude that the wavy variations in the wave pattern resistance are a consequence of the inconsistency of applying a linear analysis to a wave pattern that satisfies nonlinear boundary conditions.

While the amplitude of the resistance variations decays, they persist up to 2 ship lengths aft of the stern in the cases studied. The nonlinear effects therefore extend over a much larger distance than has always been assumed, and this will apply to experimental transverse cut analysis as well.

In order to eliminate the resistance variations, we have tried to replace the wave pattern at the location of the transverse cuts by a 'corresponding' linear wave pattern. One attempt was to use the linear (Kelvin) expression for  $\eta$ , using the free-surface velocities computed by the nonlinear method; but this turned out to increase the amplitude of variations even further. A second attempt was to use again the Kelvin expression, but in terms of the velocities at the still water level. In the case studied this eliminated most of the resistance variations (Fig. 2). However, this procedure is less suitable for routine application and seems to lack a theoretical justification.

A more obvious alternative, and the procedure adopted now, is to spread out the transverse cuts over a longer area. In all cases tried, the waviness in the resistance had a length quite close to the fundamental wave length  $\lambda = 2\pi Fn^2$ . If the 8 transverse cuts we use are distributed over an area of this length, the wavy variations are "averaged out", and a much more stable result is obtained, as Fig.2 shows.

To get some confirmation that this average value agrees with the true wave resistance as would be obtained from (3), a simple analysis has been carried out. As suggested by the appearance of the fundamental wave length, we represent the wave shape by a single 2D component and make a perturbation expansion in the wave height. For the first order wave  $\eta = \frac{1}{2} H_1 \sin x$ , substitution in (1) yields:

$$Rw_{par} = \frac{1}{16} H_1^2,$$

so for a linear wave component the resistance from wave pattern analysis is independent of  $x$ . Moreover, substituting the associated potential field into (3) produces the same expression for the resistance to leading order. However, for a second-order wave,

$$\eta = \frac{1}{2}H_1 \sin x + \frac{1}{2}H_2 \sin x - \frac{1}{8}H_1^2 \cos x,$$

the resistance from the wave pattern analysis is

$$R_{w_{pat}} = \frac{1}{16}H_1^2 + \frac{1}{8}H_1H_2 + \frac{1}{32}H_1^3 \sin x,$$

while the control volume integration produces the same but without the  $\sin x$  term. Therefore, eliminating the wavy part of  $R_{w_{pat}}$  by averaging over a wavelength brings it in agreement with the energy balance and yields the correct result in this case.

### Effect of numerical damping

We now come back to the last two features noted above: the gradual decrease of the average resistance level with  $x$ , and the fact that  $R_{w_{pat}}$  is less than the resistance from pressure integration. Both are obvious consequences of the numerical damping inherent to the method. While this damping has little effect in the near field, it causes a slightly too quick decay of the wave amplitude and affects the far field resistance evaluation (which is quadratic in wave amplitudes).

The numerical damping has been analysed theoretically in [5], and indeed there appears to be a direct correspondence between the results of that analysis and the slope of the  $R_w(x)$ -line. E.g. for the raised-panel method used, the analysis tells that the damping increases when the distance of the panels above the free surface is reduced, and this is reflected in a steeper decrease of the resistance. This resistance decrease may be supposed to be an exponential function of the distance from the point where the waves have been generated. If, as a rough approximation, this virtual origin is chosen at e.g. half the ship length, as a sort of average for bow and stern wave systems, the  $R_{w_{pat}}(x)$  line can be extrapolated backwards to that origin. This largely compensates the dependence of the wave pattern resistance on numerical parameters that affect the damping.

In principle, a better approach is to reduce the slope of the resistance line by reducing the numerical damping. This can be done by optimising the difference scheme in the free surface boundary conditions. The theoretical analysis of the dispersion and damping in [5] indicates how to design a special-purpose difference scheme that virtually eliminates the damping for panellings as coarse as 10 panels per wavelength. Experience with such schemes is now being collected.

### Conclusions

- As a result of the inconsistency of applying linear wave pattern analysis to the wave pattern computed with a nonlinear method, the wave pattern resistance has a wavy dependence on the distance aft of the stern.
- The nonlinear effects causing these resistance variations may persist to as far as 2 ship lengths astern; the same will also be true for experimental wave pattern analysis.
- The variations can and may be largely eliminated by spreading the wave cuts over a fundamental wave length.
- While the wave pattern resistance is much less sensitive to the hull panelling than the hull pressure integration, it is affected by cumulative numerical damping effects and thus poses some additional demands to the numerics. At present its use is for comparative rather than absolute predictions.

### Acknowledgment

The present study largely formed part of the Brite-Euram Project BRPR-CT96-0208, CALYPSO. This support by the EC is gratefully acknowledged.

### References

- [1] Raven, H.C., "The nature of nonlinear effects in ship wavemaking", Ship Techn. Research, Feb. 1997.

- [2] Nakos, D.E., "Transverse wave cut analysis by a Rankine panel method", 6th WWFEB, 1991.
- [3] Busch, S., "Numerische Berechnung des Wellenwiderstandes eines schnellen Sportbootes", Diplomarbeit, Univ. Duisburg, Aug. 1990.
- [4] Raven, H.C., "A Practical Nonlinear Method for Calculating Ship Wavemaking and Wave Resistance", 19th Symp. Naval Hydrodynamics, Seoul, South-Korea, 1992.
- [5] Raven, H.C., "A solution method for the nonlinear ship wave resistance problem", Doctor's Thesis, Delft Univ. Tech., June 1996.
- [6] Eggers, K.W.H., Sharma, S.D., and Ward, L.W., "An assessment of some experimental methods for determining the wavemaking characteristics of a ship form", Trans. SNAME 1967, Vol.75.

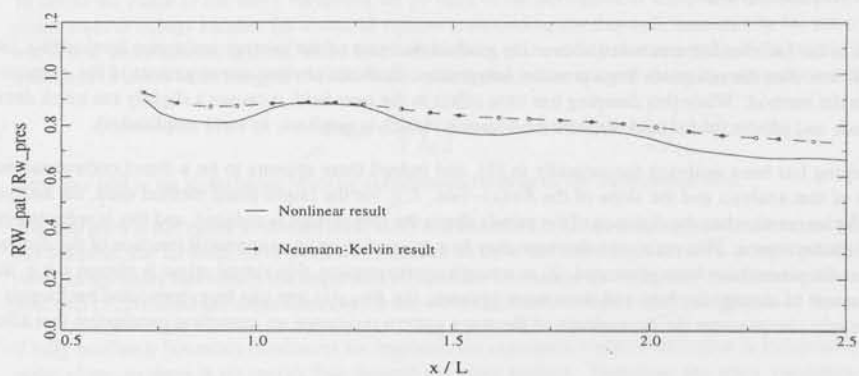


Figure 1: Wave pattern resistance as a function of position of transverse cuts, for nonlinear and linearised method.

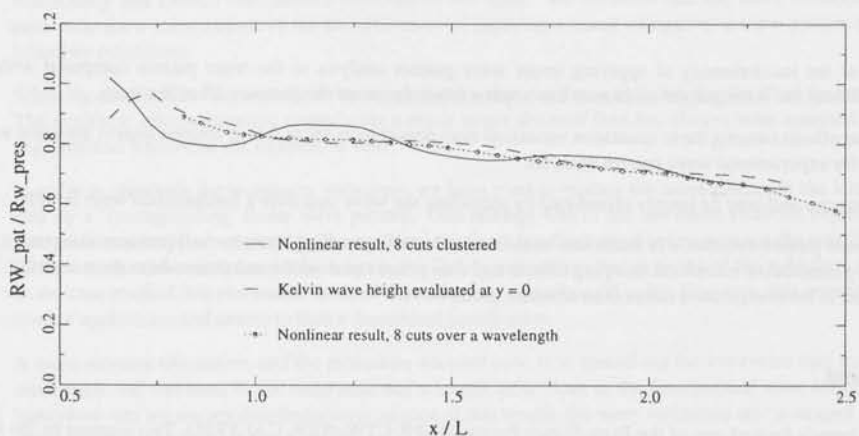


Figure 2: Wave pattern resistance as a function of position of transverse cuts, for nonlinear method. Two ways to eliminate waviness.

## Experimental and numerical second order diffracted waves around an array of 4 cylinders.

Scolan Y.-M., ESIM, Marseille, France  
Malenica Š, BUREAU VERITAS, La Défense, France

### 1. Introduction

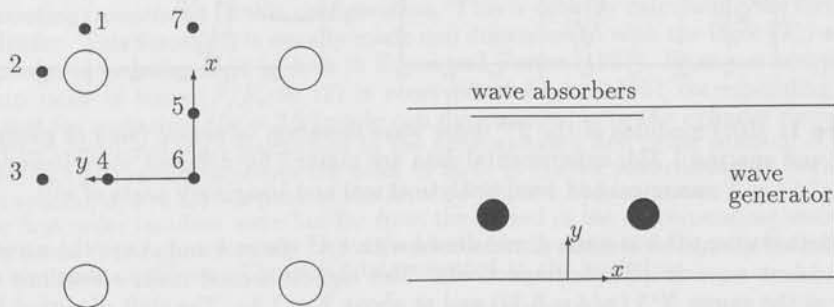
The diffraction of regular waves around an array of 4 vertical cylinders is investigated. Results from existing theoretical models are compared with experimental data acquired in the frame of a french CLAROM project started in 1996. Encouraging results are obtained for both first and second order quantities in the limit of small wave steepness.

Another aspect is also emphasized concerning the existence of high localised second order wave elevations in the spacing between the two front columns. The computations show that second order maxima is only due to diffraction and they occur precisely where the first order envelop vanishes. The existence of trapped modes may explain these resonant like phenomena.

In the following developments, the experimental set-up is first described, then the two different numerical approaches are outlined. Some significant results of comparison are finally shown.

### 2. The experimental set-up

The set-up (described below) is simply composed of bottom mounted vertical cylinders of circular cross section. One of the longitudinal walls of the basin is used as a symmetry plane; the TLP model is thus composed of 2 cylinders at incidence  $0^\circ$ . With this choice the problems of blockage are practically avoided and it significantly reduces the perturbation due to the reflected waves on the opposite longitudinal wall. An additional wave absorber is placed on this wall. These precautions are necessary to obtain a sufficiently long period for data acquisition without spurious harmonics. This is of crucial importance particularly when second order quantities are to be measured. Seven wave gauges are placed in the vicinity of the four columns as described below.



### 3. The numerical tools

The second order diffraction problem can be formulated for the corresponding potential  $\phi_D^{(2)}$  as follows:

$$P_D^{(2)} \begin{cases} \Delta \phi_D^{(2)} = 0 & \text{in the fluid domain} \\ \phi_{D,z}^{(2)} - \frac{4\omega^2}{g} \phi_D^{(2)} = \alpha^{id} + \alpha^{dd} & \text{on the free surface } z = 0 \\ \phi_{D,r}^{(2)} = -\phi_{I,r}^{(2)} & \text{on the cylinders} \\ \phi_{D,z}^{(2)} = 0 & \text{on the sea-bottom } z = -h \\ Rad(\phi_D^{(2)}) & \text{in the far field} \end{cases} \quad (1)$$

The 2<sup>nd</sup> order incident potential  $\phi_I^{(2)}$  is known analytically. The right hand side of the free surface condition exhibits in the far field two wave interactions; here  $\alpha^{id}$  and  $\alpha^{dd}$  correspond to the interactions incident/diffracted and diffracted/diffracted respectively. The radiation condition usually follows from an analysis of the far field wave decomposition into free and locked components.

To solve this BVP, two different numerical approaches are used: semi-analytical formulations and numerical diffraction programs developed in the frame of potential flow theory. Both

approaches use **semi-analytical first order solutions** to account for the interaction of cylinders. The formulation by McIver & Evans (1984) is approximate and the other one by Linton & Evans (1990) is exact. Discrepancies exist and some of them are exposed here and in Scolan *et al.* (1997).

The second order **semi-analytical approach** uses the Linton & Evans' first order solution. It is based on the decomposition of the second order potential into several potentials, each verifying a particular Boundary Value Problem (BVP) solved semi-analytically. This is presented in Malenica (1997).

The other approach is a **full numerical solution of the BVP** expressed above by using an integral equation and the Rankine Green function (see Scolan 1989). The main aspect concerns the radiation condition which is based on the decomposition of the far field into locked and free waves (see Molin 1979).

#### 4. Some results

Figures (1) compare the numerical or experimental total second order quantities. Those include the incident and diffracted components (noted  $\eta_I^{(2)}$  and  $\eta_D^{(2)}$  respectively) and the quadratic contributions (noted  $\eta_{Q(1)}^{(2)}$ ) coming from first order.

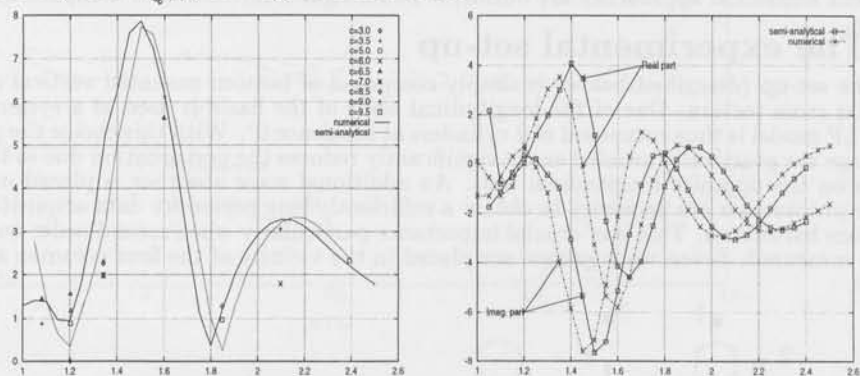


**Figure 1:** (left) modulus of the 2<sup>nd</sup> order wave elevation vs period (sec) at gauge N°5, radius 0.280 and spacing 1.334; experimental data are marked for different wave steepnesses; (right) numerical and semi-analytical real and imaginary parts of  $\eta^{(2)}$ .

The plotted quantities are non dimensioned with  $kA^2$  where  $k$  and  $A$  are the wave number and the incident wave amplitude respectively. The highest second order elevations  $\eta^{(2)}/kA^2 \approx 8$  occur at the gauge N°5 ( $x/d = 0.39$ ) and at about  $T = 1.5$ s. The shift of period illustrates the differences between the two first order formulation. The overall trend is however very similar.

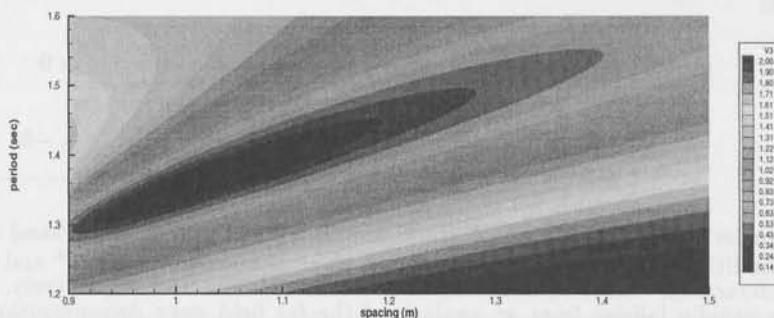


**Figure 2:** locations of  $\eta^{(1)}$  modulus minima at mid-point between the two front cylinders.

A study of the second order wave pattern shows that localised high elevations occur between the two front cylinders. This could suggest resonant like phenomena somewhere between the cylinders. A more precise study shows that first order wave elevations vanish in the same area. Hence a parametric study should first provide couples of spacing and wave period for which there exist areas where first order elevations vanish. Such locations are determined along the symmetry axis ( $y = 0$ ) and between either upstream or downstream cylinders. For example figure (2) shows the locations in the plane (*spacing, period*) of the  $\eta^{(1)}$  modulus minima calculated exactly at the mid-point between the two front cylinders. Computations are thus performed for different couples ranging along a line which joins the 2 points (1.0, 1.348) and (1.25, 1.48). As a matter of fact, the obtained results (not reproduced here) show the same characteristics. To illustrate this the total second order wave pattern is plotted in figure (3) for the data  $d = 100$  and  $T = 13.48$  with the radius  $a = 28$  (corresponding to a geometry 100 times larger than the model one). A spot of high elevation is clearly noticeable exactly between the two upstream cylinders. A question arises whether this is due to forcing term of the free surface condition or this is due to pure diffraction. For that in the left figure, the 1<sup>st</sup> order elevation is compared to the different 2<sup>nd</sup> order quantities. One may note that:

- the second order diffraction is clearly the dominant contribution,
- this component reaches its maximum precisely where the total 1<sup>st</sup> order elevation vanishes,
- the 2<sup>nd</sup> order diffraction is the only explanation for this local effect since the quadratic terms bring almost negligible contribution even if it is thought that  $\nabla^2 \phi^{(1)}$  should contribute significantly,
- the 1<sup>st</sup> order elevation, the right hand side ( $\alpha^{id} + \alpha^{dd}$ ) and the mean value have a very similar variation along the axis,
- the forcing term of the free surface condition seems not important enough to explain this phenomenon.

Another couple is then computed for a different location of vanishing first order elevation; the listed conclusions above seem confirmed as shown in figures (4). Here one should note that the forcing term of the free surface condition decreases significantly at the location of interest.

From the first studied data (see figure 3) one can compute the positions of the near-trapped modes (if existing) associated to this configuration. This is done by calculating the force acting on each cylinder. This force ( $F$ ) is usually made non dimensioned with the force ( $F_s$ ) acting on a single cylinder in isolation as it is done in Evans and Porter (1997). From our computations a very sharp peak of force ( $F/F_s \approx 12$ ) is observed at  $ka \approx 0.7957$  corresponding here to  $T \approx 11.9s$  and for a spacing  $d/a = 2.5$  (made non dimensioned with the cylinder radius). This result must be considered with precaution as the approximated first order solution is used.

However, as the spacing increases the peak of force is shifted towards higher periods. For the present spacing  $d/a \approx 3.57$ , a peak of the force ( $F/F_s \approx 1.6$ ) is at about  $T \approx 13.7s$ . This is close to the first order incident wave but far from the period of the corresponding second order free wave system. A parametric study by varying both the spacing and the period should bring some more elements of answer. Those will be presented at the workshop.

**Acknowledgements:** This work is done in a CLAROM Joint Industry Project. The authors thank the partners: Principia RD (leader), Total, Bouygues Offshore, Doris Eng., Bureau Veritas, Ifremer and Sirehna to allow the publication of the present results.

## 6. References

- Evans D.V. & Porter R., 1997, "Near-trapping of waves by circular arrays of vertical cylinders.", Applied Ocean Research, Vol.19, pp 83-99.
- Malenica Š, 1997b, "Second order interaction of water waves with arrays of vertical circular cylinders", Proceedings of the 2nd Congress of Croatian Society of Mechanics, pp. 599-606, Supetar, Croatia.
- Linton C.M. & Evans D.V., 1990, "The interaction of waves with arrays of vertical circular cylinder in a channel.", J. Fluid Mech., Vol 215, pp 549-569.
- Mc Iver P. & Evans, D.V., 1984, "Approximation of wave forces on cylinder arrays", Applied Ocean Research, Vol.6, N°2, pp 101-107.
- Molin B., 1979, "Second-order diffraction loads upon three-dimensional bodies", Applied Ocean Research, Vol. 1, N°4.
- Socolan Y.-M., 1989, "Contribution à l'Etude des Non-Linéarités de Surface Libre. Deux cas d'application...", PhD Thesis, University Paris 6.
- Socolan Y.-M., Malenica Š & Martigny D., 1997, "Experimental and numerical studies of the TLP's airgap.", to be presented at ISOPE Conf., Montreal, Canada.

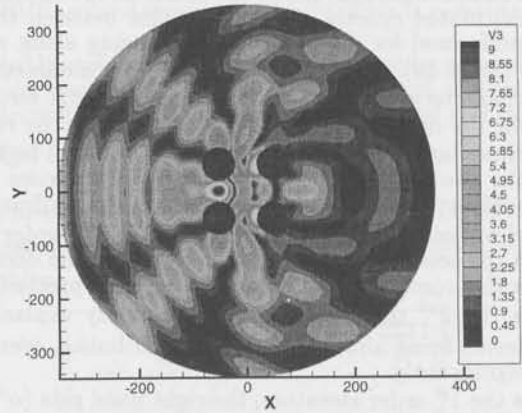
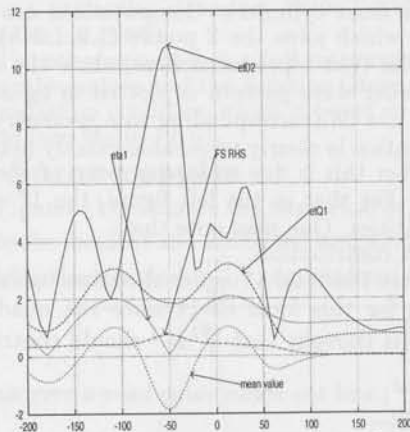


**Figure 3:** variation of the contributions to the free surface elevation  $|\eta_I^{(2)}|$ ,  $|\eta_D^{(2)}|$ ,  $|\eta_{Q(1)}^{(2)}|$ , mean value,  $|\eta^{(1)}|$ , right hand side of the free surface condition  $\alpha^{id} + \alpha^{dd}$ ; gap/radius= 100/28 and  $T = 13.48s$

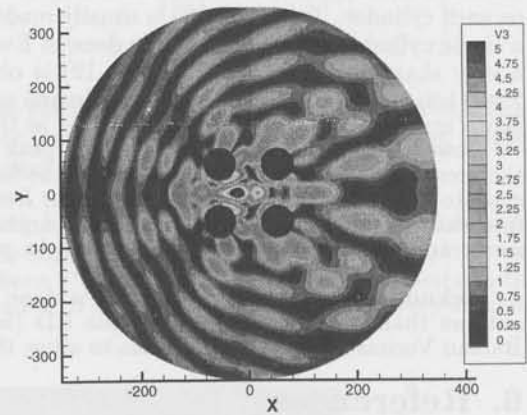
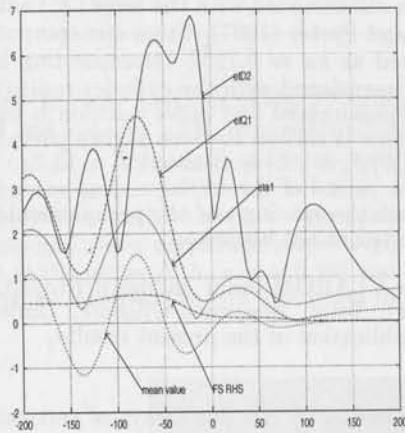


**Figure 4:** see caption above; gap/radius= 106/28 and  $T = 11.8s$

## Suppression of Wave-Breaking in Nonlinear Water Wave Computations

Anil K. Subramani, Robert F. Beck, and William W. Schultz  
The University of Michigan, Ann Arbor, Michigan 48109, U.S.A.

### INTRODUCTION

Over the past several years, a multipole-accelerated, desingularized boundary integral method has been developed to compute fully nonlinear water waves in the time domain (Scorpio and Beck, 1996). The method---denominated UM-DELTA, for University of Michigan Desingularized Euler-Lagrange Time-Domain Approach---has been successfully applied to a wide variety of problems, with marked improvements over results obtained using linearized methods. A major difficulty is encountered, though, by this and similar methods for computing nonlinear water waves and wave loads: the characteristic occurrence of spray and wave-breaking in free-surface flows causes the computations to stop, as figure 1 demonstrates. Therefore, for the present method to realize its full capability, it is important to prevent the generation of spray and breaking waves from terminating the simulations of highly nonlinear flows. However, with the goal being for the method to remain efficient and useful in the marine design process, a detailed and expensive simulation of the wave-breaking event itself is less desirable an approach than one that models the event adequately enough for the calculations to proceed.

To this end, recognizing that wave-breaking is essentially a process with which is associated a local dissipation of energy, a technique is herein proposed to absorb energy locally from waves that are about to break, thereby suppressing wave-breaking. The features of this "local absorbing patch" model are: (i) detecting the likely occurrence of wave-breaking, and (ii) determining the appropriate amount of local damping so as to render reasonably realistic waves in the post-breaking regime; these are discussed below.

### CRITERION FOR BREAKING

Important as the problem is, wave-breaking has received considerable attention, but it is not yet completely understood. A survey of the literature reveals that a number of studies have been conducted to understand why waves break and to determine a reliable criterion for the inception of breaking. For brevity, we cite only Griffin et al. (1994) for they point to the pertinent references in their review of the existing criteria.

Following Stokes' theorizing of a limiting height ( $H$ ) to a wave in terms of the wavelength ( $\lambda$ ), the

wave steepness (often measured by  $ak$ , where  $a$  is the wave amplitude and  $k=2\pi/\lambda$  is the wave number) has been the most commonly examined index for wave-breaking. Empirical data, however, show the steepness to be an imprecise criterion---see figure 1 and table 1 of Griffin et al., 1994, which indicate that waves break at lower steepnesses than that suggested by Stokes' criterion and also show the scatter in the data. Another widely pursued idea has been the prescribing of a limiting value to the fluid velocity at a crest. For example, recently, Wang et al. (1994) provided data obtained from a two-dimensional numerical wave tank in support of the criterion that a wave breaks when the horizontal particle velocity reaches the local group velocity. The possibility of breaking has also been related to the energy content in the waves, by others, but these last two criteria are difficult to extend to three-dimensional flows. Criteria based on the wave slope and accelerations of the free-surface have also been suggested, but the consensus is that none of the above constitutes a simple, precise, and universally valid criterion.

In this light, we pursue a criterion based on the wave steepness because of its simplicity and its applicability in three-dimension. A steepness criterion that requires an estimate of the local wavelength, however, is not easy to implement, especially when waves of different frequencies are present and interact. We exploit instead that when waves break---or are about to---they attain a profile with a sharp crest of infinite curvature ( $\kappa$ ). Furthermore, empirical studies of steep but non-breaking regular waves indicate that waves that do not possess a sharp crest obey the approximate non-dimensional bound,  $|\kappa\lambda| \leq 6$ . Figure 2 depicts how this applies to waves of steepness,  $H/\lambda = 1/12$ , whose leading front went on to break. We therefore seek to use the exceeding of this bound---as when any wave steepens to a sharp crest---as a "trigger" for the activation of a localized wave damper in the fully nonlinear computations.

To implement the idea, we then proceed to reformulate the steepness criterion in terms of a limiting value of  $\kappa a$ : Adopting the approximate criterion that a wave breaks when its steepness,  $H/\lambda$ , exceeds  $1/12$  and using the above bound on  $|\kappa\lambda|$ , we obtain the condition,  $|\kappa H| \leq 0.5$  for a wave not to break. We convert this into one based on  $\kappa a$  since the crest-to-trough wave-height is not as easily available; we do so on the basis of the observable geometric property of incipient breaking waves that  $a = 0.7 H$  on

an average (e.g., Bonmarin, 1989), obtaining, finally,  $|\kappa a| \leq 0.35$ .

In order to examine the reliability of this curvature-based criterion, regular, deep-water gravity waves of varying steepnesses (as generated in a two-dimensional wave tank by a wedge wave-maker) were simulated, and the variation of  $|\kappa a|$  with the steepness,  $ak$  was noted. (Note that, in the evaluation of the abscissas, the nominal wavelength given by  $k = \omega^2/g$  was used.) This variation is depicted in figure 3; for comparison, that for a second-order Stokes wave is also presented. For all waves of steepness,  $ak$  less than about 0.25, the prescribed threshold value of  $|\kappa a| = 0.35$  is never exceeded. For higher  $ak$ , this limit is exceeded at times by waves that attain a sharp crest, especially at the leading wave front. Not all waves that do so go on to break; therefore, the present threshold poses a conservative, if imprecise limit. However, a conservative criterion is necessary to ensure that all likely instances of breaking are detected so that they may be suppressed.

Although some of the scatter in the data in figure 3 is due to the non-uniformities in fully nonlinear waveforms, it is largely due to the inevitable noise in the numerical evaluation of the curvature. We compute the curvature using a local three-point formula arising from the fitting of a circle through three consecutive free-surface nodes—a formula that does give agreeable results with the analytically obtained curvatures for smoother profiles. Nonetheless, this scatter does not appear to affect the nature of the  $|\kappa a|$ - $ak$  curve or the limiting  $|\kappa a|$  value considerably.

Finally, the sensitivity of the curvature computations to the fineness of the node distribution was studied through a convergence study: The curvature of the free-surface was computed for one particular case of wave-maker motion amplitude and frequency (the resulting waves had a steepness of about  $ak=0.21$ ) using three different node distributions—25, 50, and 100 nodes per wavelength (the usual distribution adopted—the minimum recommended—is 30 nodes per wavelength; the results presented in figures 2 and 3 were obtained using 40 nodes per wavelength). A sample comparison of the results is presented in figure 4. Notice that although there is a lot more noise in the calculations as the node density increases, the important maximum values of the curvature do not change much between the three cases.

Thus, we have arrived at a curvature-based criterion for breaking that is simple and easy to implement, even when waves of different frequencies are present. The mechanism by which energy is absorbed locally from the waves when this criterion is met is discussed in the next section.

## SUPPRESSION OF A BREAKING WAVE

We employ a variation of the numerical absorbing beach used by Cao et al. (1993), in order to suppress wave-breaking locally; the basic idea, though, is the same—it consists of exerting an additional, external pressure on the wave in the vicinity of the location where the likelihood of wave-breaking has been detected. By causing the wave to work against this external pressure, the energy necessary to prevent the wave from breaking is extracted locally from the fluid (hence, "local absorbing patch"). Mathematically, this consists of the inclusion of an additional term,  $P_{damp}$ , in the dynamic free-surface boundary condition:

$$\frac{\partial \phi}{\partial t} + \frac{1}{2} \nabla \phi \cdot \nabla \phi + \frac{p}{\rho} + gz + \frac{P_{damp}}{\rho} = 0.$$

Note that  $P_{damp}$  is non-existent outside the absorbing patch; within the patch, we prescribe the following form to the damping term:

$$P_{damp} = \sigma v(x) |\nabla \phi|^2 \operatorname{sgn} \left( \frac{\partial \phi}{\partial n} \right)$$

The  $|\nabla \phi|^2$  term determines the magnitude of the damping;  $\sigma$  is a coefficient that may be varied to increase or decrease the amount of damping; the signum function ensures that the pressure is acting against the wave; and  $v(x)$  is a shape function chosen to ensure that the damper takes the form of a smoothly varying patch:

$$v(x) = 0.5 \left[ 1 + \cos \left( \frac{\pi(x-x_0)}{L_0} \right) \right]$$

Here,  $x_0$  is the location where  $|\kappa a| = 0.35$  is exceeded, and  $L_0$  is half the length, centered about  $x_0$ , over which the damper acts. We prescribe  $L_0$  to be  $a/0.35$  ( $a$  is the wave amplitude at  $x_0$ )—again, from considerations of the geometry of breaking waves, so that the energy is extracted from approximately the portion of the wave between zero-crossings.

## RESULTS

The effectiveness of the present "local absorbing patch" model is demonstrated by application to the breaking wave encountered in figure 1. As shown in figure 5, the wave-breaking is successfully detected and suppressed sufficiently for the calculations to proceed. The strength of the damping constant used was  $\sigma=12.5$ . An uncertainty with the present model, however, is that the amount of damping required to suppress

wave-breaking is not easily determined---some other calculations have required larger values of  $\sigma$  (of about 25) to suppress the wave-breaking. Moreover, it may well be that for extreme cases suppressing the tendency of waves to break while obtaining reasonable results in the post-breaking regime is an impossible task. These call for additional investigations.

The effects of prescribing a  $\sigma$  greater than that which is necessary to suppress the breaking may be small, as the results plotted in figure 6 suggest. Therein, a comparison is made of the calculations presented in figures 1 and 5 and an additional calculation obtained using damping equivalent to  $\sigma=25$ . Not only does the plot clearly show the difference in the wave profile due to the extraction of the energy associated with the breaking, but also, the difference in the calculations obtained with the two different damping strengths is imperceptible. This is due to the feature of the model that damping is present only when triggered by high values of  $|ka|$  ( $|ka|$  greater than 0.35) and only as long as  $|ka|$  is above the threshold value.

The present model therefore holds much promise for extending fully nonlinear water wave computations into the important highly nonlinear regime. An important step involves the validation of the post-breaking calculations against experimental data, which we are currently seeking. Efforts are also underway to develop a strategy for extending the model to three-dimensional flow computations. A proposed approach, especially for ship-flow calculations, is to detect the occurrence of and suppress wave-breaking along prescribed free-surface paths (these are the paths on which the Lagrangian nodes are convected in the UM-DELTA method; they generally take the appearance of free-surface streamlines).

Future work will involve the extensive testing of the model over a wide variety of breaking wave conditions. We also plan to compute the total energy in the fluid domain and the fraction of the total energy that is absorbed by the wave damper. We hope to relate the computed energy losses to the numerous experimental studies of wave-breaking.

## ACKNOWLEDGEMENTS

This research was funded by the Office of Naval Research and the University of Michigan--Sea Grant--Industry Consortium on Offshore Engineering. The computations were supported by allocations of high performance computing resources through the U.S. Department of Defense High Performance Computing Modernization Program and the National Partnership for Advanced Computational Infrastructure. We thank Mr. Eirik Malthe-Sorensen for his assistance with some of the calculations.

## REFERENCES

- Bonmarin, P., "Geometric Properties of Deep-Water Breaking Waves," *Journal of Fluid Mechanics*, Vol. 209, 1989, pp. 405-433.
- Cao, Y., Beck, R.F., and Schultz, W.W., "An Absorbing Beach for Numerical Simulations of Nonlinear Waves in a Wave Tank," *Proceedings*, Eighth International Workshop on Water Waves and Floating Bodies, Newfoundland, Canada, 1993.
- Griffin, O., Peltzer, R., Wang, H., and Schultz, W., "Kinematic and Dynamic Evolution of Deep Water Breaking Waves," *Proceedings*, Twentieth Symposium on Naval Hydrodynamics, Santa Barbara, U.S.A., 1994.
- Scorpio, S.M. and Beck, R.F., "A Multipole Accelerated Desingularized Method for Computing Nonlinear Wave Forces on Bodies," *Proceedings*, Fifteenth Offshore Mechanics and Arctic Engineering Conference, Florence, Italy, 1996; also, to appear in the *Journal of Offshore Mechanics and Arctic Engineering*.
- Wang, P., Yao, Y., and Tulin, M.P., "Wave Group Evolution, Wave Deformation, and Breaking: Simulation Using LONGTANK, a Numerical Wave Tank," *International Journal of Offshore and Polar Engineering*, Vol. 4, No. 2, 1994.

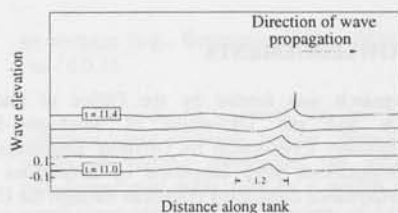


Figure 1. Time-history of the surface displacement in a numerical simulation, using UM-DELTA, of shallow-water waves generated by a piston wave-maker in a two-dimensional wave-tank. The calculations cease at about  $t=11.4$  due to the occurrence of a breaking wave caused by the coalescing of waves of different frequencies.

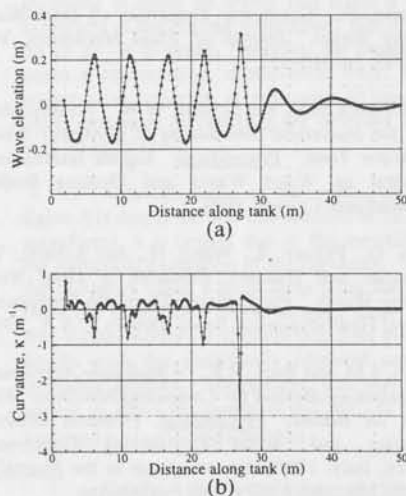


Figure 2. A representative snapshot at  $t=18.8$ : (a) the surface displacement, and (b) the curvature of the surface, for waves as generated by a wedge wave-maker of motion amplitude 0.12m and frequency 0.559Hz (nominal  $\lambda=5$ m). The leading wave front broke at about  $t=23.3$  in this simulation. Note that for the other wave crests,  $|\kappa\lambda| \leq 6$ , approximately.

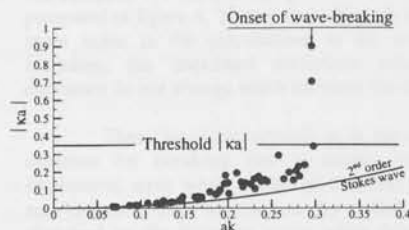


Figure 3. Observed variation with wave steepness,  $ak$ , of the proposed wave-breaking index,  $|\kappa\lambda|$ , for regular, deep-water gravity waves. The variation for a 2<sup>nd</sup> order Stokes wave is presented for comparison.

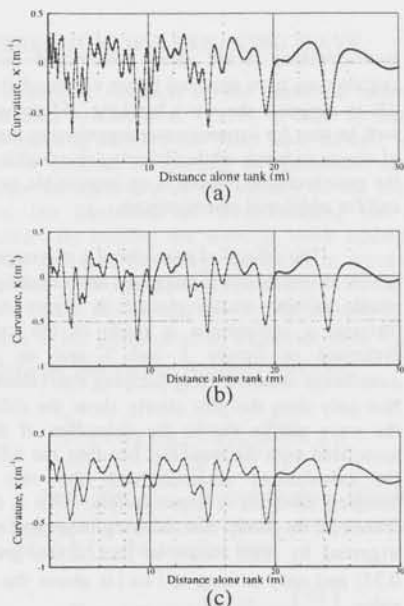


Figure 4. A representative snapshot of the computed curvature of the surface (for waves generated by a wedge wave-maker of motion amplitude 0.08m and frequency 0.559Hz), using: (a) 100 nodes per wavelength, (b) 50 nodes per wavelength, and (c) 25 nodes per wavelength.

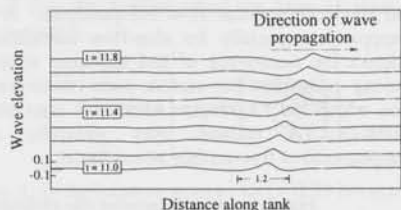


Figure 5. Time-history of the surface displacement in a repeat of the numerical simulation shown in figure 1, but differing (only) in that a "local absorbing patch" model has been implemented. The model detects the likely occurrence of and suppresses the wave-breaking.

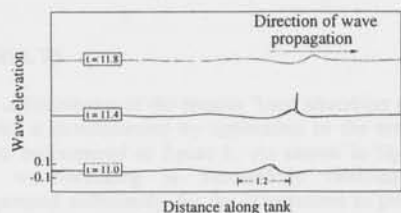


Figure 6. Time-history of the surface displacement in simulations involving: no damping (solid line); damping with  $\sigma=12.5$  (dashed line); and damping with  $\sigma=25$  (dotted line).

# WATER WAVES BENEATH A FLOATING ELASTIC PLATE

by Ken Takagi

Dept. of Naval Architecture and Ocean Engineering, Osaka University

## 1. Introduction

Recently the estimation of elastic motion of a very large floating structure (VLFS) has been carried out for the Mega-Float project in Japan. Dimensions of the floating structure in this project is 5,000 m length and 1,500 m width. The typical wave period of the installation point is 6 seconds. Several reliable numerical works have been completed, however it was very tough job to obtain the reliable result since the length of incident waves is very short compared to the dimensions of VLFS. Following the numerical results, it is found that the elastic motion of VLFS is seems like a propagation of water waves beneath a thin elastic-plate. However, since those numerical works are based on the modal analysis, it is difficult to imagine a image of the motion of VLFS as propagating waves before summing up each modes. Therefore, another approach is needed to make simple image of the motion of VLFS. Ohkus and Namba [1996] treated this problem as a wave propagation beneath a thin elastic-plate and presented a free surface condition which is imposed on the region covered with the plate. Helmans [1997] also presented a similar treatment in which he applied the assumption of very short wave length. In the present paper, a similar free surface condition for the region covered with the plate is applied and a Green function of that problem is derived. The eigen function expansion method is evolved from Green's second identity.

## 2. Free Surface Condition

Suppose a flat floating platform of draft  $d$  ( $d = 1 \sim 2m$  in Mega-Float project) located in the  $x$ - $y$  plane which coincides with the still water surface. Following previous works, the assumption of  $d/\lambda \ll 1$  is applied. Since the motion of the fluid is supposed to be invicid, irrotational and incompressible. The velocity potential satisfying Laplace's equation is introduced. Further assumption is that the motion is sinusoidal with the angular frequency  $\omega$ .

Thin elastic plate theory gives the equation of the vertical displacement  $\zeta$  of the plate.

$$m \frac{\partial^2 \zeta}{\partial x^2} = -D \left( \frac{\partial^2}{\partial x^2} + \frac{\partial^2}{\partial y^2} \right)^2 \zeta - \rho g \zeta - i \rho \omega \phi(x, y, 0) \quad (1)$$

Where,  $m$  is the mass of unit area of the plate,  $\rho$  the density of the water and  $g$  the gravitational acceleration.  $D$  is the flexural rigidity of the platform given by  $D = ET^3/12(1 - \nu^2)$ . Where  $T$  is the thickness,  $E$  the equivalent Young's modulus of the plate and  $\nu$  Poisson's ratio. Since the mass of plate is uniformly distributed, it is obvious that the left hand side of (1) is negligible.

Substituting the body boundary condition of the plate into equation (1), the free surface condition is obtained.

$$-K\phi + \left[ \hat{\beta} \left( \frac{\partial^2}{\partial x^2} + \frac{\partial^2}{\partial y^2} \right)^2 + 1 \right] \frac{\partial \phi}{\partial z} = 0 \quad \text{on } z = 0 \quad (2)$$

Where,  $\hat{\beta} = D/(\rho g)$  and  $K = \omega^2/g$ . In the two-dimensional case the free surface condition is reduced as follows:

$$-K\phi + \left(1 + \beta \frac{\partial^4}{\partial x^4}\right) \frac{\partial \phi}{\partial z} = 0 \quad \text{on} \quad z = 0 \quad (3)$$

Where,  $\beta = \frac{EI}{\rho g}$  and  $EI$  presents the bending rigidity. Suppose the plane progressive waves on the plate floating on the water of depth  $h$ . Where the water depth is assumed to be as same order as the wave length. The following dispersion relation is obtained.

$$K = \alpha(1 + \beta\alpha^4) \tanh \alpha h \quad (4)$$

It is apparent that two roots of equation (4) are located on the positive and negative real axis and innumerable roots are located on the imaginary axis. Other four roots are also found on each quarter planes.

### 3. Two-Dimensional Green Function

A two-dimensional Green function which satisfies Laplace's equation, the free surface condition (3) and the bottom condition is obtained as follows:

$$G(x, z, \hat{x}, \hat{z}) = \sum_{n=0}^{\infty} \frac{e^{-i\alpha_n|x-\hat{x}|} \{K \sinh \alpha_n \hat{z} + (1 + \beta\alpha_n^4)\alpha_n \cosh \alpha_n \hat{z}\} \cosh \alpha_n(z+h)}{\alpha_n \left\{ \frac{Kh}{\sinh \alpha_n h} + (1 + 5\beta\alpha_n^4) \sinh \alpha_n h \right\}} \quad (5)$$

Where,  $\alpha_n (n = 0, 1, 2, \dots)$  denote the roots of equation (4) located in the lower half plane. Applying Green's second identity to the region  $x \leq 0$ , the following integral equation is obtained.

$$\begin{aligned} \phi = & i\omega \frac{\beta}{K} \left( \frac{\partial G}{\partial z} \frac{d^3 \zeta}{dx^3} - \frac{\partial^2 G}{\partial x \partial z} \frac{d^2 \zeta}{dx^2} + \frac{\partial^3 G}{\partial x^2 \partial z} \frac{d \zeta}{dx} - \frac{\partial^4 G}{\partial x^3 \partial z} \zeta \right)_{x=0} \\ & - \int_{-h}^0 \left( \phi \frac{\partial G}{\partial \hat{x}} - \frac{\partial \phi}{\partial \hat{x}} G \right) d\hat{z} \end{aligned} \quad (6)$$

Where, it is assumed that the plate is infinitely long and covers all left half plane. The regular radiation condition is imposed on the left end boundary.

If the boundary condition at  $x = 0$  and the end conditions of the plate are given, above integral equation would be solved.

### 4. Eigen Function Expansion

If the integral appeared in equation (6) can be carried out in advance, the following series expansion would be obtained.

$$\phi = \sum_{n=0}^{\infty} i T_n \frac{\omega \cosh \alpha_n(z+h)}{\alpha_n \sinh \alpha_n h} e^{i\alpha_n x} \quad (7)$$

#### Orthogonality

The eigen functions appeared in equation (7) are not orthogonal. However, the following relations are obtained.

$$\hat{I}_n = \int_{-h}^0 \phi \cosh \alpha_n(z+h) dz = \hat{q}_n T_n - \frac{d^2 \zeta}{dx^2} \hat{S}_n + \zeta \alpha_n^2 \hat{S}_n \quad (8)$$

$$\tilde{I}_n = \int_{-h}^0 \frac{\partial \phi}{\partial x} \cosh \alpha_n(z+h) dz = \tilde{q}_n T_n - \frac{d^3 \zeta}{dx^3} \hat{S}_n + \frac{d \zeta}{dx} \alpha_n^2 \hat{S}_n \quad (9)$$

Where,

$$\hat{q}_n = \frac{i}{2} \frac{\omega}{\alpha_n} \left( \frac{h}{\sinh \alpha_n h} + \frac{1}{K} (1 + 5\beta \alpha_n^4) \sinh \alpha_n h \right) \quad (10)$$

$$\tilde{q}_n = -i \alpha_n \hat{q}_n \quad (11)$$

$$\hat{S}_n = -i \omega \frac{\beta}{K} \alpha_n \sinh \alpha_n h \quad (12)$$

## 5. Examples of 2-D Problem

### Transmission and Reflection of Incident Waves

When plane waves incident on the elastic plate, some are reflected at the edge of the plate and others are transmitted into the region covered with the elastic plate. The velocity potential is represented by the series of eigen functions in the region  $x \geq 0$ .

$$\phi = i \frac{\omega}{k_0} \frac{\cosh k_0(z+h)}{\sinh k_0 h} e^{ik_0 x} + \sum_{n=0}^{\infty} i R_n \frac{\omega}{k_n} \frac{\cosh k_n(z+h)}{\sinh k_n h} e^{-ik_n x} \quad (13)$$

Where,  $k_n$  denotes the roots of the dispersion relation of water waves.

$$K = k_n \tanh k_n h \quad (14)$$

The velocity potential in the region  $x \leq 0$  is represented by the series expansion (7).

It is well known that the eigen functions appeared in equation (13) are orthogonal. Therefore, employing the condition that the velocity potential and the horizontal velocity are continuous at the matching boundary, we can get the same number of equations as the number of coefficients  $R_n$  and  $T_n$ . However, we also have other unknowns  $\zeta_{xx}$  and  $\zeta$ . The end condition of the plate i.e. the shearing force and the moment at the end are free gives the following two equations.

$$\sum_{n=0}^{\infty} \alpha_n^3 T_n = 0, \quad \sum_{n=0}^{\infty} \alpha_n^2 T_n = 0. \quad (15)$$

Then, the problem can be solved, since the number of equations is as same as the number of unknowns.

### Reduction of Transmitted Waves

It is strongly required that the motion of VLFS must be very small. However, it was found in the previous works that the motion of VLFS is not negligible. Then, some ideas for the reduction of the motion is proposed. One simple method is attaching a plate or block at the tip of the VLFS to block the transmission of incident waves.

Suppose a block of draft  $\hat{d}$  and breadth  $2b$  attaching at the edge of the plate, the velocity potential under the block is represented as follows:

$$\begin{aligned} \phi = & \frac{i\omega}{2l} Z(-x^2 + z^2 + 2hz) + \frac{i\omega}{6l} \Theta(-x^3 + 3xz^2 + 6hxxz) \\ & + \sum_{n=1}^{\infty} \left( S_n \frac{\cosh \frac{n\pi x}{l}}{\cosh \frac{n\pi b}{l}} + A_n \frac{\sinh \frac{n\pi x}{l}}{\sinh \frac{n\pi b}{l}} \right) \cos \frac{n\pi}{l} (z+b) (-1)^n. \end{aligned} \quad (16)$$

Where,  $l = h - \hat{d}$ ,  $Z$  the heave amplitude and  $\Theta$  the roll amplitude. The equation of motion of the block is given by

$$\left. \begin{aligned} Z(2bg - \omega^2 \frac{W}{g}) &= F_f + EI \frac{\partial^3 \zeta}{\partial x^3} \\ \Theta(W \cdot GM - \omega^2 I_{\theta\theta}) &= M_f - EI \frac{\partial^2 \zeta}{\partial x^2} - b \cdot EI \frac{\partial^3 \zeta}{\partial x^3} \end{aligned} \right\} \quad (17)$$

Where,  $F_f$  and  $M_f$  are fluid dynamic forces,  $W$  weight of the block,  $GM$  metacentric height and  $I_{\theta\theta}$  moment of inertia of the block. End conditions of the plate are given by

$$Z - b\Theta = \zeta \quad \Theta = \frac{d\zeta}{dx} \quad (18)$$

Now the number of equations is as same as the number of unknowns. We can get the solution.

## 6. Conclusions

The treatment of the motion of VLFS as a propagation of water waves beneath a elastic plate is presented in this paper. Some examples of solution for the two-dimensional problem are shown. Further results will be demonstrated at the workshop.

## References

- Hermans, A. J. (1997) "The Excitation of Waves in a Very Large Floating Flexible Platform by Short Free-Surface Water Waves", Proc. of 12th Int. Workshop on Water Waves and Floating Bodies", Carry-le-Rouet, France
- Ohkusu, M. and Nanba, Y. (1996) "Analysis of Hydroelastic Behavior of a Large Floating Platform of Thin Plate Configuration in Waves", Proc. of Int. Workshop on VLFS, Hayama, Japan

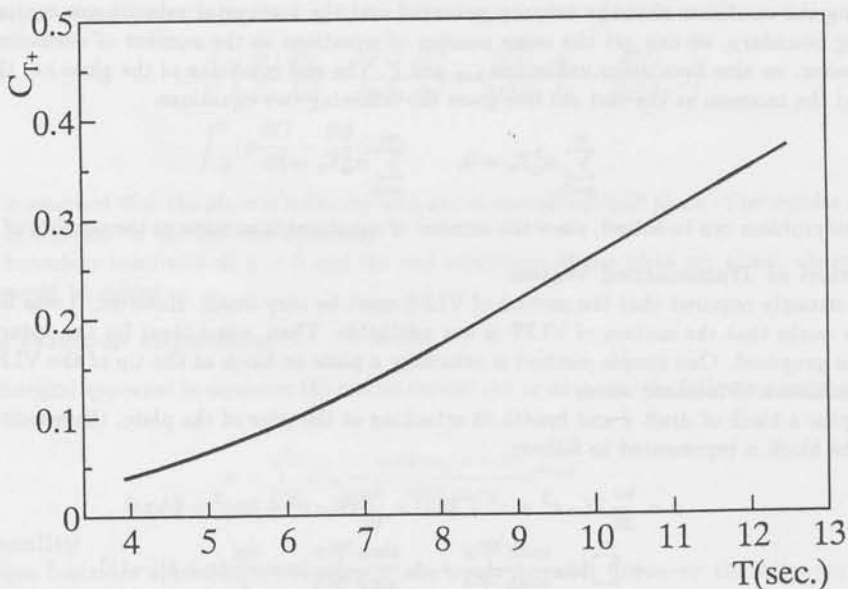


Fig.1 Transmission coefficient at the edge of infinitely long elastic plate.

### Spectral response surfaces, designer waves and the ringing of offshore structures

Peter S. Tromans (presenting author),

Shell International, PO Box 60, 2280 AB Rijswijk, The Netherlands.

Tel: +31 70 311 3565; fax: +31 70 311 2085; e-mail: p.s.tromans@sidsbv.shell.com

I. Ketut Suastika,

Dept. Civil Engineering, TU Delft.

The purpose of this paper is to present a novel approach to offshore wave load analysis, the spectral response surface method, and demonstrate its application to the ringing problem. A distinguishing feature of the method is its ability to relate an extreme response to a particular ocean surface history, the "designer wave."

We briefly overview the essential features of the method. A linear random sea can be represented by the sum of many un-correlated frequency components which obey a joint normal distribution. In many cases, a structural response (or an ocean surface property) can be expressed as a function of these frequency components and their Hilbert transforms (the same signal phase shifted by  $\pi/2$ ). A constant value of the structural response defines a hyper-plane in the multi-dimensional space of the frequency components. Since, the statistics of the spectral components are joint normal, it is straightforward to estimate the combination of frequency components (and their phases) most likely to generate an extreme response and the probability of a response level being exceeded. We summarise the method and its application to the ringing problem more fully below.

Ringing might be described as a transient structural response which resembles that generated by an impulse excitation of a linear oscillator. The response exhibits a rapid build up and slow decay of energy concentrated around the natural frequency of the structure. It has been observed in model experiments on gravity base structures during the passage of steep wave crests. The ringing response contains frequencies that are relatively high compared to the dominant frequency of the wave field, indicating that non-linearity in the load process might determine its occurrence. In this study, Newman's long wave-length force-model [1] is used for calculating the wave loads on a column standing in a random sea. Diffraction is included in the analysis. The model allows non-linear wave forces up to the third-order to be calculated using linear wave theory as input.

We have re-formulated Newman's results in terms of the frequency components of the ocean surface elevation process and their Hilbert transforms. The frequency components are all standardised; that is transformed to unit variance and zero mean variables. By treating the structure as a single degree of freedom oscillator, the dynamic response of the structure can also be expressed in terms of the standardised variables. Using these expressions, it is possible to generate surfaces of constant response level for both static and dynamic response in the space of the spectral components of the ocean surface.

A random sea can be described by the superposition of a finite number of spectral components; these are the standardised variables each multiplied by a standard deviation to match an appropriate surface energy spectrum. Each component is narrow banded (a pure harmonic modulated by a slowly varying amplitude) and is normally distributed. As the spectral components and their Hilbert transforms are un-correlated, linear processes, they obey a joint normal distribution with zero cross correlation. Surfaces of constant probability density are concentric spheres in the space of the standardised variables representing the spectral components of the ocean surface. The probability density is highest at the origin and falls monotonically as a function of distance from the origin that is independent of direction. Under these circumstances, it is straightforward to treat the response surfaces as limit states in a FORM (first order reliability method) type of analysis. The point on a surface of constant response where the distance to the origin is shortest is called the "design point." The design point is, to a good approximation, the point on the surface where a maximum is most likely to be found. The accuracy of the approximation increases as the severity of the response increases and, in consequence, the distance of the design point from the origin increases.

The design point defines the amplitude and phase of the standardised variables at the instant when the extreme occurs. Thus, it allows us to deduce the time histories of the response and related variables around the time of the extreme. These histories are the ones that are the ones most likely to be associated with a response maximum of the chosen level. Thus, in the case of the ringing problem, we can identify if ringing occurs or not; that is if ringing determines the extreme response. It allows us to identify the type of applied load history that excites a ringing response. In addition, it provides the surface history (the "designer wave") that generated the applied load and the response. Finally, we can estimate the exceedance probabilities of extreme ringing responses very efficiently. We achieve this by calculating the probability of finding a maximum above a hyper-plane tangent to the response surface at the design point.

We studied the case of a 10 m diameter column in a sea of significant wave height of 12 m and a zero crossing period of 13.5 s that obeys a JONSWAP spectrum. The water depth is 300 m. The dynamics are modelled by an oscillator with a natural frequency of 1.57 rad/s, while the peak of the surface energy spectrum is approximately 0.36 rad/s. We investigated the effects of using the Newman load model to first order, to second order and to third order and drew the following conclusions:

1. The method is tractable.
2. The non-linear terms in Newman's model have a much greater effect on dynamic response than on applied load.
3. Some ringing effects can be found in the response with only second order excitation.
4. The third order terms lead to a double impulse (positive impulse followed immediately by a negative impulse) loading that excites a strong ringing type of response. The double impulse is associated with a wave crest; the positive impulse immediately precedes it and the negative impulse follows it. Apart from the isolated

double impulse the third order excitation is insignificant. The response time series is shown in Figure 1, the associated surface history in Figure 2 and the third order component of load in Figure 3.

5. For the sea state studied, the non-linear effects and consequent ringing, lead to much larger responses for exceedance probabilities of order 1/100 and rarer.
6. The method is many times faster than random time domain simulation.

As well as presenting the ringing study and results, the paper discusses the general merits of this approach to structural analysis. The method generates ocean surface histories that generate extreme responses, "designer waves," very quickly and easily. This is potentially of great practical value since designer waves can be used to provide the type of information that would otherwise involve many hours of time domain simulation. As such, the method may be of value in engineering design as well as in general analysis.

#### References

- [1] Newman, J.N. (1996) "Non-linear scattering of long waves by a vertical cylinder," published in "Waves and non-linear processes in hydrodynamics," pp 91-102, J. Grue et al (editors), Kluwer, The Netherlands.

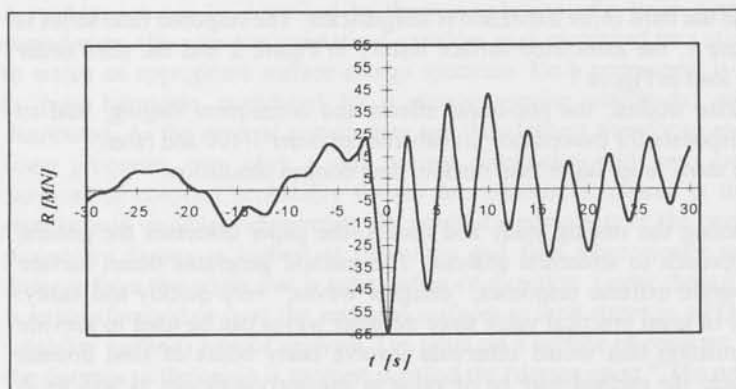


Figure 1: Negative dynamic response with first, second and third-order excitation

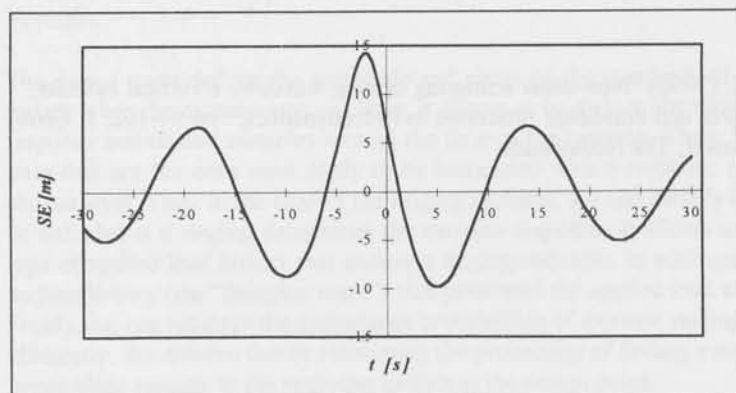


Figure 2: Surface elevation generating the response time series in Figure 1

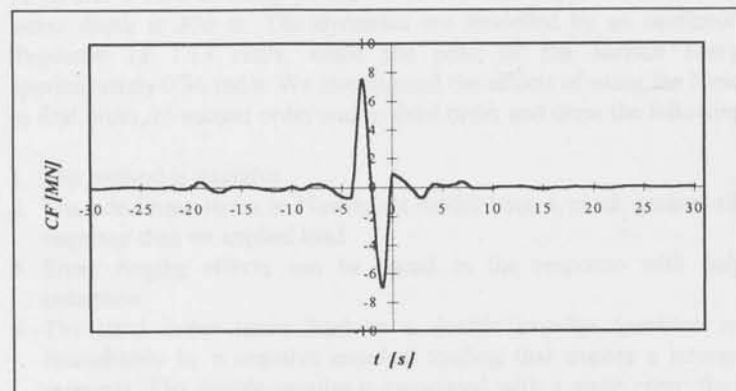


Figure 3: Third-order component of the force excitation

## FREE-SURFACE EVOLUTION AT THE EDGE OF AN IMPULSIVELY UPWELLING FLUID LAYER

Peder A. Tyvand  
Department of Agricultural Engineering  
Agricultural University of Norway  
1432 Ås, Norway

### INTRODUCTION

Impulsive free-surface flows provide opportunities for studying analytically the early evolution of hydrodynamic nonlinearities. This type of research started with the wavemaker analysis of Peregrine (1972). The wavemaker problem is difficult because of the free-surface singularity arising at the intersection between the free surface and the moving plate. This singularity reveals that the asymptotic series is not uniformly valid. The Taylor series in time constitutes an outer expansion, and an inner expansion must be introduced to remove the singularity (King & Needham 1994). When the impulsive free-surface flow is due to submerged objects, one avoids free-surface singularities.

The present paper introduces a new variety of impulsive flow problems: a given flux through a fixed bottom is turned on at time zero. The present model is one of the cases where the exact surface elevation of a small-time expansion can be calculated to third order. Other examples are the submerged line vortex (Tyvand 1991), and the line source, either submerged (Tyvand 1992) or located at a bottom (Tyvand 1998). The solution for the submerged line source has been verified numerically by Kim (1997). A review of small-time expansions for impulsive free-surface flows is given by Tyvand & Miloh (1998).

We will investigate the evolution of nonlinear free-surface effects at the border between a region of forced uniform upwelling and a region of stagnant fluid. For small times the initial depth is the only characteristic length. This implies that all early nonlinear effects will be localized within a few length units around the edge between upwelling fluid and stagnant fluid. The early wave generation must also take place at the edge of the upwelling region. But the later wave propagation away from this edge cannot be captured by our analytical small-time expansion.

### MATHEMATICAL FORMULATION

We consider an inviscid fluid layer of constant depth which is at rest at negative times. The layer depth  $h^*$  is the only

length scale of the initial flow problem. So the Froude number  $F$  is defined as :

$$F = W^*(g^* h^*)^{-1/2} \quad (1)$$

The gravitational acceleration is  $g^*$ , and  $W^*$  is the upwelling fluid velocity plus the downwelling fluid velocity. In general, the fluid is upwelling along the bottom for positive  $x$  and downwelling for negative  $x$ . From now on we work with non-dimensional quantities based on the units  $W^*$  and  $h^*$ .

The inviscid flow is governed by Laplace's equation for the velocity potential  $\Phi(x, y, t)$ . The surface elevation is  $\eta(x, t)$ . The free-surface conditions are:

$$\partial\eta/\partial t + \nabla\Phi \cdot \nabla\eta = \partial\Phi/\partial y \quad \text{at} \quad y = \eta(x, t) \quad (2)$$

$$\partial\Phi/\partial t + (1/2) |\nabla\Phi|^2 + F^{-2} \eta = 0 \quad \text{at} \quad y = \eta(x, t) \quad (3)$$

As initial state we take an impulsive start from a situation at rest with a horizontal free surface:

$$\eta(x, 0) = 0 \quad (4)$$

$$\Phi(x, 0, 0) = 0 \quad (5)$$

The dimensionless upwelling and downwelling velocities for positive and negative  $x$  will be denoted by  $V_+$  and  $V_-$ , respectively. By definition we have  $V_+ + V_- = 1$ . The impulsively forced flow is given by:

$$\partial\Phi/\partial y = V_+ \quad , \quad y=-1, \quad x>0, \quad t>0 \quad (6a)$$

$$\partial\Phi/\partial y = -V_- \quad , \quad y=-1, \quad x<0, \quad t>0 \quad (6b)$$

## RESULTS

The velocity potential and surface elevation are expanded as Taylor series in time (Tyvand 1991):

$$(\Phi, \eta) = H(t) [(\Phi_0, 0) + t (\Phi_1, \eta_1) + t^2 (\Phi_2, \eta_2) + \dots] \quad (7)$$

$H(t)$  denotes the Heaviside unit step function. We choose to develop the solution in terms of a Fourier series with an artificial periodicity of length  $L$  in  $x$ -direction. Then the first-order elevation is (sum taken over positive  $n$ ):

$$\eta_1 = (V_+ - V_-)/2 + 2\pi^{-1} \sum_{n \text{ odd}} n^{-1} \operatorname{sech}(2\pi n/L) \sin(2\pi n x/L) \quad (8)$$

The exact solution in the limit  $L \rightarrow \infty$  is:

$$\eta_1 = (V_+ - V_-) / 2 + 2 \pi^{-1} \sum_{k=1}^{\infty} (-1)^{k+1} \arctan [x / (2k-1)] \quad (9)$$

This exact solution is found by differentiating the bottom source solution (Tyvand 1998). The convergence of eq.(8) is good when  $L > 20$ . The second-order elevation consists of one odd and one even function of  $x$ :

$$\eta_2(x) = \eta_{2, \text{odd}} + \eta_{2, \text{even}} \quad (10)$$

$$\eta_{2, \text{odd}} = \quad (11a)$$

$$L^{-1} (V_+ - V_-) \sum_{n \text{ odd}} \operatorname{sech}(2\pi n/L) \tanh(2\pi n/L) \sin(2\pi n x/L) \quad (11b)$$

$$\eta_{2, \text{even}} = \quad (11b)$$

$$- (\pi L)^{-1} \sum_{n, m \text{ odd}} [ (m^{-1} - n^{-1}) \tanh(2\pi(n-m)/L) \cos(2\pi(n-m)x/L) \\ - (m^{-1} + n^{-1}) \tanh(2\pi(n+m)/L) \cos(2\pi(n+m)x/L) ] \\ \operatorname{sech}(2\pi n/L) \operatorname{sech}(2\pi m/L)$$

Both these terms are important except for the case of antisymmetric upwelling/downwelling ( $V_+ = V_- = 1/2$ ), where the odd term vanishes.

In this note we omit the third-order terms due to nonlinear interaction. We consider only the gravity-dependent term  $\eta_3^{(F)}$ , where superscript  $F$  refers to Froude number. It is proportional to the odd contribution to the second-order elevation:

$$3 F^2 \eta_3^{(F)} = 2 \eta_{2, \text{odd}} \quad (\text{evaluated for pure upwelling}) \quad (12)$$

In figure 1 some snapshots of the total surface elevation to third order is shown, for pure upwelling:  $(V_+, V_-) = (1, 0)$ . The Froude number is 0.5.

#### REFERENCES

- Kim, M.-J. 1997 Numerical study of dip formation using sink array model. Submitted to Int. J. Modern Phys. C.  
 King, A.C. & Needham, D.J. 1994 The initial development of a jet caused by fluid, body and free-surface interaction. Part 1. A uniformly accelerating plate. J. Fluid Mech. 268, 89-101.  
 Peregrine, D.H. 1972 Flow due to a vertical plate moving in a channel. Unpublished note.  
 Tyvand, P.A. 1991 Motion of a vortex near a free surface.

- J. Fluid Mech. 225, 673-686. (Appendix by R.P. Tong).  
 Tyvand, P.A. 1992 Unsteady free-surface flow due to a line source. Phys. Fluids A4, 671-676.  
 Tyvand, P.A. 1998 Impulsive free-surface flow due to a line source at a bottom. Manuscript.  
 Tyvand, P.A. & Miloh, T. 1998 Small-time asymptotic free-surface hydrodynamics. To be published in J. Engng. Math.

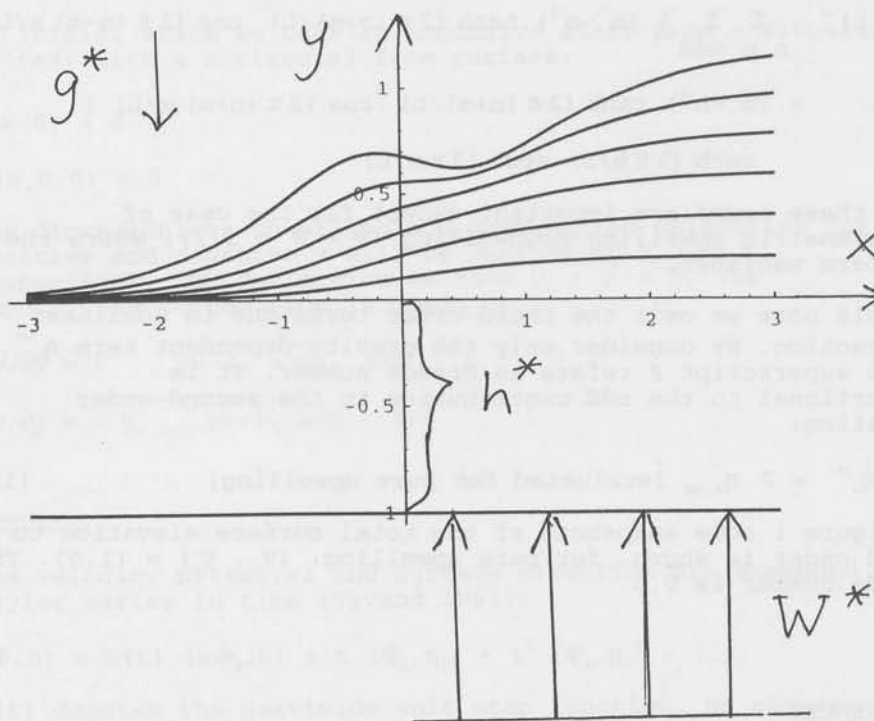


Figure 1: Snapshots of free surface shape  $y = \eta(x, t)$ , to third order in the small-time expansion. Pure upwelling:  $(V_x, V_y) = (1, 0)$ .  $F = 0.5$ . Increments of 0.2 are chosen in the dimensionless time  $t (= t^* W^*/h^*)$ .

## ON THE VALIDITY OF MULTIPOLE EXPANSIONS

by

F. URSELL

DEPARTMENT OF MATHEMATICS, MANCHESTER UNIVERSITY, M13 9PL, U.K.

### 1 Introduction

The Method of Multipoles is an effective method for solving certain scattering problems in linear wave theory, particularly those involving immersed and submerged circles (in two dimensions) and spheres (in three dimensions). An example is the submerged sphere between parallel walls which has been treated by G.X.Wu and for which an alternative treatment was suggested by me at the last Workshop. During the discussion David Evans raised the following question: Can the potential always be expressed as the sum of the appropriate multipoles? For the proof we need to find good bounds for the image potentials and there is no simple method for this. In the present note I shall show that there is a simple argument for two dimensions, and a more complicated argument for three dimensions. I have no serious doubts about the validity of multipole expansions, (including the expansions in Wu's problem, ) but it is curious that the mathematical arguments are not more obvious.

### 2 The circle

We consider first the classical problem of the submerged circle in two dimensions. The velocity potential  $\phi(x, y)e^{-i\omega t}$  is defined in the part of the region  $(-\infty < x < \infty, 0 < y < \infty)$  outside the circle

$$x^2 + (y - f)^2 = a^2,$$

where  $a < f$ , and satisfies Laplace's equation

$$\left( \frac{\partial^2}{\partial x^2} + \frac{\partial^2}{\partial y^2} \right) \phi(x, y) = 0. \quad (2.1)$$

The free-surface condition is

$$K\phi + \frac{\partial\phi}{\partial y} = 0 \text{ on } y = 0, \quad (2.2)$$

where  $K = \omega^2/g$ . On the circle the normal velocity is prescribed,

$$\frac{\partial\phi}{\partial r} = U(\theta), \quad (2.3)$$

where  $x = r \sin \theta$ ,  $y = f + r \cos \theta$ . Actually this boundary condition is not used in the following argument. There is also a radiation condition: at  $x = \pm\infty$  the waves travel outwards.

Clearly  $U(\theta)$  is the sum of an even and an odd function of  $\theta$ . We shall assume that  $U(\theta)$  is an even function, an analogous theory can evidently be given for odd functions. For the sake of simplicity we shall also assume that  $\int_{-\pi}^{\pi} U(\theta) d\theta = 0$ . (When this last condition is not satisfied a wave source

$$G_0(x, y) = \frac{1}{2} \log \frac{x^2 + (y - f)^2}{x^2 + (y + f)^2} - 2 \int_0^{\infty} e^{-k(y+f)} \cos kx \frac{dk}{k - K} \quad (2.4)$$

must be added.) There is one obvious method: According to Green's theorem, the potential can be expressed as a distribution of wave sources and wave dipoles over the submerged circle (or sphere). It is therefore sufficient to show that wave sources or dipoles can be expressed as a series of multipoles at the centre of the circle. This construction has been carried out for a half-immersed circle in [Ursell 1981] but the argument is elaborate. Here a much simpler argument will be given. We assume that a solution

$\phi(x, y)$  exists, and we wish to show that this potential can be expressed as the sum of multipoles at the centre of the circle, which (as is well known, see [Ursell 1950], ) are of the form

$$G_m(x, y) = \frac{\cos m\theta}{r^m} + \frac{(-1)^m}{(m-1)!} \int_0^\infty k^{m-1} \frac{k+K}{k-K} e^{-k(y+f)} \cos kx \, dk, \quad m = 1, 2, 3, \dots \quad (2.5)$$

where the contour of integration passes below  $k = K$  to satisfy the radiation condition. Note that the integrand in (2.5) is a solution of Laplace's equation.

PROOF: It is well known that, if the potential exists, it can be expanded in the annulus  $a < r < f$  as a Laurent series of the form

$$\phi(x, y) = \sum_1^\infty \cos m\theta \left( p_m \frac{a^m}{r^m} + q_m \frac{r^m}{f^m} \right) \quad (2.6)$$

where the series

$$\sum_1^\infty \cos m\theta p_m \frac{a^m}{r^m}$$

converges when  $a < r < \infty$ , and the series

$$\sum_1^\infty \cos m\theta q_m \frac{r^m}{f^m}$$

converges when  $0 < r < f$ , actually when  $0 < r < 2a - f$ . In particular, we have a bound

$$|p_m| < M(a')(a'/a)^m$$

for any  $a' > a$ . Now consider the expression

$$\Phi(x, y) = \sum_1^\infty p_m a^m G_m(x, y), \quad (2.7)$$

where the coefficients  $p_m$  are the same as in (2.6). We shall show that this expression is a uniformly convergent series and thus defines a potential everywhere in the field of flow. For this purpose we find bounds for the image potentials

$$\frac{(-1)^m}{(m-1)!} \int_0^\infty k^{m-1} \frac{k+K}{k-K} e^{-k(y+f)} \cos kx \, dk, \quad (2.8)$$

where, as before, the contour of integration passes below the pole  $k = K$ . (It is this pole in the integrand which complicates the mathematical argument.) In (2.8) we write

$$\cos kx = \frac{1}{2} e^{ik|x|} + \frac{1}{2} e^{-ik|x|}. \quad (2.9)$$

Then

$$\int_0^\infty k^{m-1} \frac{k+K}{k-K} e^{-k(y+f)} e^{ik|x|} dk = \int_0^\infty \frac{\exp(i\eta)}{k^{m-1}} \frac{k+K}{k-K} e^{-k(y+f)} e^{ik|x|} dk \quad (2.10)$$

$$+ 4\pi i K^m e^{-K(y+f)} e^{iK|x|} \quad (2.11)$$

$$= I(m, +) + 4\pi i K^m e^{-K(y+f)} e^{iK|x|}, \text{ say,} \quad (2.12)$$

where the term (2.11) is the residue at the pole  $k = K$  and where the acute angle  $\eta$  will be defined later; see (2.17) below. Note that the integrands in (2.10) and the term (2.11) are solutions of Laplace's equation. Similarly

$$\int_0^\infty k^{m-1} \frac{k+K}{k-K} e^{-k(y+f)} e^{-ik|x|} dk = \int_0^\infty \frac{\exp(-i\eta)}{k^{m-1}} \frac{k+K}{k-K} e^{-k(y+f)} e^{-ik|x|} dk \quad (2.13)$$

$$= I(m, -), \text{ say.} \quad (2.14)$$

In (2.10) we write  $k = \sigma e^{i\eta}$  and note that  $|\exp(ik|x|)| \leq |\exp(-i\sigma|x|\cos\eta)| \leq 1$ , and that

$$\left| \frac{\sigma e^{i\eta} + K}{\sigma e^{i\eta} - K} \right| \leq \cot(\eta/2).$$

Then

$$|I(m, +)| \leq \int_0^\infty \sigma^{m-1} \cot(\eta/2) \exp\{-\sigma(y+f)\cos\eta\} d\sigma = \frac{(m-1)! \cot(\eta/2)}{(y+f)^m \cos^m \eta}, \quad (2.15)$$

with the same bound for  $|I(m, -)|$ . Thus the contribution of this part of the image potential to the series (2.7) is bounded by

$$\frac{1}{2} \sum_{m=1}^{\infty} \frac{|p_m| a^m}{(m-1)!} (|I(m, +)| + |I(m, -)|) < M(a') \sum_{m=1}^{\infty} \frac{(a')^m \cot(\eta/2)}{(y+f)^m \cos^m \eta}, \quad (2.16)$$

and this series converges uniformly for all  $y \geq 0$ , provided that

$$\cos \eta \geq a'/f, \quad (2.17)$$

i.e. provided that the angle  $\eta$  is small enough. Now consider the contribution to  $\Phi(x, y)$  from the terms (2.11). This is bounded by the series

$$\sum_{m=1}^{\infty} |p_m| a^m \cdot 2\pi \cdot \frac{1}{(m-1)!} K^m \cdot e^{-K(y+f)} < 2\pi M(a') e^{-K(y+f)} \sum_{m=1}^{\infty} \frac{(Ka')^m}{(m-1)!}, \quad (2.18)$$

a convergent series. Thus (2.7) defines a potential in the whole field of flow.

Consider now the difference potential

$$\phi(x, y) - \Phi(x, y)$$

which is defined in the whole field of flow. In the annulus  $a < r < f$  the Laurent expansion contains no negative powers (since the coefficients  $p_m$  in (2.6) and (2.7) are identical), and  $\phi - \Phi$  is thus defined in the whole of the half-plane ( $-\infty < x < \infty$ ,  $0 < y < \infty$ ), including the interior of the circle. By a well-known uniqueness theorem it follows that

$$\phi - \Phi = A \cdot e^{-Ky} \cos Kx,$$

and this satisfies the radiation condition only if  $A = 0$ . This completes the proof of the expansion theorem.

We have now shown that any solution of our boundary value problem must have the form (2.7). To show that a solution actually exists we expand the terms in (2.7) in polar coordinates and apply the boundary condition (2.3). An infinite system of equations is obtained for the unknowns  $p_m$  see e.g. [Ursell 1950].

### 3 The sphere

We may now attempt the same method for the submerged sphere, but this leads to unexpected difficulties. Only a brief outline can be given. Let the velocity potential be denoted by  $\phi(x, y, z)$ , and let us assume, for the sake of simplicity, that  $\phi$  is an even function of  $z$ . We write  $x = r \sin \theta \cos \alpha$ ,  $y = f + r \cos \theta$ ,  $z = r \sin \theta \sin \alpha$ . The boundary condition (2.3) is replaced by

$$\frac{\partial \phi}{\partial r} = U(\theta, \alpha) = \frac{1}{2} U_0(\theta) + \sum_{m=1}^{\infty} U_m(\theta) \cos m\alpha. \quad (3.1)$$

Then the typical multipole potential can be shown to be

$$G_n^m = \frac{P_n^m(\cos \theta)}{r^{n+1}} \cos m\alpha + \frac{(-1)^n}{(n-m)!} \int_0^\infty \frac{k+K}{k-K} k^n e^{-k(y+f)} J_m(k\rho) dk \cos m\alpha. \quad (3.2)$$

We must find a bound for the image potential

$$\frac{(-1)^n}{(n-s)!} \int_0^\infty \frac{k+K}{k-K} k^n e^{-k(y+f)} J_s(k\rho) dk \cos s\alpha, \quad (3.3)$$

which appears in (3.2). The obvious analogue to (2.9) is the decomposition

$$J_s(k\rho) = \frac{1}{2} \left( H_s^{(1)}(k\rho) + H_s^{(2)}(k\rho) \right), \quad (3.4)$$

but for  $s \geq 1$  this evidently leads to integrals which are divergent at  $k=0$ , and the earlier method is no longer applicable. Instead, in the upper-half  $k$ -plane we use the function  $\chi_s^{(1)}(Z)$  defined by

$$\chi_s^{(1)}(Z) = \frac{1}{\pi} \int_0^\pi \exp(iZ \sin v - isv) dv = J_s(Z) - i\mathbf{E}_s(Z), \quad (3.5)$$

where  $\mathbf{E}_s(Z)$  is H.F. Weber's function ([Watson 1922], ch.10). Then, when  $Y \geq 0$ ,

$$|\chi_s^{(1)}(X+iY)| \leq \frac{1}{\pi} \int_0^\pi |\exp(i(X-Y) \sin v - isv)| dv = \frac{1}{\pi} \int_0^\pi \exp(-Y \sin v) dv \leq 1, \quad (3.6)$$

and it is not difficult to show that  $\chi_s^{(1)}(Z) \sim \text{const. } e^{iZ}/Z^{1/2}$  when  $Z \rightarrow \infty$  in the upper-half  $Z$ -plane. Similarly in the lower-half  $Z$ -plane we use the conjugate function

$$\chi_s^{(2)}(Z) = \frac{1}{\pi} \int_0^\pi \exp(-iZ \sin v + isv) dv = J_s(Z) + i\mathbf{E}_s(Z). \quad (3.7)$$

It follows that

$$\int_0^\infty \frac{k+K}{k-K} k^n e^{-k(y+f)} J_s(k\rho) dk \quad (3.8)$$

$$= \frac{1}{2} \int_0^\infty \frac{\exp(in)}{k-K} \frac{k+K}{k-K} k^n e^{-k(y+f)} \chi_s^{(1)}(k\rho) dk + \frac{1}{2} \int_0^\infty \frac{\exp(-in)}{k-K} \frac{k+K}{k-K} k^n e^{-k(y+f)} \chi_s^{(2)}(k\rho) dk \quad (3.9)$$

$$+ 2\pi i K^{n+1} e^{-K(y+f)} \chi_s^{(1)}(K\rho), \quad (3.10)$$

and the convergence of the resulting series for the potential can now be shown as for (2.7) above. Note, however, that products like

$$e^{-k(y+f)} \chi_s^{(1)}(k\rho) \cos s\alpha \quad (3.11)$$

are not solutions of Laplace's equation.

Another obvious approach is by means of Poisson's Integral which expresses the values of a potential inside a sphere as an integral over the values on the surface on the sphere. (An analogous argument was used in [Ursell 1950].) The bounds for derivatives which I have obtained by this method are adequate only when the radius of the sphere is sufficiently small and not for all values of  $a < f$ .

## References

- [Ursell 1950] Ursell, F. Surface waves on deep water in the presence of a submerged circular cylinder I. Proc. Cambridge Philos. Soc. 46, 141-152
- [Ursell 1981] Ursell, F. Irregular frequencies and the motion of floating bodies. J. Fluid Mech 105, 143-156
- [Watson 1922] Watson, G.N. *Bessel Functions*, Cambridge University Press.

## Analogies for resonances in wave diffraction problems

T. Utsunomiya\* and R. Eatock Taylor  
*Department of Engineering Science*  
*University of Oxford, OX1 3PJ, U.K.*

### Introduction

It has been reported that on large numbers of equally spaced, bottom-mounted circular cylinders in line, large wave forces will be excited on each of the cylinders at particular wavenumbers close to those of trapped modes [1]. Similar observations have been made for circular arrays of bottom mounted circular cylinders, and these may be understood as "near-trapping" [2].

The existence of trapped modes for a bottom mounted circular cylinder placed on the centreline of a wave channel was first established by Callan et al. [3]. It is now known that they may arise not only at the wavenumbers below the cut-off value ( $k^N d/\pi = 1/2$  for a Neumann boundary condition (B.C.) applied on the channel walls, and  $k^D d/\pi = 1$  for a Dirichlet B.C., both for anti-symmetric waves with respect to the centreline of the channel, where  $k$  is the wavenumber and  $d$  is the half width of the channel); but also in the region above the cut-off wavenumber, or in the continuous spectrum [4, 5].

This paper first discusses other examples of trapped modes embedded in the continuous spectrum, e.g. when  $N$  bottom-mounted circular cylinders having the same radius  $a$  are equally spaced in line along the perpendicular plane to the channel walls in the wave channel. Evans and Porter [6] examined the trapped modes for multiple cylinders along the centreline of the channel, and observed the existence of up to  $N$  trapped modes below the cut-off wavenumber. In this paper, we will show numerically the existence of  $N$  trapped modes for the Neumann B.C., and up to  $N$  trapped modes for the Dirichlet B.C., for the case  $a/s = 0.5$ . In both cases, the trapped modes except that corresponding to the lowest frequency are shown to be embedded in the continuous spectrum region.

Next, an analogy is given between the trapped modes for a row of equally-spaced cylinders in the channel and the near-resonant modes for cylinders in the open sea. Another analogy with a spring-mass oscillating system is also given, which may offer some insights into such resonant phenomena in wave diffraction problems.

### Trapped modes for equally spaced cylinders in a channel

The complex potential  $\phi(x, y)$  which satisfies the Helmholtz equation  $(\nabla^2 + k^2)\phi = 0$  is considered here. The boundary conditions on the channel walls are  $\phi_y = 0$  on  $y = \pm d$  (Neumann B.C.), or  $\phi = 0$  on  $y = \pm d$  (Dirichlet B.C.). A Neumann B.C. is applied on each cylinder, i.e.,  $\phi_{r_j} = 0$  on  $r_j = a$ , where the centre of each cylinder is placed at  $(0, y_j)$ ,  $y_j = -d + (2j - 1)s$ ,  $j = 1, \dots, N$ , and polar coordinates  $(r_j, \theta_j)$  are employed with their origins at  $(0, y_j)$ . Moreover, the radiation condition  $\phi \rightarrow 0$  for  $x \rightarrow \pm\infty$  must be satisfied for trapped modes.

The multipole expansion method is employed here. The appropriate expressions for this problem can be found in McIver and Bennett [7] and in Linton and McIver [8]. The complex potential  $\phi(x, y)$  is expressed in the following form:

$$\phi = \sum_{j=1}^N \sum_{n=0}^{\infty} Z_n (A_n^j \phi_n^j + B_n^j \psi_n^j), \quad (1)$$

where

$$\begin{aligned} \phi_n^j &= H_n(kr_j) \cos n\theta_j \\ &+ \frac{i^{n-1}}{2\pi} \int_{-\infty}^{\infty} \frac{e^{k\gamma(y-d)}(e^{-2k\gamma d} \pm e^{2k\gamma y_j}) + e^{-k\gamma(y-d)}(e^{-2k\gamma d} \pm e^{-2k\gamma y_j})}{\gamma \sinh 2k\gamma d} e^{-ikxz} \cosh n\tau dt, \end{aligned} \quad (2)$$

$$\begin{aligned} \psi_n^j &= H_n(kr_j) \sin n\theta_j \\ &+ \frac{i^n}{2\pi} \int_{-\infty}^{\infty} \frac{e^{k\gamma(y-d)}(e^{-2k\gamma d} \mp e^{2k\gamma y_j}) - e^{-k\gamma(y-d)}(e^{-2k\gamma d} \mp e^{-2k\gamma y_j})}{\gamma \sinh 2k\gamma d} e^{-ikxz} \sinh n\tau dt, \end{aligned} \quad (3)$$

\*Permanent address: Department of Civil Engineering, Kyoto University, Kyoto 606, Japan

and  $Z_n = J'_n(ka)/H'_n(ka)$ ,  $\tau = \cosh^{-1}t$ ,  $\gamma = \sinh \tau$ . Also, the upper and lower signs of  $\pm$  and  $\mp$  correspond to Neumann and Dirichlet B.C. respectively, on the sides of the channel. Expanding the multipoles singular at one point  $(0, y_j)$  about another point,  $(0, y_p)$ , and applying the boundary conditions on each of the cylinder surfaces, we obtain the following homogeneous systems of equations [8]:

$$A_m^p + \sum_{n=0}^{\infty} (\bar{A}_n^p \alpha_{nm}^p + \bar{B}_n^p a_{nm}^p) + \sum_{j=1, \neq p}^N \sum_{n=0}^{\infty} [\bar{A}_n^j (C_{nm}^{jp} + \alpha_{nm}^{jp}) + \bar{B}_n^j (E_{nm}^{jp} + a_{nm}^{jp})] = 0, \quad (4)$$

$$B_m^p + \sum_{n=0}^{\infty} (\bar{A}_n^p \beta_{nm}^p + \bar{B}_n^p b_{nm}^p) + \sum_{j=1, \neq p}^N \sum_{n=0}^{\infty} [\bar{A}_n^j (D_{nm}^{jp} + \beta_{nm}^{jp}) + \bar{B}_n^j (F_{nm}^{jp} + b_{nm}^{jp})] = 0, \quad (5)$$

where  $p = 1, \dots, N$ ;  $m = 0, 1, \dots$ , in both cases, and the expressions  $\bar{A}_n^j = Z_n A_n^j$  and  $\bar{B}_n^j = Z_n B_n^j$  are used.

The infinite systems of equations are then truncated with  $m, n = 0, 1, \dots, M$ . (In the following numerical computations,  $M = 7$  has been employed). The symmetry of the trapped modes about the  $y$ -axis can be assumed [3], and thus  $A_{2k+1}^j = B_{2k}^j = 0$  for  $k = 0, 1, \dots$  have been applied. Also, from the symmetry of the cylinder arrangements, it can easily be proved that  $A_n^j = A_n^{N-j+1}$  and  $B_n^j = -B_n^{N-j+1}$  for symmetric modes with respect to centreline of the channel; and that  $A_n^j = -A_n^{N-j+1}$  and  $B_n^j = B_n^{N-j+1}$  for anti-symmetric modes; so these have been employed to reduce the computations.

The complex determinants of the truncated systems of equations (4) and (5) have been calculated for various values of  $k$ , and it has been found that points exist where both real and imaginary parts of the complex determinants vanish. The homogeneous equations were then solved numerically in order to obtain non-trivial solutions for the values of  $k$  where the complex determinants vanish. Substituting the obtained values of  $k$ ,  $A_n^j$  and  $B_n^j$  into Eq. (1), we have obtained numerically pure imaginary potentials, which indicate that we have obtained pure-trapped modes. The above procedure was repeated for the equations having only the imaginary parts of Eqs. (4) and (5), and we obtained the same results, which also shows that the complex potential becomes pure imaginary when the determinant vanishes.

The trapped wavenumbers at which the determinants vanish are shown in Table 1 for Neumann B.C. and in Table 2 for Dirichlet B.C., both for the case  $a/s = 0.5$ . In Tables 1 and 2, (s) indicates the symmetric mode of the corresponding trapped wave with respect to the centreline of the channel, and (a) indicates the anti-symmetric mode. Figure 1 shows equipotential contours of the trapped waves for  $N = 4$ . It can be seen that only the lowest trapped wavenumbers for each arrangement of cylinders are below the corresponding cut-off wavenumber in both Neumann and Dirichlet boundary conditions, and all except those are embedded in the continuous spectrum. The highest trapped mode in each case is equivalent to that for the case of one cylinder, since the same trapped wavenumber is obtained and the trapped wave satisfies  $\phi_y = 0$  for a Neumann B.C. or  $\phi = 0$  for a Dirichlet B.C. along the centreline between two adjacent cylinders. For a Neumann B.C., the second mode for four cylinders is also identical to the first mode for two cylinders. Similar relationships can be found between the trapped modes for five cylinders and those for ten cylinders. It should be noted that the trapped wavenumber  $ks/\pi = 0.442869$  for a Dirichlet B.C. can not be obtained, in which case the non-existence of the trapped mode has already been proved [9].

Next, we focus our attention on the total wave forces induced on each cylinder. We have found that the coefficients  $B_1^j$ , which directly relate to the first-order force on cylinder  $j$  in the  $y$ -direction, precisely follow the formulae below:

$$B_1^{j(r)} = \sin \frac{r(2j-1)}{2N} \pi, \quad 1 \leq j \leq N; 1 \leq r \leq N; N \geq 1, \quad (\text{for Neumann B.C.}), \quad (6)$$

$$B_1^{j(r)} = \cos \frac{(r+1)(2j-1)}{2N} \pi, \quad 1 \leq j \leq N; 1 \leq r \leq N-2; N \geq 3, \quad (\text{for Dirichlet B.C.}), \quad (7)$$

where  $r$  is the mode number of the trapped mode.

Figure 2 indicates the distribution of wave forces at the trapped wavenumbers given by  $ks/\pi = 0.442099$  ( $r = 48$ ) and  $ks/\pi = 0.439844$  ( $r = 47$ ) for  $N = 50$  with Dirichlet B.C. As seen in Figure 2, the distribution of forces in these trapped mode conditions for a row of cylinders in a wave "channel"

with Dirichlet boundary conditions has close similarities with the forces on the arrays in the open seas discussed by Maniar and Newman [1]. Table 3 compares the trapped wavenumbers of the second highest modes in the channel with the wavenumber at which the peak load occurs within a finite array of  $N$  cylinders in the open sea. For a sufficient number of cylinders they agree very well, in spite of the different boundary conditions between these two cases.

### Analogy with a spring-mass oscillating system

The basic unit in the mechanical analogue corresponds to one cylinder. It consists of a uniform massless cylindrical bar of unit cross-section, unit length and unit modulus elasticity, with a unit point mass attached at its mid-length. The mass is allowed to oscillate in the direction of the axis of the bar. If the two free ends of the bar are fixed, the square of the natural frequency of vibration of the point mass is 4, which may correspond to the trapped mode for one cylinder with Neumann B.C. The basic unit is now replicated  $N$  times in a straight line, by attaching the right hand end of one unit to the left hand end of the neighbouring unit. Both ends are then fixed (fixed B.C.) or allowed to be free to move (free B.C.). In both cases, we can deduce the eigenvalues of the discrete system (omitting the rigid-body mode of the free B.C. system) as [10]

$$\omega_r^2 = 2 - 2 \cos\left(\frac{r\pi}{N}\right), \quad r = 1, \dots, N \text{ (for fixed B.C.); and } r = 1, \dots, N-1 \text{ (for free B.C.).} \quad (8)$$

The corresponding eigenvectors giving the displacements are

$$d_j^{(r)} = \sin \frac{r(2j-1)}{2N} \pi, \quad 1 \leq j \leq N; 1 \leq r \leq N; N \geq 1, \quad \text{(for fixed B.C.),} \quad (9)$$

$$d_j^{(r)} = \cos \frac{r(2j-1)}{2N} \pi, \quad 1 \leq j \leq N; 1 \leq r \leq N-1; N \geq 2, \quad \text{(for free B.C.),} \quad (10)$$

where index  $r$  designates the number of the mode, and the subscript  $j$  identifies the mass.

We see that such a mechanical model appears to display some of the characteristics of the array of cylinders in water waves. In particular, the distribution of displacements in the eigenmodes for the free B.C. case is identical to the distribution of forces on the cylinders at the Dirichlet mode trapped wavenumbers. These analogies open up several opportunities for the analysis of hydrodynamic resonances in periodic systems.

### References

- [1] H.D. Maniar and J.N. Newman, Wave diffraction by a long array of cylinders. *J. Fluid Mech.* **339** (1997) 309-330.
- [2] D.V. Evans and R. Porter, Near-trapping of waves by circular arrays of vertical cylinders. *Applied Ocean Research* **19** (1997) 83-99.
- [3] M. Callan, C.M. Linton and D.V. Evans, Trapped modes in two-dimensional waveguides. *J. Fluid Mech.* **229** (1991) 51-64.
- [4] D.V. Evans, C.M. Linton and F. Ursell, Trapped mode frequencies embedded in the continuous spectrum. *Q. Jl Mech. Appl. Math.* **46** (1993) 253-274.
- [5] R. Porter and D.V. Evans, Recent results on trapped modes and their influence on finite arrays of vertical cylinders in waves. *12th WWFEB, Marseille* (1997) 211-214.
- [6] D.V. Evans and R. Porter, Trapped modes about multiple cylinders in a channel. *J. Fluid Mech.* **339** (1997) 331-356.
- [7] P. McIver and G.S. Bennett, Scattering of water waves by axisymmetric bodies in a channel. *J. Engrg. Math.* **27** (1993) 1-29.
- [8] C.M. Linton and P. McIver, The scattering of water waves by an array of circular cylinders in a channel. *J. Engrg. Math.* **30** (1996) 661-682.
- [9] M. McIver and C.M. Linton, On the non-existence of trapped modes in acoustic waveguides, *Q. Jl Mech. Appl. Math.* **48** (1995) 543-555.
- [10] M.G. Faulkner and D.P. Hong, Free vibrations of a mono-coupled periodic system, *Journal of Sound and Vibration* **99** (1985) 29-42.

Table 1 Trapped wavenumber  $ks/\pi$  for Neumann boundary conditions.

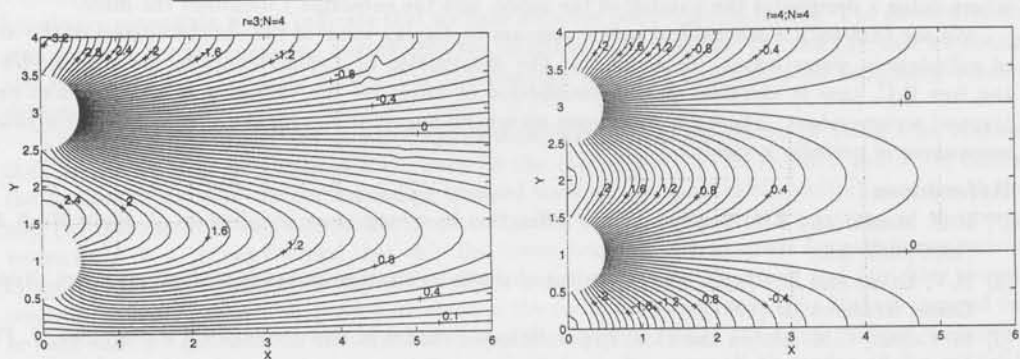
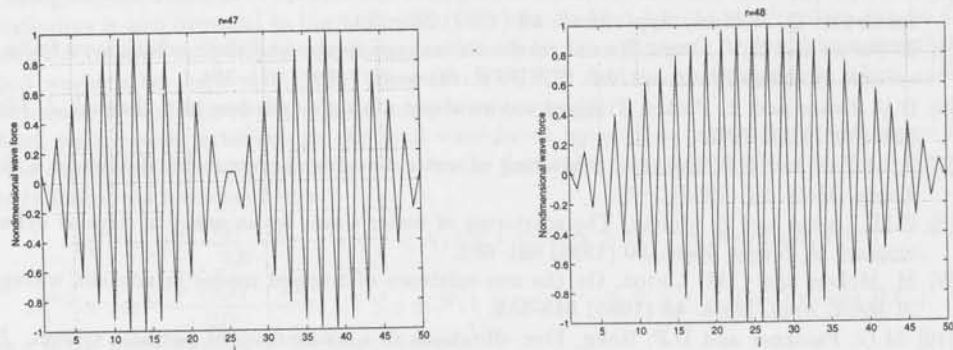
Mode number	1/6	2/7	3/8	4/9	5/10
1 cylinder	0.442869(a)	—	—	—	—
2 cylinders	0.248370(a)	0.442869(s)	—	—	—
3 cylinders	0.166245(a)	0.328444(s)	0.442869(a)	—	—
4 cylinders	0.124830(a)	0.248370(s)	0.366671(a)	0.442869(s)	—
5 cylinders	0.0999145(a)	0.199238(s)	0.296807(a)	0.388389(s)	0.442869(a)
10 cylinders	0.0499896(a) 0.296807(s)	0.0999145(s) 0.343958(a)	0.149699(a) 0.388389(s)	0.199238(s) 0.425787(a)	0.248370(a) 0.442869(s)

Table 2 Trapped wavenumber  $ks/\pi$  for Dirichlet boundary conditions.

Mode number	1/6	2/7	3/8	4/9	5/10
1 cylinder	0.977759(a)	—	—	—	—
2 cylinders	0.977759(a)	—	—	—	—
3 cylinders	0.328444(a)	0.977759(a)	—	—	—
4 cylinders	0.248370(a)	0.366671(s)	0.977759(a)	—	—
5 cylinders	0.199238(a)	0.296807(s)	0.388389(a)	0.977759(a)	—
10 cylinders	0.0999145(a) 0.343958(s)	0.149699(s) 0.388389(a)	0.199238(a) 0.425783(s)	0.248370(s) 0.977759(a)	0.296807(a) —

Table 3 Comparison of the trapped wavenumber for Dirichlet B.C. and the near-resonant wavenumber for an array of  $N$  cylinders in the open sea (in  $ks/\pi$ ,  $a/s = 0.5$ ).

Number of cylinders, $N$	100	50	25	10
Trapped wavenumber	0.442676	0.442099	0.439844	0.425783
Near-resonant wavenumber[1]	0.442676	0.442104	0.439921	0.428557

Figure 1 Equipotential contours of the trapped waves for  $N = 4$ .Figure 2 Distribution of wave forces for  $N = 50$  with Dirichlet B.C.

## Experimental validation of a Rankine Panel Method

Riaan van 't Veer

Ship Hydromechanics Laboratory, Delft University of Technology

### 1 Introduction

Over the past four years, a Rankine panel method has been designed at Delft University. The resulting program SEASCAPE can be applied to catamaran vessels. Special flow conditions are implemented to model the smooth separation of a transom stern flow. To validate the numerical work, a series of experiments with a catamaran model has been carried out in the towing tanks of Delft University and MARIN. The test results presented in this abstract are heave and pitch measurements in oblique waves.

### 2 First-order Rankine panel method

A first-order Rankine panel method has been implemented using flat quadrilateral panels and a constant singularity distributions on each panel. The nonlinear free-surface and hull boundary conditions have been linearised to, respectively, the calm water surface  $z = 0$  and the mean position of the vessel, by means of Taylor expansions. The resulting boundary conditions have been presented in e.g. Van 't Veer (1997), and are almost similar to the linearisations used by Nakos (1990). The overall velocity potential is represented by a summation of three different potentials, the double-body base-flow potential  $\Phi(\vec{x})$  (solved using the Hess and Smith (1962) method), the steady wave resistance potential  $\phi(\vec{x})$ , and the unsteady ship motion potential  $\varphi(\vec{x}, t)$ . The latter two potentials are solved using the Green's identity form of the boundary value problem. The motion response functions of the (catamaran) are solved in the frequency domain. The quadratic spline technique presented by Scлавounos and Nakos (1988) is used to discretise the tangential derivatives of the hull and free-surface boundary condition.

To obtain the motion responses in oblique waves, the calculation procedure is slightly different than for head waves. Besides the effect on the wave encounter frequency, the hydrodynamic coefficients (radiation potentials) are not influenced by the wave angle. The diffraction force however, is influenced by the wave heading, due to the effect of the incident wave in the hull and free-surface boundary conditions. This will result in different wave loading on both hulls.

If the solution vector on the port hull (or port side of the vessel) is denoted as  $\vec{x}_p$  and  $\vec{x}_s$  represents the solution on the starboard hull, the following matrix equation can be written down to solve the unsteady potentials,

$$\begin{bmatrix} G_{pp} & G_{ps} \\ G_{sp} & G_{ss} \end{bmatrix} \begin{bmatrix} \vec{x}_p \\ \vec{x}_s \end{bmatrix} = \begin{bmatrix} \vec{b}_p \\ \vec{b}_s \end{bmatrix} \quad \text{symmetry} \Rightarrow \begin{bmatrix} A & B \\ B & A \end{bmatrix} \begin{bmatrix} \vec{x}_p \\ \vec{x}_s \end{bmatrix} = \begin{bmatrix} \vec{b}_p \\ \vec{b}_s \end{bmatrix} \quad (1)$$

The matrix  $G_{pp}$  represents the influences of a singularity on the port hull in a collocation point on the port hull, while the matrix  $G_{ps}$  represents the cross-influences between the two hulls. The elements of the matrices are calculated using the Green's influence coefficients and the discretised boundary conditions. Due to the geometrical symmetry around the centreline of the vessel, the sub-matrices with influence coefficients have symmetric properties as well, resulting in the matrix equation with  $A$  and  $B$ .

From equation (1) the two matrix equations can be extracted from which the solution vector on both hulls can be obtained by summation and subtraction of the two solution vectors,

$$\begin{aligned} [A + B](\vec{x}_p + \vec{x}_s) &= (\vec{b}_p + \vec{b}_s) \\ [A - B](\vec{x}_p - \vec{x}_s) &= (\vec{b}_p - \vec{b}_s) \end{aligned} \quad \text{leading to} \Rightarrow \begin{aligned} \vec{x}_p &= \frac{1}{2}(\vec{x}_p + \vec{x}_s) + \frac{1}{2}(\vec{x}_p - \vec{x}_s) \\ \vec{x}_s &= \frac{1}{2}(\vec{x}_p + \vec{x}_s) - \frac{1}{2}(\vec{x}_p - \vec{x}_s) \end{aligned}$$

Using this technique only two matrix equations have to be solved and the forcing on each hull can then be derived by simple mathematics.

### 3 Influence of the $m$ -terms on hydrodynamic coefficients

The exact hull boundary condition for the radiation potentials are nonlinear since the instantaneous hull location and orientation are unknown a priori. Linearisation of the boundary condition (to the mean position  $S_0$  of the vessel) has been carried out by Timman and Newman (1962), and can be written in an elegant way using the  $m$ -terms defined by Ogilvie and Tuck (1969),

$$\frac{\partial \varphi_k}{\partial n} = \frac{\partial \vec{a}_k}{\partial t} \cdot \vec{n} - ((\vec{a}_k \cdot \nabla) \nabla \Psi_0 - (\nabla \Psi_0 \cdot \nabla) \vec{a}_k) \cdot \vec{n} = n_k \dot{\eta}_k + m_k \eta_k \quad k = 1, \dots, 6 \quad (2)$$

where  $\vec{a}_k$  is the oscillatory displacement vector of the hull, for the  $k^{\text{th}}$  mode, in respect to the mean position of the vessel:  $\vec{a} = (\eta_1, \eta_2, \eta_3) + \vec{x} \times (\eta_4, \eta_5, \eta_6)$ . The steady flow field is expressed by the potential  $\Psi_0$ . The last term in equation (2) is the correction term which accounts for the effect that the integration is carried out on  $S_0$  and not on the instantaneous hull surface  $S$ .

The overall steady flow field can be written as:  $\nabla \Psi_0 = \vec{U} + \nabla \Phi' + \nabla \phi$ , where  $\vec{U}$  is the ship's velocity. Using this decomposition, the exact  $m$ -terms consist of three different contributions. In view of general linearisations, the following  $m$ -terms are defined: 1) the Neumann-Kelvin  $m$ -terms, which include only the effect of  $\vec{U}$ , 2) the double-body  $m$ -terms, which include the effect of  $\vec{U}$  and  $\nabla \Phi'$ , and finally 3) the complete  $m$ -terms, which include all three components.

**Neumann-Kelvin  $m$ -terms:** The Neumann-Kelvin  $m$ -terms are most commonly used in seakeeping theories. They are calculated using only the uniform stream velocity  $U$  and neglect thereby the correction term in the linearised hull boundary condition, which accounts for the effect of the oscillating body in the steady flow field. The resulting expression for the  $m$ -terms is:

$$\begin{aligned} (m_1, m_2, m_3) &= -(\vec{n} \cdot \nabla)(\vec{U}) = (0, 0, 0) \\ (m_4, m_5, m_6) &= \vec{x} \times (m_1, m_2, m_3) - \vec{n} \times \vec{U} = (0, -Un_3, Un_2) \end{aligned} \quad (3)$$

The Neumann-Kelvin  $m$ -terms are used in the strip-theory calculations and can be used in 3D Rankine panel methods as well, as approximation for the more complicated double-body  $m$ -terms.

**The double-body  $m$ -terms:** The double-body flow is a more realistic base-flow for describing the velocity perturbations around the (fully submerged) vessel than the uniform Neumann-Kelvin flow. The resulting  $m$ -terms are complicated due to the second derivatives of the base-flow potential,

$$\begin{aligned} (m_1, m_2, m_3) &= -(\vec{n} \cdot \nabla)(\nabla \Phi) \\ &= -(n_1 \Phi_{xx} + n_2 \Phi_{xy} + n_3 \Phi_{xz}, n_1 \Phi_{yx} + n_2 \Phi_{yy} + n_3 \Phi_{yz}, n_1 \Phi_{zx} + n_2 \Phi_{zy} + n_3 \Phi_{zz}) \\ (m_4, m_5, m_6) &= \vec{x} \times (m_1, m_2, m_3) - \vec{n} \times \nabla \Phi \\ &= \vec{x} \times (m_1, m_2, m_3) + (n_3 \Phi_y - n_2 \Phi_z, n_1 \Phi_z - n_3 \Phi_x, n_2 \Phi_x - n_1 \Phi_y) \end{aligned} \quad (4)$$

Since the double-body velocities can be written as  $\nabla \Phi = \vec{U} + \nabla \Phi'$ , it is easily verified that the double-body  $m$ -terms include the Neumann-Kelvin  $m$ -terms. Since only the pitch and yaw Neumann-Kelvin terms are nonzero, the double-body contributions are of first-order for all other terms.

The spatial derivatives of the double-body velocities, are calculated on the hull surface using the spatial derivatives in the fluid domain. For each collocation point, three extra points are selected (in the direction of the panel normal vector) in which the second derivatives of the velocity potential are calculated. Using a quadratic spline, the derivatives on the hull surface are obtained.

**The complete  $m$ -terms:** The definition of the  $m$ -terms up till now only include contributions due to the velocity potential around a fully submerged body. The free-surface steady potential  $\phi$  has not been incorporated in the hull boundary condition, while this free-surface velocity field is certainly present. However, based on order analysis, it can be verified that the contributions of  $\nabla \phi$  are of secondary order compared to the  $\nabla \Phi$  terms, and they are therefore not included in SEASCAPE.

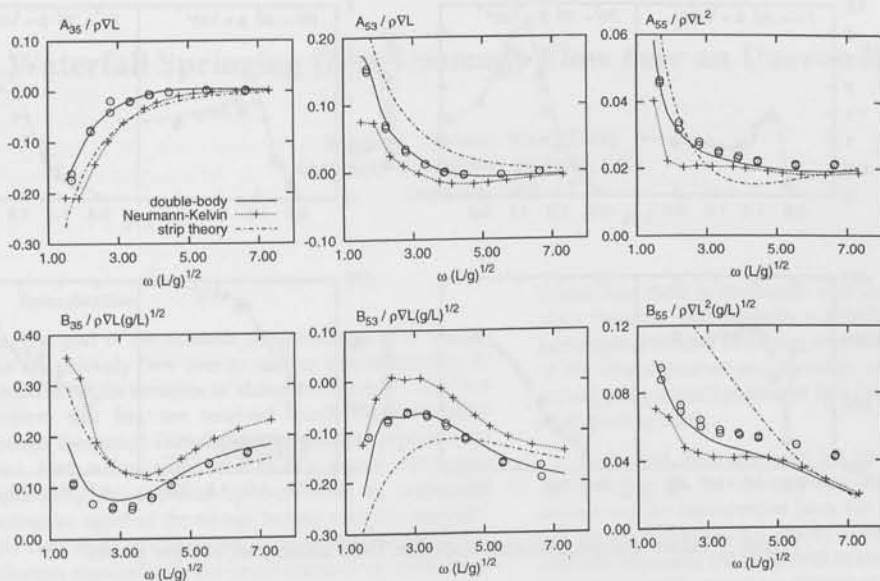


Figure 1: Comparison of added mass and fluid damping coefficients using different definitions for the  $m$ -terms. Wigley III,  $F_n = 0.30$ . Double-body and Neumann-Kelvin coefficients from SEASCAPE. Strip theory calculations from SEAWAY.

#### 4 Test case: the Wigley III

The influence of the  $m$ -terms on the hydrodynamic coefficients for the Wigley III has been investigated. The Wigley hull form is often chosen for numerical validation since the hull surface can be easily discretised by any number of panels, and extensive experimental data exist, presented by Journée (1992). The calculations presented here, are all carried out using 30 panels lengthwise and 8 panels girthwise on the hull surface. The main parameters of the Wigley III model were  $L = 3.0$  m,  $L/B = 10$ , and  $B/T = 1.6$ .

The hydrodynamic mass and damping coefficients, calculated using different  $m$ -term definitions, are presented in Figure 1. The experimental data obtained by Journée (1992), and the calculated coefficients using a strip-theory method (SEAWAY, developed at Delft University) are included as well.

Although the vessel is rather slender Figure 1 shows remarkable differences. In general, the 3D calculations using the double-body  $m$ -terms correlate excellent with the experimental data. All other predictions show a slightly worse correlation with the experiments, especially for the coupled fluid damping terms,  $B_{35}$  and  $B_{53}$ . It is interesting to notice that the strip-theory generally predicts more fluid damping in the coupling terms and pitch-to-pitch term  $B_{55}$ . While the trend in the fluid damping terms is much better predicted by the Neumann-Kelvin method, the error is opposite in the coupling terms;  $B_{35}$  is over-predicted and  $B_{53}$  is under-predicted. Similar conclusions follow from the comparison of the added mass values. Due to space limitations the results for  $A_{33}$  and  $B_{33}$  are not included, but the predictions for the heave-to-heave coefficients were all close to each other.

#### 5 Test case: the DUT catamaran in oblique waves

The aim of the research project was to develop a seakeeping prediction tool applicable to catamarans. Therefore, a series of experiments have been carried out with a catamaran model. A lines plan of the vessel is presented in Figure 2.

Model experiments in head waves have been carried out at Delft University and at MARIN the model has been tested in oblique waves,  $\beta = 165$  and  $135$  degrees. In oblique waves, the experiments were carried out at three different Froude numbers,  $F_n$  0.35, 0.60 and 0.75. In Figure 3 the heave and pitch results are presented

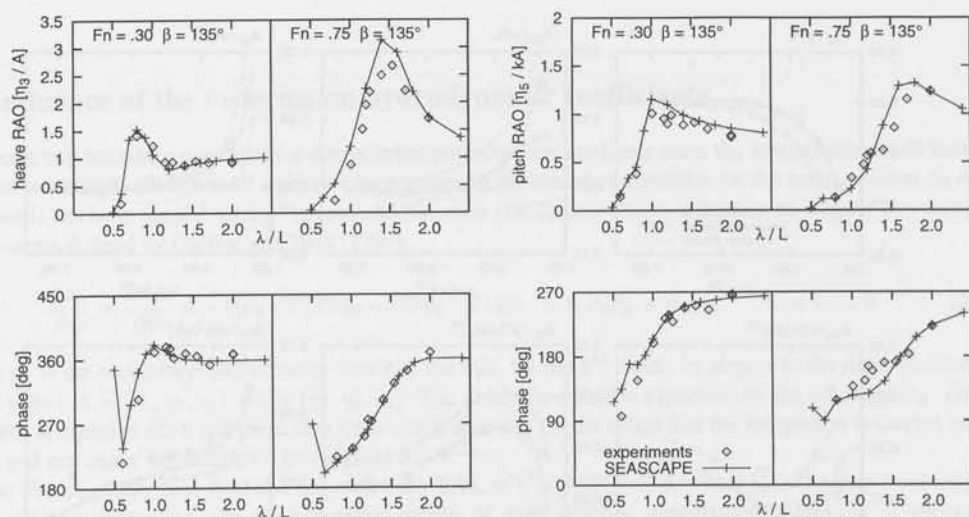


Figure 3: Heave and pitch motion response, DUT catamaran, oblique waves

for  $\beta = 135$  degrees. The calculations are performed using the double-body  $m$ -terms. The hull surface grid consisted of 20 panels lengthwise and 10 panels girthwise along one demi-hull. The steady trim and sinkage (significant at  $F_n = 0.75$ ) are taken into account in the calculations.

## 6 Conclusions

It has been shown that the  $m$ -terms have a significant influence on the hydrodynamic coefficients. Using the double-body  $m$ -terms good correlations with experimental data were obtained.

Using the proposed calculation procedure for oblique waves, good correlations between experiments and calculations were obtained for the heave and pitch motions of a catamaran vessel.

## References

- Hess, J. L. and Smith, A. M. O.: 1962, Calculation of non-lifting potential flow about arbitrary three-dimensional bodies, *Technical Report Report No. E.S. 40622*, Douglas Aircraft Co., Inc.
- Journée, J. M. J.: 1992, Experiments and calculations on four wigley hullforms, *Technical Report MEMT 21*, Delft University of Technology, Ship Hydromechanics Laboratory.
- Nakos, D. E.: 1990, *Ship Wave Patterns and Motions by a Three Dimensional Rankine Panel Method*, PhD thesis, Massachusetts Institute of Technology.
- Ogilvie, T. F. and Tuck, E. O.: 1969, A rational strip theory of ship motions: Part 1, *Technical Report 013*, Dept. of Nav. Arch. and Mar. Eng., University of Michigan.
- Sclavounos, P. D. and Nakos, D. E.: 1988, Stability analysis of panel methods for free-surface flows with forward speed, *Proc. 17th Symp. on Naval Hydrodynamics*, The Hague, The Netherlands, pp. 173-193.
- Timman, R. and Newman, J. N.: 1962, The coupled damping coefficients of a symmetric ship, *Journal of Ship Research* 5(4), 1-7.
- Van 't Veer, A. P.: 1997, Analysis of motions and loads on a catamaran vessel in waves, *Proc. 4th Int. Conf. FAST*, pp. 439-446.

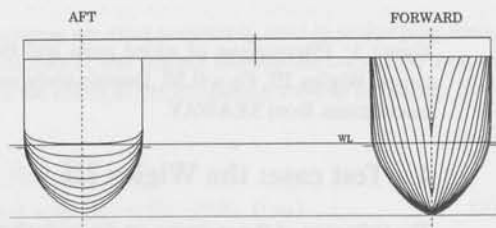


Figure 2: Lines plan DUT catamaran

## A Waterfall Springing from Unsteady Flow over an Uneven Bottom

William C. Webster, Xinyu Zhang  
University of California, Berkeley, USA  
December 1997

### 1. Introduction

The goal of the research presented here is to investigate the unsteady flow over an uneven bottom resulting in a waterfall at its terminus as shown in Figure 1. This is a problem that has not received much attention either through theoretical investigation or through experimentation. Such a flow might arise from a stream with waves approaching the waterfall or even from an earthquake causing an uplift of the stream bottom near the waterfall. This flow itself is clearly not of immediate practical significance, especially for the naval architect or ocean engineer, but it is related in a way to the flow in a plunging breaking wave as we shall describe later in this paper. The work described here is still in its formative stage and the results presented here are only for the steady flow over an uneven bottom.

### 2. Model

The model chosen for this study, the Green-Naghdi (GN) method of fluid sheets, always yields a three-dimensional, unsteady model for such flows. The GN approach is a continuum model in which the kinematic character of the flow is prescribed in the vertical direction. With this restriction, the equations for modeling the flow satisfy the boundary conditions exactly, satisfy conservation of mass and momentum exactly and are Gallilean invariant. In the GN method surface tension and viscosity can be included without real penalty although such flows are limited to laminar flows (see, for instance, Kim and Webster, 1995). For the flow here, both surface tension and viscosity will be neglected. Different levels of GN theory depending on the degree of specified kinematic complexity in the flow.

This approach is very different from the more classical approach in that the model for the flow (inviscid flow) is combined with the simplification (proscription of the vertical kinematic complexity) right from the outset. In the classical approach, the model of inviscid flow as a po-

tential flow field is developed with an appeal to Kelvin's theorem. Subsequently a simplification, usually perturbation scheme involving a systematic expansion of the field equations and boundary conditions, is involved using a small parameter as a gauge for retaining or discarding terms.

In the end, each approach has its advantages and its blemishes. In the GN approach, the boundary conditions and the conservation laws are satisfied exactly but the fluid field is not exactly irrotational. In the classical approach, the fluid field is irrotational but the boundary conditions and the conservation laws are only approximately satisfied (i.e., satisfied only up to the order of the terms discarded in the expansions). Another way of looking at the difference is that the classical method is correct locally but approximate globally, and the GN method is the opposite. As with all modeling problems, determination of which approximation scheme is the most appropriate for a given problem must be left to comparison with physical experiments. After all, both approaches ignore the vorticity due to viscosity that is certainly there. Some approximation schemes result in models with other blemishes. For instance the Korteweg-DeVries (KdV) and super KdV models are not Gallilean invariant.

### 3. Waterfall problem

Consider the steady two-dimensional flow of an incompressible, inviscid fluid under the action of gravity over a cliff leading to a free overfall (as shown in Fig. 1). Three distinct regions of flow may be associated with this problem. The upstream region (region I) is characterized by a free top surface and an even bottom. The middle region (Region II) is characterized by a free top surface and an uneven bottom. For the study here we shall restrict the unevenness to be a uniform slope, although there is no limitation in the theory in this regard. In the downstream region (labeled as III) both the top and bottom surface of the fluid are free. Far upstream the fluid is assumed to flow as a uniform stream, while downstream the fluid falls freely under the action of gravity. Of particular interest in analyzing the problem is the prediction of the height of the whole flow region and the determination of the downstream solution, i.e., the shape of the free surfaces and the vertical thickness of the jet.

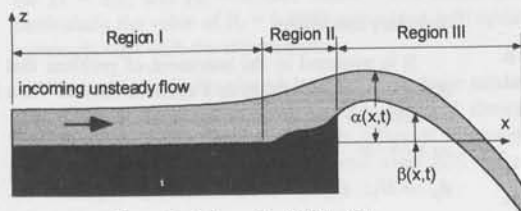


Figure 1. Schematic of Waterfall

## Green-Naghdi Theory Level-I

Here we use Green-Naghdi theory level-I with the formulae and notations derived by J. Shields and W. Webster (1988). We consider here only two-dimensional problems. The Level-I theory is summarized as follows:

The velocity profile (u,v) is assumed to be of the form:

$$\begin{aligned} u(x, z, t) &= u_0(x, t) \\ v(x, z, t) &= v_0(x, t) + v_1(x, t)\zeta. \end{aligned} \quad (1)$$

The kinematic boundary conditions are:

$$\begin{aligned} v_0 + v_1\alpha &= \alpha_t + u_0\alpha_x; \\ v_0 + v_1\beta &= \beta_t + u_0\beta_x. \end{aligned} \quad (2)$$

where  $\beta = \beta(x, t)$  and  $\alpha = \alpha(x, t)$  represent the top and bottom surfaces respectively.

The continuity equation is

$$u_{0x} + v_1 = 0 \quad (3)$$

The momentum equations are as follows:

$$\begin{aligned} u_{0t}\phi_0 + \phi_0 u_{0x} &= \frac{1}{\rho}(-P_{0x} + \hat{p}\beta_x - \bar{p}\alpha_x) \\ u_{0t}\phi_1 + \phi_1 u_{0x} &= \frac{1}{\rho}(-P_{1x} + \hat{p}\beta_x - \bar{p}\alpha_x) \\ v_{0t}\phi_0 + \phi_0 v_{0x} + \phi_0 v_{0t} &+ \\ v_{1t}\phi_1 + \phi_1 v_{0x} + \phi_1 v_{1t} & \\ &= \frac{1}{\rho}(-\rho g\phi_0 - \hat{p} + \bar{p}) \\ v_{0t}\phi_1 + \phi_1 v_{0x} + \phi_1 v_{0t} &+ \\ v_{1t}\phi_2 + \phi_2 v_{0x} + \phi_2 v_{1t} & \\ &= \frac{1}{\rho}(P_0 - \rho g\phi_1 - \hat{p}\beta + \bar{p}\alpha) \end{aligned} \quad (4)$$

where  $\hat{p}$  and  $\bar{p}$  are the pressure on the top and bottom surfaces respectively, and where

$$\begin{aligned} \phi_0 &= \beta - \alpha; \\ \phi_1 &= \frac{1}{2}(\beta^2 - \alpha^2); \\ \phi_2 &= \frac{1}{3}(\beta^3 - \alpha^3); \\ P_n &= \int_{\alpha}^{\beta} p \zeta^n d\zeta. \end{aligned} \quad (5)$$

Since  $P_1$  only exists in the second equation of (4), it is then only a dependent variable and need not be solved simultaneously with the other variables.

## Formulation of the problem

A statement of the problem under consideration is given in section 1 and for this study we consider only

steady flow. With reference to Figure 2, we choose the x-y co-ordinate axes as shown in Figure 2: Region I is the domain  $x < -a$ ; Region II is the domain  $-a \leq x < 0$  and Region III is the domain  $x \geq 0$ . It follows that the pressure  $\hat{p}$  at the top surface equals the atmospheric pressure  $p_0$  in the whole region. The given quantities and unknowns are as follows:

$$\begin{aligned} \text{Region I } (x < -a) & \left\{ \begin{array}{l} \hat{p} = p_0, \alpha = 0 \\ \bar{p}, \beta \text{ unknown} \end{array} \right\} \\ \text{Region II } (-a \leq x < 0) & \left\{ \begin{array}{l} \hat{p} = p_0, \alpha(x) = Kx + Ka \\ \bar{p}, \beta \text{ unknown} \end{array} \right\} \\ \text{Region III } (x > 0) & \left\{ \begin{array}{l} \hat{p} = p_0, \bar{p} = p_0 \\ \alpha, \beta \text{ unknown} \end{array} \right\} \end{aligned}$$

where K is the slope of the bottom in region II. After Simplifying, we can obtain the governing equations for three regions:

Region I:

$$\begin{cases} \frac{1}{3}Q^2\phi_{0x}^2 - Q^2 + g\phi_0^3 - 2R_1\phi_0^2 + 2S_1\phi_0 = 0 \\ \bar{p} = g\phi_0 - \alpha_x Q^2 \frac{\phi_{0x}}{\phi_0^2} - \frac{1}{2}Q^2 \frac{\phi_{0x}^2}{\phi_0^2} + \frac{1}{2}Q^2 \frac{\phi_{0xx}}{\phi_0} \end{cases}$$

Region II:

$$\begin{cases} \frac{\phi_{0xx}}{\phi_0} - \frac{1}{2} \frac{\phi_{0x}^2}{\phi_0^2} + \frac{3}{2}(1 + \alpha_x^2) \frac{1}{\phi_0^2} \\ \quad + \frac{3g}{Q^2}(\phi_0 + \alpha) + \frac{3}{2} \frac{\alpha_{xx}}{\phi_0} = 3 \frac{R_2}{Q^2} \\ \bar{p} = g\phi_0 - \alpha_x Q^2 \frac{\phi_{0x}}{\phi_0^2} - \frac{1}{2}Q^2 \frac{\phi_{0x}^2}{\phi_0^2} + \frac{1}{2}Q^2 \frac{\phi_{0xx}}{\phi_0} \end{cases} \quad (6)$$

Region III:

$$\begin{cases} \frac{Q^2}{12} \phi_{0x}^2 = Q^2 - 2S_3\phi_0 + 2R_3\phi_0^2 \\ Q^2 \left( \frac{\psi_x}{\phi_0} \right)_x = -g\phi_0 \end{cases}$$

where  $R_1, R_2, R_3, S_1$  and  $S_3$  are constants of integration, which can be determined by boundary conditions and matching conditions.  $Q$  is the total flow through any section.

## Boundary conditions

It is assumed in the statement of problem that far upstream the fluid flows as a uniform stream. Then the far upstream boundary conditions are as follows:

$$\begin{aligned} \text{as } x \rightarrow -\infty & \quad (7) \\ \phi_0 & \rightarrow H_1, \phi_{0x} \rightarrow 0, u_0 \rightarrow u_1, P_0 \rightarrow \frac{1}{2}\rho g H_1^2 \end{aligned}$$

where the constants  $H_1$  and  $u_1$  denotes the depth and velocity far upstream respectively.

As for the far downstream boundary conditions, we follow Naghdi's assumption, i.e., far downstream the pressure distribution (in the three-dimensional theory) is uniform throughout the thickness of the fluid sheet and is equal to the atmospheric pressure  $p_0$ . This assumption leads to the following boundary conditions:

$$\begin{aligned} \text{as } x \rightarrow +\infty \\ \phi_o \rightarrow H_4, \quad \phi_{ox} \rightarrow 0, \quad \phi_{oxx} \rightarrow 0, \quad P_o \rightarrow 0 \end{aligned} \quad (8)$$

where the constant vertical thickness  $H_4$  of the fluid sheet far downstream is to be determined in the course of solution.

#### Matching conditions

In order to obtain a solution which holds throughout ( $-\infty < x < +\infty$ ), the solutions in region I, II and III must be matched at  $x=-a$  and  $x=0$ . This matching is accomplished by using the standard jump conditions associated with the integral balance laws of the theory of a directed fluid sheet. Assuming that the fluid flows smoothly at  $x=-a$  and leaves the edge of the cliff smoothly at  $x=0$ , the appropriate two-dimensional form of the jump conditions for a fluid sheet of variable initial depth may be written as:

$$\begin{aligned} [\mu_o \phi_o]_{x=-a} = 0; \quad [\phi_o]_{x=-a} = 0; \\ [\phi_{ox}]_{x=-a} = -K; \quad [P_o]_{x=-a} = 0 \end{aligned} \quad (9)$$

and

$$\begin{aligned} [\mu_o \phi_o]_{x=0} = 0; \quad [\phi_o]_{x=0} = 0; \\ [\phi_{ox}]_{x=0} = 0; \quad [P_o]_{x=0} = 0 \end{aligned}$$

where the notation  $[f]$  stands for

$$[f]_x = f^{x+} - f^{x-}.$$

#### Results

Unfortunately, to date we have not been able to find experimental data for comparison with this development. Naghdi and Rubin (1981) using different (but equivalent) form of the Green-Naghdi method analyzed the waterfall spring from the flow over a flat bottom. For this case there are some experimental results from Rouse (1936). Figure 2 shows our calculated profile for this special case for  $Fr = 2.0$ , and  $H_1 = 0.9201$  meter. The shape and particularly the value of  $H_3 = 0.8889$  meter (at  $x = 0$ ) agree extremely well with the experiments.

Several cases with sloped bottoms have been calculated. The upstream height  $H_1 = 1$  meter. Figure 3 shows the flow profiles of fluid sheet with different upstream Froude Number ( $Fr=1.25, 1.5, 2.5$  and even  $8.0$ ) for a bottom slope  $K = 0.1$ .

#### 4. Future Research

Progress is now being made on performing similar calculations using GN Level II theory where the kinematic model for the vertical variation in velocity involves an additional term in both the horizontal and vertical velocities. That is, for Level II, the kinematic approximation corresponding to (1) is

$$\begin{aligned} u(x, z, t) = u_o(x, t) + u_1(x, t)\zeta \\ v(x, z, t) = v_o(x, t) + v_1(x, t)\zeta + v_2(x, t)\zeta^2 \end{aligned} \quad (10)$$

With this kinematic model it is possible to treat the flow over a weir (Figure 4). In particular, it is possible to model the jet streaming vertically from the gate of the weir.

#### Relation to Plunging Breakers

Consider the flow in a wave approaching a beach and experiencing the effects of shoaling. At any instant of its evolution, a stagnation streamline separates the flow downstream of the crest (i.e., towards the beach) from that upstream (towards the ocean). Before the wave breaks this streamline terminates at the crest. However, as the wave begins to break, this streamline bends over and a jet is formed creating the plunging part of the breaker. The upstream flow including the jet is not unlike the unsteady flow over a weir as sketched in Figure 5. Use of the GN method to model this evolution would require treating the downstream (beachside) flow as a separate fluid sheet with appropriate matching conditions. Further, such a model would also require some treatment of the impact of the jet with the water in the downstream sheet. This process is clearly non-conservative and would take some care to develop.

#### 5. References

- Shields, J. and Webster, W. "Applications of High-Level, Green-Naghdi theory to Fluid Flow Problems". IUTAM Symposium on Marine Dynamics, Brunel University, London, June 1990.
- Kim, J.-W. and Webster, W. C., "A numerical computation of capillary-gravity waves in deep water" (with J.-W. Kim). 11<sup>th</sup> Workshop on Water Waves and Floating Bodies, Hamburg, Germany, 1996.
- Naghdi, P.M. and Rubin, M.B., "On inviscid flow in a waterfall". J. Fluid Mech., Vol.103, pp 375-387, 1981.
- Rouse, H. 1936 Civil Engineering, Vol 6, pp257.

## 6. Acknowledgement

The research reported herein was supported in part by a grant from the National Sea Grant College Program, National Oceanic and Atmospheric Administration, US Department of Commerce, under grant number NA36RG0537, project number R/OE-34 through California Sea Grant College, and in part by the California State Resources Agency. The views expressed herein are those of the author and do not necessarily reflect the views of NOAA or any of its sub-agencies. The US Government is authorized to reproduce and distribute for governmental purposes.

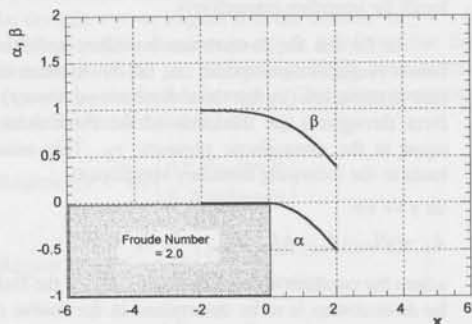


Figure 2. Waterflow springing from a flat bottom

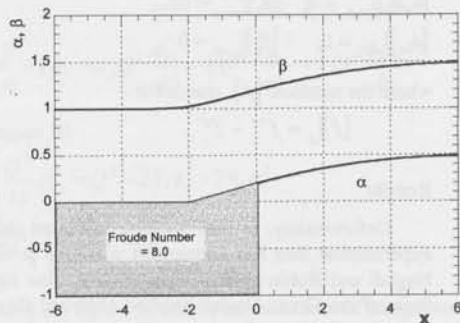
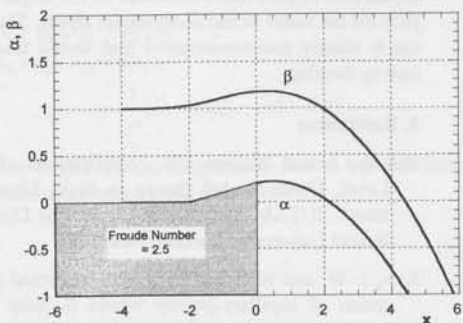
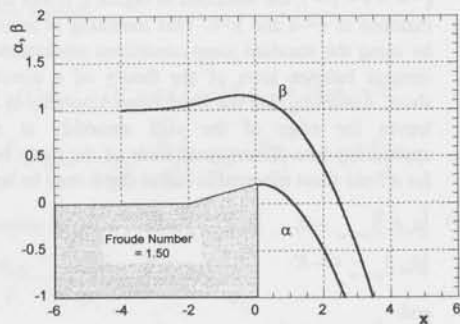
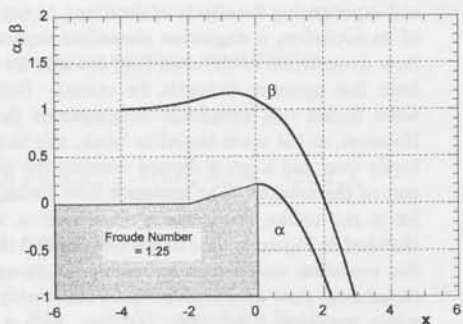


Figure 3. Effect of Froude number on waterfall springing from a sloped bottom

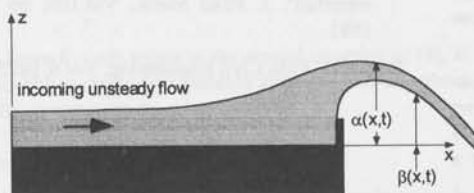


Figure 4. Schematic of Flow over a Weir

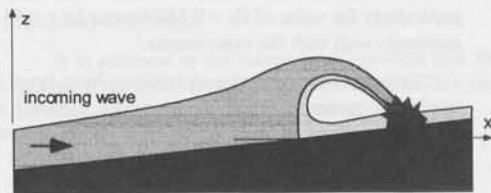


Figure 5. Schematic of Plunging Breaker Flow

## Applying the Finite Element Method in numerically solving the two dimensional free-surface water wave equations

Jaap-Harm Westhuis

Faculty of Applied Mathematics, University of Twente, The Netherlands  
& MARIN, Wageningen, The Netherlands

Andonowati

Faculty of Applied Mathematics,  
University of Twente, The Netherlands

### 1 Introduction

As part of the research project 'a scientific infrastructure for laboratory generated surface waves', we have been developing a computer code to simulate free surface water waves on a two dimensional bounded domain. It is well known that if the water is assumed to be inviscid, incompressible and irrotational, the velocity field of the water can be characterized with a potential function.

The set of equations describing the dynamic behaviour contains two time dependent conditions at the free surface (dynamic and kinematic boundary conditions) and Laplace's equation for the potential in the interior of the water domain. At this moment we have assumed the other boundaries to be fixed and impermeable, but our research aims at including moving wave generators and beaches.

When the equations are linearized, they can be solved in the frequency domain, but for some applications solutions of the original equations are necessary. In order to solve the nonlinear equations, the nonlinear time dependent free surface equations have to be integrated over time and at every time stage Laplace's equation has to be solved on the region bounded by the free surface and the fixed walls.

Solving Laplace's equation is the most computer-time consuming part of the numerical computations. For this reason a boundary integral description of Laplace's equation is usually discretized (e.g. boundary element method), thus reducing the number of unknowns. However, computing the coefficient matrix and solving the full matrix associated with the BEM formulation are computational intensive procedures.

Instead of using a boundary element method, we have implemented a finite element method (triangular elements and linear base functions) to solve Laplace's equation. The use of a finite element method was initiated by the article 'A finite element method for fully nonlinear water waves' by Xing Cai, et. al. (1996). In this article a method based on a time-dependent mapping of the water domain to a fixed computational rectangle is proposed. Numerical calculations have shown however that discretizing

the domain directly and thus regriding the nodes at every time-stage gives more accurate results.

Although the number of unknowns using FEM is larger than using BEM, evaluation of the elements of the associated sparse matrix is relatively fast and because of the banded and symmetric structure of the matrix an efficient Gauss-Elimination solver can be used.

## 2 Contents of the presentation

We will discuss the benefits and limitations of applying a finite element method to solve the nonlinear wave equations numerically. The main advantages seem to be:

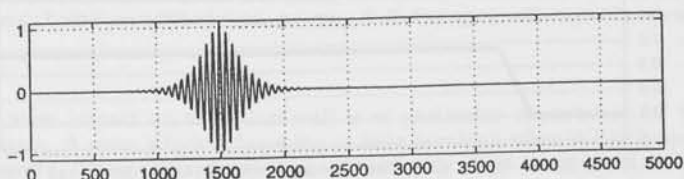
- speed and memory usage: we have applied our code (on a pentium PC) to a wavegroup propagation problem that could not be computed using a BEM without domain decomposition (on a Cray C98)
- flexibility: the finite element grid is constructed inside the domain, providing more control over the numerical accuracy near critical geometries.

Results will be presented of comparisons in which we have applied the numerical code to the following three problems that have relative simple geometries:

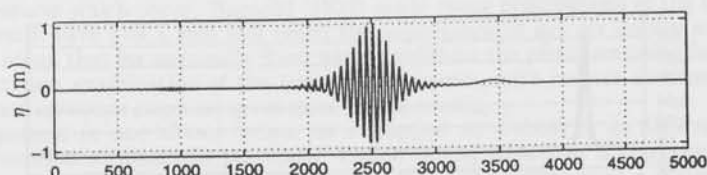
- Sloshing wave: compared with results of the sloshing wave problem in 'Comparative study of fully non-linear wave simulation programs' initiated by Det Norske Veritas, 1994. Given the dimensions of the water tank ( $70m \times 160m$ ) and an initially steady surface profile, participants in the comparative study were asked to compute the surface elevation at  $t=9.2s$  at  $x=60m$ . For our computations we used a  $70 \times 160$  grid, a 5 stage 4'th order RK method and a timestep of  $\Delta t = 0.1$ . The table below summarizes their results added with the result obtained by using our code.

part. nr.	results	part nr.	result
1	-3.803	5	-3.820
2	-3.860	6	-3.803
3	-3.815	7	-3.720
4	-3.759	our result	-3.798

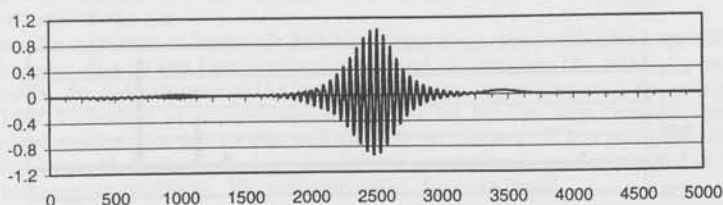
- Propagation of wavegroups: compared with results in the PhD thesis 'Numerical simulation of nonlinear water waves using a panel method; domain decomposition and applications' by Paul de Haas, 1997. The figures on the next page show the initial surface of the wavegroup (propagating to the right), the result obtained by Paul de Haas at  $t = 180$  and the result of our computations at  $t = 180$  using a  $2001 \times 7$  grid. The depth of the water is 12 meters and in both computations  $\Delta t = 0.3$



- Wavegroup: initial surface profile of the wavegroup

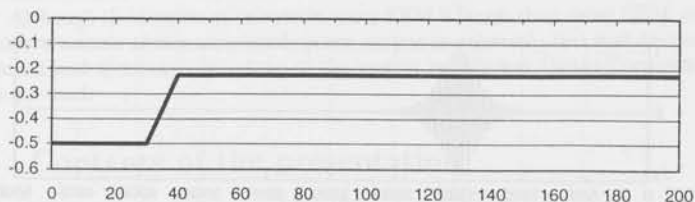


- Wavegroup: surface after 180 seconds computed by Paul de Haas using a panel method and domain decomposition (copied from his thesis)

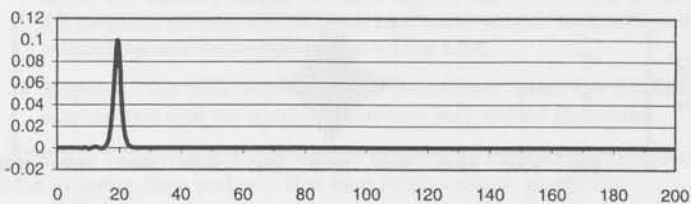


- Wavegroup: surface after 180 seconds computed with our code (no domain decomposition and on a desktop PC)

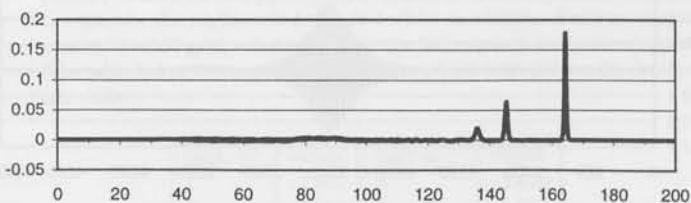
- Soliton splitting over a varying bottom: compared with results from the paper 'BEM-numerics and KdV-model analysis for solitary wave split-up' by E. van Daalen, E. van Groesen and S. Pudjaprasetya in *Computation Mechanics*, vol 19: 197-187, 1997. The figures on the next page show the topography and the computed surface at  $t=8$  and  $t=80$  of a solitary wave propagating to the right and splitting into three solitons. For this computation a uniform grid ( $2001 \times 6$ ) and a 5 stage 4<sup>th</sup> order Runge-Kutta time integration with  $\Delta t = 0.1$  were used.



-Soliton splitting: used bottom topography



-Soliton splitting: solitary wave before splitting at  $t = 8s$  propagating to the right.



-Soliton splitting:  $t = 80s$ , original solitary wave has split into three separate solitons

### 3 Conclusion

A FEM based numerical solver for the kind of problems as described above seems to be a good alternative for conventional boundary integral methods. Although more work has to be done to investigate accuracy, stability and applicability to a wider range of problems, results so far are encouraging. Future objectives are to implement higher order FEM base functions, incorporate moving boundaries, introduce realistic wave absorbers (as are being used in hydrodynamic laboratories) and to implement the code for three dimensional situations.

## Pressure-impulse theory for water wave impact on a structure with trapped air.

D.J.Wood and D.H. Peregrine

School of Mathematics, University of Bristol, Bristol BS8 1TW, UK  
e-mail: deb.wood@bristol.ac.uk, D.H.Peregrine@bristol.ac.uk

### Introduction

Research into wave impact on a vertical wall is of particular importance for the design of sea walls and breakwaters. A wave which is breaking or near breaking when it hits a structure can cause large peaks in pressure. These pressures though often of very short duration (1ms in the laboratory, 10-50ms in prototype), are sometimes substantial enough to shift or blow holes in a coastal structure. When a wave is breaking or near breaking when it hits a structure often a large amount of air becomes trapped. The amount of air which is trapped and the manner in which it is present has a significant effect on the pressures which occur. Bagnold (1939) made many observations of the impact pressures which occur when a wave hits a wall and noted the importance of any air pocket which may occur. In particular he noted that for nominally fixed wave conditions the pressures occurring vary from one wave to the next, but examination of the integral of pressure, with respect to time, over the short duration of impact (pressure-impulse) gives more stable results.

Air can be present in one of two forms: as a trapped air bubble or as dispersed air, or most likely as a combination of both. In particular Topliss (1994) looked at a theoretical model of the trapped air using an oscillating cylindrical air bubble. Peregrine (1994) gives a review of some of the methods used to model air entrainment/trapping during impact. Peregrine and Thais (1996) model scaling for entrained air in violent water wave impacts by using a 'filling flow' model (where a region is rapidly filled with liquid), following on from Peregrine and Kalliadasis (1996). This model has many similarities to the 'flip through' flow. Peregrine and Thais give an estimate of the reduction in pressure caused by the presence of the air.

In this section we consider a large air bubble trapped at the wall which produces oscillatory pressures. The impulse due to the first oscillation instead of bringing the water to rest, may bounce the water backwards. So the velocity of the part of the wave impacting may reverse in sign. Cooker and Peregrine (1990 b) looked at a pressure-impulse model for the 'flip through' conditions which corresponds to water motion normal to the wall ceasing on impact. If the compressed air causes the water to be pushed back, then the boundary conditions corresponding to a reversal of the component of velocity may be more appropriate. We call this effect 'bounce back'.

### Pressure-impulse for 'bounce back'

We extend the Cooker and Peregrine (1990 a,b, 1992, 1995) model for impact of a wave on a vertical wall to allow for a trapped air bubble. We begin by assuming that the bounce back velocity is equal in magnitude, but opposite in sign to the ingoing velocity of the wave. Figure 1 shows pressure-impulse contour plots for the no 'bounce back' and 'bounce back' situations, where the bubble is supposed to be thin. The peak  $P$  is almost twice as big for the bounce back situation as for the no bounce back case. Pressure-impulse contours give a fair approximation to maximum pressure contours if a good estimate of impact duration is available. However in the case of bounce back, the time scale is dependent on the compression of the air, and hence is longer. Since bounce back gives a longer duration the estimated maximum pressures are generally smaller. If the duration is too long the pressure-impulse approximation becomes inappropriate.

### Experimental comparisons

Experimental comparisons are full of complications. Firstly it is unclear over which period of time we should integrate the pressures to obtain the pressure-impulse. To begin with we have made comparisons with data from Hattori and Arami (1992 and private communication) using a very simple analysis procedure. A triangular distribution of pressure against time was chosen. Hence the pressure-impulse was calculated by multiplying the rise time (the time taken for the pressure to rise from zero to its first peak value) by the first peak in pressure. Figure 2 shows a comparison of the pressure-impulse

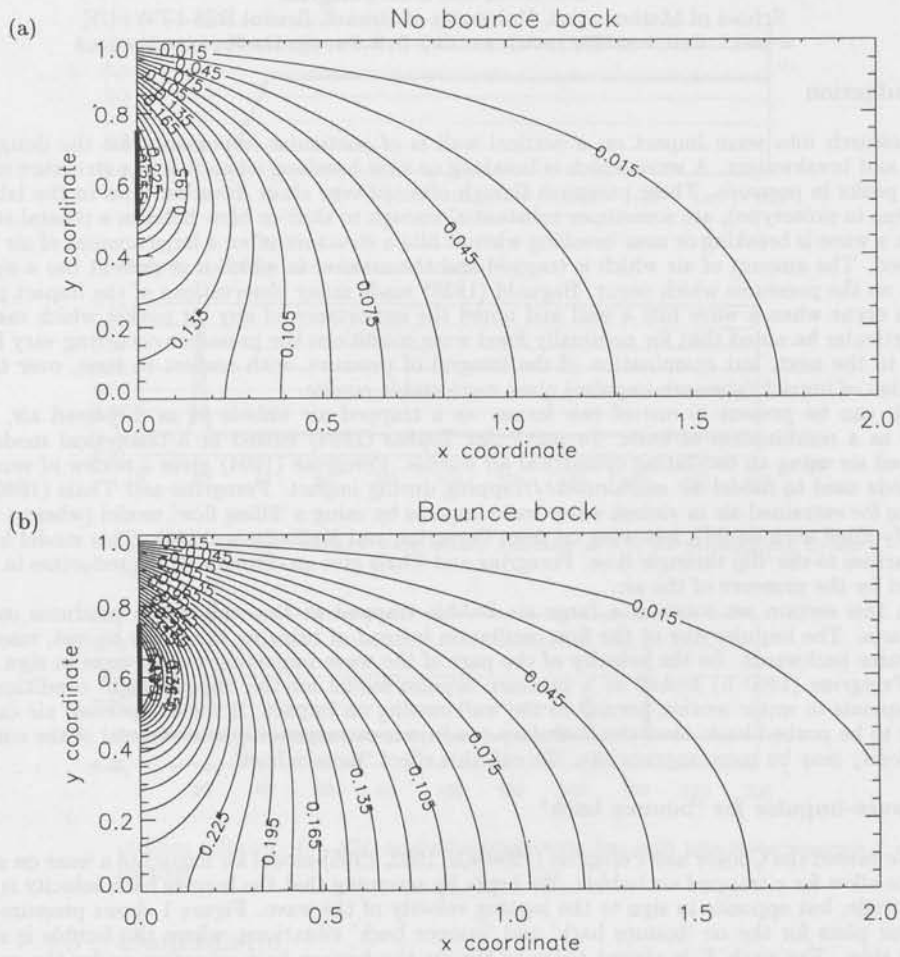


Figure 1: (a) Pressure-impulse contours for wave impact on a wall with no bounce back. (b) Pressure-impulse contours for wave impact on a wall with bounce back.

down the wall obtained in these experiments and the pressure-impulse predicted by the Cooker and Peregrine 2D wall impact model and the 'bounce back' model. The bubble position is denoted by a dark line. The 'bounce back' and 'no bounce back' are over and under predictions in comparison with some of the experimental data. The magnitude of the pressure-impulse is predicted reasonably well, but the shape of the pressure-impulse distribution is not reflected in the theoretical values. Total impulse for the 'bounce back', no bounce back and Hattori data are 1.746, 1.078 and 1.742 respectively. The value of total impulse is predicted well by using the 'bounce back' method, whereas the 'no bounce back' method under predicts.

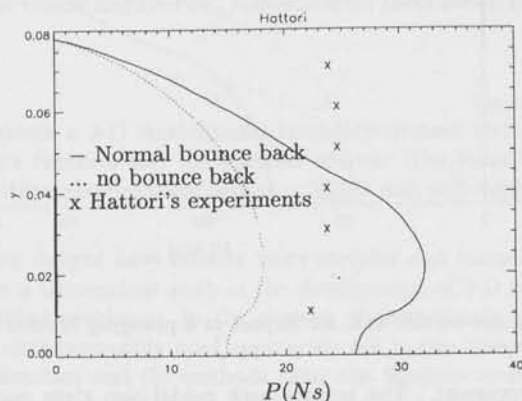


Figure 2: Pressure-impulse along the left hand wall, for 'bounce back', 'no bounce back' and Hattori's experiments (1992).

### Further comparisons

A relatively new method of experimentally obtaining a velocity profile for an impact is Particle Image Velocimetry (PIV). Oumeraci, Bruce, Klammer and Easson (1995) and Oumeraci, Partensky, Klammer and Kortenhaus (1997) describe PIV measurements made at the University of Edinburgh. We use these experiments to make further comparisons.

Two further improvements were carried out firstly in the numerical model and secondly in the analysis of the experimental data. As mentioned in the analysis of Hattori's experimental values, the 'bounce back' method produces values of pressure-impulse which are too high as we make an assumption that the bubble bounces back with the in going velocity. A more realistic approach is to consider the bubble bouncing back with a cosine velocity profile, i.e. that there is no 'bounce back' at the edges of the bubble and the maximum 'bounce back' is at the centre of the bubble. This is similar to considering the bubble as being spherical and just 'bouncing back' with a component of the velocity. This gives a slightly better prediction of the pressure-impulse.

Secondly a more complex analysis of the experimental data was used in order to separate the relatively slowly varying part of the pressure from the impulsive part. The pressure-impulse was calculated by integrating from the start in the rise in force, to the first 'flat' part of the force graph after the peak, keeping within the time limit within which pressure-impulse theory is valid. A triangular (or trapezoidal) distribution of pressure was subtracted off the pressure-impulse so as to remove the effect of a background pressure. Figure 3 shows the comparison of the Edinburgh PIV data and the 'bounce back' and no 'bounce back' prediction methods. The distribution prediction is far from perfect but adequate. The 'bounce back' model also gives good predictions along the berm in front of the wall.

### Conclusion

The 'bounce back' model gives predictions of within 40% of the experimental pressure-impulse values. Currently there has been little theoretical work carried out to model this problem, so even these

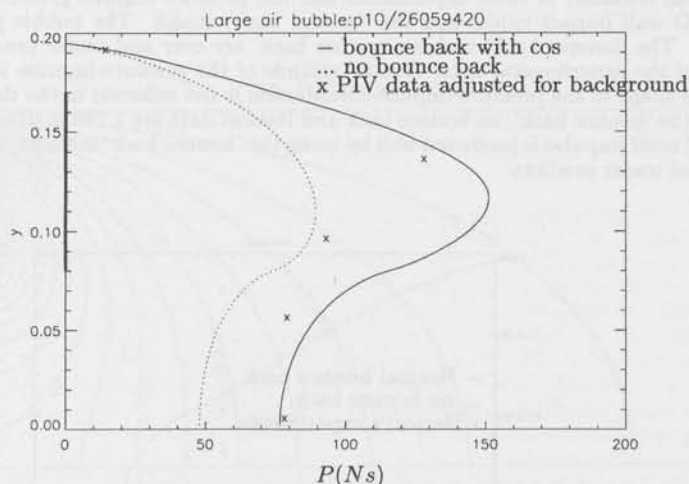


Figure 3: Pressure-impulse on the wall, for impact of a plunging breaker trapping a large air pocket

estimates are an improvement. The bounce back model also gives good predictions for pressure-impulse along a berm in front of a vertical wall. It is hoped to use new experimental data from the MAST 3 project (details below) to compare and improve the model of impact with air.

#### Acknowledgements

Support of the U.K. EPSRC, and the European Commission, Directorate General XII, Science, Research and Development, contract number MAS3-CT95-0041, is gratefully acknowledged.

#### References

- BAGNOLD, R.A. (1939). Interim report on wave pressure research. *J. Inst. Civil Engrs* **12**, 201-226.
- COOKER, M.J. & PEREGRINE, D.H. (1990a). Violent water motion at breaking wave impact. *Proc. 22nd Internat. Conf. Coast. Engng., ASCE* 164-176.
- COOKER, M.J. & PEREGRINE, D.H. (1990b). A model for breaking wave impact pressures. *Proc. 22nd Internat. Conf. Coast. Engng., ASCE* 1473-1486.
- COOKER, M.J. & PEREGRINE, D.H. (1992). Wave impact pressure and its effect upon bodies lying on the sea bed. *Coastal Engng.* **18**, 205-229.
- COOKER, M.J. & PEREGRINE, D.H. (1995). Pressure-impulse theory for liquid impact problems. *J. Fluid Mech.* **297**, 193-214.
- HATTORI, M. & ARAMI, A. (1992). Impact breaking wave pressures on vertical walls. *Proc. 23rd Internat. Conf. Coast. Engng., ASCE*, vol2, 1785-1798.
- OUMERACI, H., BRUCE, T., KLAMMER, P., EASSON, W.J. (1995). Breaking wave kinematics and impact loading of caisson breakwaters. *Proceedings Internat. Conference on Coastal and Port Engng. in Developing Countries (COPEDEC), Rio de Janeiro, Brazil* Vol. 4, Part 3, 2394-2410.
- OUMERACI, H., PARTENSKY, H.-W., KLAMMER, P., KORTENHAUS, A. (1997). Entwicklung von Bemessungsgrundlagen fuer monolithische wellenbrecker. *Abschlussbericht zum forschungsvorhaben, Braunschweig, Germany* 49pp, 5 Annexes. Unpublished. In German.
- PEREGRINE, D.H. (1994). Pressure on breakwaters: a forward look. *Internat. Workshop on Wave Barriers in Deep Waters*, Port and Harbour Research Institute, Japan, ed. T. Takayama, 553-573.
- PEREGRINE, D.H. & KALLIADASIS, S. (1996). Filling flows, coastal erosion and cleaning flows. *J. Fluid Mech.* **310**, 365-374.
- PEREGRINE, D.H. & THAIS, L. (1996). The effect of entrained air in violent water wave impacts. *J. Fluid Mech.* **325**, 377-397.
- TOPLISS, M.E. (1994). Water wave impact on structures. Ph.D. dissertation, University of Bristol.

## A Hybrid Boundary-Element Method for Non-Wall-Sided Bodies with or without Forward Speed

Sheguang Zhang, Woei-Min Lin & Kenneth Weems  
Ship Technology Division, SAIC, Annapolis, MD 21401, U.S.A.  
Dick K.P. Yue

Department of Ocean Engineering, Massachusetts Institute of Technology, USA

### 1. Introduction

This paper presents a 3-D time-domain boundary-element method using a combination of the transient Green's function and the Rankine source. The focus of this study is to solve free-surface ship hydrodynamics problems involving highly non-wall-sided ship geometries with or without forward speed.

As practical ship designs have become more complex and computer capabilities have advanced, there has been a tremendous push in the development of 3-D time-domain methods for solving sea-keeping related problems. In the context of time-domain potential flow boundary-element methods, the most commonly used approaches fall in two categories: (1) methods using the transient Green's function and (2) methods using the Rankine source. In the first category (e.g. Lin, et al, 1994), the transient Green's function satisfies the linearized free-surface boundary condition and the far field radiation condition, so that the singularities need to be distributed on the wetted body surface only. For ships with highly non-wall-sided geometry, numerical difficulties may arise in the area where the intersection angles between the body surface and the free surface become small. This is mainly due to the highly oscillatory nature of the transient Green's function adjacent to the free surface. In the second category (e.g. Nakos, Kring & Sclavounos, 1993), the Rankine source is used as a kernel in the boundary integral equation. The Rankine source is fairly robust for modeling either wall-sided or non-wall-sided geometry. To satisfy the free-surface boundary condition, the Rankine source has to be distributed not only on the body surface but also on the free surface. In order to limit the size of the computation domain, the free surface region is typically truncated at several ship lengths away from the ship and an ad-hoc numerical damping zone has to be employed to absorb the wave energy.

In view of the pros and cons of the two methods, a natural and optimal choice is to take full advantage of the two methods by using a combination of the transient Green's function and the Rankine source in formulating the approach. This hybrid method has recently been developed by the authors for motion and load computations of modern hull forms with highly non-wall-sided geometry. In this method, the fluid domain is divided, through a matching surface, into an inner domain and an outer domain. In the inner domain, the Rankine source is employed. In the outer domain, the transient Green's function is used. The transient Green's function satisfies both the linearized free-surface boundary conditions and radiation condition, implying that the matching surface can be placed fairly close to the body.

Some developments based on this type of hybrid method have been made in recent years. Dommermuth & Yue (1987) solved a nonlinear axisymmetrical flow with a free surface; Yeung & Cermelli (1993) calculated forced heaving motion of a 2-D submerged body with a free surface. Using similar approach but a different Green's function in the outer domain, Sierewogel, Hermans & Huijsmans (1996) solved the linear problem of a 3-D floating body with forward speed. The progress made in the present study includes development and validation of a body-nonlinear hybrid

boundary-element method as well as application of the method to highly non-wall-sided bodies with or without forward speed.

## 2. Approach

The fluid flow is described by the potential flow theory. As shown in Figure 1, the fluid domain is decomposed into an inner domain ( $I$ ) and an outer domain ( $II$ ). The inner domain is enclosed by the wetted body surface  $S_b$ , a part of the free surface  $S_f$  surrounding the body, and a matching surface  $S_m$  away from the body, while the outer domain is enclosed by  $S_m$ , the remaining free surface and an imaginary surface  $S_\infty$  at infinity. In the inner domain, the boundary integral equation in terms of the Rankine source is expressed as

$$2\pi\Phi^I(\vec{p}) + \int_{S^I} (\Phi^I G_n - \Phi_n^I G) dS = 0 \quad (1)$$

where  $\Phi^I$  is the disturbance velocity potential in domain  $I$ ,  $G = 1/|\vec{p} - \vec{q}|$ ,  $(\vec{p}, \vec{q}) \in S^I = S_b \cup S_f \cup S_m$  with  $\vec{p}$  and  $\vec{q}$  denoting the field point and source point, respectively. The subscript  $n$  denotes the directional derivative with respect to the outward normal  $n$  on  $S^I$ . In the outer domain, the boundary integral equation in terms of the transient Green's function is written as

$$2\pi\Phi^{II}(\vec{p}) + \int_{S_m} (\Phi^{II} G_n^0 - \Phi_n^{II} G^0) dS = M(\vec{p}, t) \quad (2)$$

where  $\Phi^{II}$  is the disturbance velocity potential in domain  $II$ . The memory function  $M(\vec{p}, t)$  is

$$M(\vec{p}, t) = \int_0^t d\tau \left\{ \int_{S_M} (\Phi^{II} G_{\tau n}^I - \Phi_n^{II} G_\tau^I) dS + \frac{1}{g} \int_{\Gamma_M} (\Phi^{II} G_{\tau\tau}^I - \Phi^{II} \tau G_\tau^I) V_N dL \right\} \quad (3)$$

where  $\Gamma_M$  is the water line of the matching surface,  $V_N$  is the outward normal velocity of  $\Gamma_M$  relative to domain  $I$ , and  $G^0$  and  $G^I$  are associated with the transient Green's function (see Lin & Yue (1990) for details). The matching surface  $S_m$  is treated as a control surface and moves with the body. On  $S_m$ , the matching conditions are imposed, requiring the disturbance velocity potentials in the inner and outer domains are continuous, so are their normal derivatives. This forms a coupled equation system for the velocity potential  $\Phi^I$  on  $S_b$ ,  $\Phi_n^I$  on  $S_f$ , and  $\Phi^I$  and  $\Phi_n^I$  on  $S_m$ .

On the body surface  $S_b$ , the nonlinear body-boundary condition is satisfied on the wetted body surface under the undisturbed incident wave profile. On the free surface  $S_f$  in the inner domain, the linearized free-surface boundary conditions are satisfied on the incident wave surface. The resulting hyperbolic equations for the disturbance velocity potential and the disturbance free surface elevation are solved with fourth order Adams-Bashforth-Moulton formulas for time integration and the second order upwind finite difference for the gradient calculations. The solution is obtained at each time step in order to update the linearized free-surface boundary condition on  $S_f$ .

## 3. Results

To illustrate that the present method is suitable for non-wall-sided bodies, the calculation of a flared body undergoing forced large-amplitude heaving motion is carried out. The calculated hydrodynamic force as shown in Figure 2 agrees quite well with the experimental result (Troesch & Wang, 1994) and a fully nonlinear calculation. This is a significant improvement over the method using the transient Green's function, which gives non-physical high-frequency oscillations in the hydrodynamic force results for this non-wall-sided body.

Another example related to a non-wall-sided body moving with forward speed is presented in Figure 3. In this figure, the motion of a modern Navy ship (CG47) with a large bow flare traveling in storm-sea condition is presented. It shows that the calculation using the present hybrid boundary-element method is very close to experimental measurements.

Further validation of the method is underway concerning the calculation of large amplitude ship motions involving "bow-out-of-water" and water-entry phenomena.

### References

- Dommermuth, D.G. & Yue, D.K.P. (1987), "Numerical Simulations of Nonlinear Axisymmetric Flows with a Free Surface", *J. Fluid Mech.*, Vol. 178, pp. 195-219
- Sierevogel, L., Hermans, A. & Huijsmans, R. (1996), "Time-Domain Calculations of First- and Second-Order Forces on a Vessel Sailing in Waves", *Proc. 21st Symp. Naval Hydro.*, Trondheim, Norway.
- Lin, W.M., Meinhold, M., Salvesen, N. & Yue, D.K.P. (1994), "Large-Amplitude Motions and Wave Loads for Ship Design", *Proc. 20th Symp. Naval Hydro.*, The University of California, Santa Barbara, CA, U.S.A.
- Nakos, D.E., Kring, D. & Sclavounos, P.D. (1993), "Rankine Panel Methods for Transient Free-Surface Flows", *Proc. 16th Symp. Naval Hydro.*, Iowa City, Iowa, U.S.A.
- Troesch, A.W. & Wang, M. (1994), "An Experimental Study for Slamming Flow and Green Water on Deck", *Technical Report No. 327*, Dept. of Naval Arch. & Marine Eng., Univ. of Michigan.
- Yeung, R. & Cermelli, C.A. (1993), "The Shell Functions: A Global Method for Computing Free-Surface Time-Dependent Flows", *Proc. 8th Int. Workshop Water Waves & Floating Bodies*, St. John's, Newfoundland,

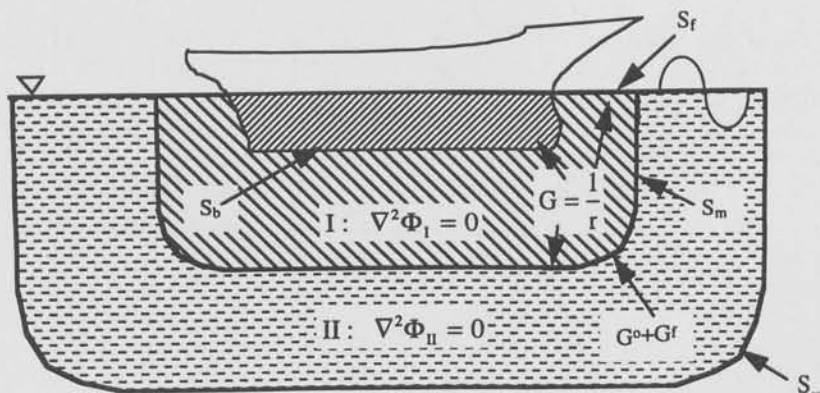


Figure 1: The definitions of the two fluid domains and boundaries used in the hybrid boundary-element method

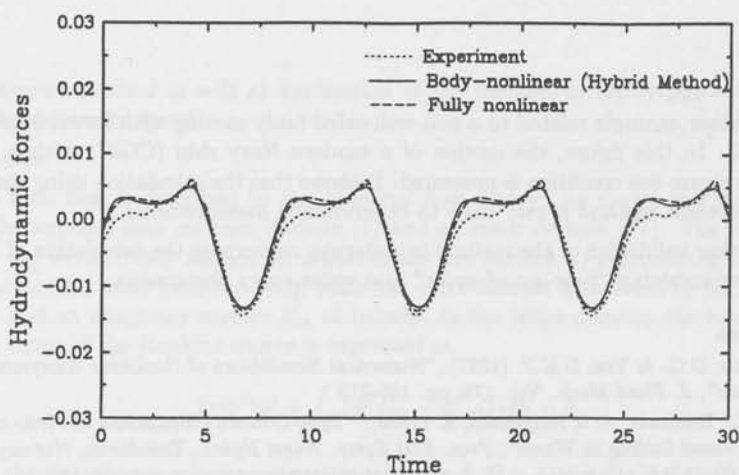


Figure 2: The nondimensional hydrodynamic heaving force versus time for a forced-heaving flared body with  $f = 0.6H_z$  and  $a = 2.1in$ .

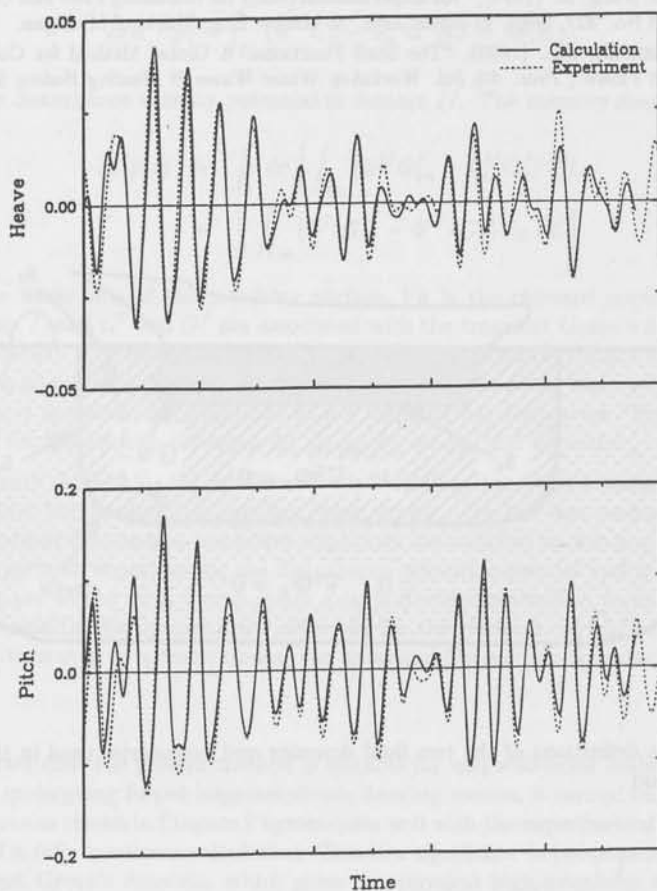


Figure 3: Nodimensional heave and pitch motions of CG47 traveling at 10 knots in head sea and storm condition.

